STRUCTURAL SYSTEMS

RESEARCH PROJECT

Report No.
SSRP-06/22

CYCLIC BEHAVIOR OF STEEL COLUMNS WITH COMBINED HIGH AXIAL LOAD AND DRIFT DEMAND

by

JAMES NEWELL

CHIA-MING UANG

Final Report to American Institute of Steel Construction, Inc.

December 2006

Department of Structural Engineering
University of California, San Diego
La Jolla, California 92093-0085

University of California, San Diego
Department of Structural Engineering
Structural Systems Research Project

Report No. SSRP-06/22

Cyclic Behavior of Steel Columns with Combined High Axial Load and Drift Demand

by

James Newell
Graduate Student Researcher

Chia-Ming Uang
Professor of Structural Engineering

Final Report to American Institute of Steel Construction, Inc.

Department of Structural Engineering
University of California, San Diego
La Jolla, California 92093-0085

December 2006

ABSTRACT

Nonlinear time-history analysis of steel braced frames, especially buckling-restrained braced frames (BRBF), subjected to earthquake ground motions has revealed that columns in the bottom stories are often subjected to combined high axial load and inelastic rotation demand resulting from story drift. The reliability of column members under this reversing high axial loads and drift demand has not been previously experimentally verified. To provide a basis for performance evaluation of columns under high axial load and drift demand, nine W14 section column specimens have been subjected to laboratory and analytical investigation.

Since a loading protocol for column testing did not exist, the first phase of this project consisted of development of a statistically based loading sequence for braced frame column testing. 3-story and 7-story BRBF prototype building models were designed and analyzed. Nonlinear time-history analysis of frame models, subjected to a suite of 20 properly scaled earthquake ground motions, was conducted. Time histories of first-story drift ratio for the 20 records were processed using a rainflow cycle counting procedure. Statistical analysis was used to quantify maximum and cumulative story drift and maximum column axial load demand for development of a reasonable loading sequence for experimental testing. The first step in the developed loading protocol consisted of imposing a compressive axial load offset of $0.15P_n$ to simulate gravity load. Then in-phase, increasing amplitude cyclic axial load and story drift were applied.

The experimental program consisted of cyclic testing nine full-scale fixed-base columns. ASTM A992 steel wide-flange sections typical of braced frame columns, representing a practical range of flange and web width-to-thickness ratios, and 15 ft story height were subjected to different levels of axial force demand (35%, 55%, and 75% of column yield strength) combined with story drift demand of up to 10% for these simulated first-story columns. Column specimens were tested at the University of California, San Diego (UCSD) Seismic Response Modification Device (SRMD) Test Facility.

The test data agreed well with the established *P-M* interaction surface. Significant overstrength was observed between the test data and the *P-M* interaction

surface based on nominal material properties. Specimens achieved drift capacities of 7% to 9%, corresponding to a ductility of approximately 10. These drift capacities were calculated assuming a 10% reduction from peak moment resistance was used to define the drift capacity. These drift capacities were more than four times the expected BRBF story drift from earthquake nonlinear time-history analysis. For all specimens only minor yielding was observed at a story drift of 1.5%, the maximum expected drift from nonlinear time-history analysis. Flange local buckling was observed for all specimens with the exception of Specimen W14×370-35. No web local buckling was observed. The relatively small amplitude of flange local buckling observed at 6% drift (more than three times the maximum expected drift) provided an indication that strength degradation due to flange local buckling is not expected to present a problem for the seismic design of the tested W14 column sections.

The finite element program ABAQUS was used to model the steel column specimens. Models predicted global behavior, yielding, and strength degradation resulting from local buckling at large drifts. Models were subjected to both monotonic and cyclic loading sequences. Analysis results were observed to be well correlated with experimental results. It was determined that a typical initial residual stress distribution did not significantly effect the *P-M* interaction or moment versus drift response. The behavior of deep columns with higher width/thickness ratios than the tested W14 sections was also investigated. Models of W27 deep column sections showed significant strength degradation due to flange and web local buckling.

ACKNOWLEDGEMENTS

Funding for this project was provided by the American Institute of Steel Construction; Mr. Tom Schlafly was the project manager. Nucor-Yamato Steel Company donated specimen wide-flange sections and Mittal Steel donated material for specimen base plates. Fabrication services were donated by Schuff Steel Company. Review comments from the AISC Task Oversight Committee were very helpful in the loading protocol development phase of this project. Dr. Atsushi Sato and Mr. Jong-Kook Hong provided much appreciated assistance with instrumentation and testing. Technical assistance from the staff at the Seismic Response Modification Device (SRMD) Test Facility at the University of California, San Diego was greatly appreciated.

TABLE OF CONTENTS

LIST OF FIGURES

LIST OF TABLES

LIST OF SYMBOLS

A_{sc}	Area of Buckling-Restrained Brace steel core
D	Dead load
E	Modulus of elasticity
H	Column clear length
I_x	Moment of inertia about the x-axis
K	Initial stiffness
L	Live load
M	Moment
M_p	Plastic moment
M_{pa}	Actual plastic moment of the column
M_{pn}	Nominal plastic moment of the column
P	Axial load
P_G	Axial load from gravity load
P_L	Longitudinal force from SRMD
P_n	Nominal axial strength
P_S	Axial load from seismic load
P_T	Target column compressive axial load
P_y	Yield strength
P_{yn}	Nominal yield strength
P_{ya}	Actual yield strength
P_{yc}	Compressive yield strength
P_{yt}	Tensile yield strength
S_a	Site-specific MCE spectral response acceleration
S_{D1}	5% damped design spectral response acceleration parameter at a period of 1 sec.
S_{DS}	5% damped design spectral response acceleration parameter at short periods
T	Fundamental period of the building
T_0	$=0.2\ S_{D1}/S_{DS}$
T_1	First mode period of vibration

T_2 Second mode period of vibration

T_a Approximate fundamental period of the building

T_S $=S_{D1}/S_{DS}$

V Lateral force from SRMD

b_f Flange width

d_c Column depth

h Clear distance between flanges less the fillet or corner radius for rolled shapes

h_n Height above base to uppermost level of building

t_f Flange thickness

t_w Web thickness

Δ Lateral displacement from SRMD

θ_y Yield rotation

λ_{ps} Limiting slenderness parameter for compact element

1. INTRODUCTION

1.1 General

Use of buckling-restrained braced frames (BRBFs) as a seismic force resisting system is gaining increased popularity among the U.S. structural engineering community. It is anticipated this trend will continue as the *2005* AISC *Seismic Provisions for Structural Steel Buildings*, and U.S. model building codes adopt this system. Experimental testing has shown stable hysteretic behavior of individual buckling-restrained braces (BRBs) tested in a uniaxial and subassembly configuration (Wantanabe et al. 1988, Wantanabe 1992, Aiken et al. 2000, Black et al. 2002, Merritt et al. 2003a, 2003b, 2003c, Uang and Nakashima 2004, Newell et al. 2005, 2006).

Nonlinear static and time-history analysis of BRBFs conducted for research purposes and design validation has revealed columns in BRBFs are subjected to high axial loads combined with large drift demand. BRBF models typically employ fixed-base columns and rigid beam-column joints where BRBs frame in with gusset plate connections. Analysis results have shown expected maximum story drift ratios of about 2% (Sabelli 2001). This level of drift results in inelastic rotational demand combined with high axial force demand at column bases and often at intermediate stories. Columns in concentrically braced frames and eccentrically braced frames are also subjected to inelastic rotational demand and high axial forces. The reliability of columns under this level of combined loading has not been experimentally validated.

1.2 Scope and Objectives

To provide the basis for performance evaluation of columns in braced frames subjected to reversing high axial loads combined with high drift demand, the objectives of this research are to: (1) develop a statistically based loading sequence for experimental testing beam-columns, (2) cyclically test nine full-scale W14 wide-flange section columns subjected to reversed, increasing amplitude axial load and drift demand, and (3) perform additional parametric studies using finite element analysis to extrapolate test results to columns that were beyond the scope of experimental testing.

2. LOADING PROTOCOL DEVELOPMENT

2.1 General

To develop a rational, statistically based loading sequence for braced frame column testing, 3-story and 7-story BRBF prototype building models were designed and analyzed. Nonlinear time-history analysis of frame models, subjected to a suite of 20 earthquake ground motions, was conducted. Time-histories of first-story drift ratio for the 20 records were processed using a rainflow cycle counting procedure. Statistical analysis was used to quantify maximum and cumulative story drift as well as maximum column axial load demand for development of a loading sequence for experimental testing.

2.2 Buildings for Column Demand Study

A 3-story and 7-story prototype buckling-restrained braced frame building, designed for a typical Los Angeles site, were used for loading protocol development. The 7-story building was a design example from *Steel TIPS* (Lopez and Sabelli 2004). Figure 2.1 shows a plan view and dimensions of the 7-story buildings. BRBFs in the north-south direction (2 braced bays per floor) were modeled as part of this study. Gravity loads used in the design of both the 3-story and 7-story buildings are given in Table 2.1. The 3-story building was specifically design for this study using the same plan dimensions and gravity loading as the 7-story *Steel Tips* building, except that the 3-story design used 10 psf partition load, whereas the 7-story design used 20 psf. Elevation views, dimensions, and member sizes for the two frames are provided in Figures 2.2 and 2.3.

2.3 Buckling-Restrained Braced Frame Models

2.3.1 Geometry

Models of the 3-story and 7-story BRBF were developed and analyzed with the nonlinear structural analysis program DRAIN-2DX (Prakash et al. 1992). Beam and column centerline dimensions were used to define model geometry. Beam-column connections with buckling-restrained braces (BRBs) framing in were modeled as fixed

connections to account for rigidity provided by the gusset plate connections. Panel zones were not modeled explicitly and panel zone deformations were neglected.

2.3.2 Modeling Technique

Beams and columns were modeled with inelastic beam-column elements. The axial force-moment yield surface for the beam-column elements is shown in Figure 2.4. A yield stress of 55 ksi and a post-yield stiffness equal to 5% of the elastic stiffness were used for all beam and column members.

BRBs were modeled with inelastic truss elements. It is common to specify a brace core plate yield stress of 42 ksi (±4 ksi) based on project specific tensile coupon testing (Lopez and Sabelli 2004). A brace tensile yield stress of 42 ksi was therefore used in the model. The compressive yield stress was 110% of the tensile yield stress, and the post-yield stiffness equal to 3% of the elastic stiffness, as is typical of BRB component test results (Black et al. 2002).

Gravity loads used in the models are given in Table 2.1. The gravity load combination of $1.2D + 0.5L$ per *International Building Code* (ICC 2006) was applied to the model frames during the static pushover and time-history analyses. Gravity loads for the half of the structure associated with each frame, but not directly acting on it, were applied to a P-delta column (see Figures 2.2 and 2.3). Rayleigh damping (mass and stiffness proportional damping) was used for all elements. Damping coefficients were based on 2% damping in the first and second modes for each frame.

2.3.3 Modal and Pushover Analyses

Fundamental natural periods determined from eigenvalue analysis of both model frames are given in Table 2.2. Also provided are the approximate first mode periods calculated using the empirical formula [Equation 12.8-7 in *Minimum Design Loads for Buildings and Other Structures* (SEI-ASCE 2005)].

A pushover analysis was performed for both model frames. The base shear was distributed over the height of the building as specified in the *International Building Code*. Figure 2.5(a and b) shows the base shear versus roof drift relationship and sequence of yielding for the 3-story BRBF. A plot of column axial load versus story drift ratio is

provided in Figure 2.5(c). Note that the column gravity load offset was equal to $0.12P_n$, where P_n equals the nominal axial compression strength. Figure 2.5(d) shows the axial load-moment (*P-M*) interaction curve for the first-story column base up to the point where the yield surface was reached at 2.5% first-story drift ratio. Figure 2.6 provides similar plots for the 7-story BRBF pushover analysis. The *P-M* interaction curve [Figure 2.6(d)] is shown up to 2.2% first-story drift ratio when the yield surface was reached. Column gravity load offset in this case was equal to $0.13P_n$. In both cases the column axial load versus story drift ratio shows an essentially bi-linear relationship similar to BRB demand.

2.4 Time-History Analysis

2.4.1 Earthquake Records

A suite of twenty large magnitude, small distance (LMSR) Los Angeles ground motion records were used for loading protocol development. These records have been used recently for other loading sequence studies (Krawinkler et al. 2003, Medina 2003, Richards and Uang 2003). The ground motion records are herein referred to as P01 to P20. Table 2.3 provides information on the event, source, peak ground acceleration, and duration of each record. Un-scaled acceleration time-histories are shown in Figure 2.7.

The typical LA site acceleration response spectrum for 5% damping, with S_{DS} = 0.64 and S_{D1} = 1.1 (see Figure 2.8), was adjusted to a 2% damping spectrum using the scaling procedure in FEMA 356 (FEMA 2000). The 5% damping spectrum values were divided by 0.8 to obtain the 2% damping spectrum. Both the 2% and 5% damping acceleration response spectra are shown in Figure 2.9.

Scale factors for the earthquake records were calculated to set the 2% damping spectral acceleration of each record equal to the 2% damping design spectral acceleration, at the fundamental natural period of each frame. Each ground motion record was scaled differently for each frame. Scale factors are provided in Table 2.4. Figures 2.10 and 2.11 show the response spectra for the scaled records along with the design spectrum. The vertical lines on these plots indicate the fundamental natural period of the frames. Figure 2.12 shows the average response spectra for the scaled earthquake records along with the design spectrum.

2.4.2 Analysis and Data Reduction

Both model frames were subjected to each of the 20 specifically scaled ground motion records. Story drift ratio (SDR), column, and BRB time-history responses were extracted from the analysis results. Typical results are provided in Appendix A for the 3-story BRBF subjected to records P09 and P14 and the 7-story BRBF for records P08 and P19. The figures show story drift ratio, first-story column axial load, and end moment time-histories along with the axial load-moment (*P-M*) interaction for one first-story column and BRB hysteretic response for each brace.

For loading protocol development, story drift ratio time-histories were converted into series of cycles using a simplified rainflow cycle counting procedure (Krawinkler et al. 2001, Ricahrds and Uang 2003). This process resulted in symmetric cycles defined by their *range* (change in peak-to-peak values from time-history) and ordered with decreasing range. Figures 2.13 and 2.14 provide story drift ratio rainflow cycle counting results for both frames and each of the 20 ground motions.

2.5 Column Demands

2.5.1 Story Drift Demand Parameters

The moment frame connection loading protocol in the AISC *Seismic Provisions* (2005) is an interstory drift angle based sequence. Similarly, the eccentrically braced frame (EBF) link-to-column connection protocol is a link rotation angle based sequence. Unlike the moment frame and EBF loading protocols, for testing of columns under high axial load and drift demand a dual parameter (i.e., axial load and story drift ratio) loading sequence is required. The development of this braced frame column testing protocol follows the same basic framework as was used in development of the steel moment frame connection loading sequence (Krawinkler et al. 2000) and the EBF link-to-column connection loading sequence (Richards and Uang 2003).

Number of Significant Cycles

The majority of story drift cycles that a column experiences during an earthquake are very small and do not significantly contribute to cumulative damage. But for almost all excursions greater than the yield drift, column axial load is close to its maximum

value. Thus, large elastic cycles and inelastic cycles need to be considered in loading protocol development. Cycles with ranges greater than one-half of the elastic range are considered to be damaging (Krawinkler et al. 2000). Columns are expected to remain elastic for all but a few excursions during even a significant earthquake. A loading sequence developed based on cycles greater than one-half the elastic range of the column would be unrealistically short. Demand on braced frame columns is directly related to demand imposed by the braces, which in the case of BRBs, are expected to undergo moderate inelastic deformation during a significant earthquake. The range of significant (damaging) story drift ratio cycles has been selected to correspond to one-half that expected at yield of the prototype building BRBs. A typical BRB axial yield displacement of 0.25 in. (Newell et al. 2005) would correspond to a story drift ratio at yield of 0.002 rad. for the prototype frames (chevron bracing configuration and brace inclination angle, θ, equal to about 45°). The elastic *range* (defined as peak-to-peak response) is, therefore, 0.004 rad. and one-half this range is 0.002 rad. Story drift ratio cycles with a range greater than 0.002 rad. are considered to be significant.

Number of "Large" Cycles

Large story drift ratio cycles are considered to be those with a range greater than 0.005 rad. These cycles contribute the most to column damage.

Cumulative Range

Damage to steel members under cyclic loading is assumed to be described by a cumulative damage model (Krawinkler 1996). Therefore, the sum of significant cycle ranges is an important measure of cumulative demand and, combined with experimental results, can provide an indication of when failure of a particular member may occur.

Maximum Drift Range and Maximum Drift

The maximum drift range is the largest symmetric cycle coming from the rainflow counting procedure (first cycle in the ordered cycles). The maximum drift is the largest excursion from the time-history results. This maximum drift should correspond to the point in the developed loading protocol where the cumulative demand is reached**.**

2.5.2 Demand from Time-History Analysis

Story drift ratio demand parameters for the 3-story BRBF under each ground motion record are shown in Figure 2.15. Story drift ratio demand parameters for the 7-story BRBF are shown in Figure 2.16. Column axial load demands for the 3-story and 7 story BRBFs are shown in Figures 2.17 and 2.18, respectively. Note that the axial load shown is a combination of gravity and seismic loads. Percentile values of demand parameters, shown in part (b) of Figures 2.15 to 2.18, are based on a lognormal distribution fit to the data shown in the corresponding part (a) figure. For loading protocol development, the number of significant cycles should be represented on average, so 50th percentile values are of interest. All other demand parameters should be represented conservatively in a loading protocol, so 90th percentile values are of interest (Krawinkler et al. 2000). Tables 2.5 and 2.6 summarize story drift ratio and column axial load demand parameters for the 3-story and 7-story frames. The 90th percentile values of column compressive axial load indicate that the target loads (e.g., $0.35P_y$, $0.55P_y$, $0.75P_y$) for this project were within a reasonable range.

2.6 Proposed Braced Frame Column Testing Protocol

A proposed loading sequence for braced frame columns subject to combined axial load and story drift ratio demand was developed, based on the results of the time-history analysis described above. The protocol is prescribed in terms of story drift ratio (see Table 2.7). Note that the initial step in the experimental protocol is application of gravity (compressive) load.

It was observed from the time history analysis that for all excursions larger than the yield drift the column axial load approached a constant maximum value. Therefore, column axial loads for the testing protocol were determined based on the elastic-perfectly plastic column axial load versus story drift ratio relationship shown in Figure 2.19. Calculation of column axial loads at the protocol drift levels are based on reaching the target column compressive axial load, P_T, (e.g., $0.35P_y$, $0.55P_y$, $0.75P_y$) at 0.002 rad. story drift ratio (yield drift) and axial loads for all excursions larger than the yield drift were equal to the maximum level for that specimen. The story drift and column axial load were in phase (see Figure 2.20) to represent realistic frame action.

Figure 2.21 shows the cumulative density functions (CDFs) from the first-story column drift cycle data and discrete CDFs for the proposed loading sequence. The CDF indicates the percentage of cycles having a range less than some given range. The protocol CDFs are below the analysis data CDFs, indicating that the protocol is conservative and contains a greater percentage of large amplitude cycles as compared with the data.

Table 2.1 Weights Used for Design and Analysis

(a) Roof Weights

Element	Loading (psf)
Roofing and Insulation	7.0
Steel and Concrete Deck	47.0
Steel Framing and Fireproofing	8.0
Ceiling	3.0
Mechanical/Electrical	2.0
Curtain Wall	15.0

(b) Floor Weights

Element	Loading (psf)
Steel and Concrete Deck	47.0
Steel Framing and Fireproofing	8.0
Partition Walls	10.0[a], 20.0[b]
Ceiling	3.0
Mechanical/Electrical	2.0
Curtain Wall	15.0

[a]3-Story
[b]7-Story (Lopez and Sabelli 2004)

Table 2.2 Predicted Natural Periods

Frame	T_1 (sec.)	T_2 (sec.)
3-Story BRBF	0.510 (0.300)[a]	0.207
7-Story BRBF	0.909 (0.550)	0.328

[a]Values in parentheses calculated using $T_a=(0.02)h_n^{3/4}$ per ASCE 7-05

Table 2.3 LMSR Ground Motion Records

Name	Event	Year	Station	R (km)	PGA (g)	Duration (sec.)
P01	Loma Prieta	1989	Agnews State Hospital	28.2	0.172	40.0
P02	Loma Prieta	1989	Capitola	14.5	0.443	40.0
P03	Loma Prieta	1989	Gilroy Array #3	14.4	0.367	39.9
P04	Loma Prieta	1989	Gilroy Array #4	16.1	0.212	40.0
P05	Loma Prieta	1989	Gilroy Array #7	24.2	0.226	40.0
P06	Loma Prieta	1989	Hollister City Hall	28.2	0.247	39.1
P07	Loma Prieta	1989	Hollister Differential Array	25.8	0.279	39.6
P08	Loma Prieta	1989	Sunnyvale-Colton Ave.	28.8	0.207	39.3
P09	Northridge	1994	Canoga Park-Topanga Can.	15.8	0.420	25.0
P10	Northridge	1994	LA-N Faring Rd.	23.9	0.237	30.0
P11	Northridge	1994	LA-Fletcher Dr.	29.5	0.240	30.0
P12	Northridge	1994	Glendae-Las Palmas	25.4	0.206	30.0
P13	Northridge	1994	LA-Hollywood Store FF	25.5	0.231	40.0
P14	Northridge	1994	La Crescenta-New York	22.3	0.159	30.0
P15	Northridge	1994	Northridge-17645 Saticoy St.	13.3	0.368	30.0
P16	San Fernando	1971	LA-Hollywood Store Lot	21.2	0.174	28.0
P17	Superstition Hills	1987	Brawley	18.2	0.156	22.1
P18	Superstition Hills	1987	El Centro Imp. Co. Cent	13.9	0.358	40.0
P19	Superstition Hills	1987	Plaster City	21.0	0.186	22.2
P20	Superstition Hills	1987	Westmoreland Fire Station	13.3	0.172	40.0

Table 2.4 Ground Motion Scaling Factors

Name	Scaling Factor	
	3-Story BRBF	7-Story BRBF
P01	2.940	2.899
P02	1.253	2.303
P03	1.461	2.166
P04	1.195	2.182
P05	2.313	5.715
P06	1.649	1.160
P07	1.154	0.930
P08	2.707	2.723
P09	1.490	1.052
P10	2.686	2.782
P11	1.304	2.798
P12	2.630	11.603
P13	1.914	3.869
P14	3.036	6.873
P15	1.699	2.105
P16	2.875	3.835
P17	3.743	4.238
P18	2.120	1.776
P19	1.691	5.028
P20	2.593	2.642

Table 2.5 Column Story Drift Demand

(a) 3-Story BRBF

Parameter	Story Drift Ratio	
	Analysis	Protocol
Number of Significant Cycles	31	36
Number of Large Cycles	11	18
Cumulative Demand	0.22 rad.	0.28 rad.
Maximum Cycle Range	0.023 rad.	0.03 rad.
Maximum Cycle	0.015 rad.	0.015 rad.

(b) 7-Story BRBF

Parameter	Story Drift Ratio	
	Analysis	Protocol
Number of Significant Cycles	28	36
Number of Large Cycles	18	18
Cumulative Demand	0.20 rad.	0.28 rad.
Maximum Cycle Range	0.021 rad.	0.03 rad.
Maximum Cycle	0.013 rad.	0.015 rad.

Table 2.6 Column Axial Load Demand

(a) 3-Story BRBF

Parameter	Column Axial Load			
	Tension		Compression	
	(kips)	(P/P_y)	(kips)	(P/P_y)
Maximum	80.6	0.057	358	0.254
Minimum	23.0	0.016	326	0.231
Average	37.4	0.027	339	0.241
Standard Deviation	13.2	0.009	11.6	0.008
90th Percentile	52.1	0.037	354	0.251

(b) 7-Story BRBF

Parameter	Column Axial Load			
	Tension		Compression	
	(kips)	(P/P_y)	(kips)	(P/P_y)
Maximum	856	0.276	1774	0.572
Minimum	1013	0.327	1624	0.524
Average	924	0.298	1691	0.546
Standard Deviation	40.7	0.013	39.4	0.013
90th Percentile	977	0.315	1742	0.562

Table 2.7 Proposed Story Drift Ratio Loading Sequence

Load Step	Story Drift Ratio	Number of Cycles
0	Apply column axial gravity load	
1	0.001	6
2	0.0015	6
3	0.002	6
4	0.003	4
5	0.004	4
6	0.005	4
7	0.0075	2
8	0.01	2
9	0.015	2
10[a]	0.02	1

[a]Continue with increments in Story Drift Ratio of 0.01, and perform one cycle at each step

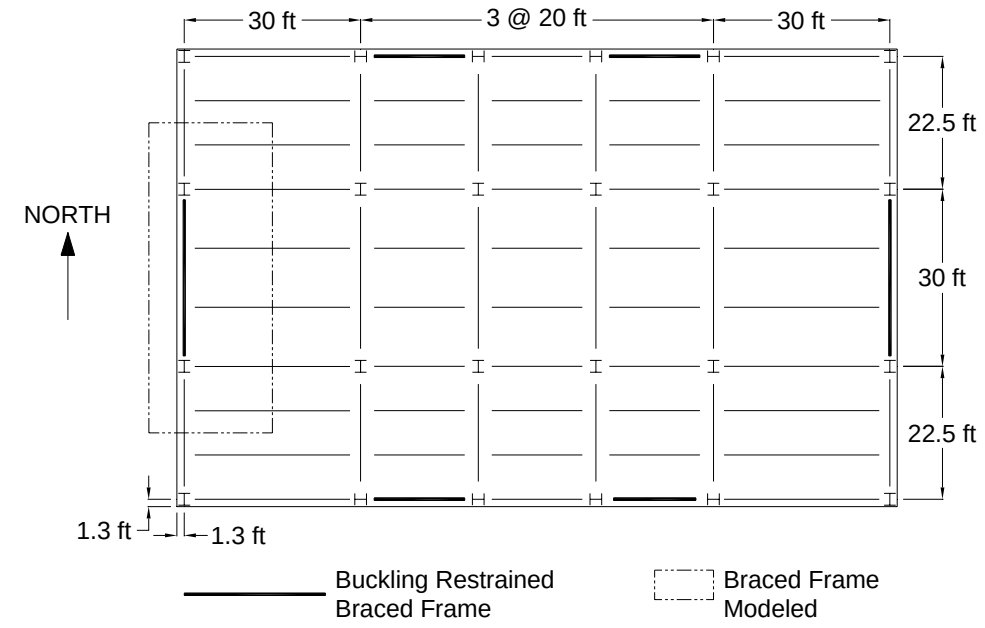

Figure 2.1 Plan View

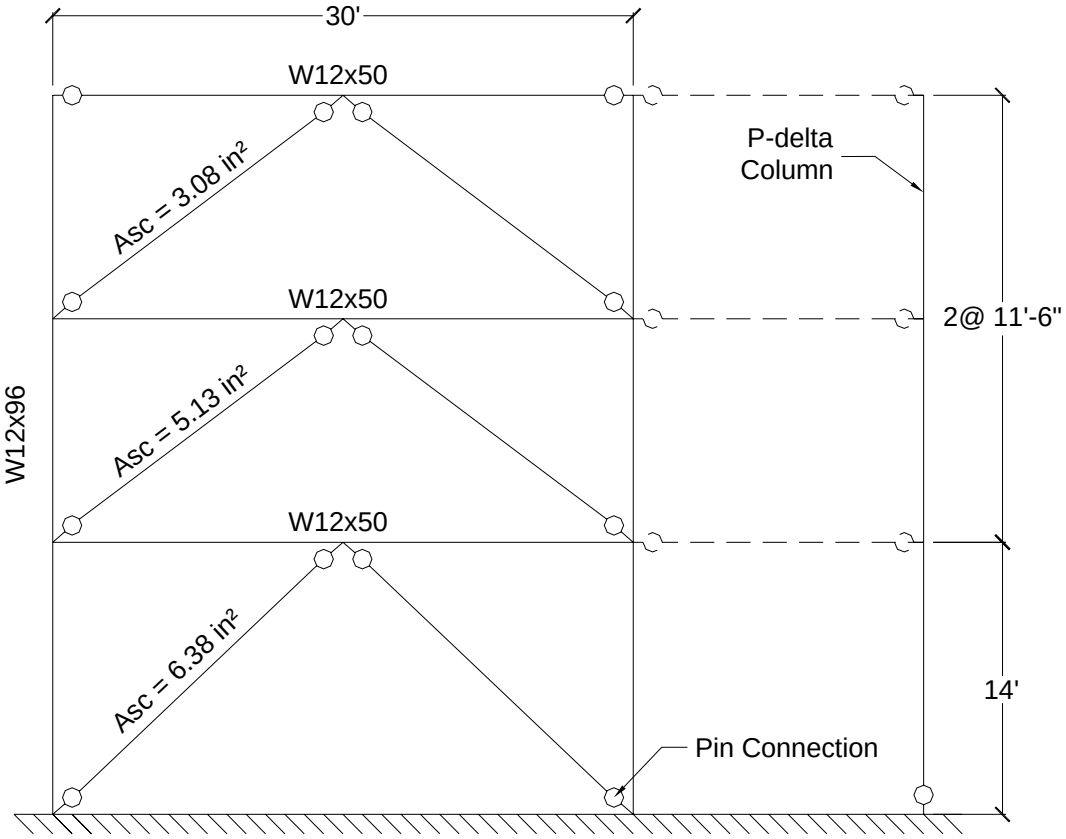

Figure 2.2 Elevation of 3-Story BRBF Model

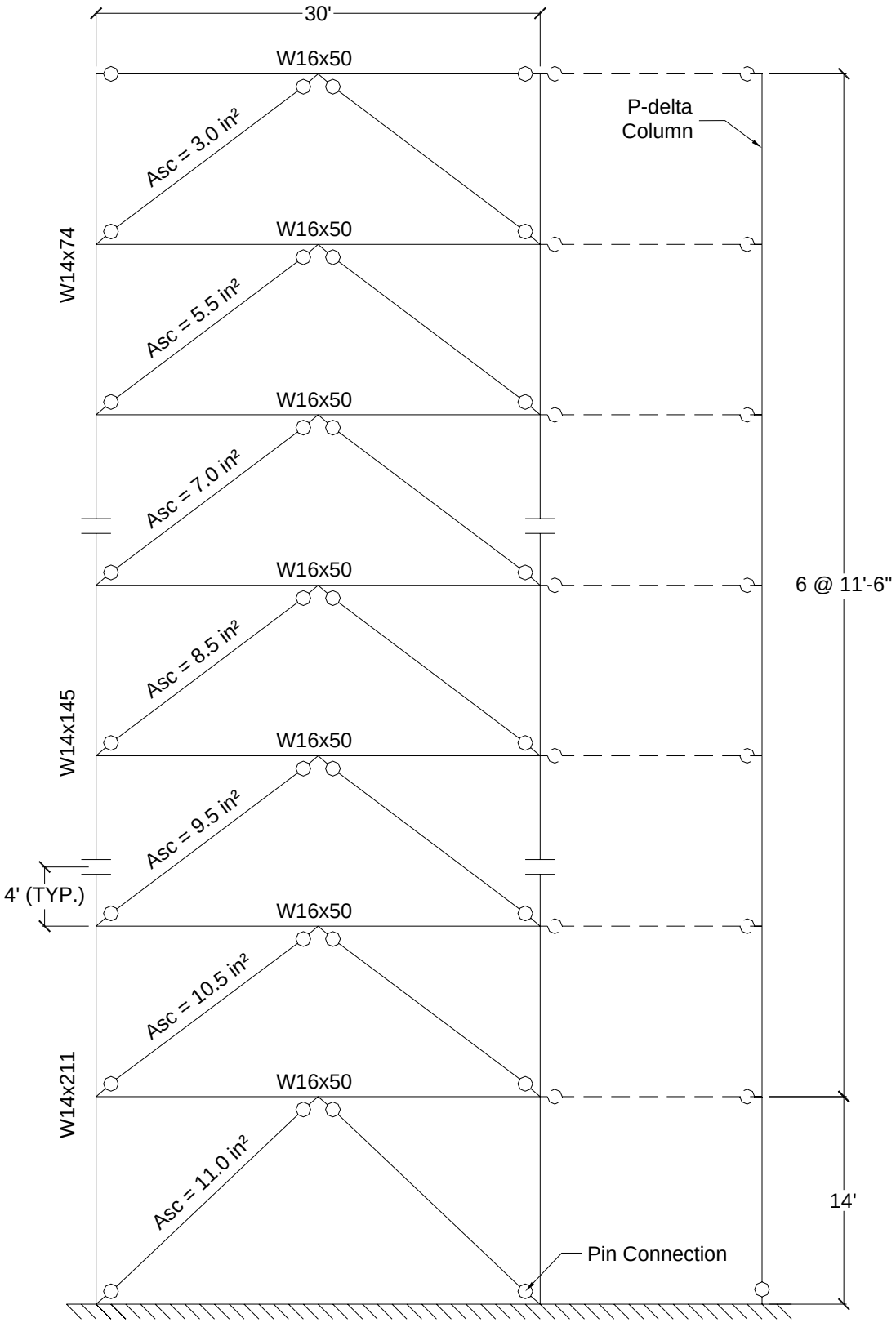

Figure 2.3 Elevation of 7-Story BRBF Model

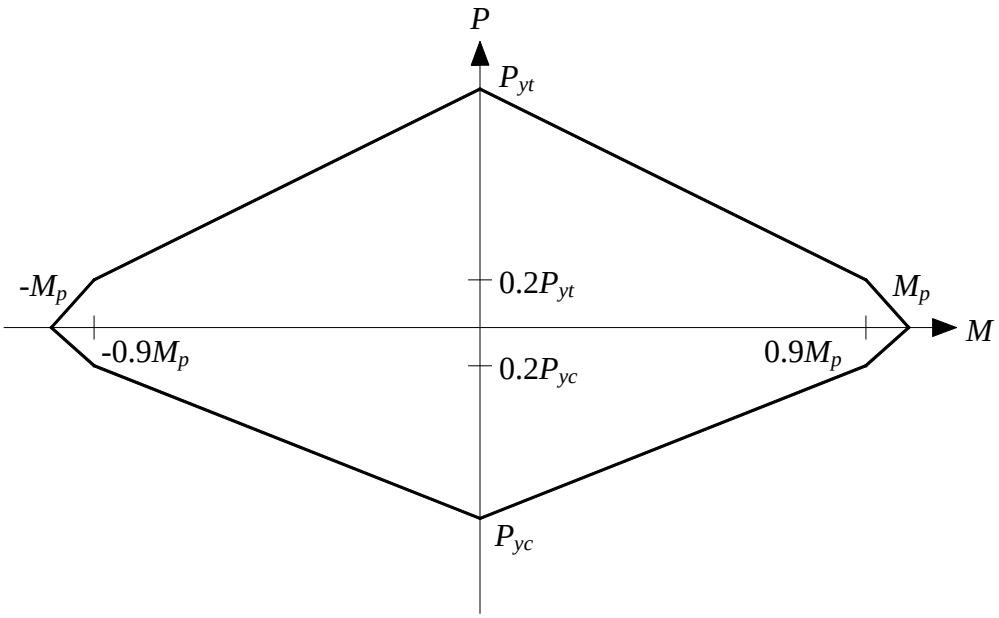

Figure 2.4 *P*-*M* Interaction Curve for Beam-Column Elements

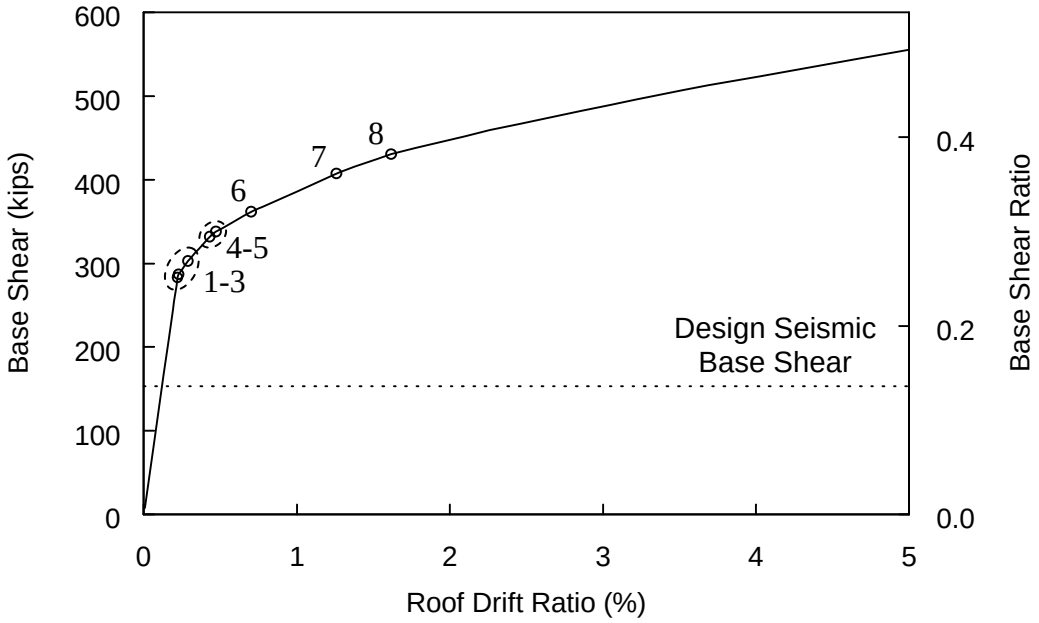

(a) Pushover Response

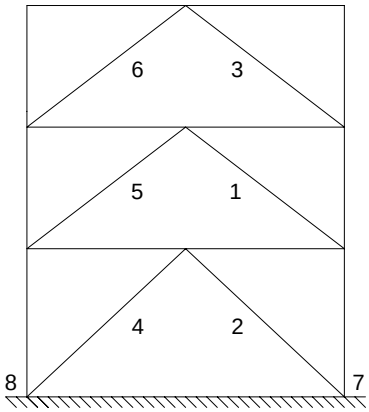

(b) Sequence of Yielding

Figure 2.5 3-Story BRBF: Pushover Analysis Results

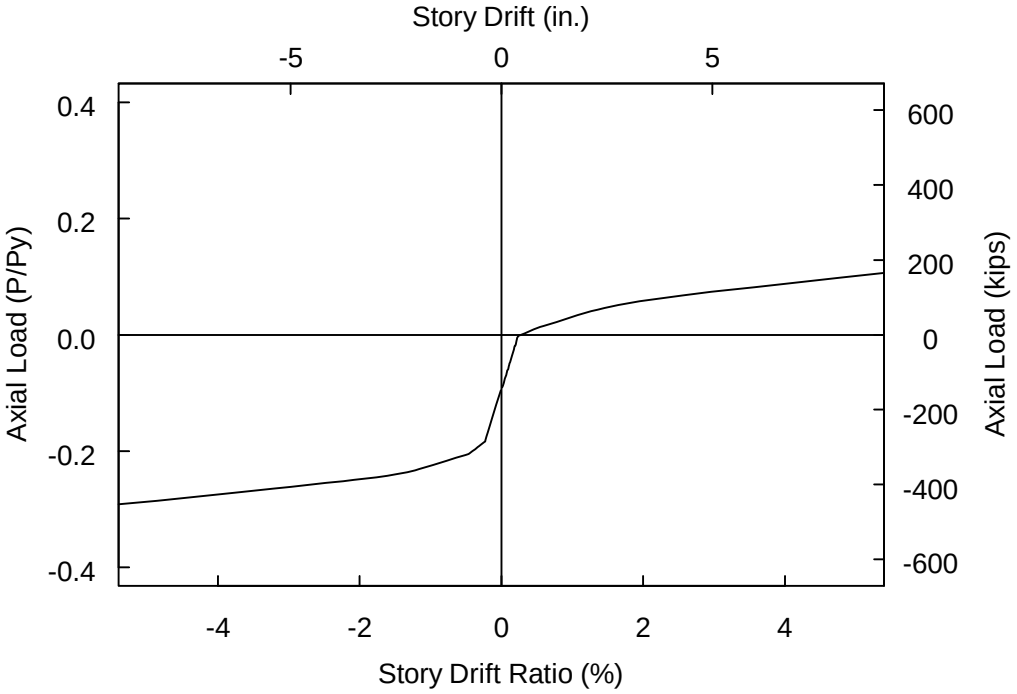

(c) First-Story Column Axial Load versus Story Drift Ratio

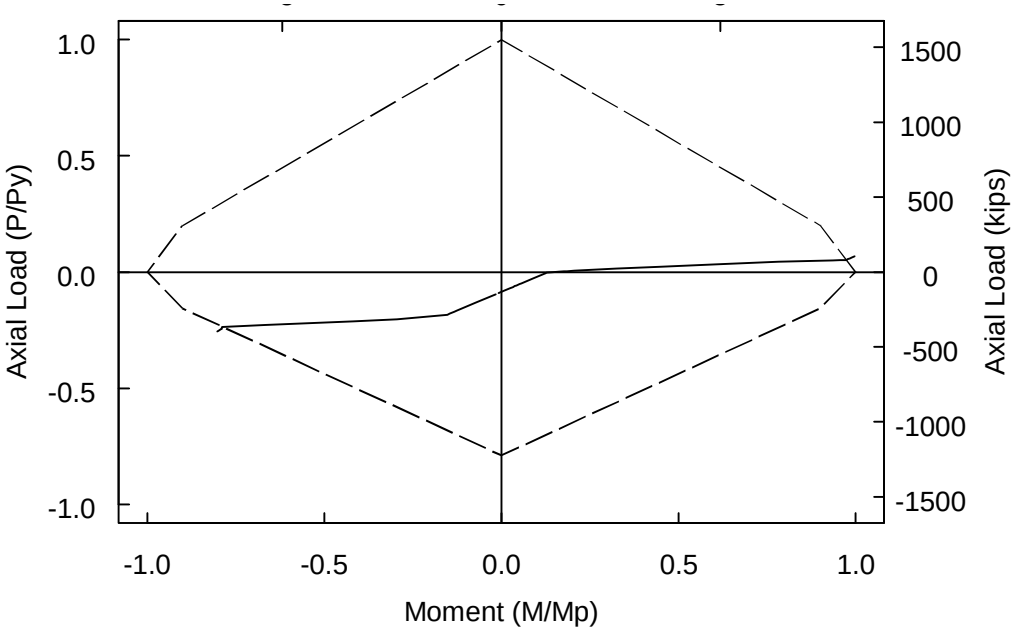

(d) First-Story Column Axial Load-Moment Interaction

Figure 2.5 3-Story BRBF: Pushover Analysis Results (cont.)

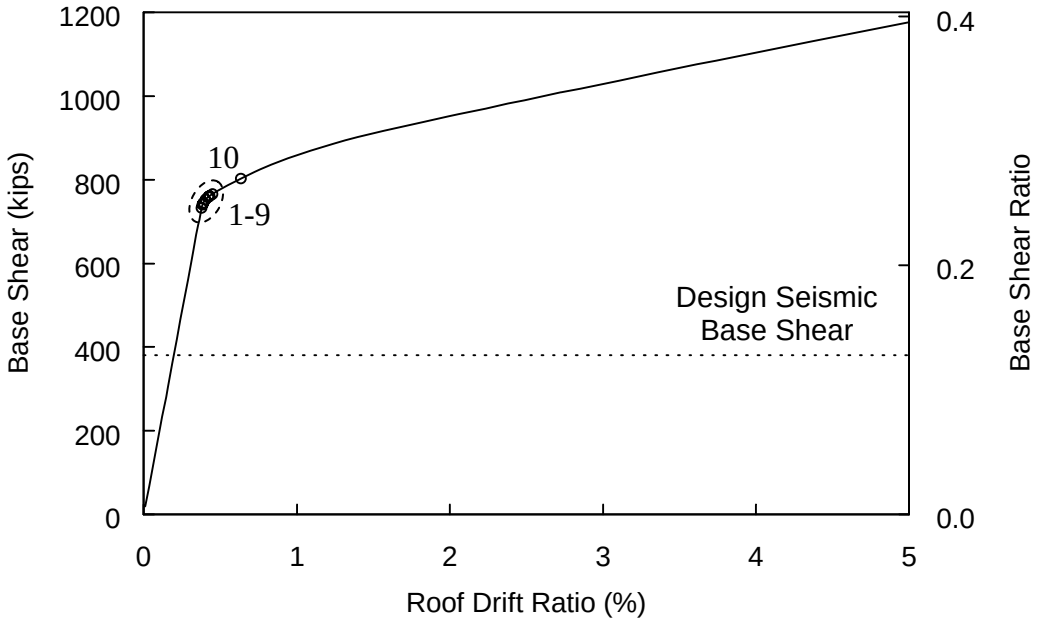

(a) Pushover Response

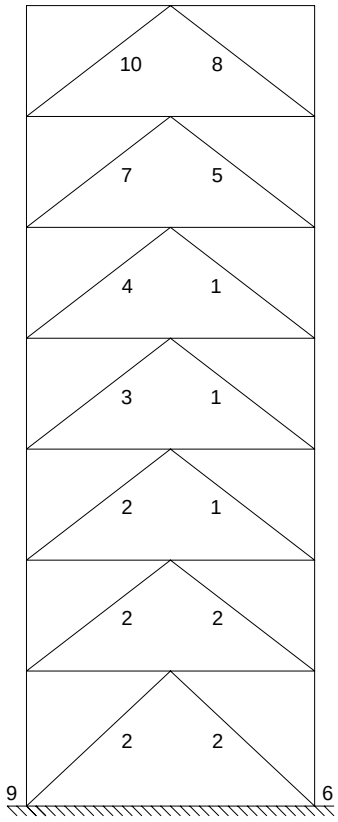

(b) Sequence of Yielding

Figure 2.6 7-Story BRBF: Pushover Analysis Results

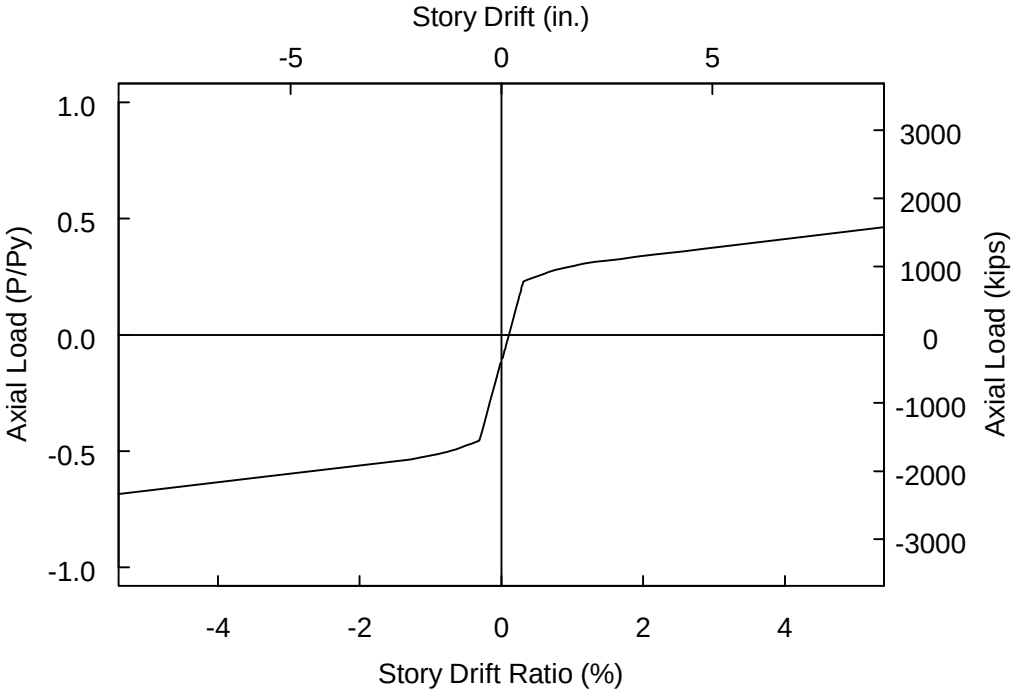

(c) First-Story Column Axial Load versus Story Drift Ratio

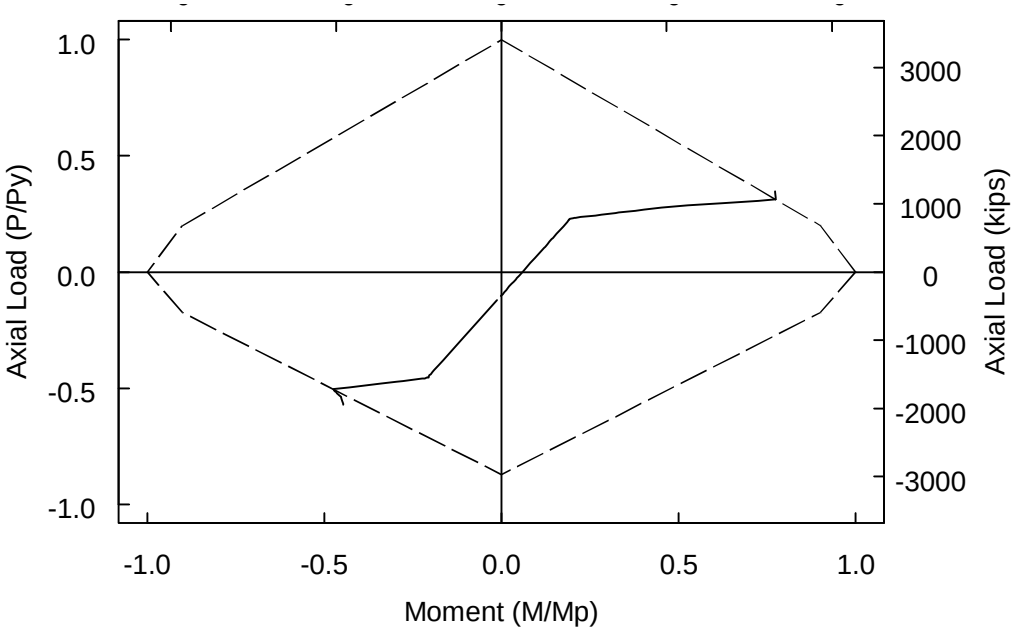

(d) First-Story Column Axial Load-Moment Interaction

Figure 2.6 7-Story BRBF: Pushover Analysis Results (cont.)

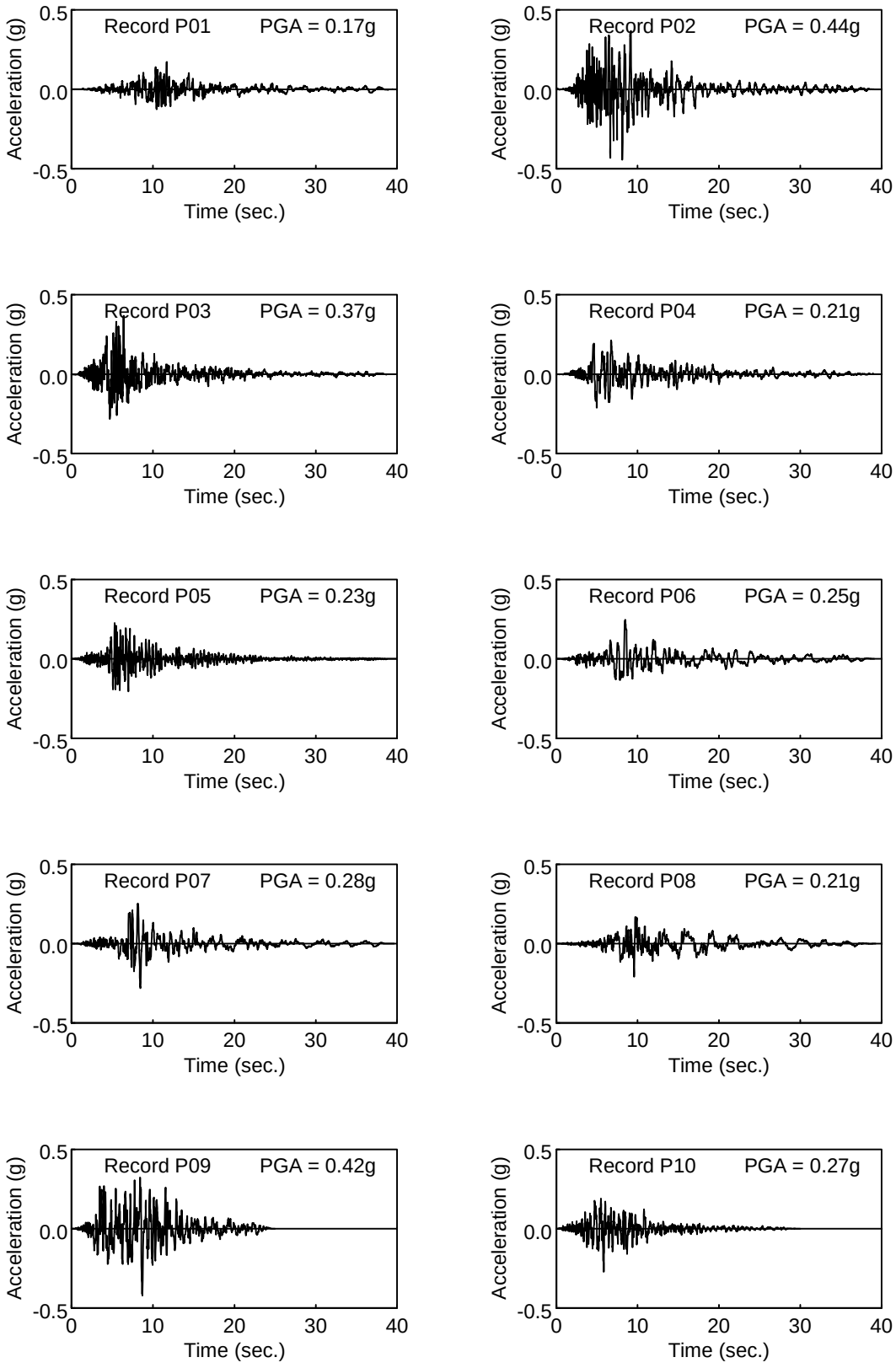

Figure 2.7 Acceleration Time Histories of Un-scaled Ground Motions

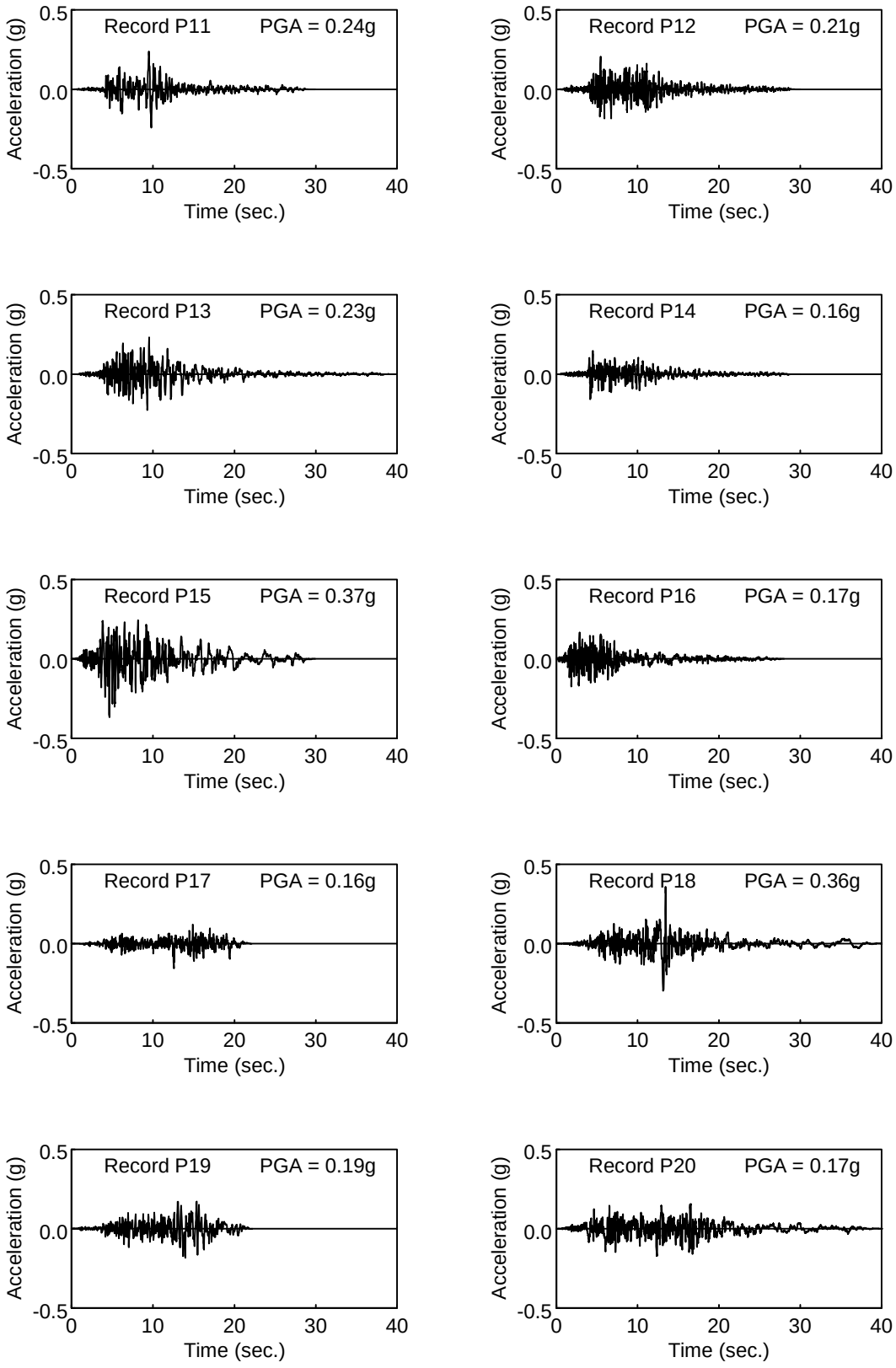

Figure 2.7 Acceleration Time Histories of Un-scaled Ground Motions (cont.)

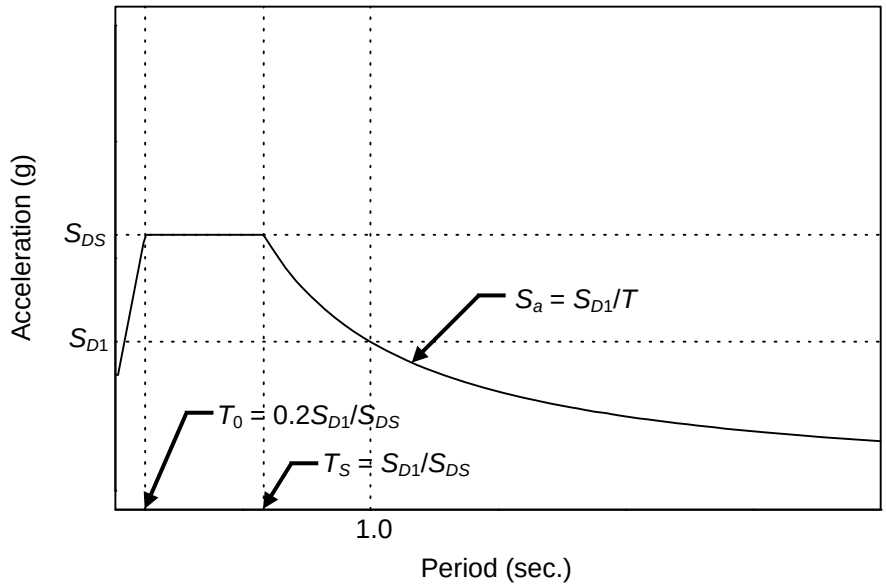

Figure 2.8 IBC Design Acceleration Response Spectrum (5% Damping)

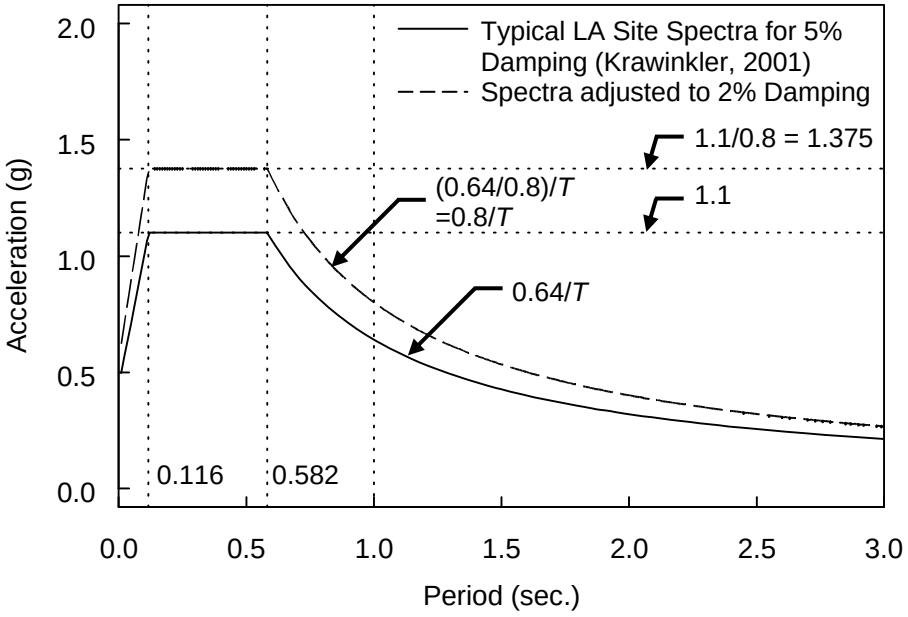

Figure 2.9 Design Acceleration Response Spectra for 2% and 5% Damping

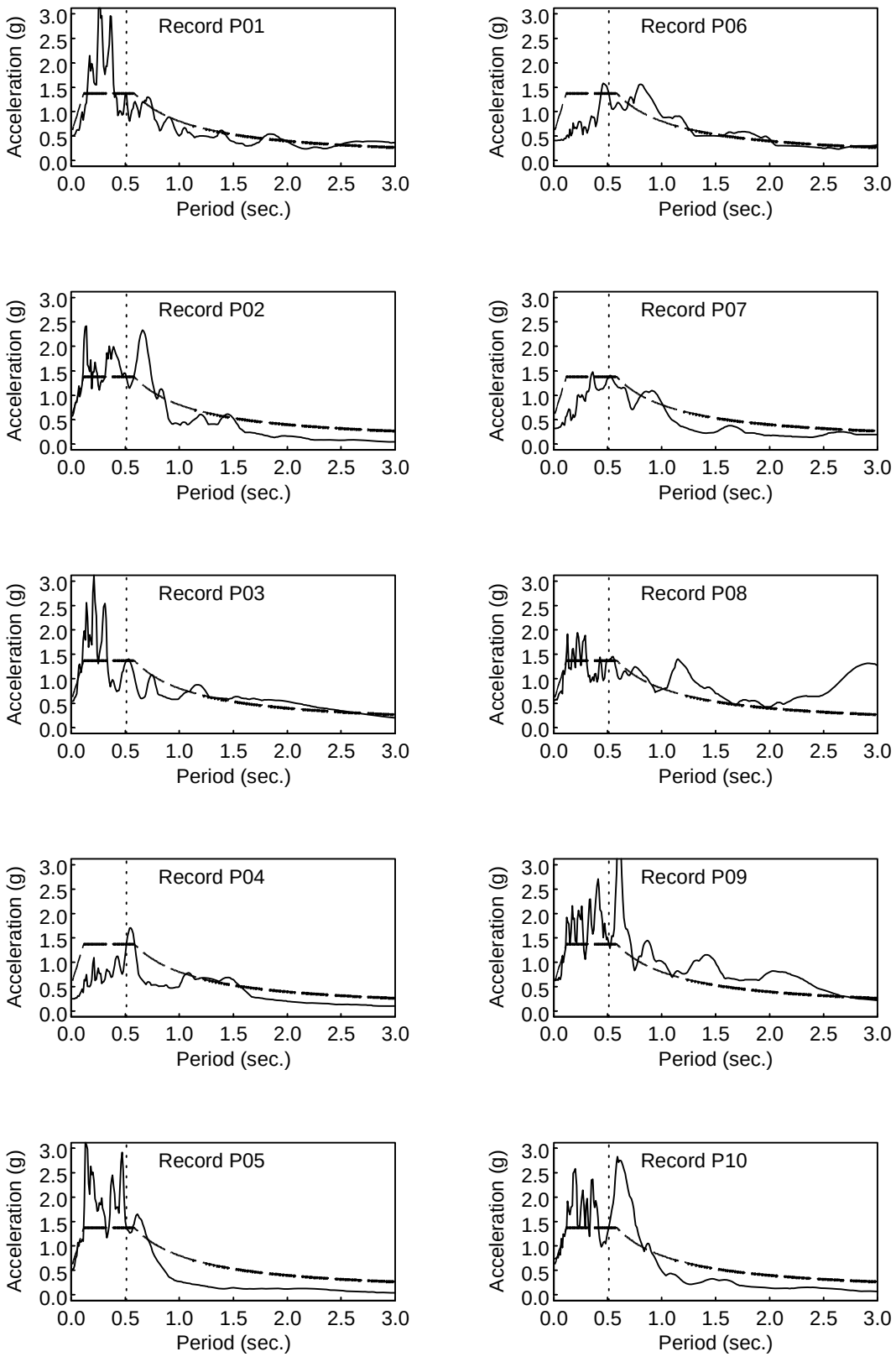

Figure 2.10 3-Story BRBF: Scaled 2% Damped Acceleration Response Spectra

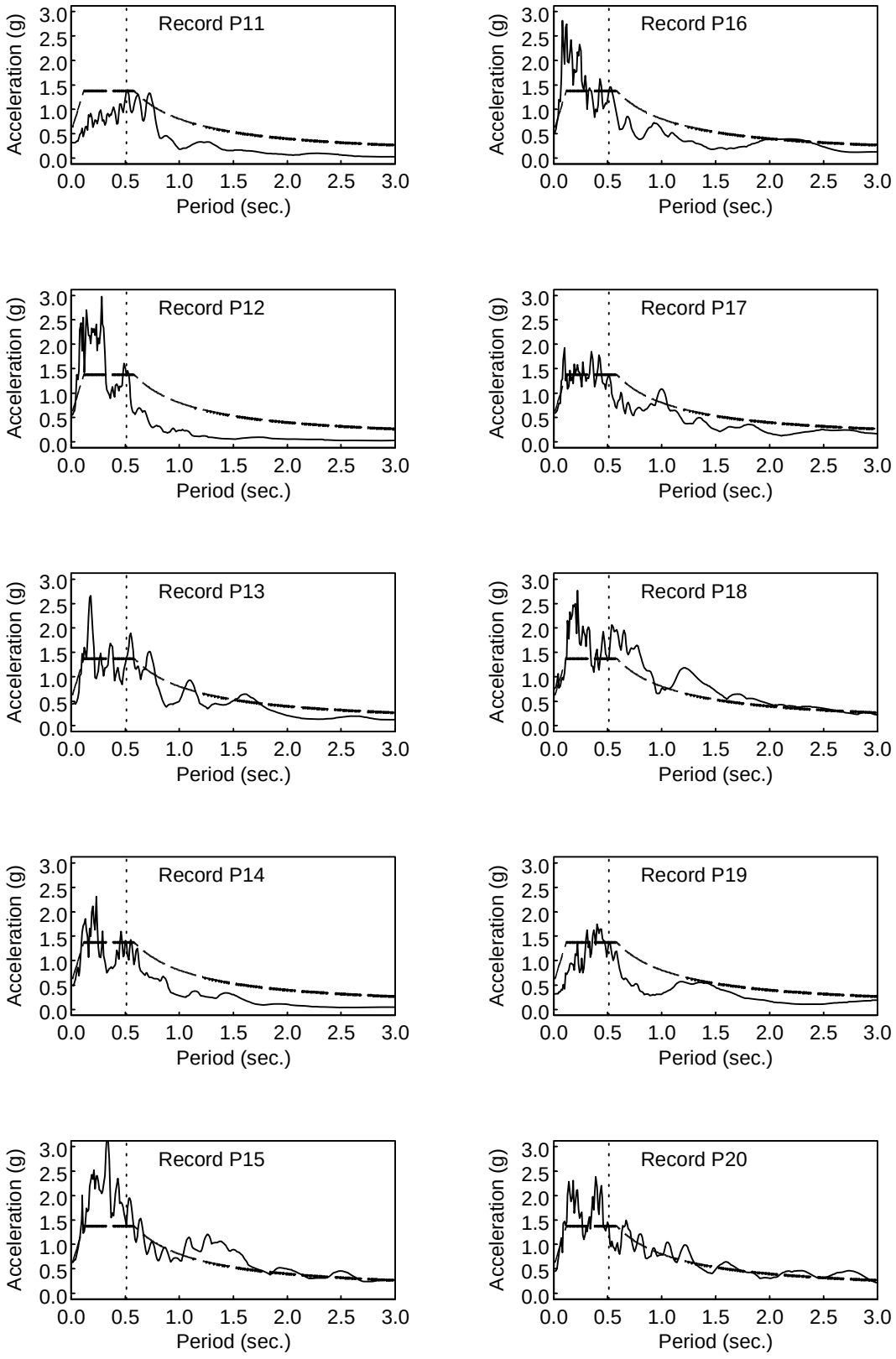

Figure 2.10 3-Story BRBF: Scaled 2% Damped Acceleration Response Spectra (cont.)

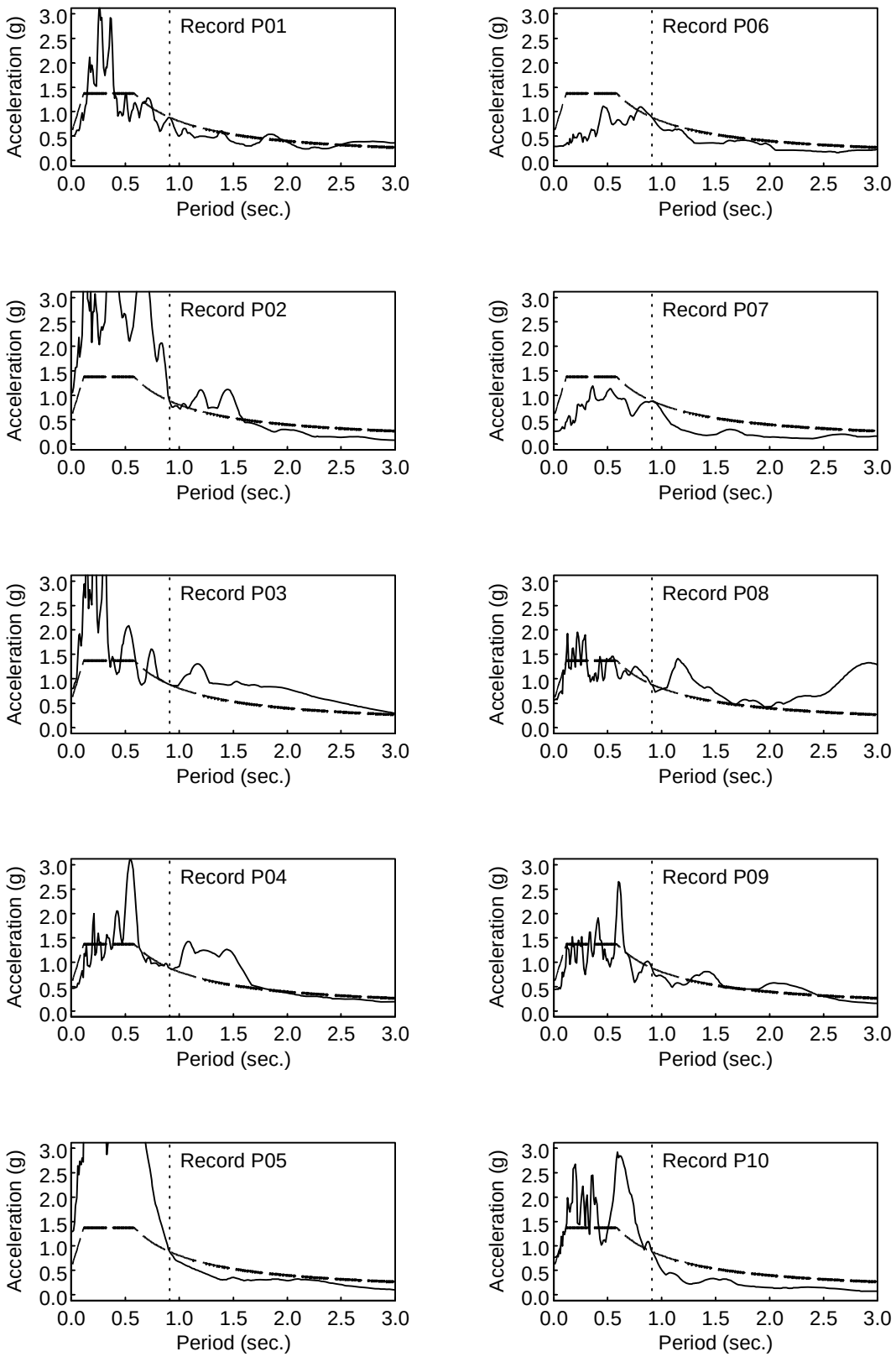

Figure 2.11 7-Story BRBF: Scaled 2% Damped Acceleration Response Spectra

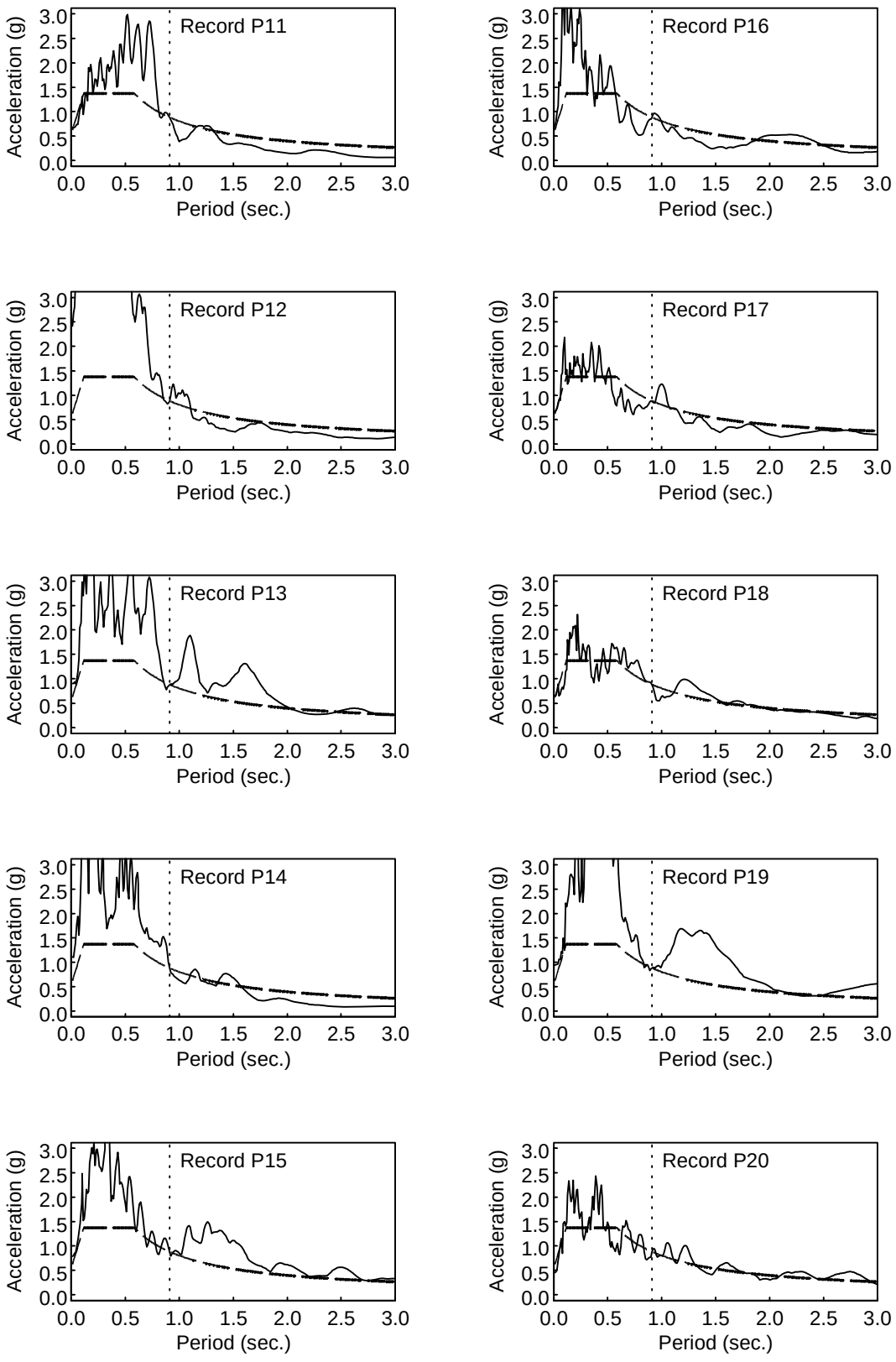

Figure 2.11 7-Story BRBF: Scaled 2% Damped Acceleration Response Spectra (cont.)

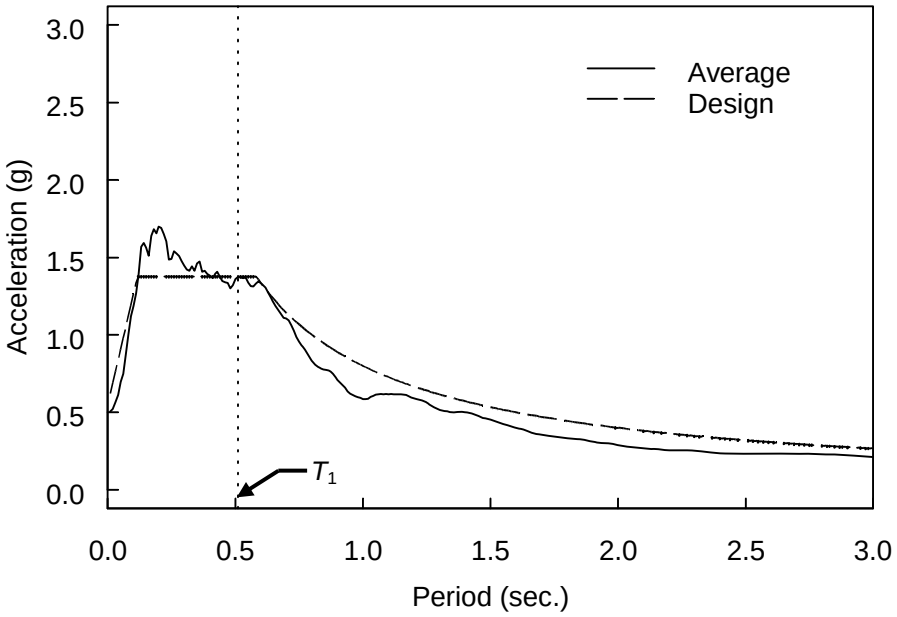

(a) 3-Story BRBF

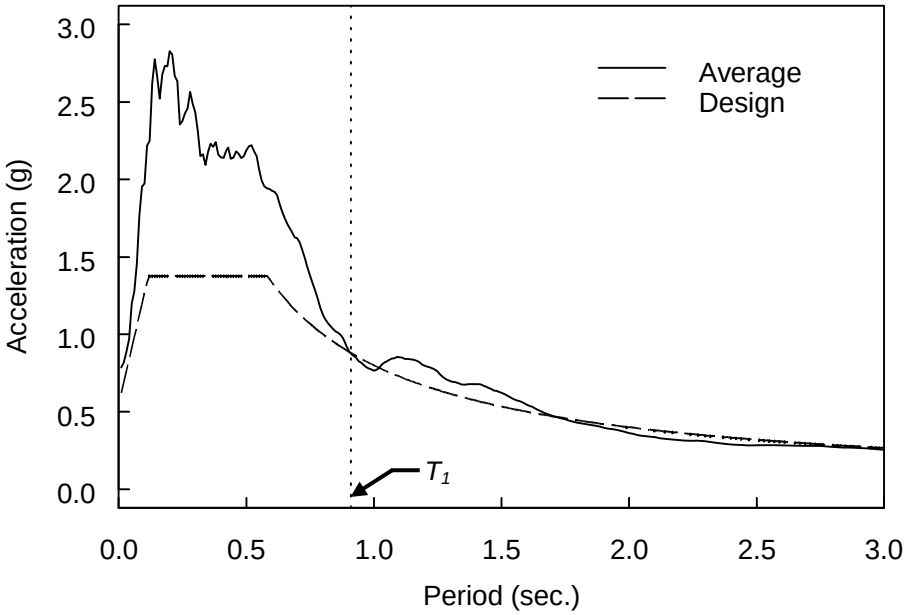

(b) 7-Story BRBF

Figure 2.12 Average Scaled and Design Acceleration Response Spectra (2% Damping)

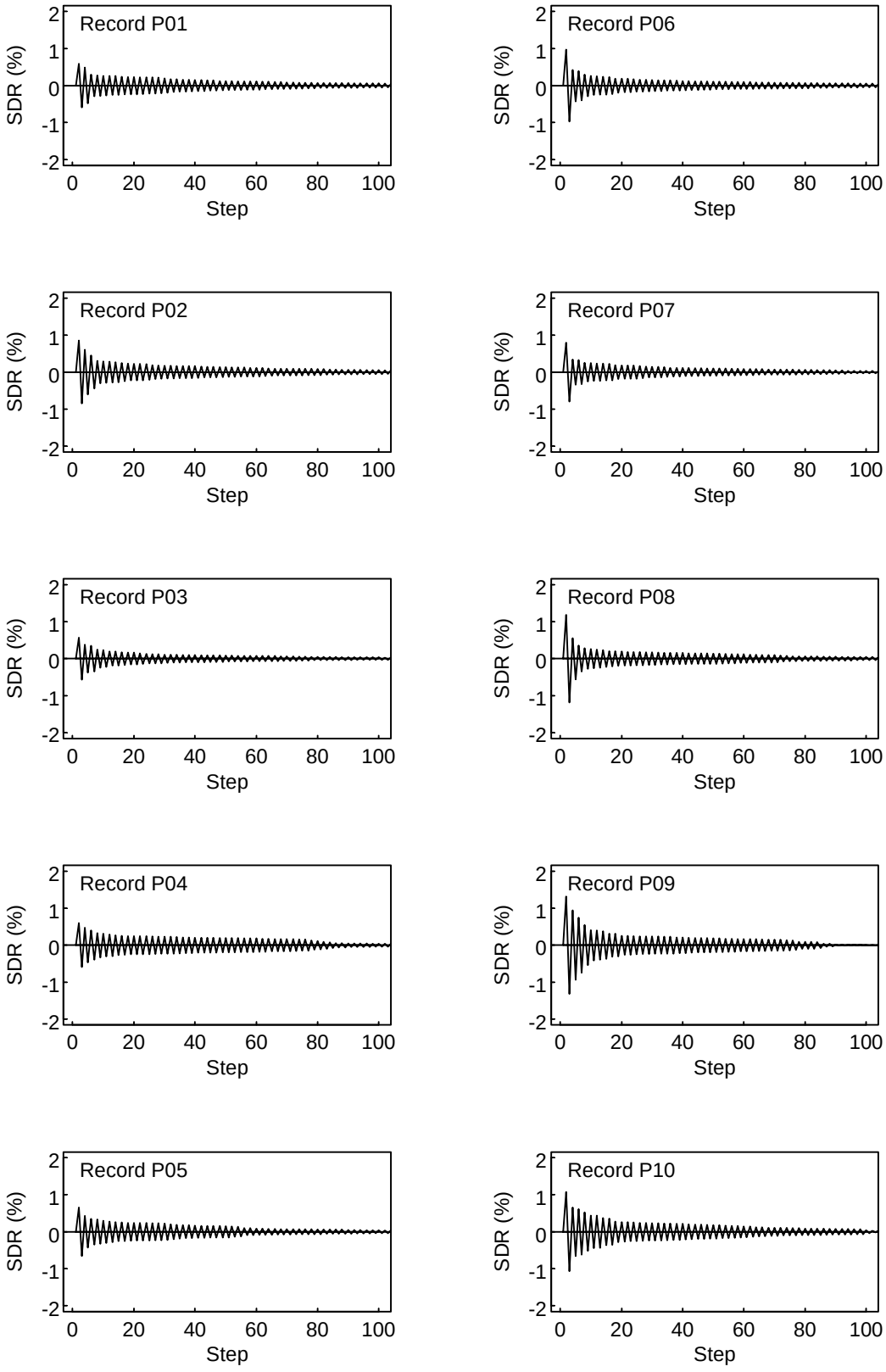

Figure 2.13 3-Story BRBF: First Story Drift Ratio Rainflow Counting Cycles

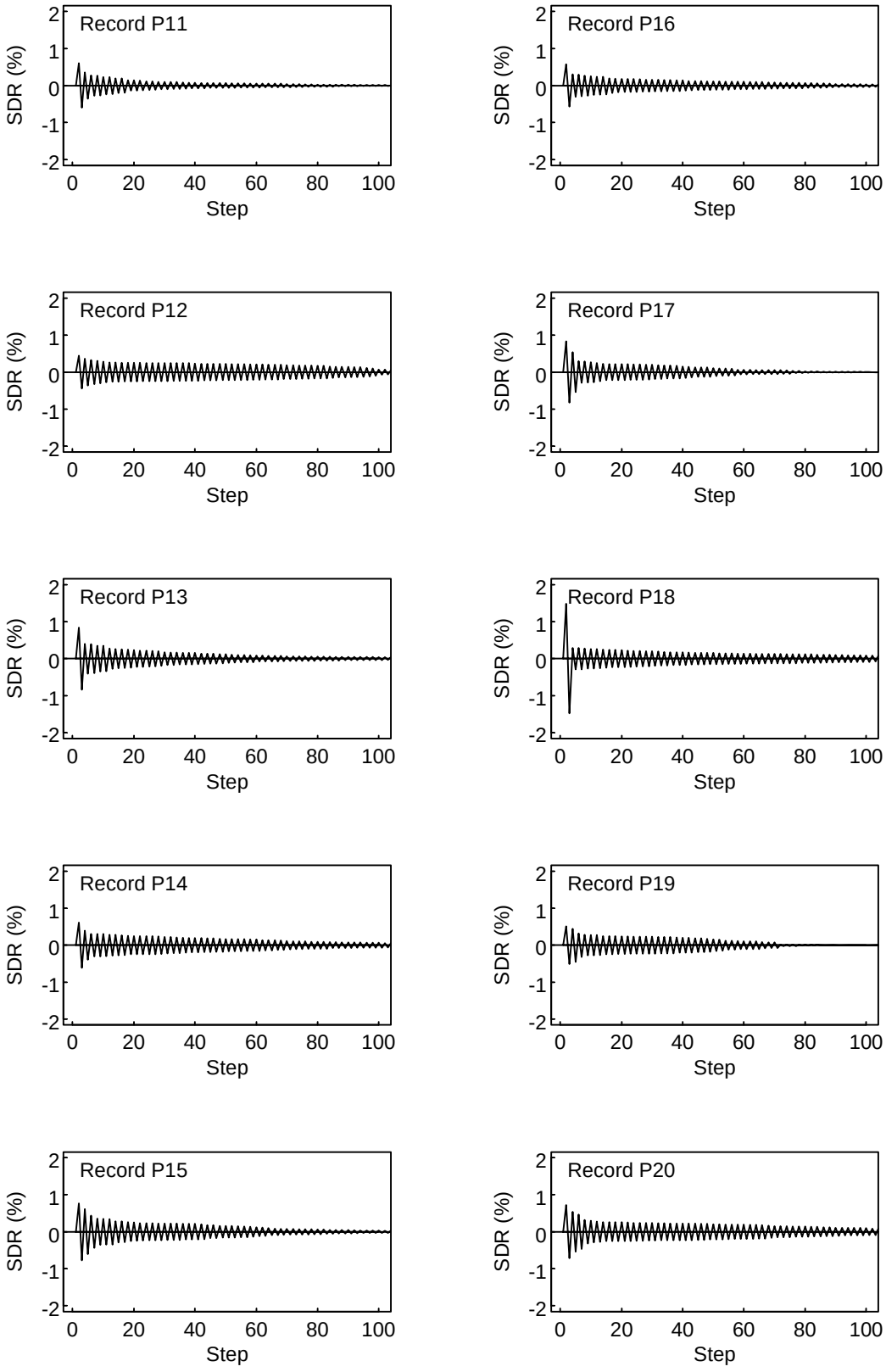

Figure 2.13 3-Story BRBF: First Story Drift Ratio Rainflow Counting Cycles (cont.)

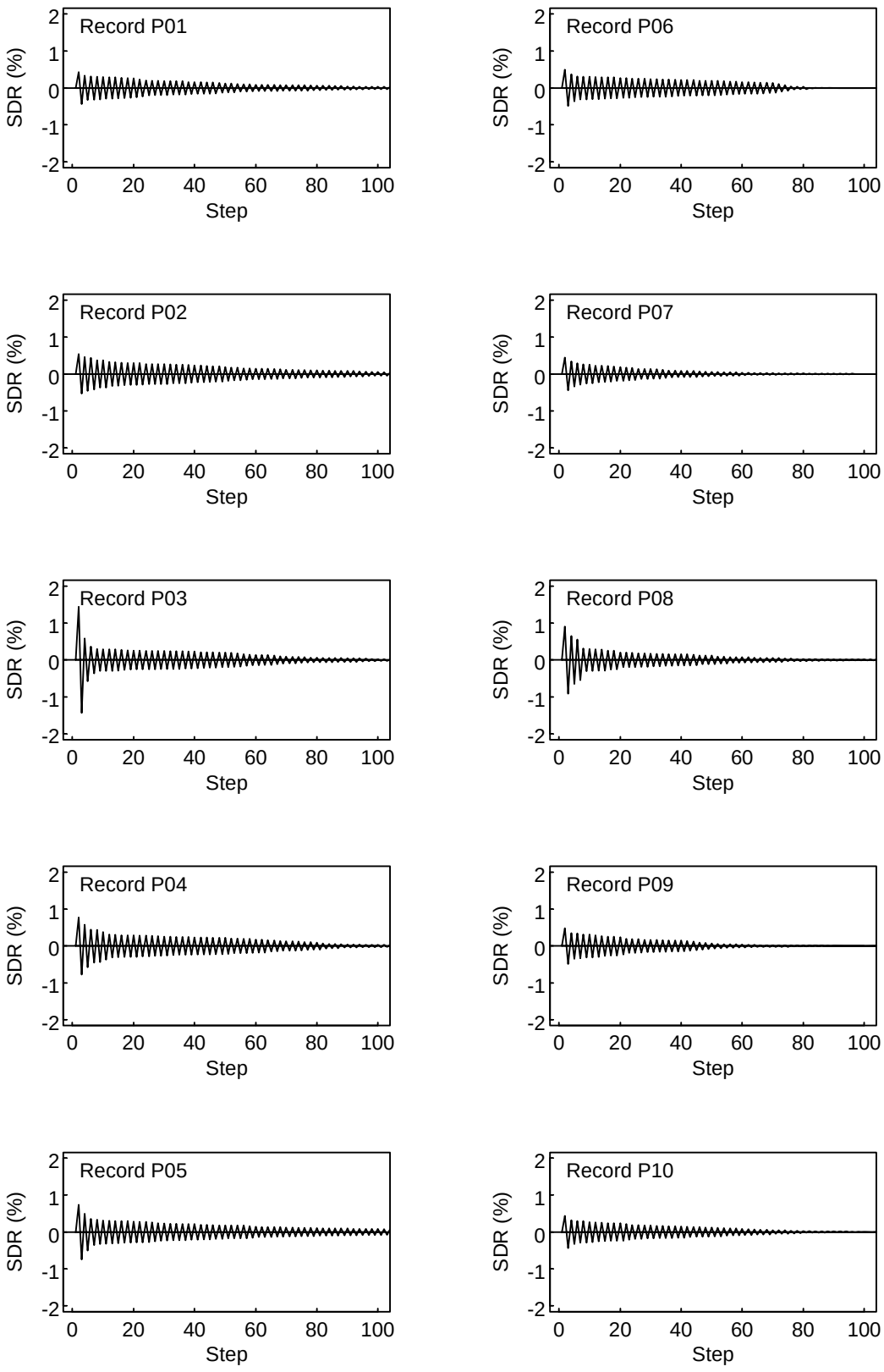

Figure 2.14 7-Story BRBF: First Story Drift Ratio Rainflow Counting Cycles

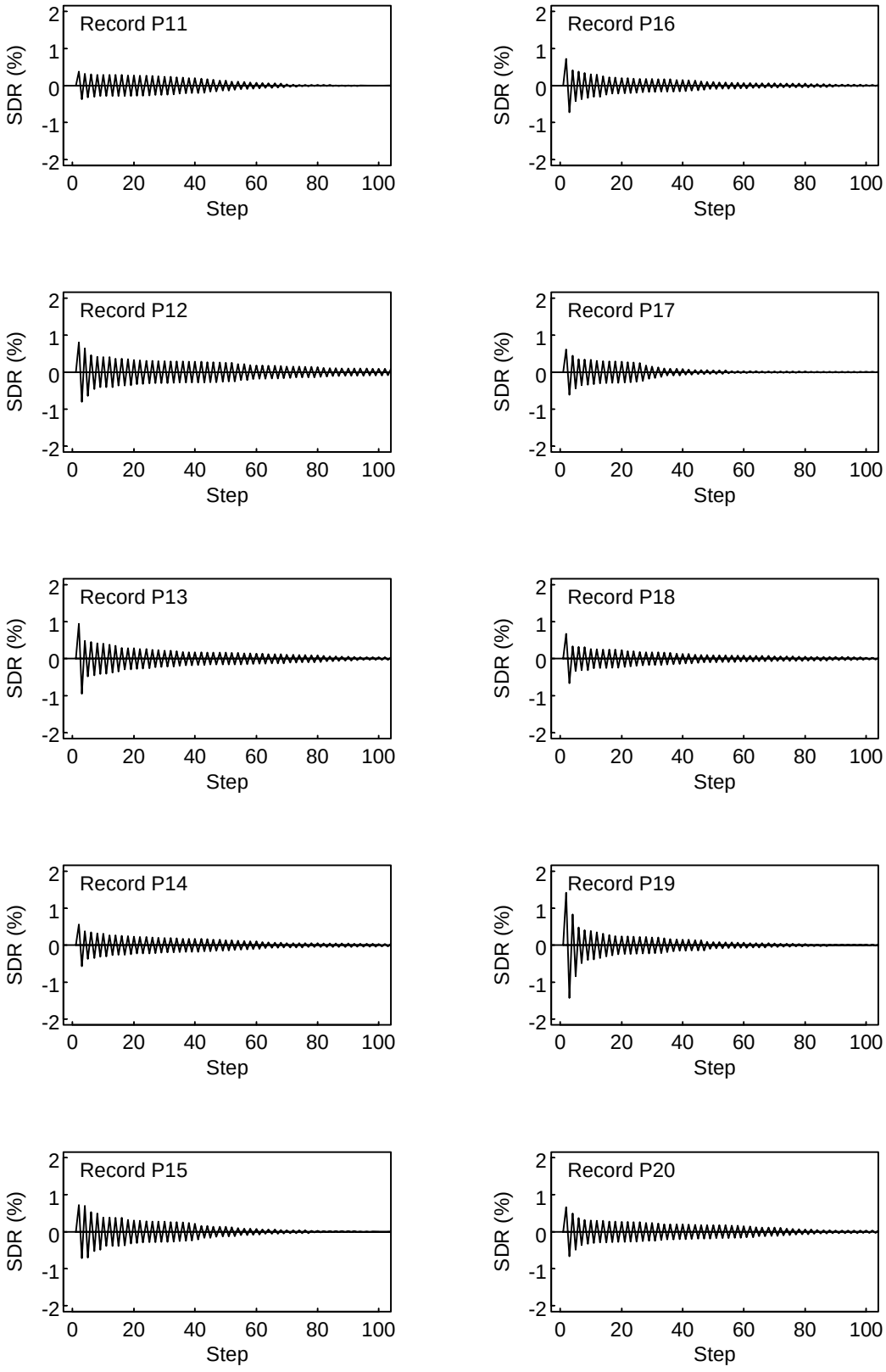

Figure 2.14 7-Story BRBF: First Story Drift Ratio Rainflow Counting Cycles (cont.)

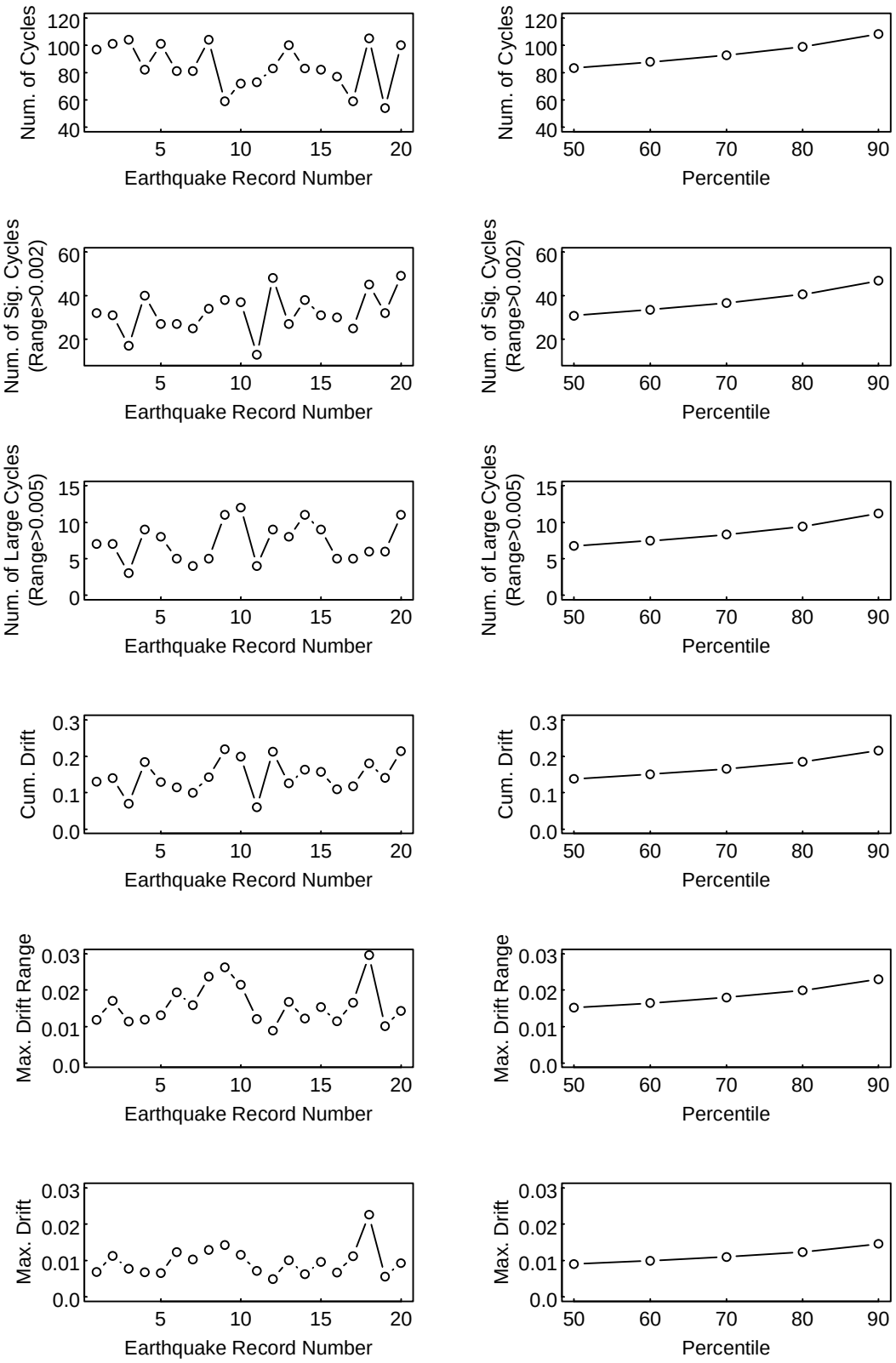

(a) Data for Each Record (b) Percentile Values

Figure 2.15 3-Story BRBF: Story Drift Ratio Demand

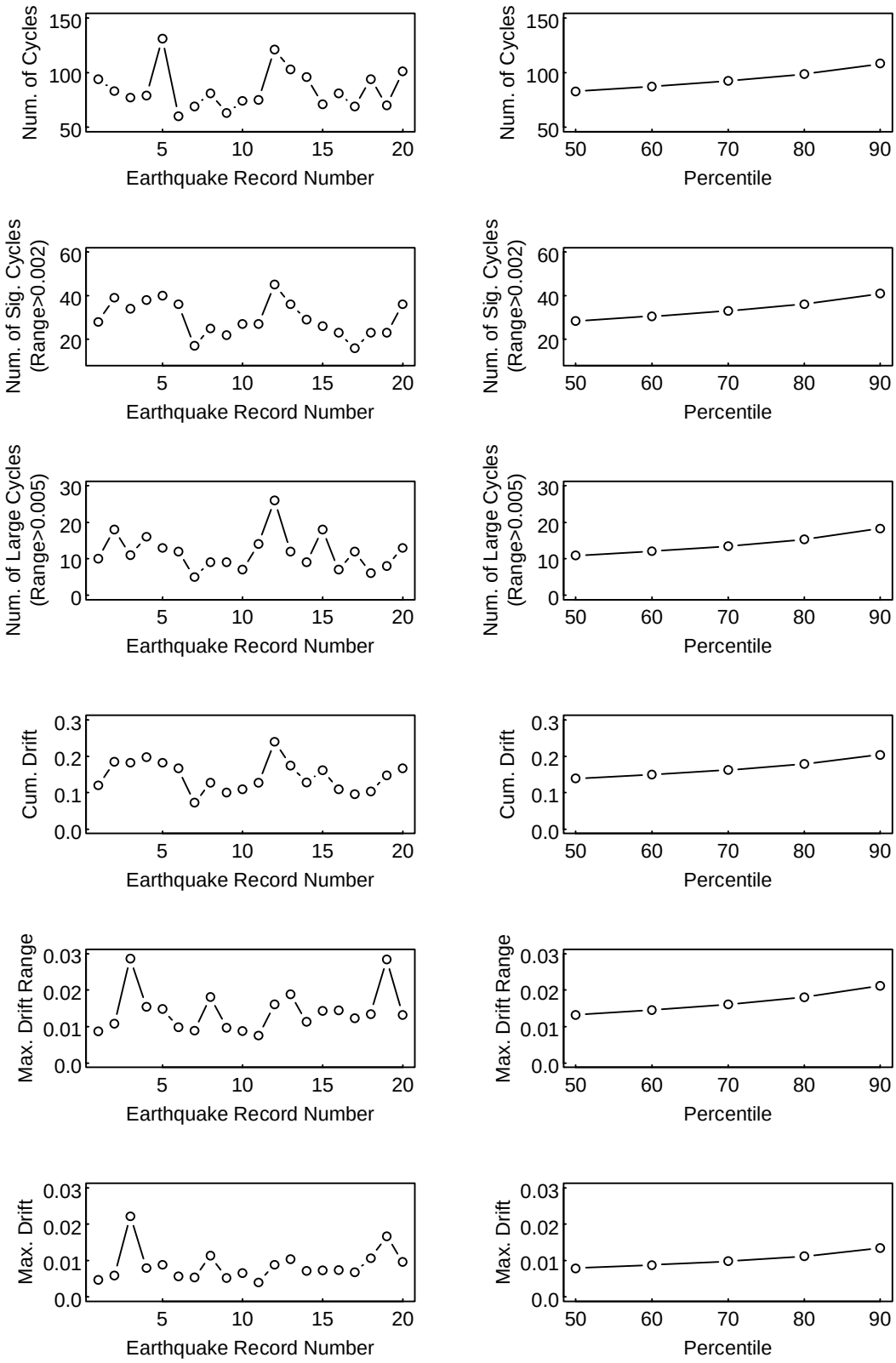

(a) Data for Each Record (b) Percentile Values

Figure 2.16 7-Story BRBF: Story Drift Ratio Demand

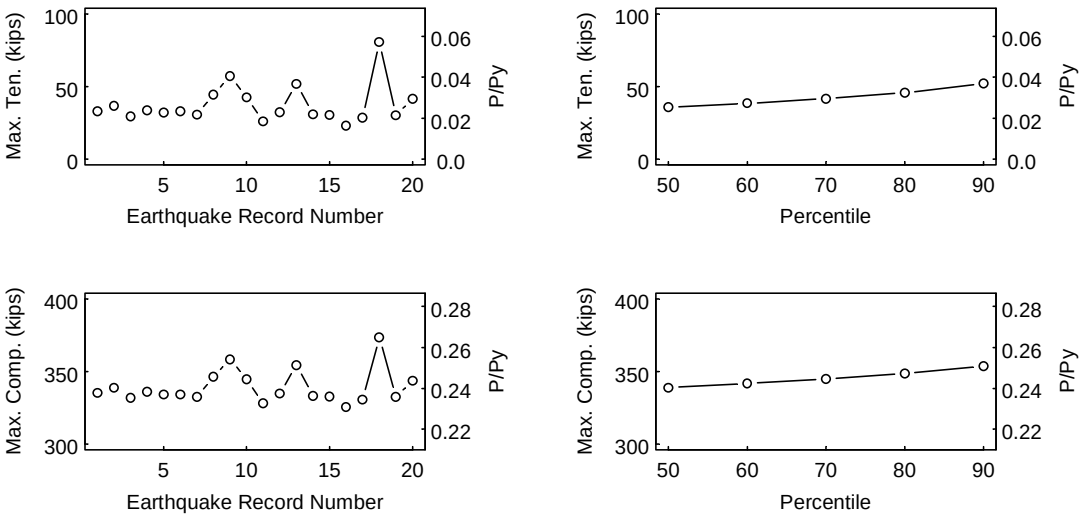

(a) Data for Each Record (b) Percentile Values

Figure 2.17 3-Story BRBF: Column Axial Load Demand

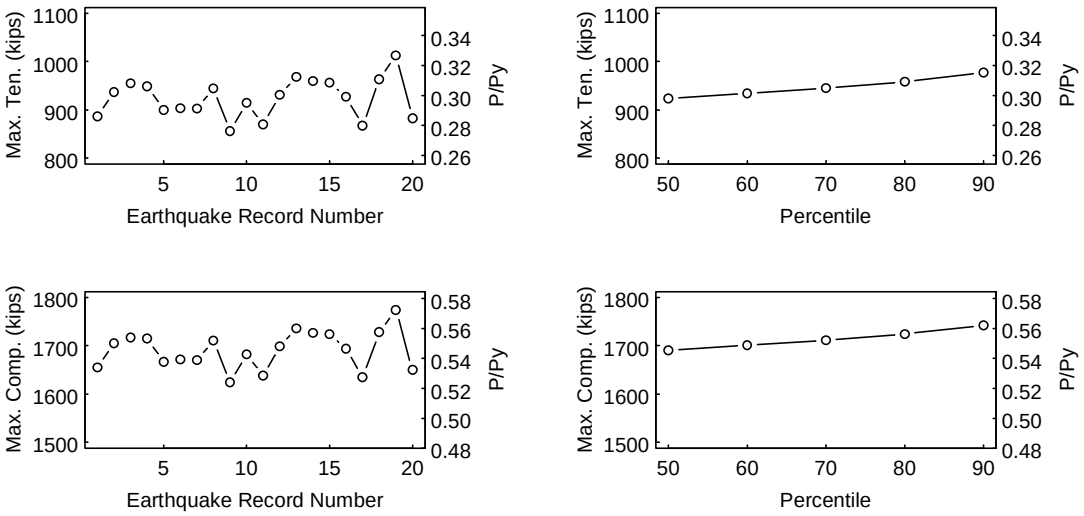

(a) Data for Each Record (b) Percentile Values

Figure 2.18 7-Story BRBF: Column Axial Load Demand

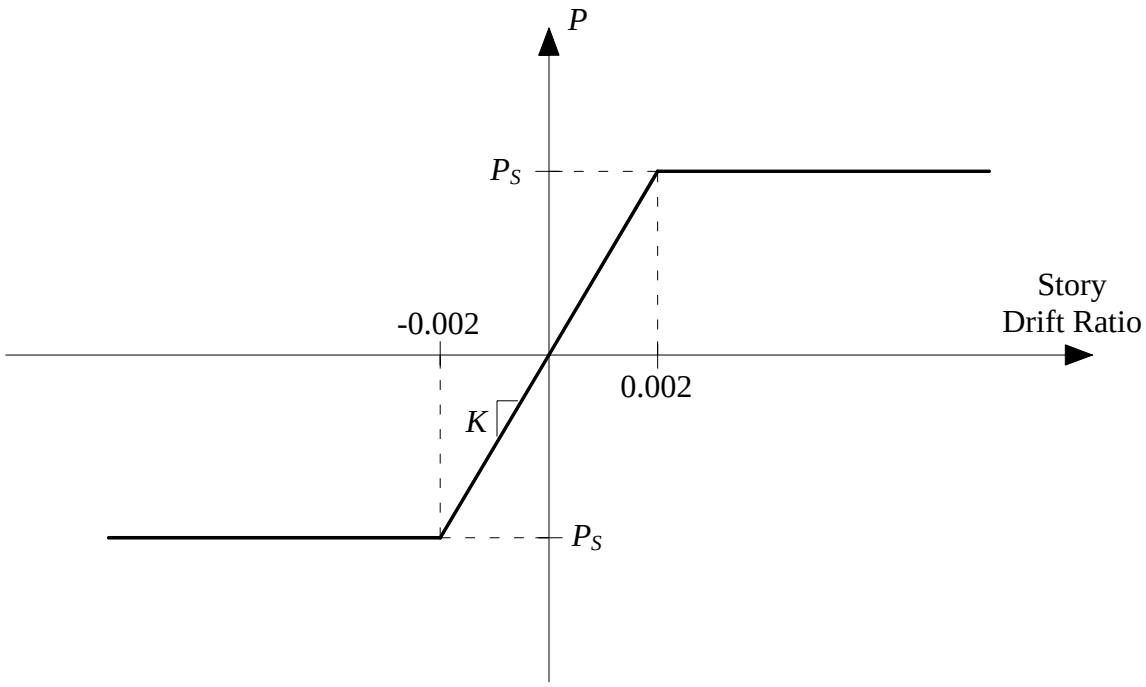

(a) Seismic Load

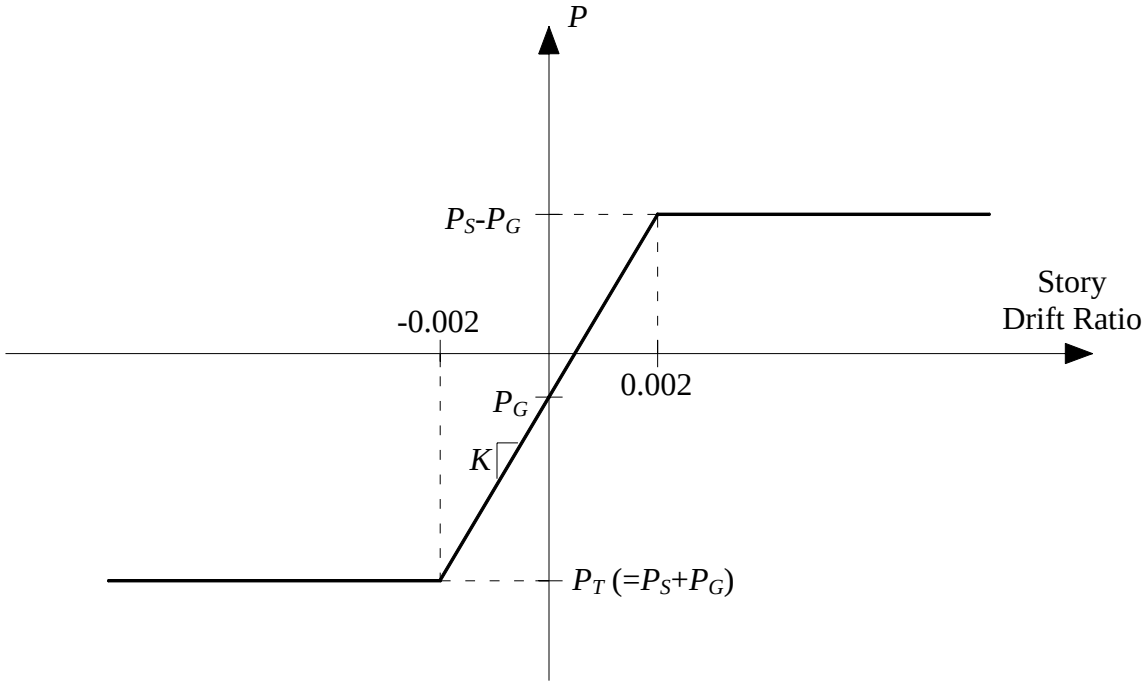

(b) Combined Seismic and Gravity Load

Figure 2.19 Elastic-Perfectly Plastic Column Axial Load versus Story Drift Ratio Relationship

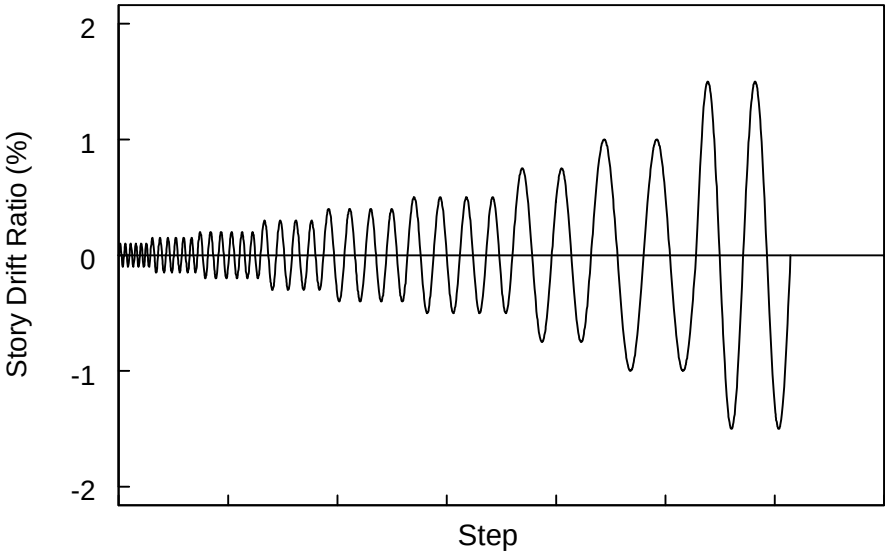

(a) Lateral Deformation

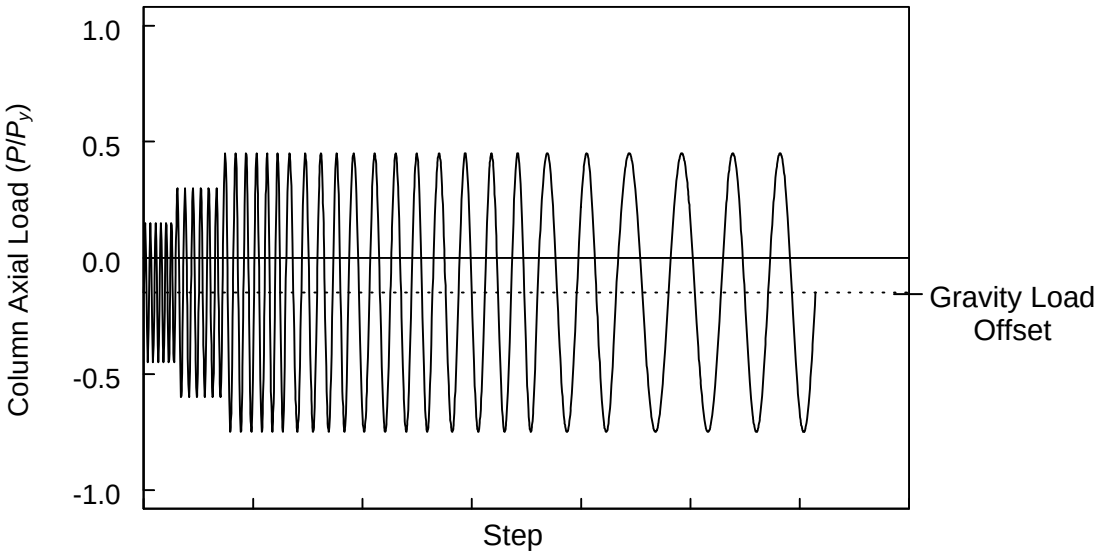

(b) Axial Load

Figure 2.20 Story Drift and Column Axial Loading Sequence (to 1.5% drift)

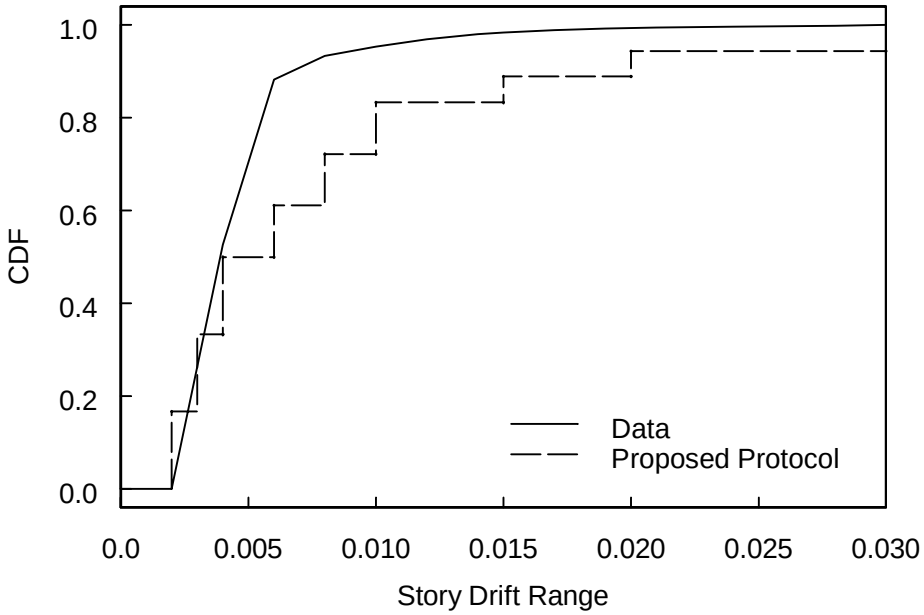

(a) 3-Story BRBF

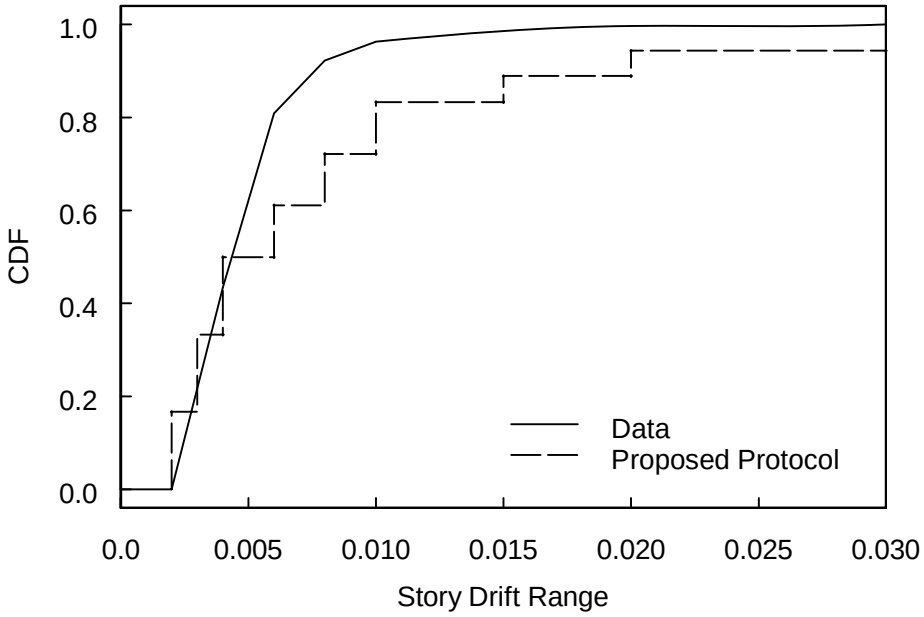

(b) 7-Story BRBF

Figure 2.21 Comparison of First-Story Drift Ratio CDFs

3. TESTING PROGRAM

3.1 General

The experimental program consisted of testing nine full-scale fixed-base columns. ASTM A992 steel wide-flange sections typical of braced frame columns, representing a practical range of flange and web width-to-thickness ratios, and 15 ft story height were subjected to different levels of axial force demand combined with story drift demand for these simulated bottom-story columns. The test matrix is summarized in Table 3.1. A total of four W14 sections were selected such that the effect of width-thickness ratios on cyclic local buckling behavior could also be investigated. The axial load capacity of the test facility precluded testing of a W14×233 specimen at an axial load of $0.75P_y$ and a W14×370 specimen at an axial load of $0.55P_y$ or $0.75P_y$. However, these two sections were tested at axial loads within the equipment capacity.

3.2 Test Setup

The testing used the UCSD SRMD Test Facility as shown in Figure 3.1. Column specimens were tested in a horizontal configuration with one end of the specimen attached to a reaction fixture that was attached to a strong-wall. The other end of the specimen was attached to a reaction fixture attached to the SRMD shake table platen. Longitudinal (E-W) and lateral (N-S) movement of the shake table platen imposed load in both directions. Lateral movement was applied to induce strong-axis bending of the specimen. Control software for the SRMD Test Facility automatically resolved applied loads into longitudinal and lateral components.

3.3 Test Specimens

In practical applications, the column fixed-base condition in the first-story is created by either extending and embedding steel columns in basement walls, if used, or connecting the column base to grade beams. Since the objective of this research was focused on strength and ductility capacities of steel columns, not the column base connection to surrounding members, both ends of the column specimen were strengthened by stiffeners or re-usable haunches to simulate the fixed-end condition (see

Figure 3.1). As described above, this fixed-end condition is appropriate for column bases but underestimates the potential for column lateral-torsional buckling (due to higher moment gradients in an actual building column). Accounting for the flexibility of the column top connection would have required a more complicated test setup and an additional variable would have been added to the testing matrix. Except for both ends, specimens were not braced laterally to inhibit weak-axis buckling. The clear length of column between the haunches at both ends represented the column height of 15 ft. Testing in this manner allowed for investigation of steel column behavior without placing excess demand on the welded column base plate connection.

Specimens consisted of an 18 ft column section with 3 in. thick base plates welded on each end (see Figure 3.2). Column flange to base plate welds were electro-slag welds and the column web was fillet welded to the base plate. Specimens were attached the reaction fixtures with 28 high-strength threaded rods per base plate. Re-usable haunches, shown in Figures 3.3 and 3.4, were bolted to both flanges and each side of the web on both ends of the specimen. The 18 in. length of haunches on each end of the specimen resulted in a clear column length of 15 ft. Shim plates were used between the haunches and column to accommodate the variation in column section dimensions for the different specimen sizes.

3.4 Material Properties

Wide-flange column sections were specified to be ASTM A992 material. The values shown in Table 3.2 are the material properties of the column sections obtained from tension coupon testing by Testing Services & Inspection (TSI), Inc. and Certified Mill Test Reports.

Column base plates and plate material for the haunches were specified to be ASTM A36. Haunch-to-column bolts were 1-1/2 in. dia. ASTM A490 high-strength structural bolts and were tensioned to a minimum of 148 kips, the minimum specified pretension for slip-critical connections (AISC 2005b).

3.5 Instrumentation

A combination of displacement transducers, strain gage rosettes, and uni-axial strain gages were placed in specific locations on the specimen to measure global and local response. Displacement transducers were positioned as shown in Figure 3.5. The various strain gage rosettes and uni-axial strain gages were used to measure strain throughout the column length (see Figure 3.6). In addition, longitudinal and lateral displacement of the SRMD platen and longitudinal and lateral load applied to move the platen (load applied to specimen) were recorded.

3.6 Loading History

The loading history for the test specimens was developed as described in Chapter 2. Three different loading schemes were used during testing to overcome difficulties encountered in simultaneously controlling the SRMD input longitudinal and lateral displacements to achieve both the desired column axial load targets and story drift targets. Table 3.3 provides the specimen testing sequence and loading scheme (A, B, or C) used for each specimen. For all loading schemes the story drift ratio combined with a column clear length of 15 ft was used to compute the input lateral displacements for the SRMD platen. The target column axial load was used to calculate a target axial displacement based on specimen axial stiffness and a known SRMD system stiffness in the longitudinal direction.

Loading Scheme A (Specimens W14×132-35 and W14×176-35) was based on an earlier version of the loading sequence than presented in Chapter 2. BRBs were assumed to yield at 0.003 rad. story drift ratio and a bilinear column axial load versus story drift relationship (see Figure 3.7) was used to calculate column axial loads. This calculation was based on reaching the target column compressive axial load, P_T, ($0.35P_y$) at 6% story drift. Table 3.4 provides the Loading Scheme A story drift ratio sequence. The loading sequences for Specimens W14×132-35 and W14×176-35 are shown in Figures 3.8 and 3.9, respectively. Axial load and drift were in-phase to represent realistic frame action. Note that Specimen W14×132-35 was tested to 6% drift and Specimen W14×176-35 was tested to 10% drift. It was observed during testing and data analysis of these two specimens that for large cycles, greater than 2% drift, the column axial load targets were

not achieved. This was in part due to the significant column axial displacement component from applied lateral displacement (drift) and in part due to softening of column response from yielding and local buckling.

Loading Scheme B (Specimens W14×132-55) was based on the loading sequence presented in Chapter 2 (see Table 3.5). Axial load and drift were simultaneously applied in-phase with each other. Loading Scheme B was different from Loading Scheme A in that it accounted for the significant column axial displacement component from drift in calculation of the applied longitudinal displacements. However, the column axial load targets for large drift cycles were still not achieved due to softening of column response from yielding and local buckling and, therefore, Loading Scheme C was developed.

Loading Scheme C (all remaining specimens) was identical to Loading Scheme B through the 1.5% drift cycles. Calculation of column axial loads at the protocol drift levels were based on reaching the target column compressive axial load, P_T, (e.g., $0.35P_y$, $0.55P_y$, $0.75P_y$) at 0.002 rad. story drift ratio (yield drift) and axial loads for all excursions larger than the yield drift were equal to the maximum level for that specimen. The story drift and column axial load were in-phase (see Figure 2.20) to represent realistic frame action. For cycles at 2% drift and beyond the drift component of displacement was applied first, followed by application of longitudinal displacement until the target axial load was achieved. This part of the loading scheme is illustrated in Figure 3.10. By loading in this manner the tests could still be safely conducted in displacement control and the combined target axial loads and story drifts could be achieved.

Figure 3.11 shows typical *P-M* interaction and moment versus drift response for the 4% drift cycle of Specimen W14×132-75 (Loading Scheme C). The labeled points on the graphs correspond to points from the loading sequence shown in Figure 3.11(a) and indicate the direction of motion in these responses. The trends observed from this single cycle are typical of those observed for this form of the loading sequence. Points 2 and 5 correspond to points where the target values of axial load and drift were reached. These points will be indicated as discrete points in the results presented in Chapters 4 to 6. In particular, point 5 (target compressive axial load and drift) was of primary interest for defining the test specimen drift capacity under high axial load.

3.7 Axial Load-Moment Interaction Surface

The axial load-moment (*P*-M) interaction surface, shown in Figure 3.12, is provided along with the experimental and analytical results in the following chapters. Plastic moment capacity, M_p was calculated as the plastic section modulus times the yield strength. Tension axial load capacity, P_{yt} was calculated as the section area times the yield strength. Compression axial load capacity, P_{yc} was calculated based on weak axis buckling with an effective length factor equal to 0.6 (fixed-fixed end condition). The column length in these calculations was assumed to equal 16.5 ft (average of 18 ft total length and 15 ft clear length) to account for the fact that the haunches did not provide a perfectly fixed end condition. Chapter 4 presents *P-M* interaction surfaces calculated using both nominal and actual material properties. Where not indicated, the interaction surface was based on nominal material properties. Note that no LRFD strength reduction factors were applied in determination of the *P-M* interaction surface ordinates.

3.8 Drift Capacity

To determine specimen ductility a definition of the yield rotation and drift capacity are required. The yield rotation for the W14 sections tested, calculated from Eq. (3.1), ranged from 0.70% to 0.79%.

$$\theta_y = \frac{M_p H}{6EI_x} \tag{3.1}$$

where

E = modulus of elasticity (29,000 ksi)
I_x = moment of inertia about the x-axis
H = column clear length (180 in.)
M_p = plastic moment
θ_y = yield rotation

This calculation neglects the decrease in yield rotation due to the presence of axial load. Ductility of beam-columns calculated using this value of yield rotation will therefore provide a conservative approximation of the actual ductility.

An example plot of the end moment versus drift response based on the target points on the compression side is shown in Figure 3.13. An allowable 10% reduction from peak moment resistance, M_{max} has been used to define the drift capacity. The horizontal line shown is at 90% of the maximum moment. This 10% reduction from the peak moment resistance may be conservative, but given the critical function of columns, was deemed appropriate at this time. An approximation of the specimen ductility is, therefore, determined as the drift capacity divided by the yield rotation.

Table 3.1 Test Matrix

Specimen Designation	Width-Thickness Ratio		Gravity Load ($0.15P_n$)	Total Column Axial Load
	$b_f/2t_f$	h/t_w		
W14×132-35	7.2	17.7	246 kips	$0.35P_y$ (679 kips)
W14×132-55				$0.55P_y$ (1067 kips)
W14×132-75				$0.75P_y$ (1455 kips)
W14×176-35	6.0	13.7	335 kips	$0.35P_y$ (907 kips)
W14×176-55				$0.55P_y$ (1425 kips)
W14×176-75				$0.75P_y$ (1943 kips)
W14×233-35	4.6	10.7	446 kips	$0.35P_y$ (1199 kips)
W14×233-55				$0.55P_y$ (1884 kips)
W14×370-35	3.1	6.9	718 kips	$0.35P_y$ (1908 kips)

Table 3.2 Steel Mechanical Properties

Member	Steel Grade	Yield Strength[a] (ksi)	Tensile Strength[a] (ksi)	Elongation[a,b] (%)	Heat No.	Steel Mill
W14×132 Flange Web	A992	68.7 (55.5) 55.9	77.9 (71.5) 79.0	36 (24) 37	249171	Nucor-Yamato
W14×176 Flange Web	A992	59.4 (56.5) 58.3	80.5 (75.5) 79.7	46 (23.5) 32	238477	Nucor-Yamato
W14×233 Flange Web	A992	61.0 (60.0) 59.7	85.6 (77.0) 85.3	38.5 (24.5) 42	251442	Nucor-Yamato
W14×370 Flange Web	A992	60.0 (54.5) 55.0	81.1 (72.5) 76.0	44 (26) 40	251259	Nucor-Yamato

[a]Values in parentheses are based on Certified Mill Test Reports, others from testing by TSI.
[b]Certified Mill Test Report elongation in parentheses based on 8 in. gage length, others based on 2 in. gage length.

Table 3.3 Test Sequence and Loading Scheme

Specimen Designation	Test Sequence	Loading Scheme
W14×132-35	1	A
W14×132-55	3	B
W14×132-75	5	C
W14×176-35	2	A
W14×176-55	4	C
W14×176-75	6	C
W14×233-35	7	C
W14×233-55	8	C
W14×370-35	9	C

Table 3.4 Loading Scheme A: Story Drift Ratio Loading Sequence

Load Step	Story Drift Ratio	Number of Cycles
0	Apply column axial gravity load	
1	0.001	6
2	0.002	6
3	0.003	6
4	0.004	6
5	0.005	4
6	0.0075	2
7	0.01	2
8	0.015	2
9[a]	0.02	1

[a]Continue with increments in Story Drift Ratio of 0.01, and perform one cycle at each step

Table 3.5 Loading Schemes B and C: Story Drift Ratio Loading Sequence

Load Step	Story Drift Ratio	Number of Cycles
0	Apply column axial gravity load	
1	0.001	6
2	0.0015	6
3	0.002	6
4	0.003	4
5	0.004	4
6	0.005	4
7	0.0075	2
8	0.01	2
9	0.015	2
10[a]	0.02	1

[a]Continue with increments in Story Drift Ratio of 0.01, and perform one cycle at each step

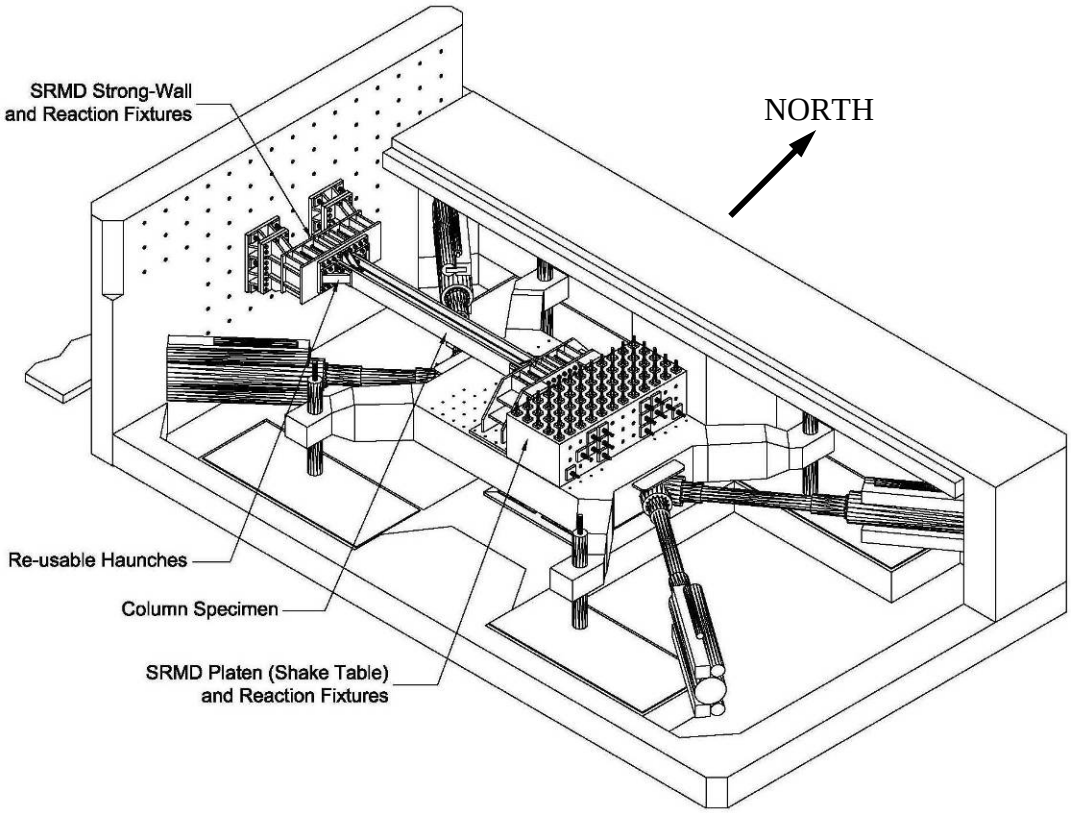

(a) Schematic View

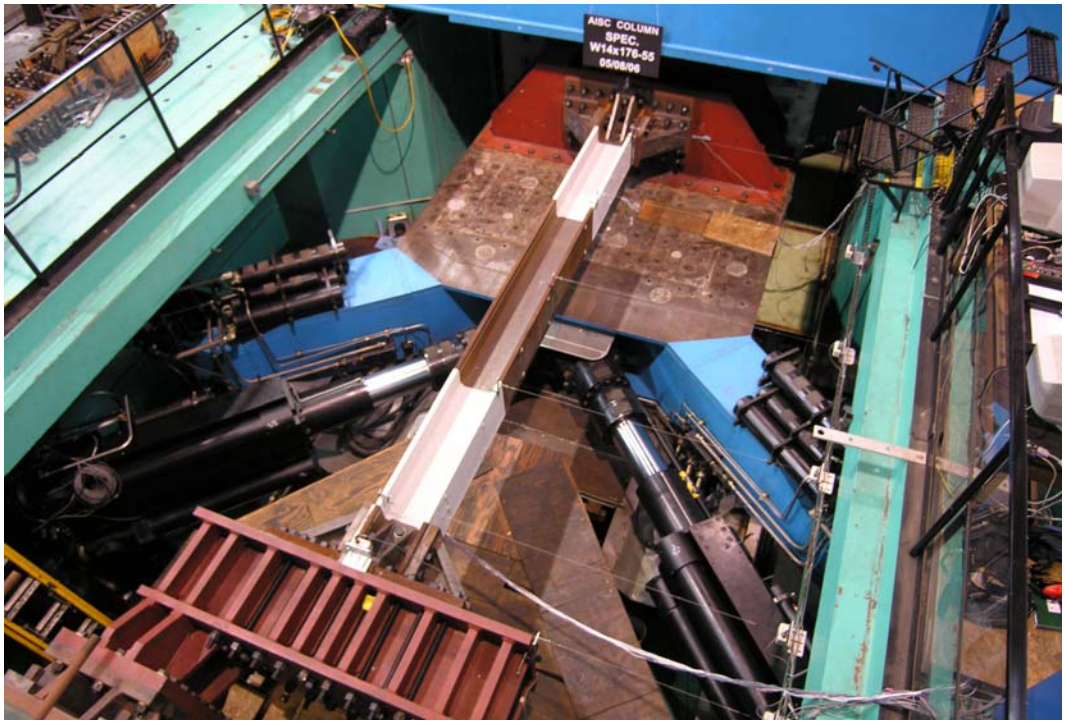

(b) Overview of Specimen

Figure 3.1 SRMD Test Facility

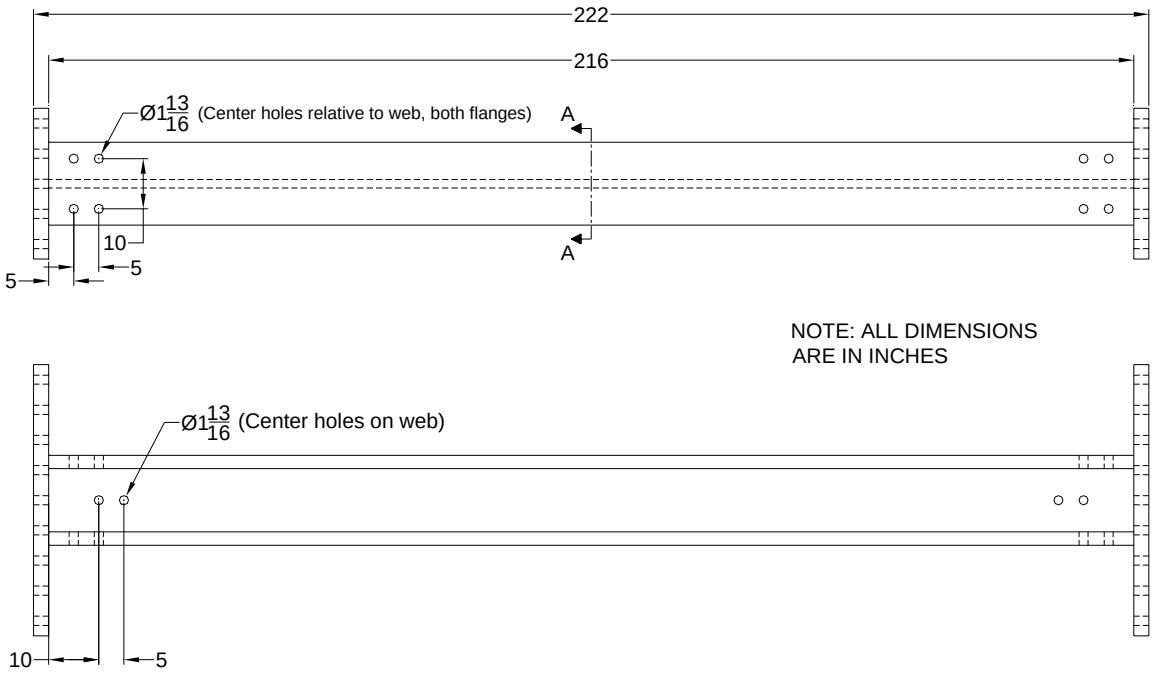

(a) Overall Dimensions

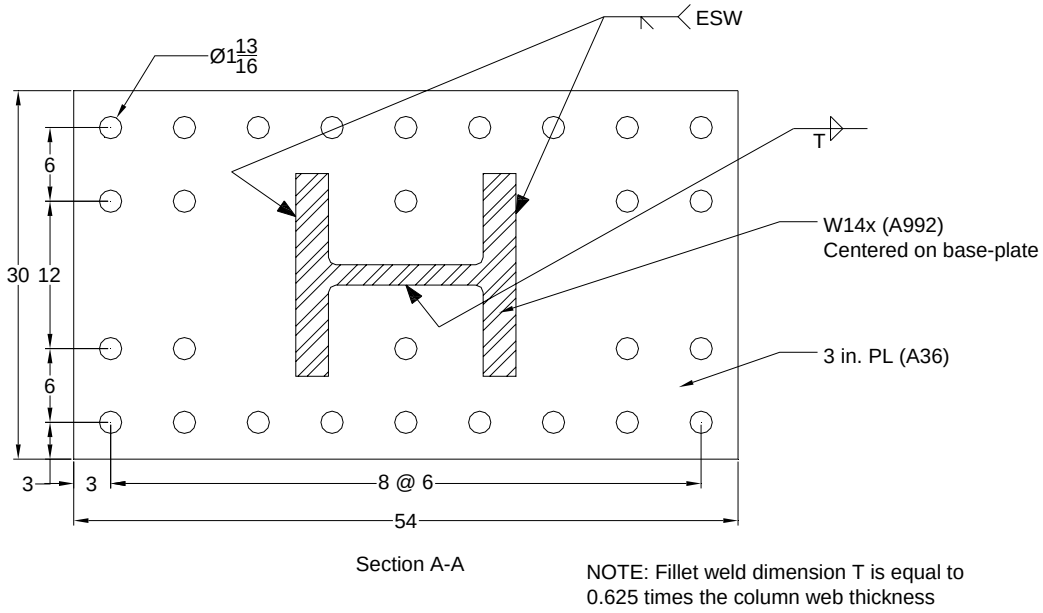

(b) Base Plate

Figure 3.2 Specimen Details

Figure 3.3 Re-Usable Haunches

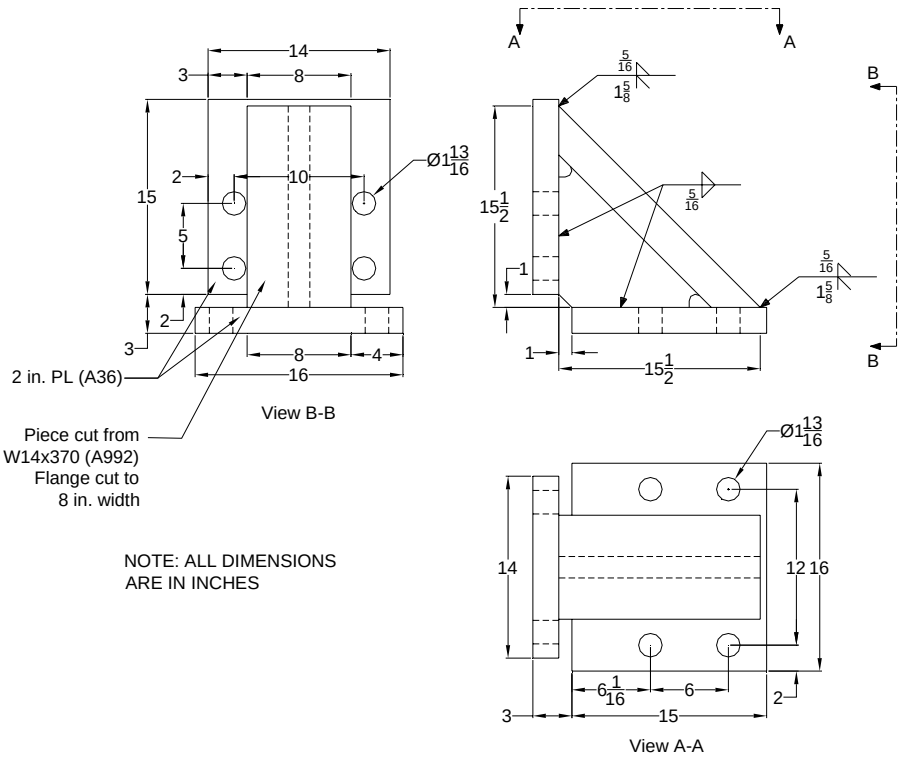

(a) Flange Haunch

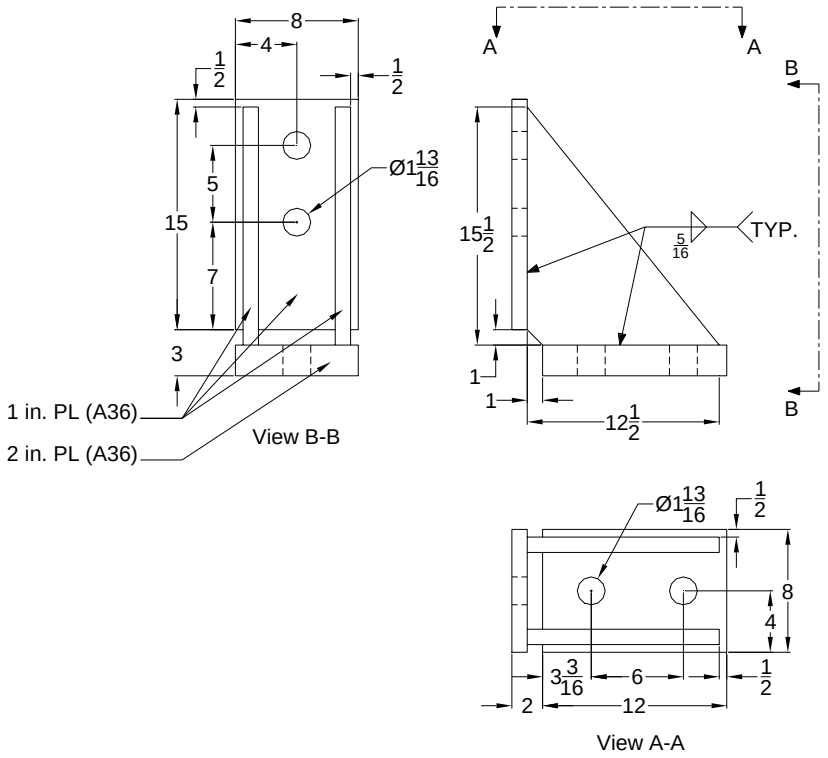

(b) Web Haunch

Figure 3.4 Re-Usable Haunch Details

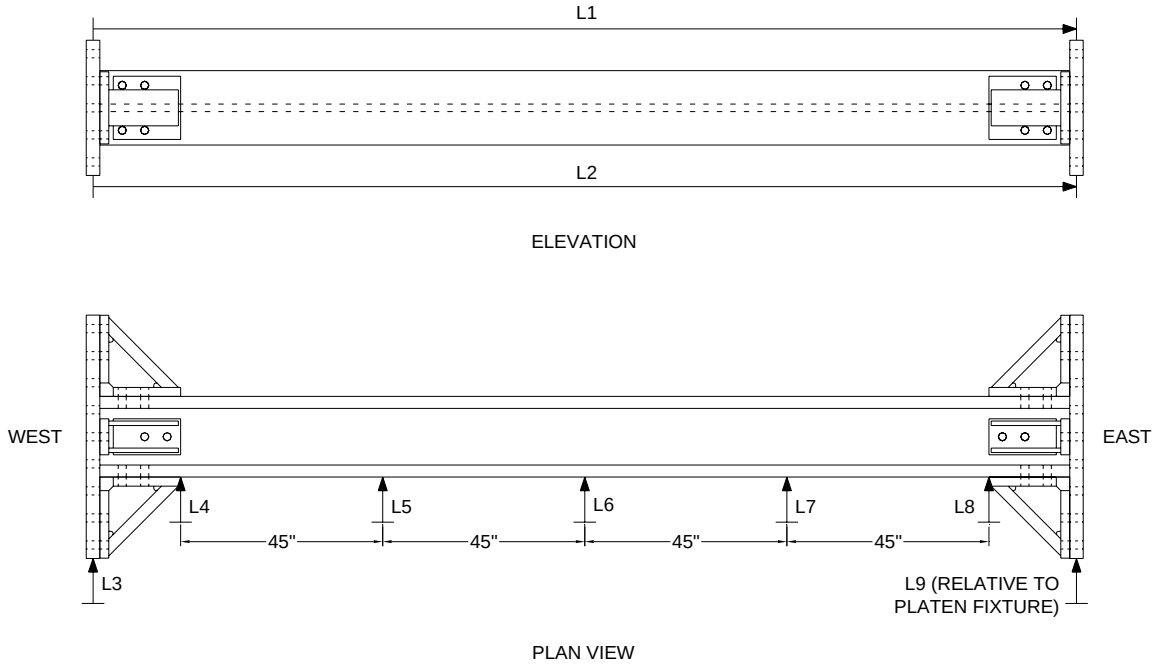

Figure 3.5 Specimen Displacement Transducers

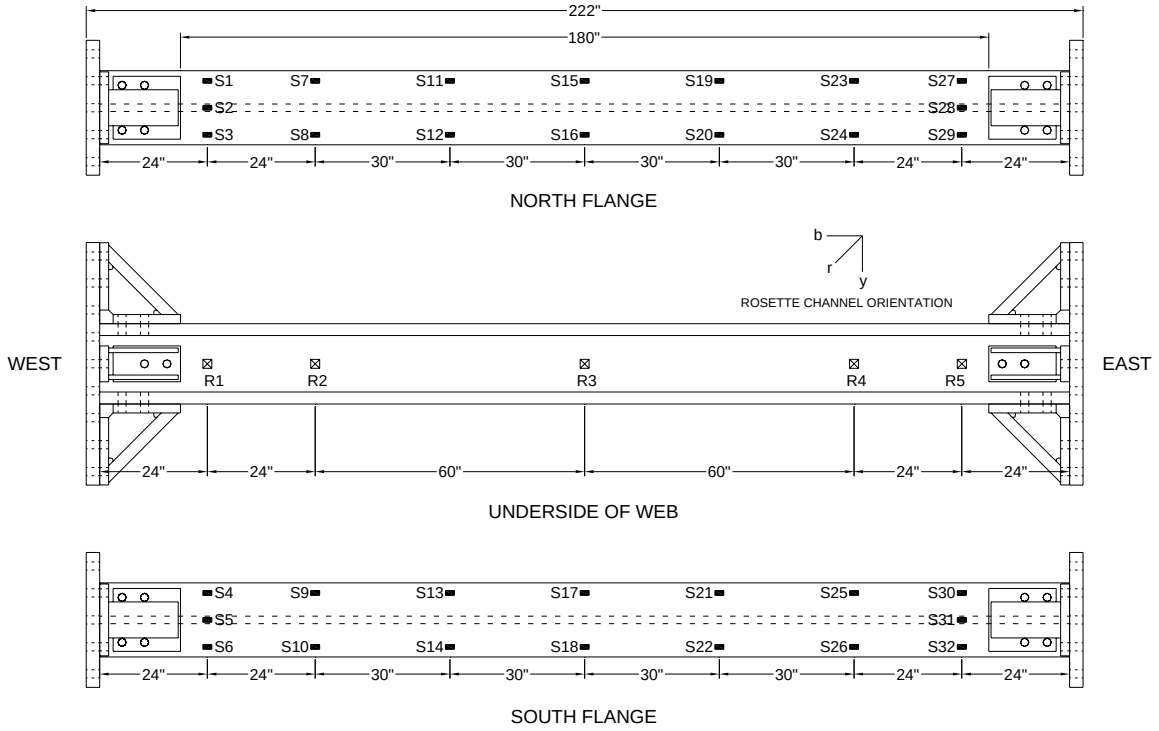

Figure 3.6 Specimen Strain Gages and Rosettes

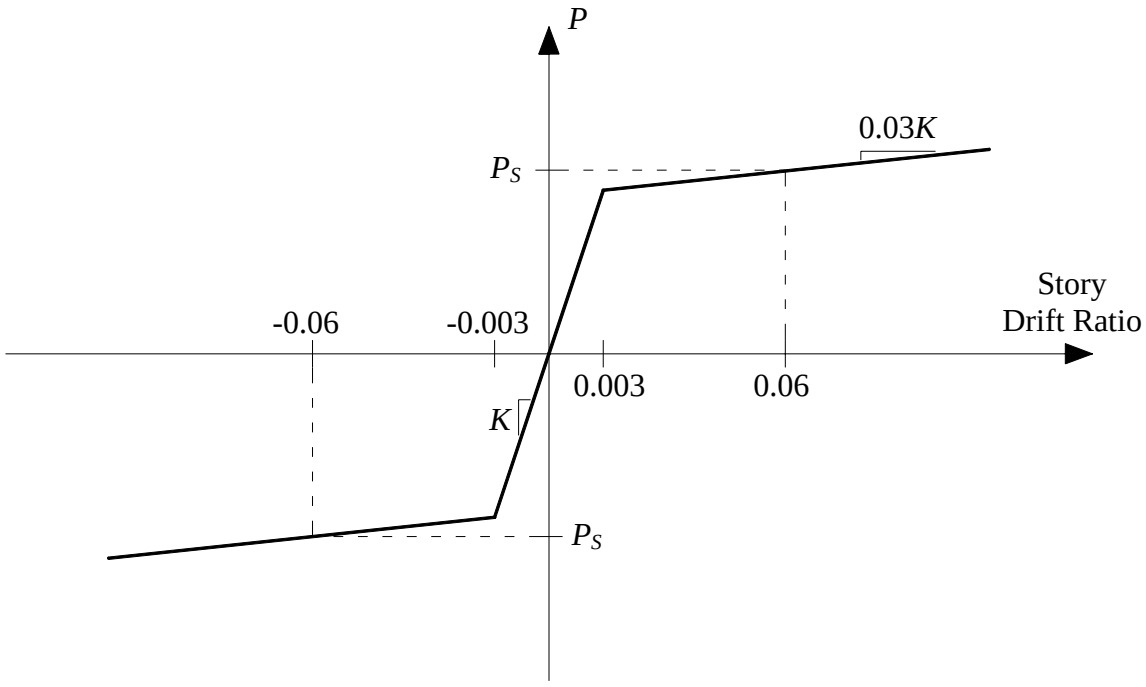

(a) Seismic Load

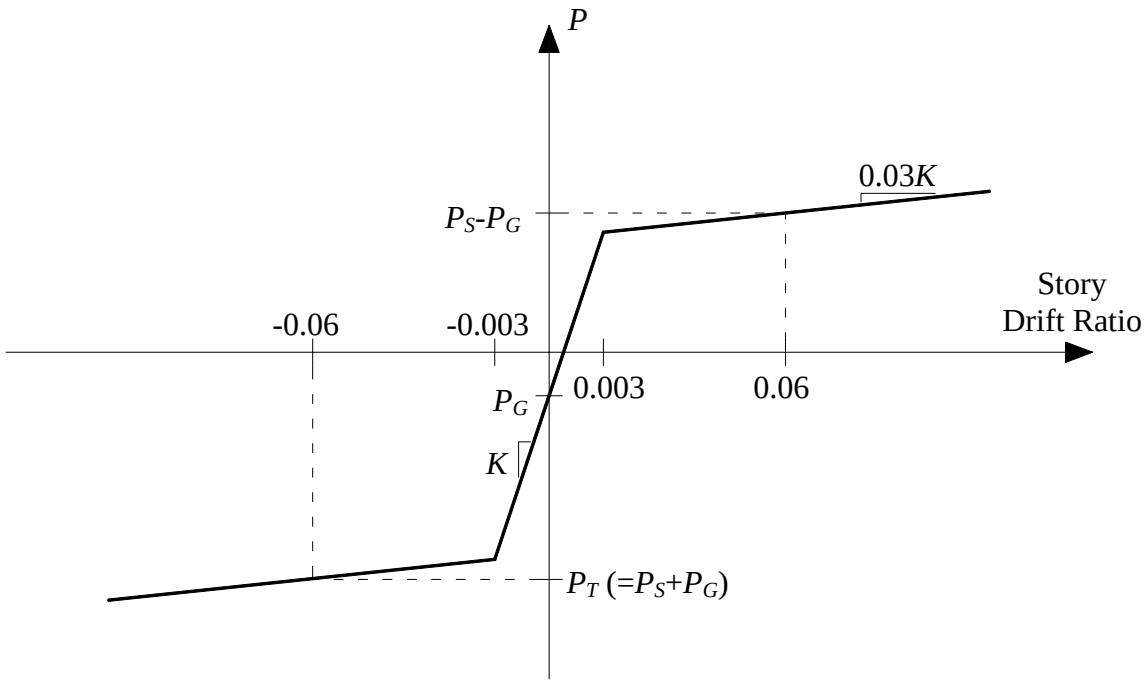

(b) Combined Seismic and Gravity Load

Figure 3.7 Bilinear Column Axial Load versus Story Drift Ratio Relationship

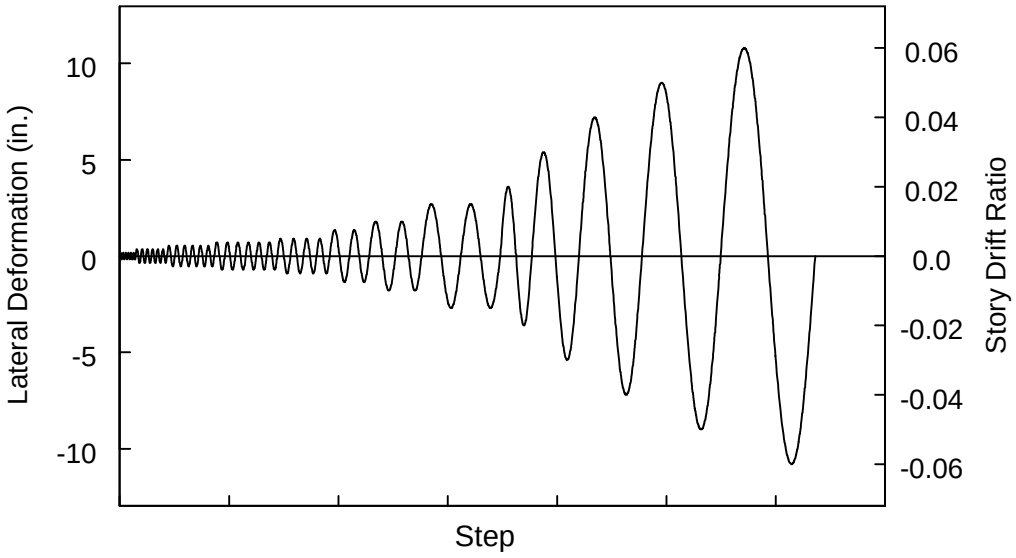

(a) Lateral Deformation

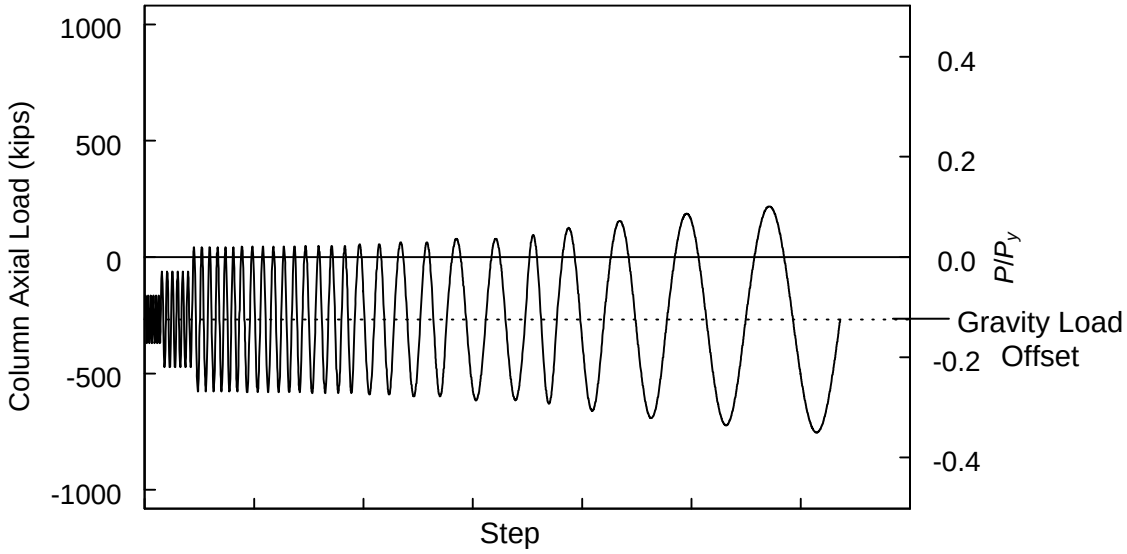

(b) Axial Load

Figure 3.8 Specimen W14×132-35: Loading Sequence

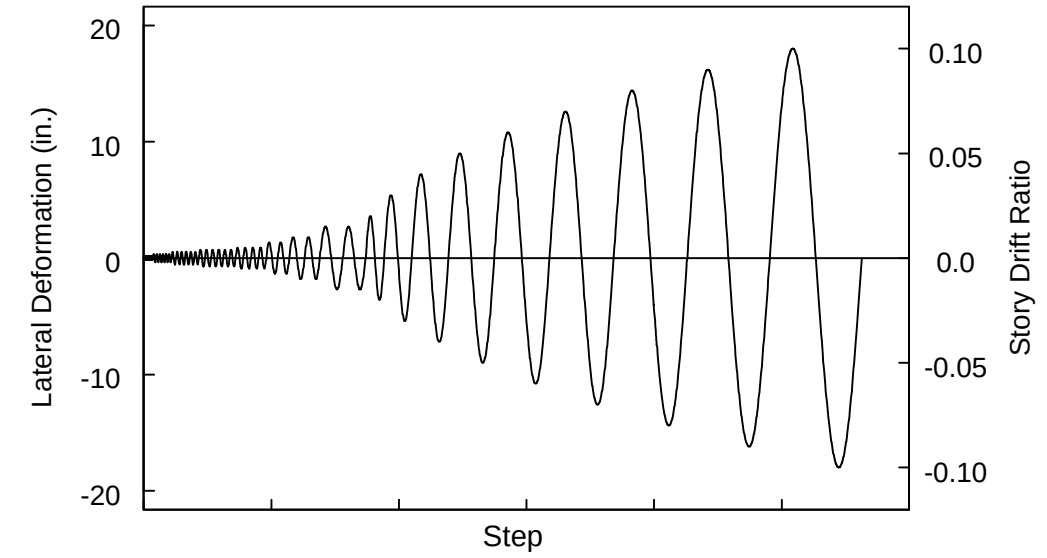

(a) Lateral Deformation

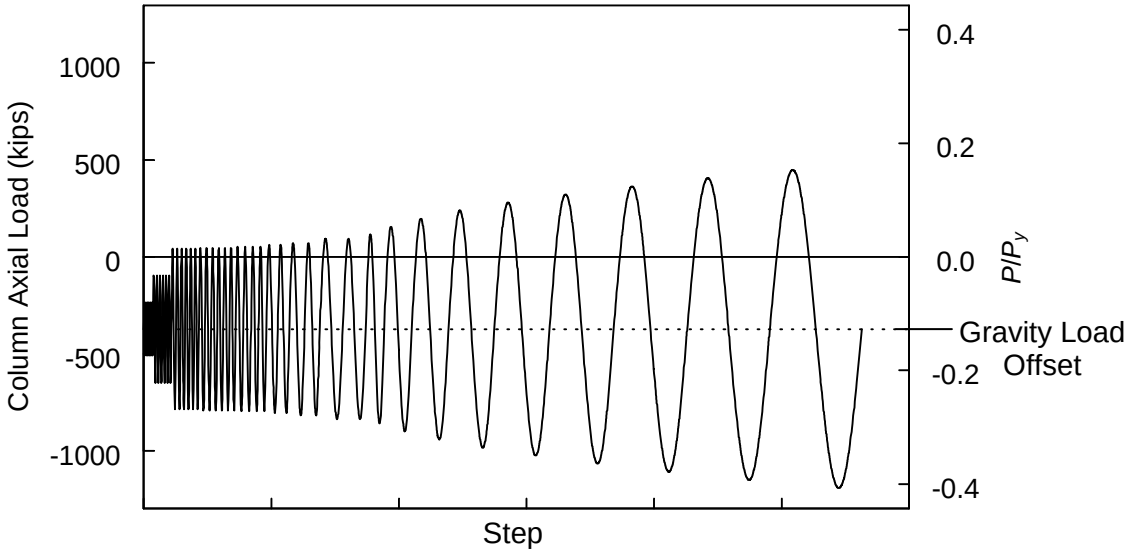

(b) Axial Load

Figure 3.9 Specimen W14×176-35: Loading Sequence

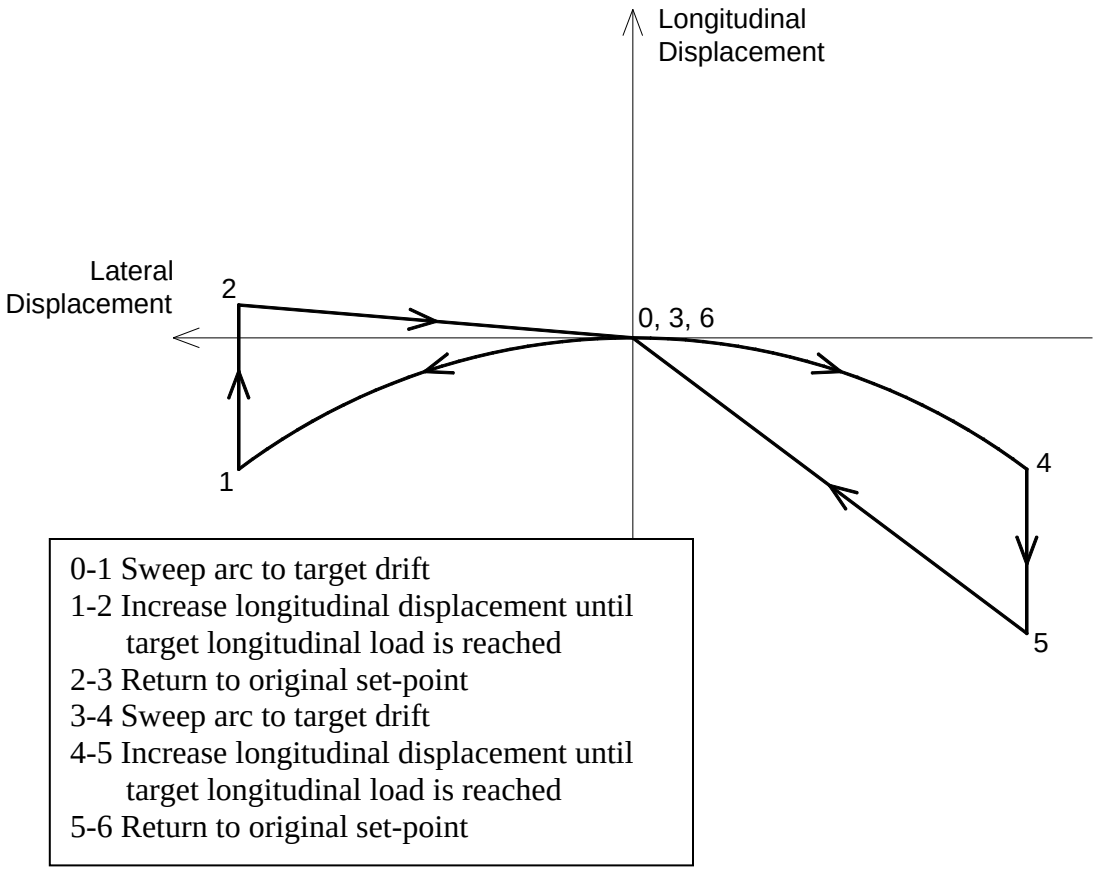

Figure 3.10 Sequence for Loading Scheme C (2% Drift and Beyond)

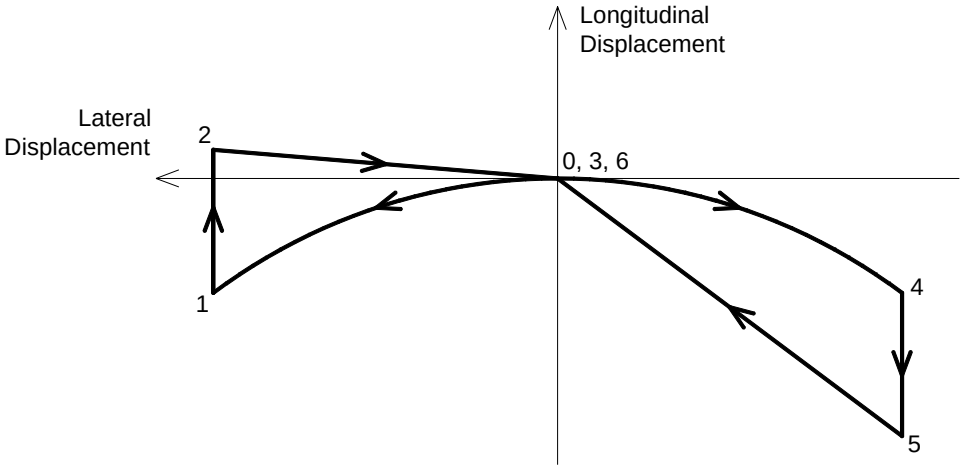

(a) Loading Sequence

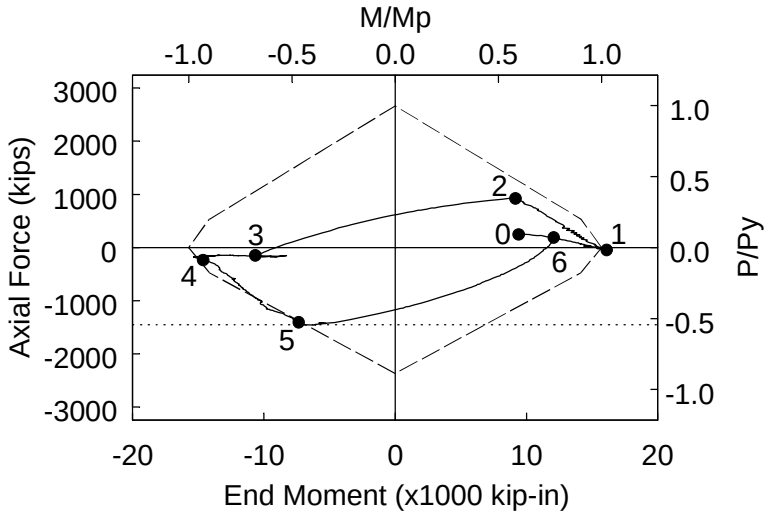

(b) *P*-*M* Interaction

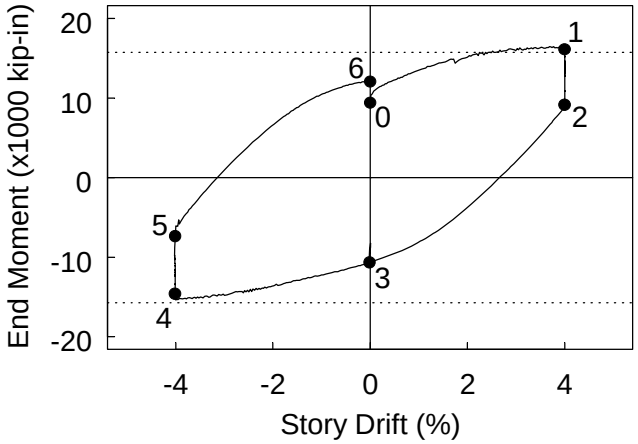

(c) End Moment versus Drift

Figure 3.11 Specimen W14×132-75: 4% Drift Cycle

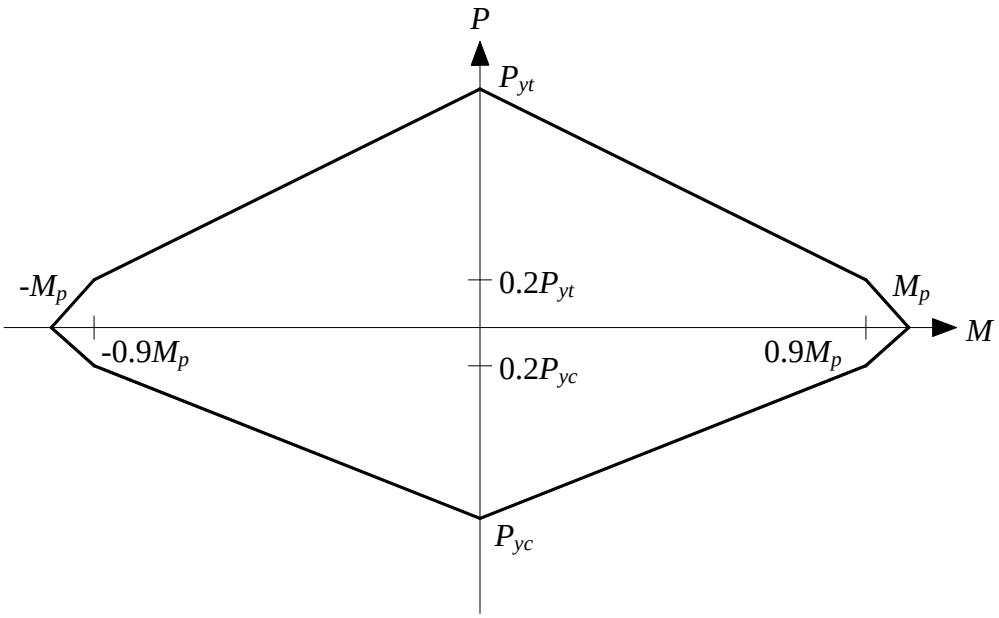

Figure 3.12 *P-M* Interaction Curve for Column Specimens

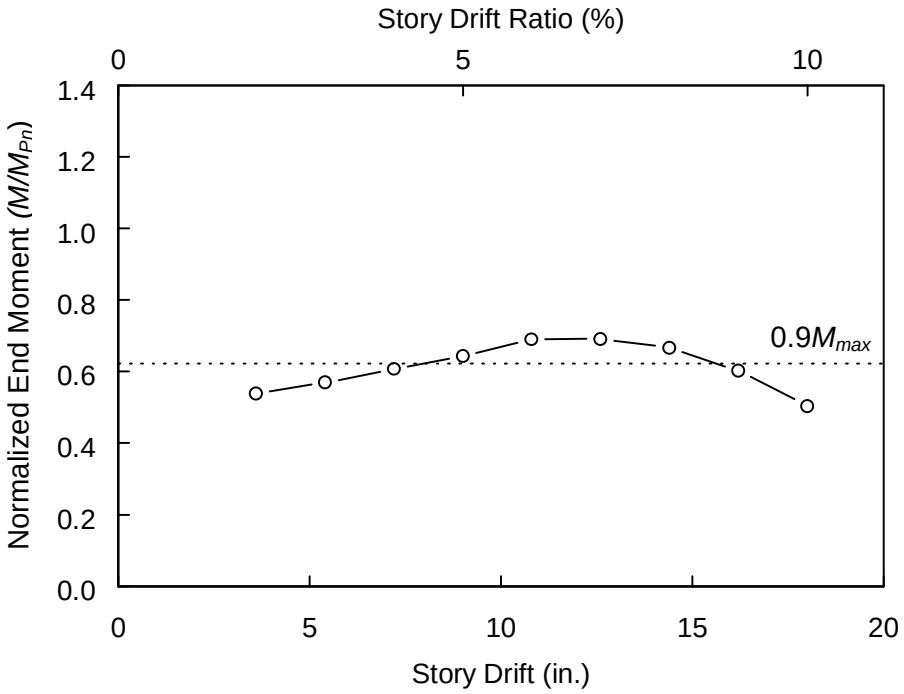

Figure 3.13 Target Point End Moment versus Drift Response

4. TEST RESULTS

4.1 Introduction

This chapter presents the observed performance and recorded response for the nine column specimens. Figures are included which show the progression of yielding, flange local buckling, and overall deformation with increasing drift. Also included, where appropriate, are figures showing specimen fracture. Plots of axial load-moment (*P-M*) interaction and moment versus drift response illustrate specimen global behavior. Table 4.1 provides a summary of the drift achieved by each specimen and well as a description of any specimen fractures. Selected plots of specimen strain versus story drift ratio for all specimens are provided in Appendix B.

The specimen end moment was calculated from Eq. (4.1) with the assumption that the inflection point (double curvature bending) was in the middle of the column length.

$$M = \frac{1}{2}(VH - P_L\Delta) \tag{4.1}$$

where

H = column clear length (180 in.)
M = end moment
P_L = longitudinal force from SRMD (positive for tension)
V = lateral force from SRMD
Δ = lateral displacement from SRMD

4.2 Specimen W14×132-35

4.2.1 General

Specimen W14×132-35 ($0.35P_y$ axial load target) was tested on November 22, 2005 using Loading Scheme A. Lateral drifts of up to 6% (10.8 in.) were applied. For large cycles, greater than 2% drift, the column axial load targets were not achieved for the reasons described in Chapter 3. An axial compressive load offset of $0.15P_n$ (246 kips) was initially applied for the W14×132 specimens, followed by cyclic, increasing amplitude longitudinal and lateral displacement.

4.2.2 Observed Performance

Figure 4.1 shows the progression of yielding at each end of the specimen. Flange local buckling, as shown in Figure 4.2, began to develop at 5% drift. Photos showing the specimen overall deformed configuration at 4% and 6% drift are shown in Figure 4.3. No fracture of the test specimen was observed.

4.2.3 Recorded Response

The axial load-moment interaction is shown in Figure 4.4, along with the *P-M* interaction surfaces based on actual and nominal material properties. The horizontal line shown is at the target compressive axial load level of $0.35P_{yn}$. Figure 4.5 shows the end moment versus story drift relationship. The horizontal lines shown are at the nominal plastic moment capacity of the section. Plots of longitudinal force versus lateral force, longitudinal force versus column axial displacement, and lateral force versus lateral displacement are provided in Figure 4.6. The column axial displacement shown in Figure 4.6(b) was calculated from the average of displacement transducers L1 and L2 (see Figure 3.5).

4.3 Specimen W14×132-55

Specimen W14×132-55 ($0.55P_y$ axial load target) was tested on May 1, 2006 using Loading Scheme B. Lateral drifts of up to 8% (14.4 in.) were applied. For large cycles, greater than 2% drift, the column axial load targets were not achieved for the reasons described in Chapter 3.

4.3.1 Observed Performance

Figure 4.7 shows the progression of yielding at each end of the specimen. The progression of flange local buckling is shown Figure 4.8. Photos showing the specimen overall deformed configuration at 4% and 8% drift are shown in Figure 4.9. No fracture of the test specimen was observed.

4.3.2 Recorded Response

The recorded *P-M* interaction is shown in Figure 4.10 and the end moment versus story drift response is shown in Figure 4.11. Plots of longitudinal force versus lateral force, longitudinal force versus column axial displacement, and lateral force versus lateral displacement are provided in Figure 4.12. The jagged response observed in these global response plots resulted from using manual control of the input displacements in the refinement of the Loading Scheme C.

4.4 Specimen W14×132-75

Specimen W14×132-75 ($0.75P_y$ axial load target) was tested on May 11, 2006 using Loading Scheme C. Lateral drifts of up to 10% (18 in.) were applied.

4.4.1 Observed Performance

Figure 4.13 shows the progression of yielding at each end of the specimen. The progression of flange local buckling is shown Figure 4.14. Photos showing the specimen overall deformed configuration at large drifts are shown in Figure 4.15. On the +10% drift excursion the column flange completely fractured through the bolt hole net section and propagated partially through the web (see Figure 4.16). Despite the fracture, the 10% drift cycle was completed with drift and axial load targets being achieved.

4.4.2 Recorded Response

The overall *P-M* interaction is shown in Figure 4.17. Figure 4.18 shows the *P-M* interaction surface and *P-M* interaction for discrete points corresponding to points in the loading history (from 2% to 10% drift) when the target values of axial load and drift were achieved. These points correspond to points 2 and 5 of the loading sequence shown in Figure 3.10. The overall moment versus drift response is shown in Figure 4.19 along with points corresponding to when the target values of axial load and drift were achieved. These points represent the response of primary interest in this study of columns under combined high axial load and drift demand. Figure 4.20 provides a plot of the end moment versus drift response based on the target points on the compression side. The maximum moment (combined with the target axial load) was reached at 6% drift. The

horizontal line shown is at 90% of this maximum moment. Using a 10% reduction from M_{max} to define the drift capacity, the drift capacity for this specimen was 7%. Additional force-displacement response plots are shown in Figure 4.21.

4.5 Specimen W14×176-35

Specimen W14×176-35 (0.35P_y axial load target) was tested on November 29, 2005 using Loading Scheme A. Lateral drifts of up to 10% (18 in.) were applied. For large cycles, greater than 2% drift, the column axial load targets were not achieved for the reasons described in Chapter 3. An axial compressive load offset of 0.15P_n (335 kips) was initially applied for the W14×176 specimens.

4.5.1 Observed Performance

Figure 4.22 shows the progression of yielding at each end of the specimen for 2% to 10% drift. Flange local buckling, as shown in Figure 4.23, began to develop at 6% drift. Photos showing the specimen overall deformed configuration at large drifts are shown in Figure 4.24. The specimen completed the 10% drift cycle. After testing a partial fracture of the column flange was observed, as shown in Figure 4.25.

4.5.2 Recorded Response

The *P-M* interaction and moment versus drift response are shown in Figures 4.26 and 4.27 respectively. Plots of longitudinal force versus lateral force, longitudinal force versus column axial displacement, and lateral force versus lateral displacement are provided in Figure 4.28.

4.6 Specimen W14×176-55

Specimen W14×176-55 (0.55P_y axial load target) was tested on May 8, 2006 using Loading Scheme C. Lateral drifts of up to 10% (18 in.) were applied.

4.6.1 Observed Performance

Figure 4.29 shows the progression of yielding at each end of the specimen. The progression of flange local buckling is shown in Figure 4.30. Photos showing the

specimen overall deformed configuration at large drifts are shown in Figure 4.31. Near the end of the 10% drift cycle the column flange completely fractured through the bolt hole net section and propagated partially through the web (see Figure 4.32).

4.6.2 Recorded Response

Figure 4.33 shows the overall *P-M* interaction and Figure 4.34 shows the *P-M* interaction for points where the axial load and drift target points were achieved. Figure 4.35 shows the overall moment versus drift response along with the points where the targets were reached. The plot of the end moment versus drift response based on the target points on the compression side, shown in Figure 4.36, indicates the drift capacity for this specimen was 9%, based on an allowable 10% reduction in moment from M_{max}. Figure 4.37 provides additional force-displacement response plots.

4.7 Specimen W14×176-75

Specimen W14×176-75 (0.75P_y axial load target) was tested on May 15, 2006 using Loading Scheme C. Lateral drifts of up to 10% (18 in.) were applied.

4.7.1 Observed Performance

Figure 4.38 shows the progression of yielding at each end of the specimen. Increasing amplitude of flange local buckling from 4% to 10% drift is shown in Figure 4.39. Photos showing the specimen overall deformed configuration at large drifts are shown in Figure 4.40. On the 10% drift cycle the column flange completely fractured through the bolt hole net section and propagated partially through the web (see Figure 4.41). Despite the fracture, the 10% drift cycle was completed with drift and axial load targets being achieved.

4.7.2 Recorded Response

The recorded overall *P-M* interaction is shown in Figure 4.42, along with the *P-M* interaction yield surface. Figure 4.43 shows the *P-M* interaction for the target points. Notice on the tension side that the moment was essentially reduced to zero at 10% drift after fracture of the column flange but the target axial load was still achieved. Figure 4.44 shows the overall and target point moment versus drift response. A drift capacity of

8% was observed from Figure 4.45, which shows the end moment versus drift response based on the target points on the compression side. Longitudinal and lateral force versus displacement response is shown in Figure 4.46.

4.8 Specimen W14×233-35

Specimen W14×233-35 ($0.35P_y$ axial load target) was tested on May 18, 2006 using Loading Scheme C. Lateral drifts of up to 8% (14.4 in.) were applied. An axial compressive load offset of $0.15P_n$ (446 kips) was initially applied for the W14×233 specimens.

4.8.1 Observed Performance

Figure 4.47 shows the yielding pattern at each end of the specimen for 2% to 8% drift. The progression of flange local buckling is shown in Figure 4.48. Photos showing the specimen overall deformed configuration at large drift are shown in Figure 4.49. On the +9% drift cycle the specimen experienced a "divot" pull out fracture of the flange-to-base plate welded joint (see Figure 4.50) and testing was suspended.

4.8.2 Recorded Response

Figure 4.51 shows the *P-M* interaction and Figure 4.52 shows the *P-M* interaction for points where the axial load and drift target points were achieved. Figure 4.53 shows the overall moment versus drift response along with the points where the targets were reached. The plot of the end moment versus drift response based on the target points on the compression side, shown in Figure 4.54, indicates the drift capacity for this specimen was 8%, as limited by fracture of the column flange to base plate welded joint on the +9% drift excursion. Figure 4.55 provides additional force-displacement response plots.

4.9 Specimen W14×233-55

Specimen W14×233-55 ($0.55P_y$ axial load target) was tested on May 22, 2006 using Loading Scheme C. Lateral drifts of up to 10% (18 in.) were applied.

4.9.1 Observed Performance

Figure 4.56 shows the yielding pattern at each end of the specimen. The progression of flange local buckling is shown Figure 4.57. Photos showing the specimen overall deformed configuration at large drift are shown in Figure 4.58. Testing of the specimen was suspended just prior to achieving the -9% drift targets due to an issue with the SRMD machine. No fracture of the test specimen was observed.

4.9.2 Recorded Response

The recorded *P-M* interaction is shown in Figure 4.59, along with the *P-M* interaction yield surface. Figure 4.60 shows the *P-M* interaction for the target points. Figure 4.61 shows the overall and target point moment versus drift response. A drift capacity of at least 8% was observed from Figure 4.62, which shows the end moment versus drift response based on the target points on the compression side. A higher allowable drift would have likely been observed if there had not been a mechanical issue with the SRMD machine. Longitudinal and lateral force versus displacement response is shown in Figure 4.63.

4.10 Specimen W14×370-35

Specimen W14×370-35 ($0.35P_y$ axial load target) was tested on May 26, 2006 using Loading Scheme C. Lateral drifts of up to 2% (3.6 in.) were applied. An axial compressive load offset of $0.15P_n$ (718 kips) was initially applied, followed by cyclic testing.

4.10.1 Observed Performance

Figure 4.64 shows the specimen before testing. The yielding pattern at 2% drift is shown in Figure 4.65; only very minor yielding was observed. On the +3% drift cycle the specimen experienced a fracture of the column flange-to-base plate welded joint (see Figure 4.66). Note that no local buckling was observed during testing.

4.10.2 Recorded Response

The *P-M* interaction and moment versus drift response are shown in Figures 4.67 and 4.68, respectively. Plots of longitudinal force versus lateral force, longitudinal force

versus column axial displacement, and lateral force versus lateral displacement are provided in Figure 4.69.

Table 4.1 Testing Summary

Specimen Designation	Testing Summary
W14×132-35	-Achieved 6% drift -Did not achieve axial load targets at high drift due to use of Loading Scheme A -Specimen did not fracture
W14×132-55	-Achieved 8% drift -Did not achieve axial load targets at high drift due to use of Loading Scheme B -Specimen used to further refine loading scheme -Specimen did not fracture
W14×132-75	-Achieved 10% drift -Complete flange net section fracture at haunch bolt holes on +10% drift excursion but was able to complete 10% drift cycle and achieve drift and axial load targets
W14×176-35	-Achieved 10% drift -Did not achieve axial load targets at high drift due to use of Loading Scheme A -Partial flange net section fracture at haunch bolt holes
W14×176-55	-Achieved 10% drift -Complete flange net section fracture at haunch bolt holes on return to zero from -10% drift
W14×176-75	-Achieved 10% drift -Complete flange net section fracture at haunch bolt holes on +10% drift excursion but was able to complete 10% drift cycle and achieve drift and axial load targets
W14×233-35	-Achieved 8% drift -“Divot” pull out fracture of flange to base plate welded joint on +9% drift excursion
W14×233-55	-Achieved 8% drift -Test ended due to SRMD machine issue -Specimen did not fracture
W14×370-35	-Achieved 2% drift -Fracture of flange to base plate welded joint on +3% drift excursion

East End West End

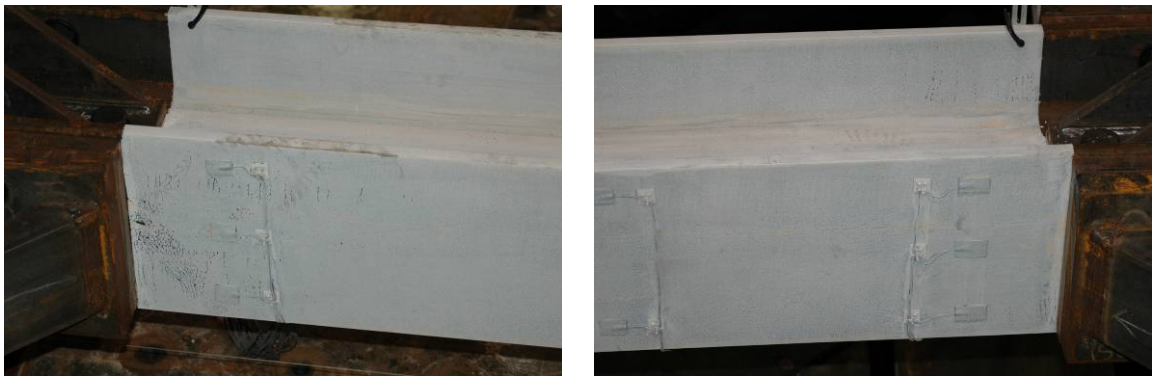

(a) 2% Drift

(b) 4% Drift

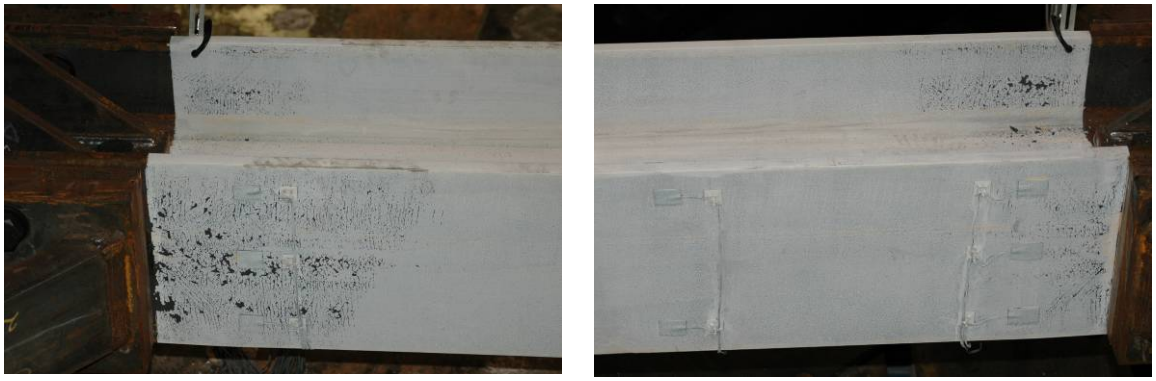

(c) 6% Drift

Figure 4.1 Specimen W14×132-35: Yielding Pattern

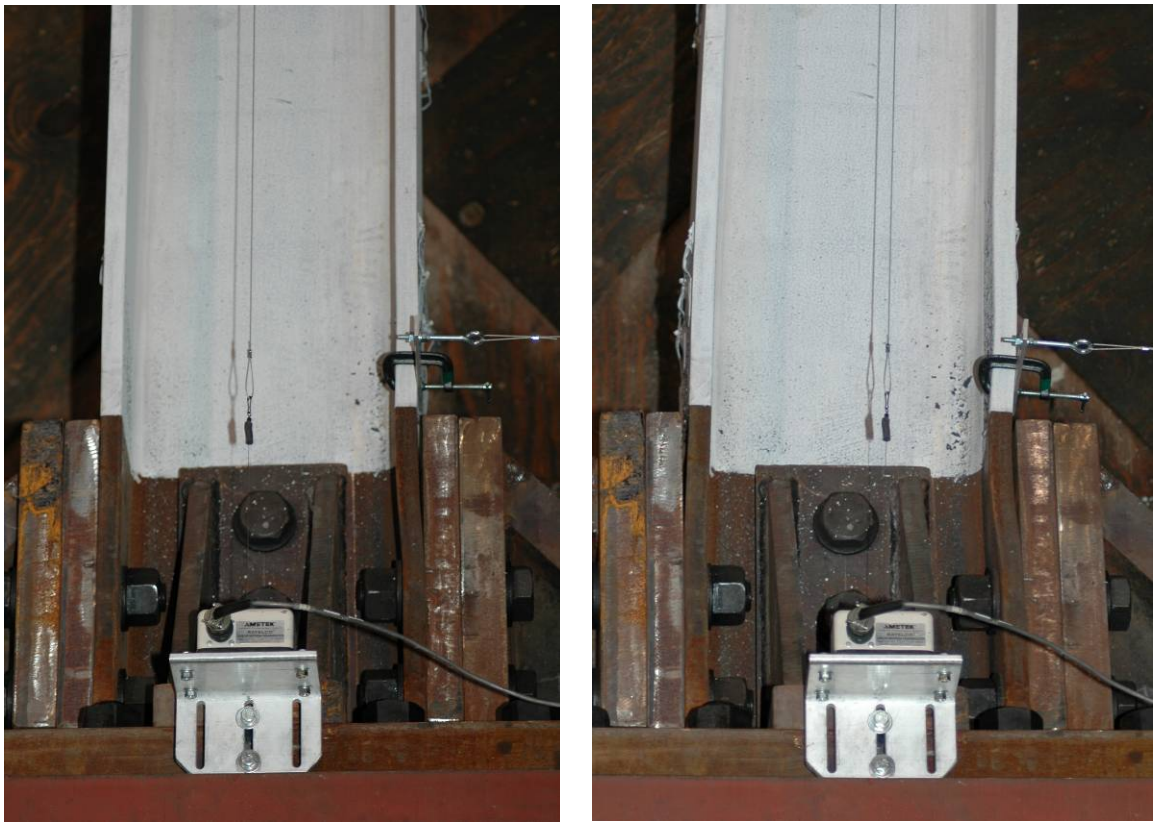

(a) -5% Drift (b) -6% Drift

Figure 4.2 Specimen W14×132-35: Flange Local Buckling (West End)

Tension Excursion | Compression Excursion

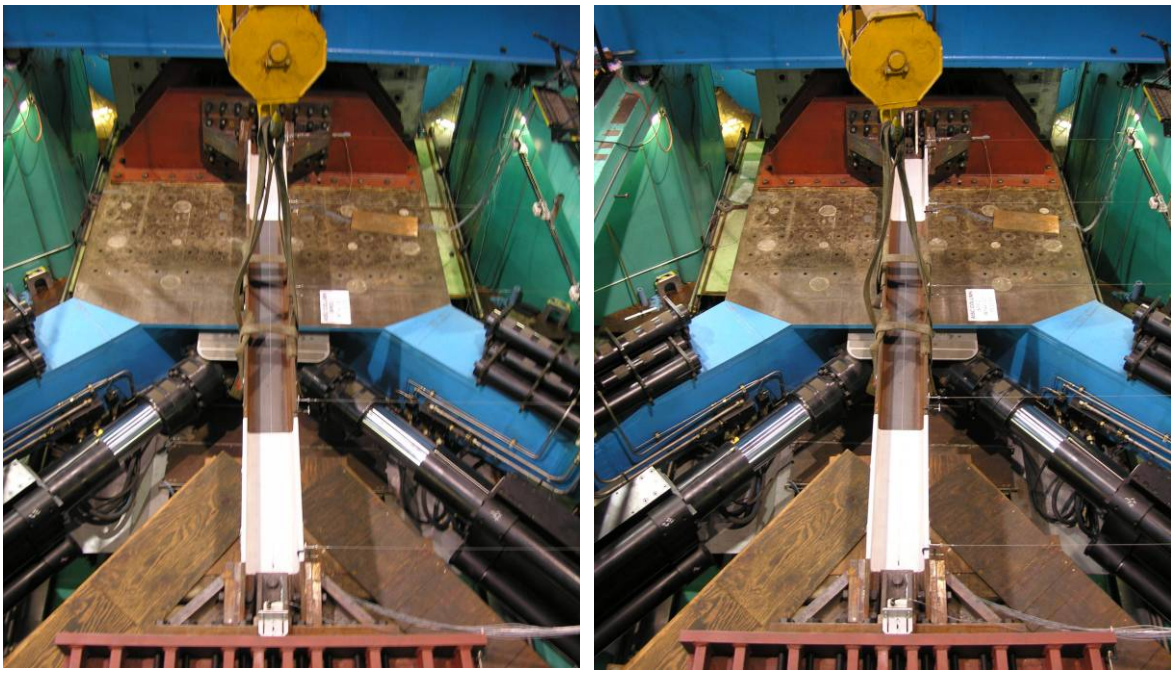

(a) 4% Drift

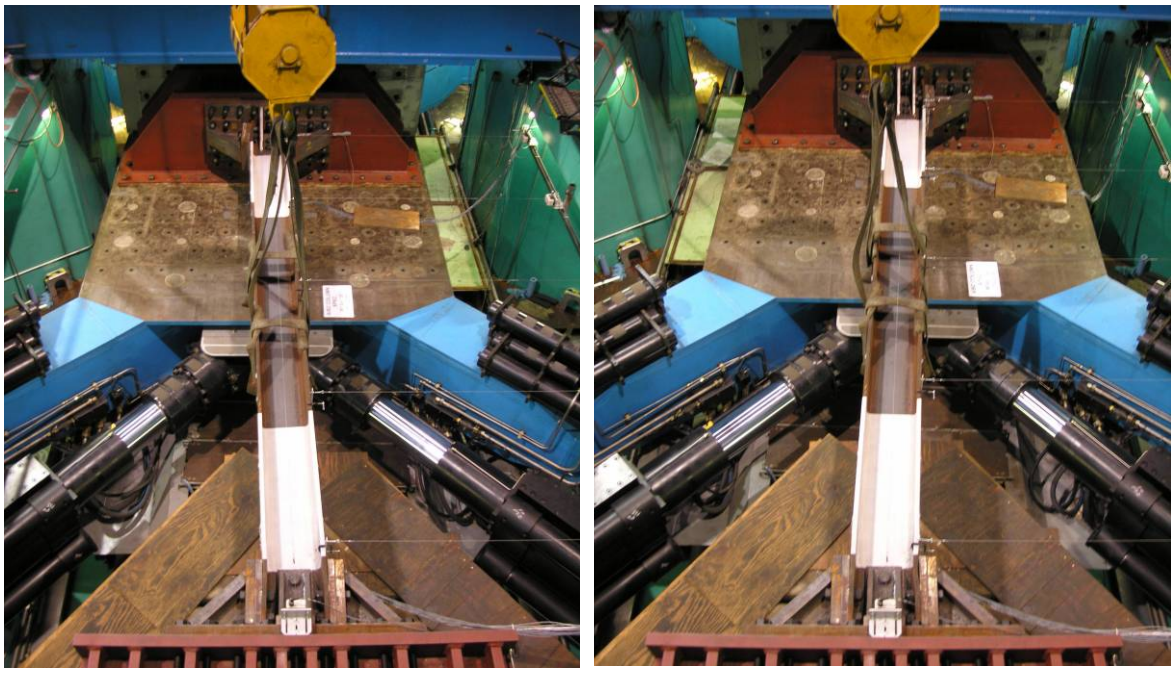

(b) 6% Drift

Figure 4.3 Specimen W14×132-35: Overall Deformed Configuration

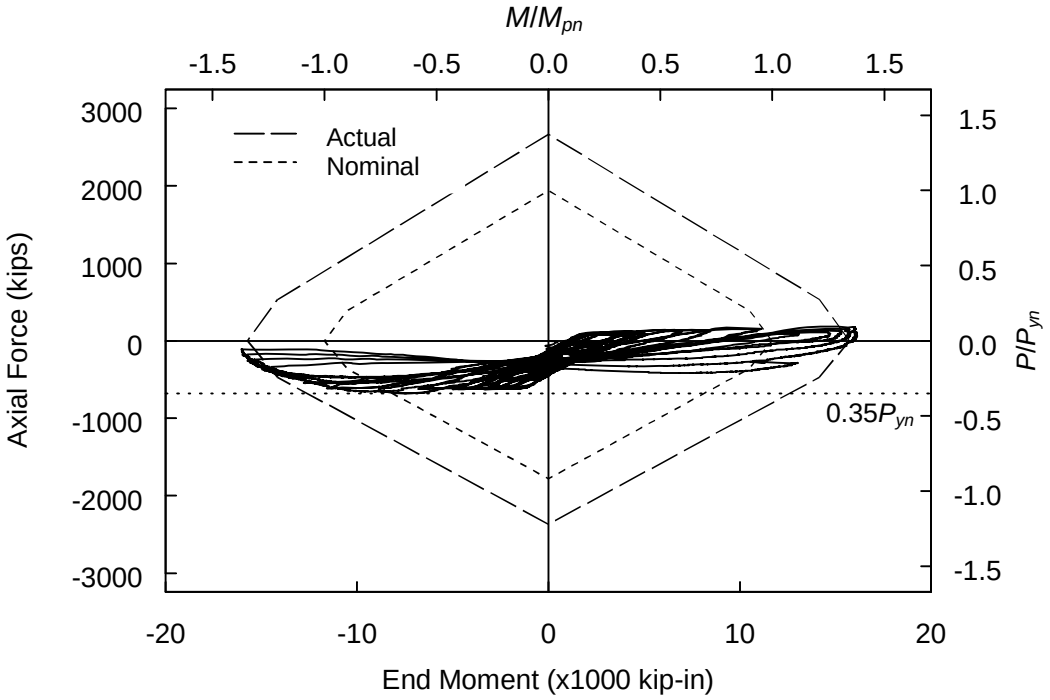

Figure 4.4 Specimen W14×132-35: *P*-*M* Interaction

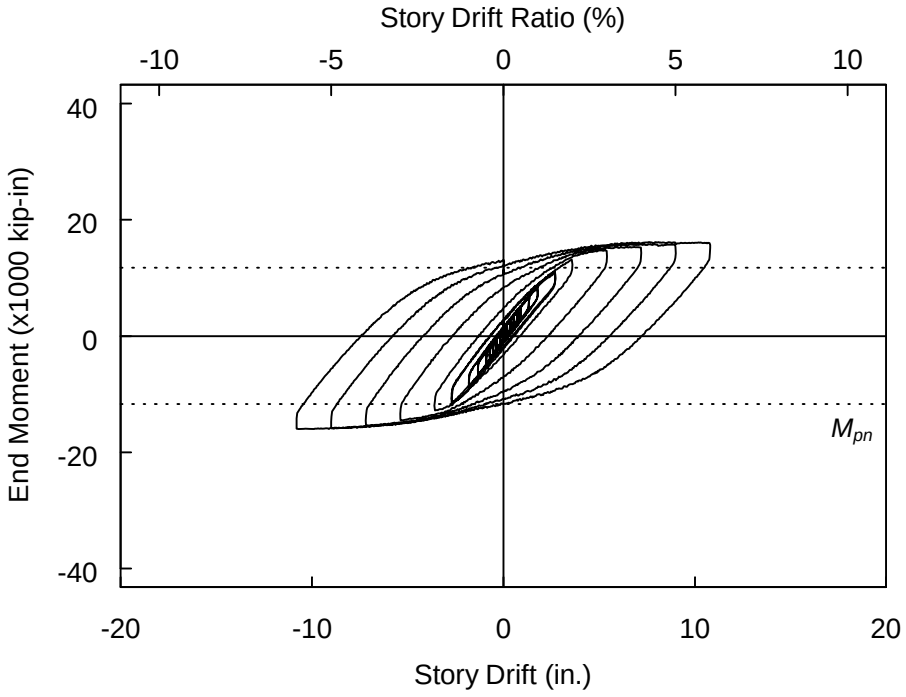

Figure 4.5 Specimen W14×132-35: End Moment versus Drift Response

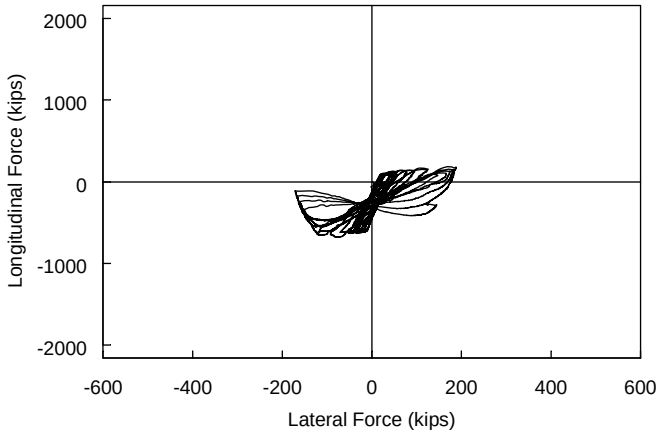

(a) Longitudinal Force versus Lateral Force

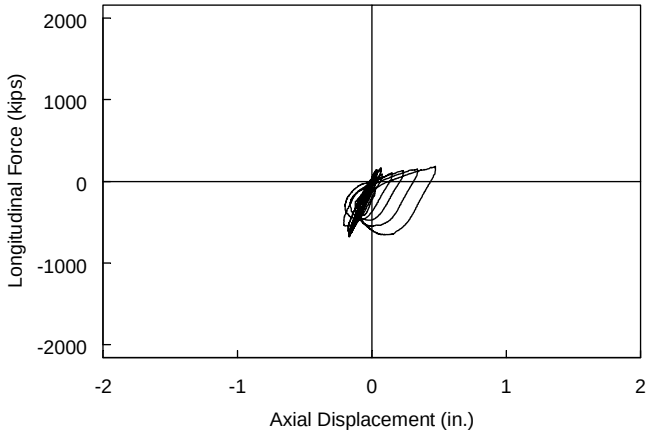

(b) Longitudinal Force versus Column Axial Displacement

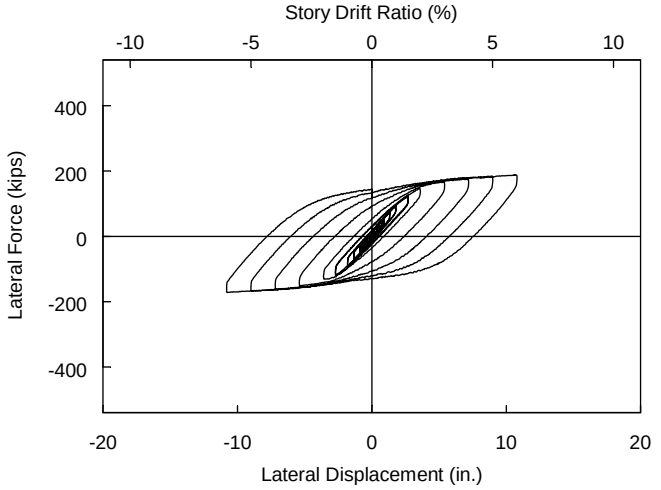

(c) Lateral Force versus Lateral Displacement

Figure 4.6 Specimen W14×132-35: Force-Displacement Response

East End West End

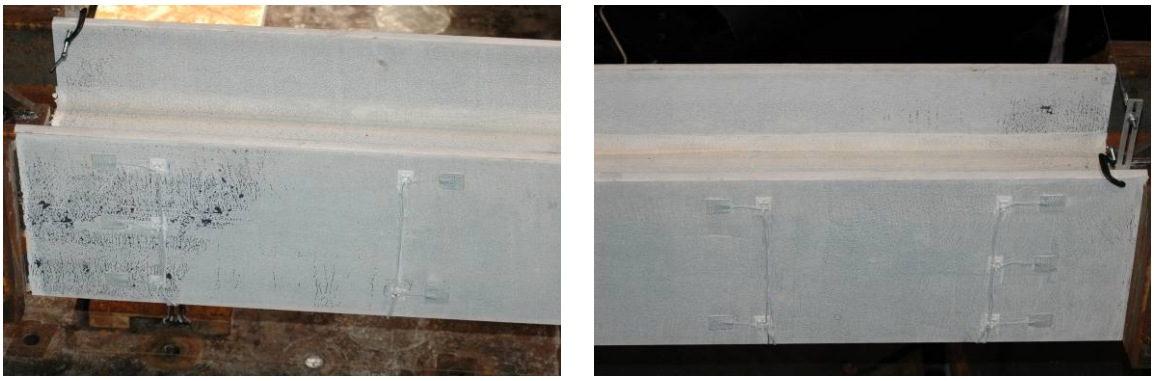

(a) 2% Drift

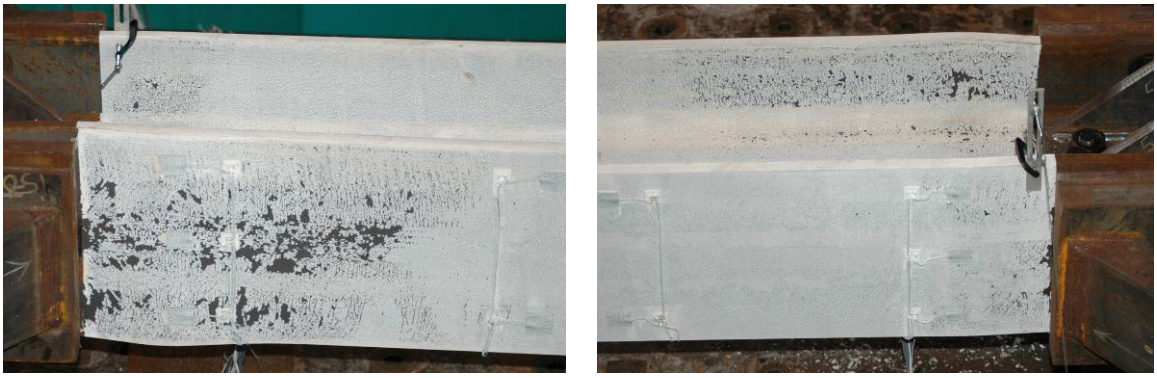

(b) 4% Drift

(c) 6% Drift

Figure 4.7 Specimen W14×132-55: Yielding Pattern

East End West End

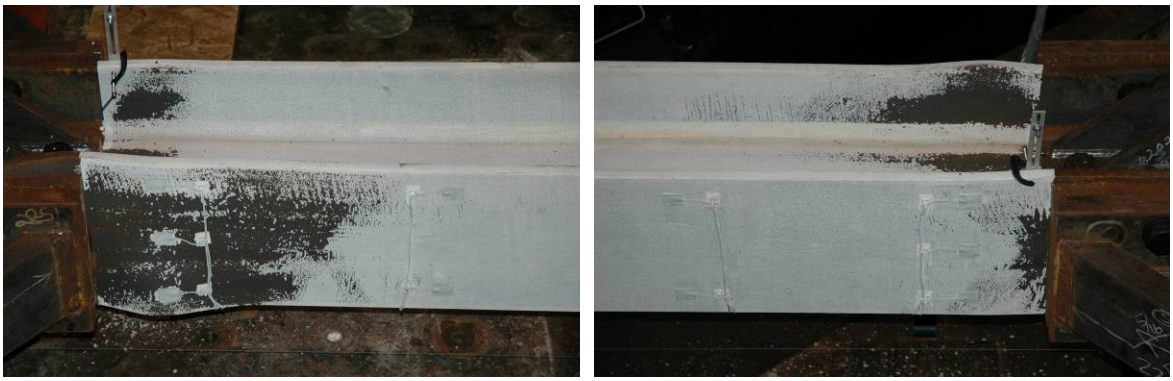

(d) 8% Drift

Figure 4.7 Specimen W14×132-55: Yielding Pattern (cont.)

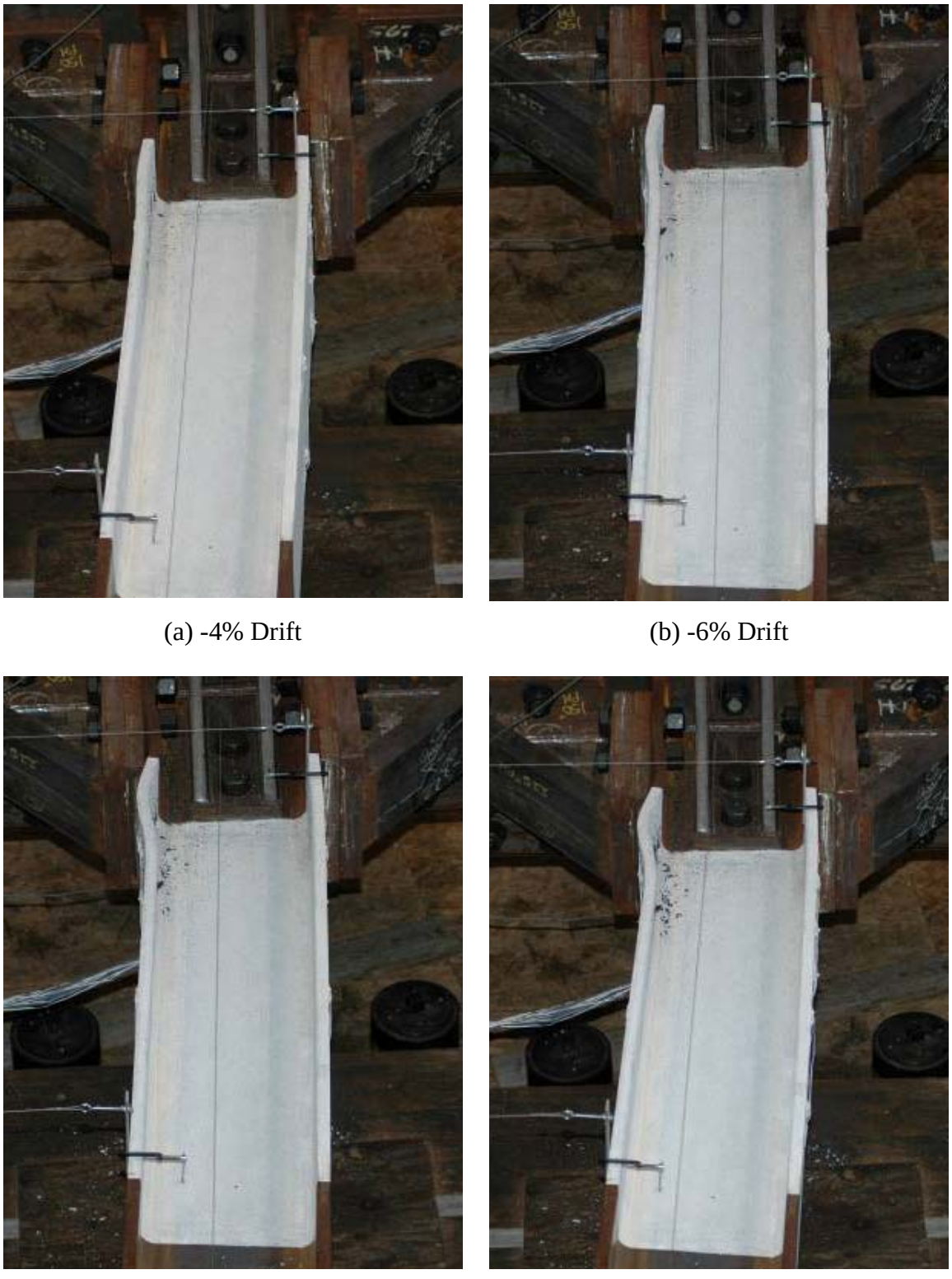

(a) -4% Drift (b) -6% Drift

(c) -8% Drift (d) -10% Drift

Figure 4.8 Specimen W14×132-55: Flange Local Buckling (West End)

Tension Excursion | Compression Excursion

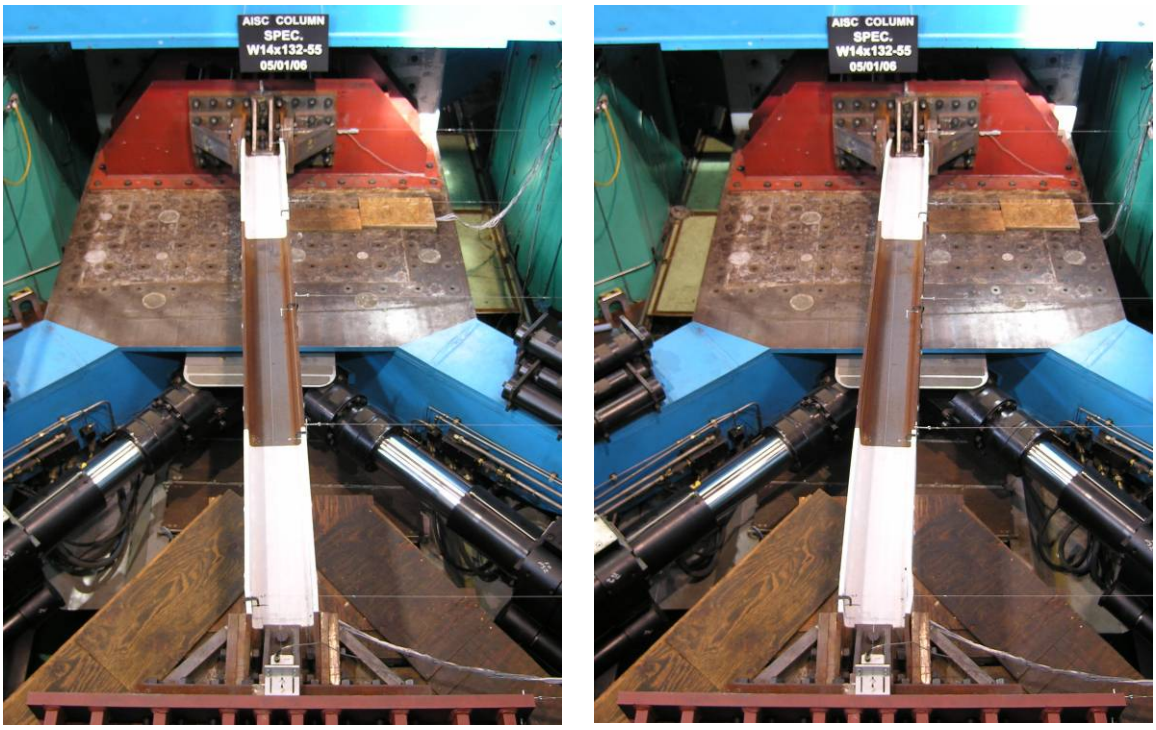

(a) 4% Drift

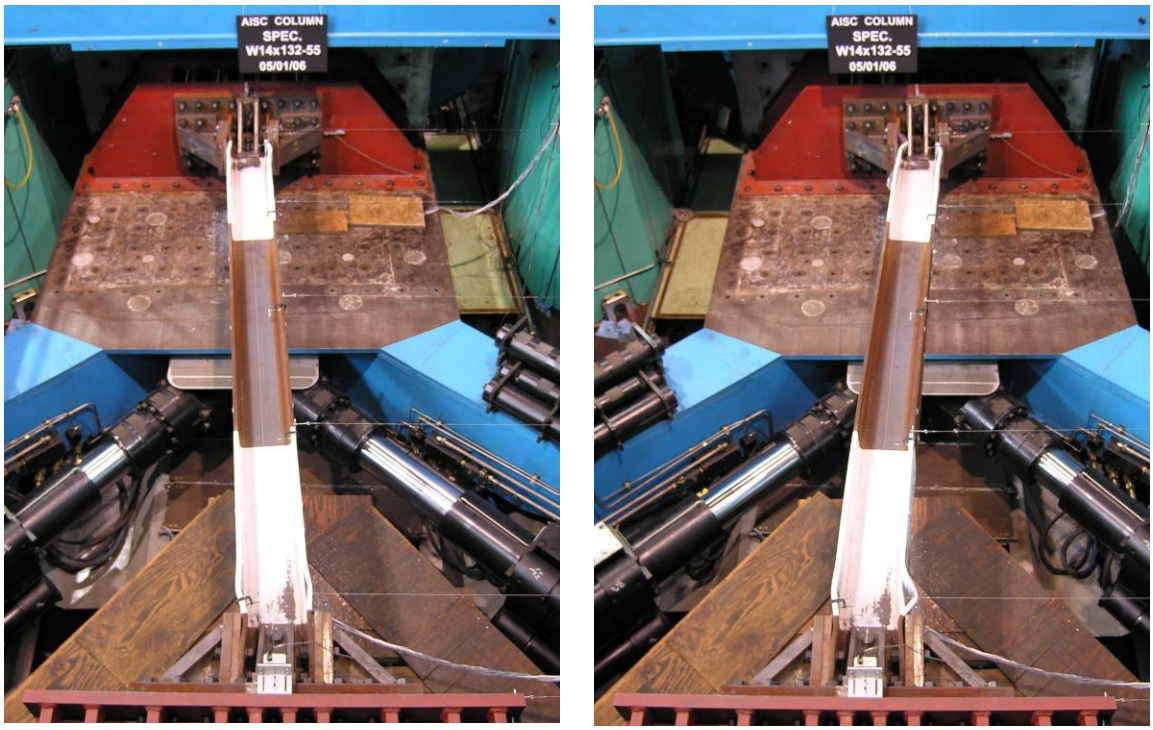

(b) 8% Drift

Figure 4.9 Specimen W14×132-55: Overall Deformed Configuration

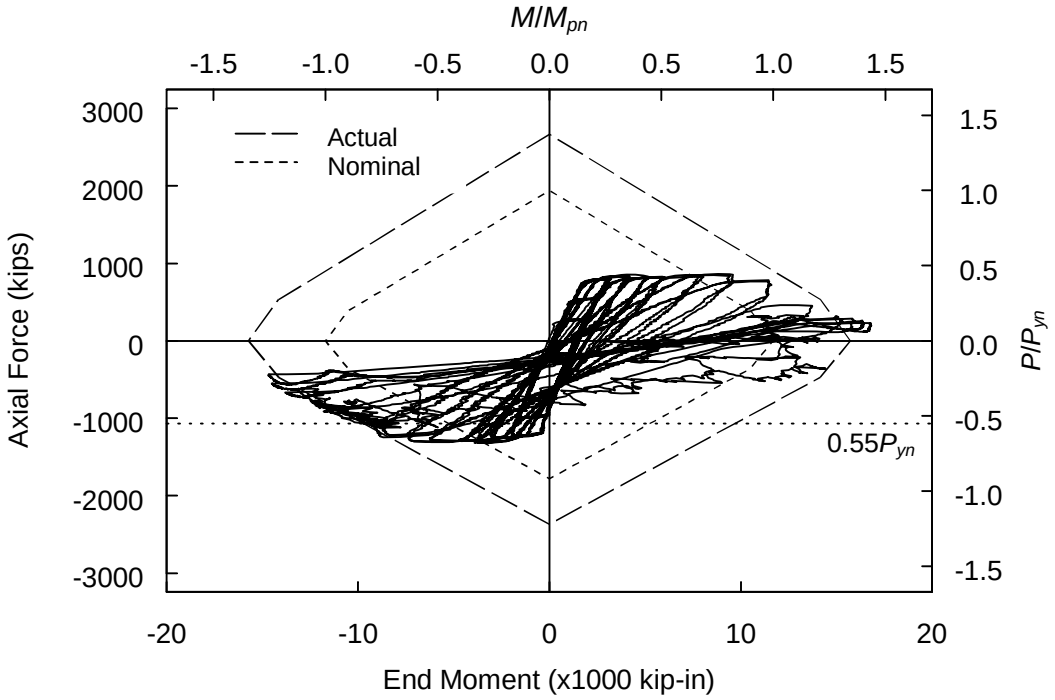

Figure 4.10 Specimen W14×132-55: *P*-*M* Interaction

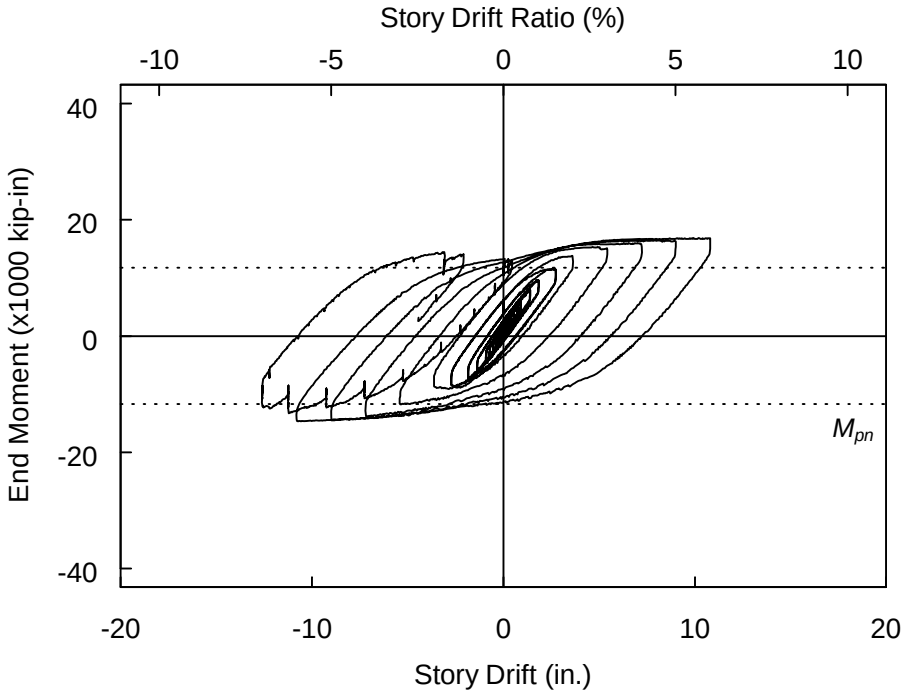

Figure 4.11 Specimen W14×132-55: End Moment versus Drift Response

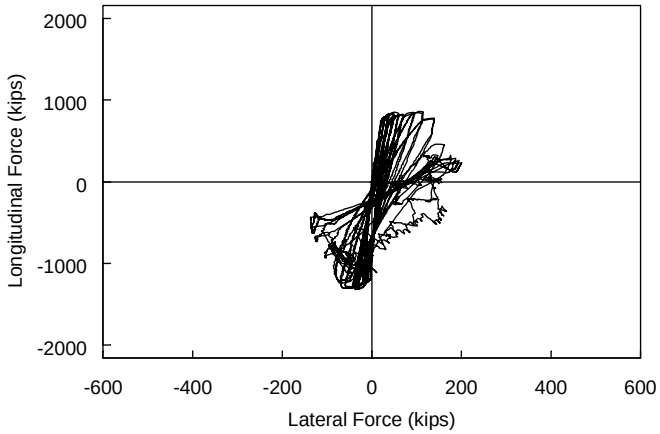

(a) Longitudinal Force versus Lateral Force

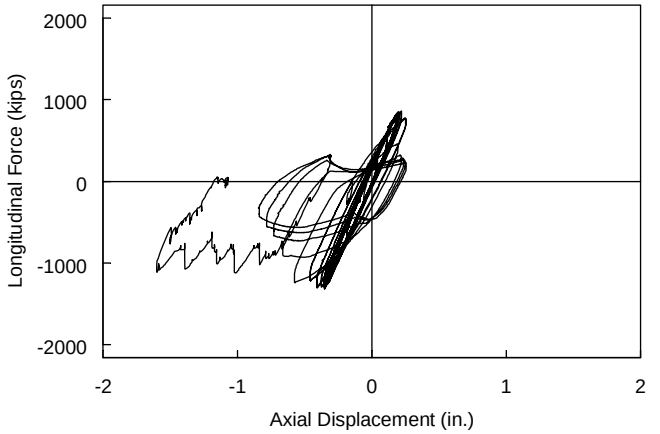

(b) Longitudinal Force versus Column Axial Displacement

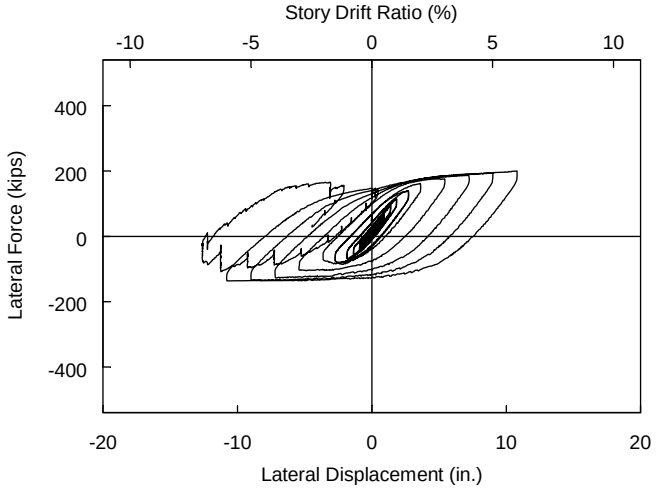

(c) Lateral Force versus Lateral Displacement

Figure 4.12 Specimen W14×132-55: Force-Displacement Response

East End West End

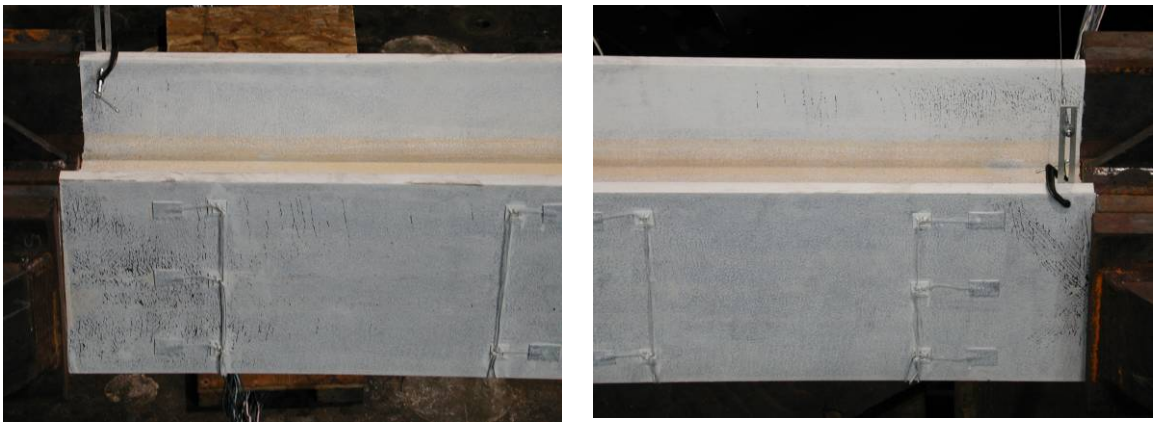

(a) 2% Drift

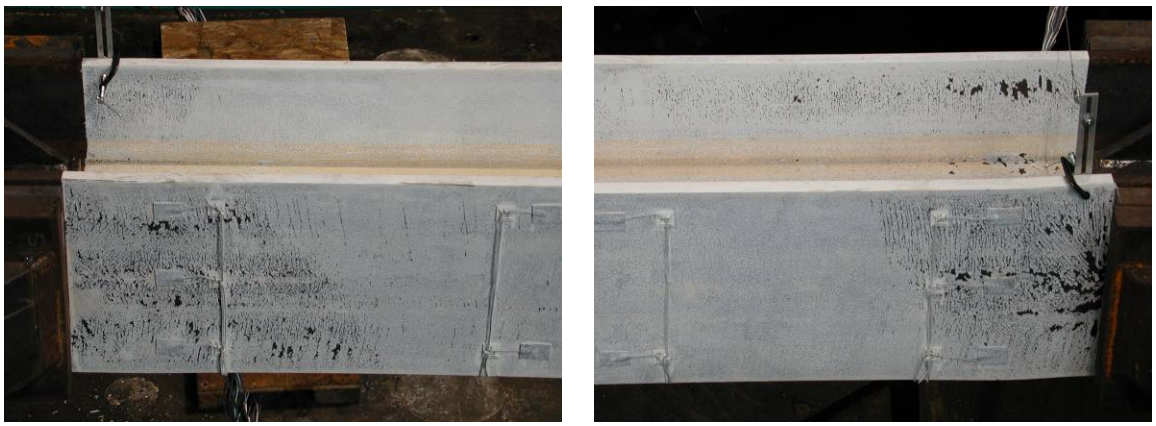

(b) 4% Drift

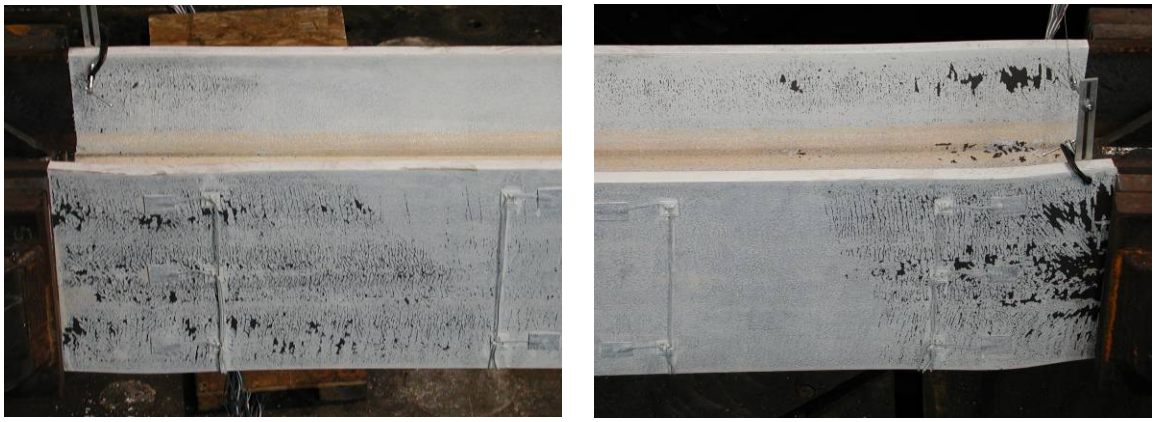

(c) 6% Drift

Figure 4.13 Specimen W14×132-75: Yielding Pattern

East End West End

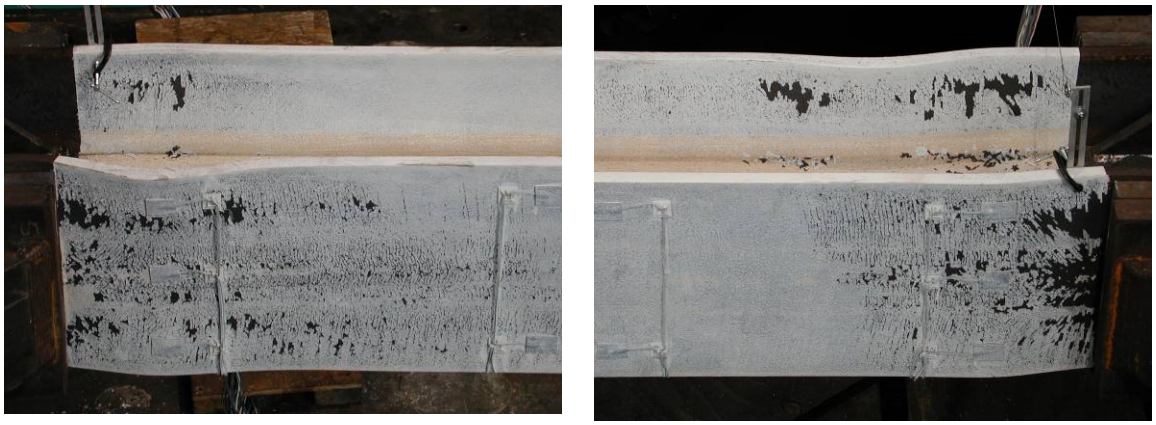

(d) 8% Drift

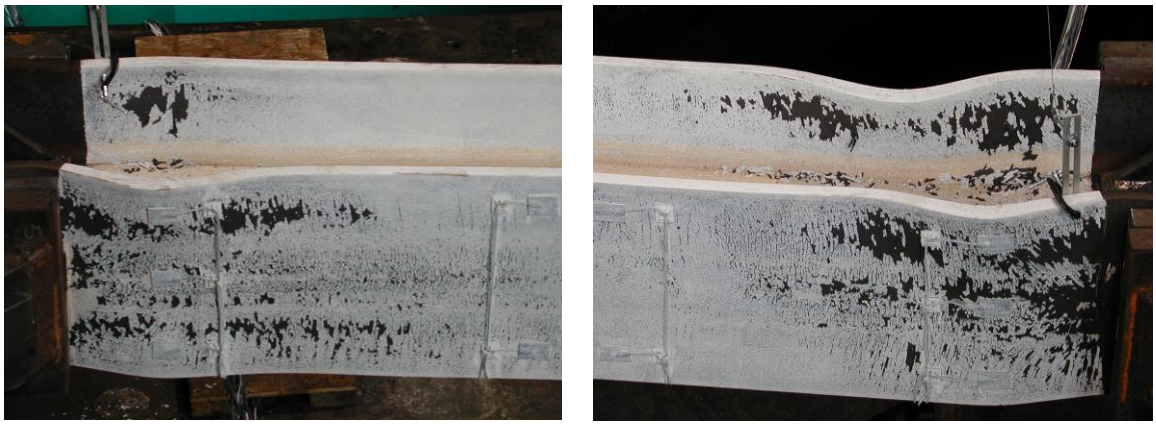

(e) 10% Drift

Figure 4.13 Specimen W14×132-75: Yielding Pattern (cont.)

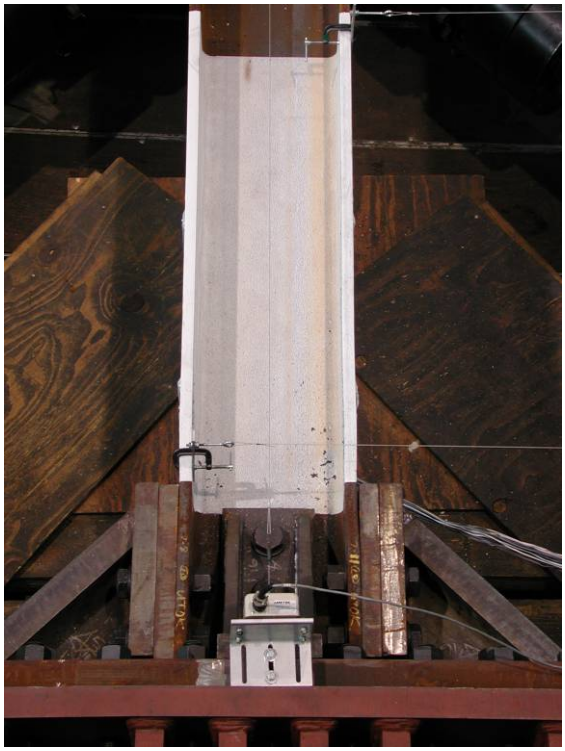

(a) -4% Drift

(b) -6% Drift

(c) -8% Drift

(d) -10% Drift

Figure 4.14 Specimen W14×132-75: Flange Local Buckling (West End)

Tension Excursion | Compression Excursion

(a) 4% Drift

(b) 6% Drift

Figure 4.15 Specimen W14×132-75: Overall Deformed Configuration

Tension Excursion | Compression Excursion

(c) 8% Drift

(d) 10% Drift

Figure 4.15 Specimen W14×132-75: Overall Deformed Configuration (cont.)

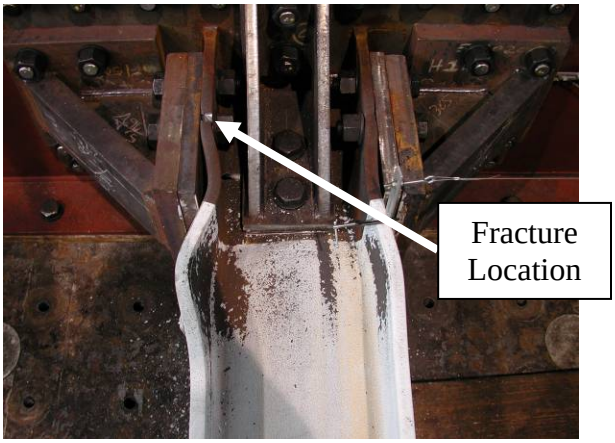

(a) Overall View of Fracture Location

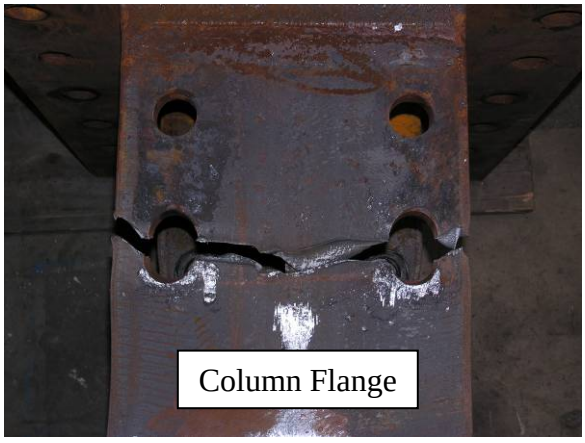

(b) View of Fracture from Exterior Side of Flange (with Haunches Removed)

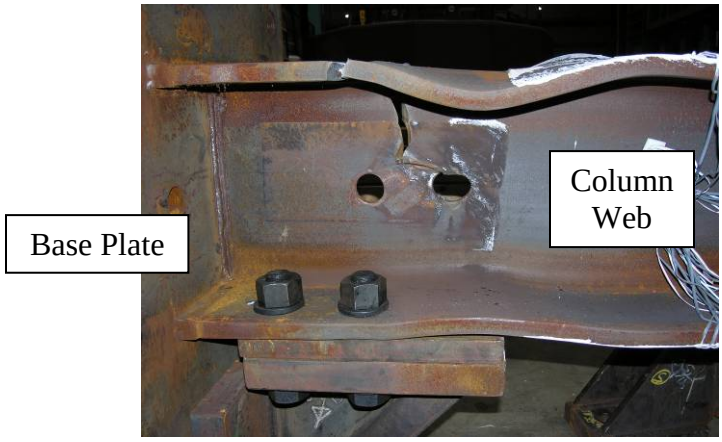

(c) View of Fracture from Interior Side of Flange (with Haunches Removed)

Figure 4.16 Specimen W14×132-75: Column Fracture (10% Drift)

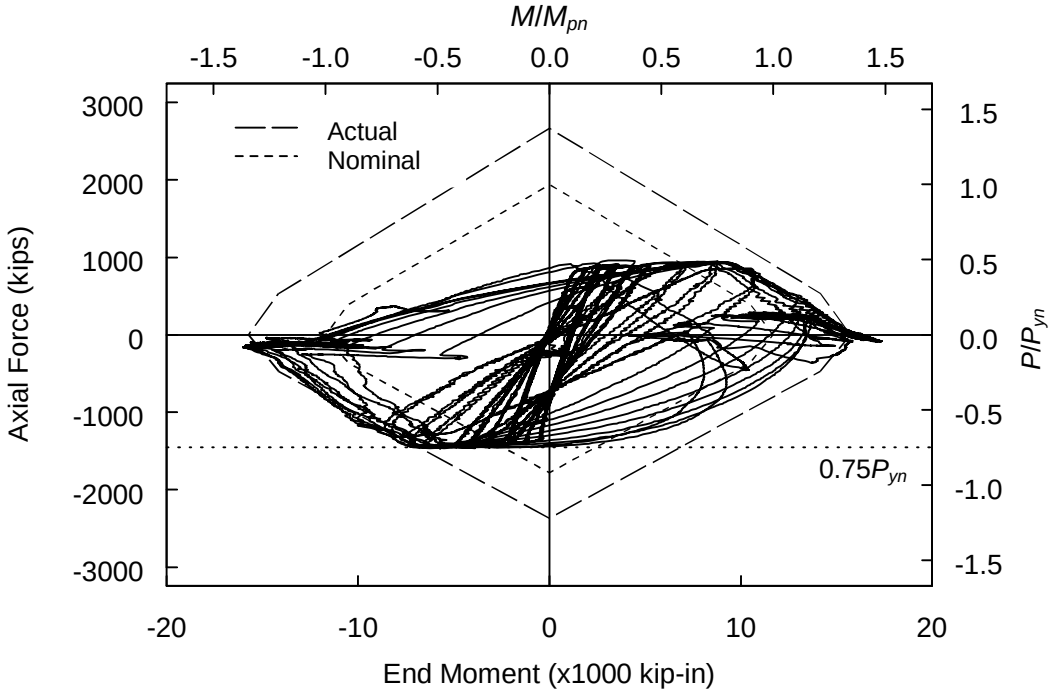

Figure 4.17 Specimen W14×132-75: *P-M* Interaction

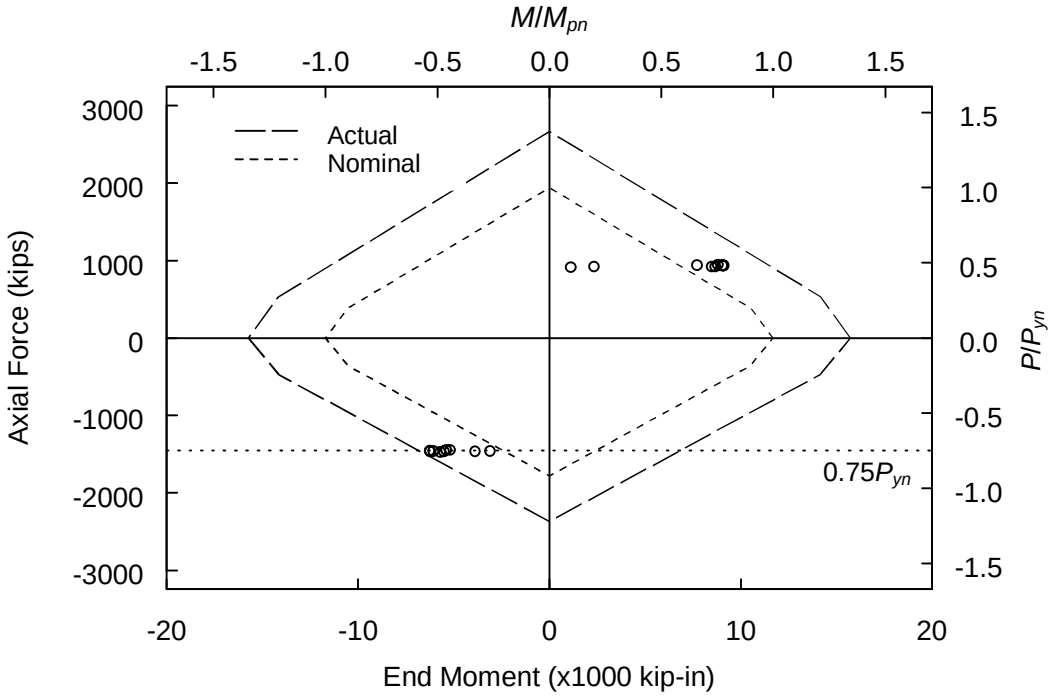

Figure 4.18 Specimen W14×132-75: *P-M* Interaction (Target Points)

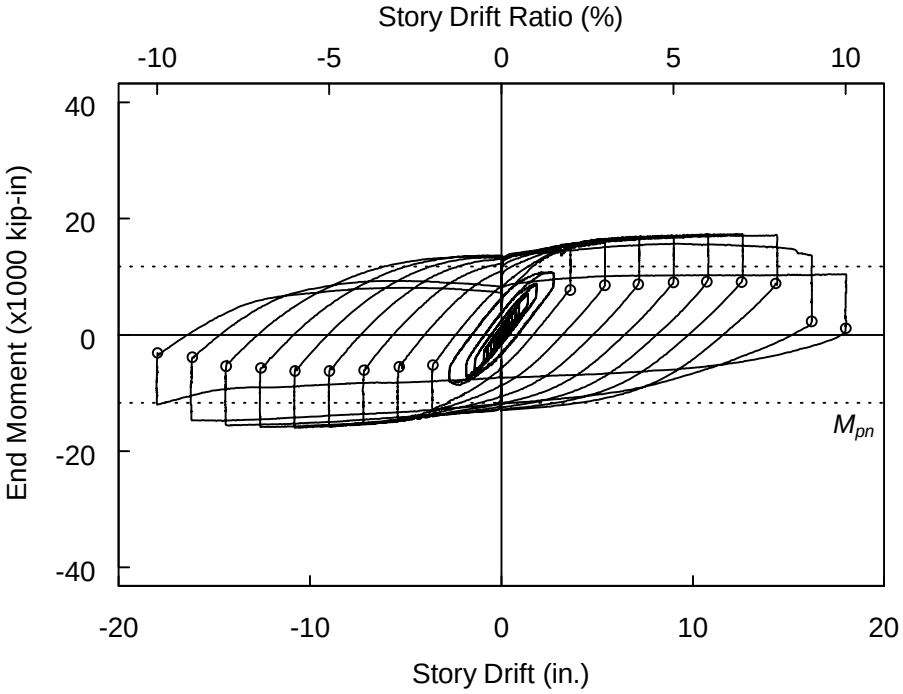

Figure 4.19 Specimen W14×132-75: End Moment versus Drift Response

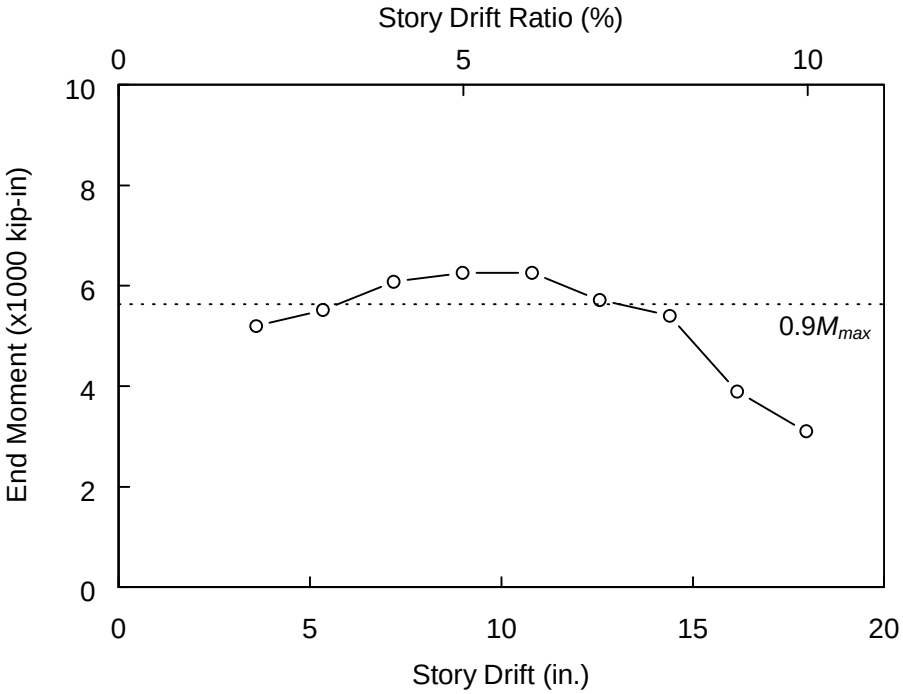

Figure 4.20 Specimen W14×132-75: Compression Side Target Points End Moment versus Drift Response

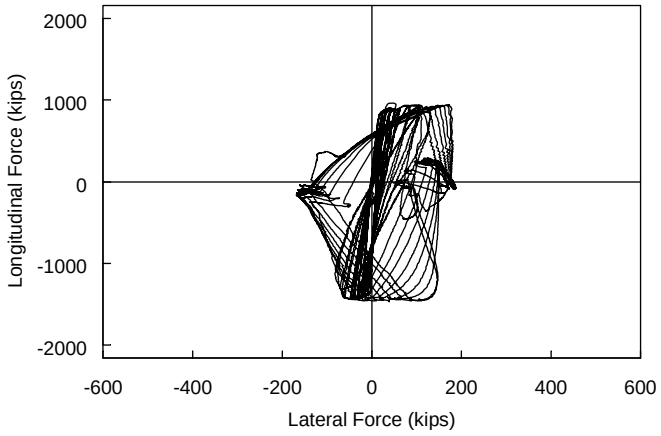

(a) Longitudinal Force versus Lateral Force

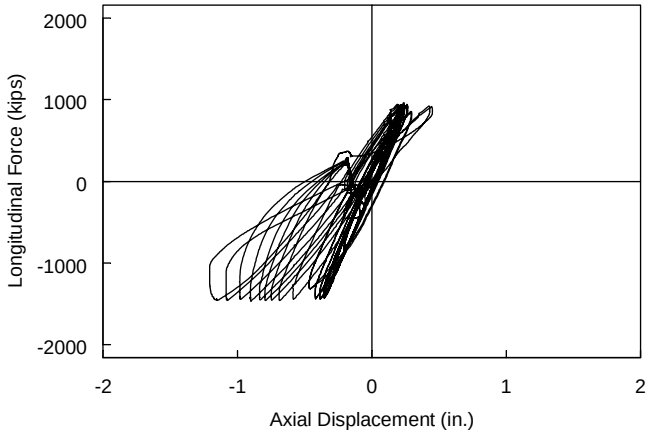

(b) Longitudinal Force versus Column Axial Displacement

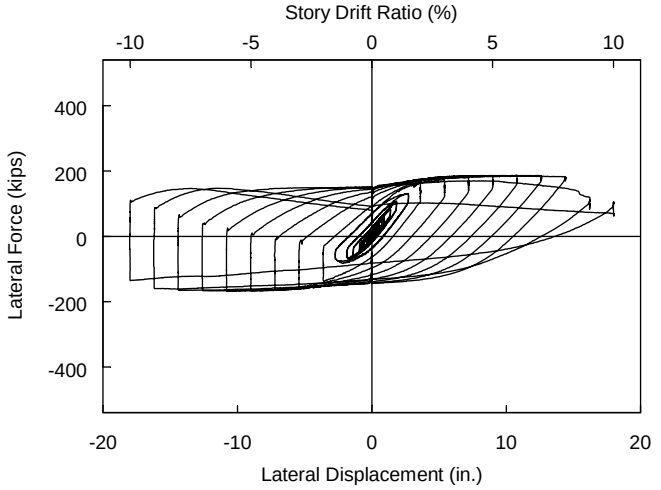

(c) Lateral Force versus Lateral Displacement

Figure 4.21 Specimen W14×132-75: Force-Displacement Response

East End West End

(a) 2% Drift

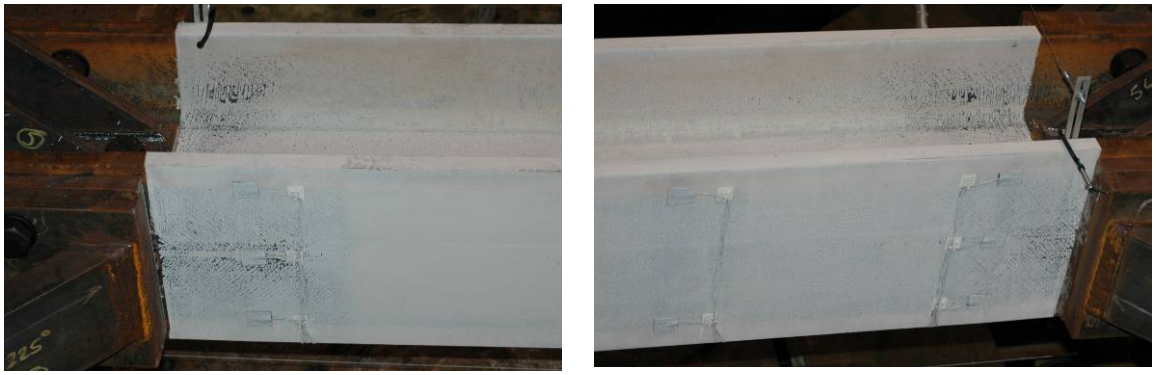

(b) 4% Drift

(c) 6% Drift

Figure 4.22 Specimen W14×176-35: Yielding Pattern

East End West End

(d) 8% Drift

(e) 10% Drift

Figure 4.22 Specimen W14×176-35: Yielding Pattern (cont.)

(a) -4% Drift

(b) -6% Drift

(c) -8% Drift

(d) -10% Drift

Figure 4.23 Specimen W14×176-35: Flange Local Buckling (West End)

Tension Excursion | Compression Excursion

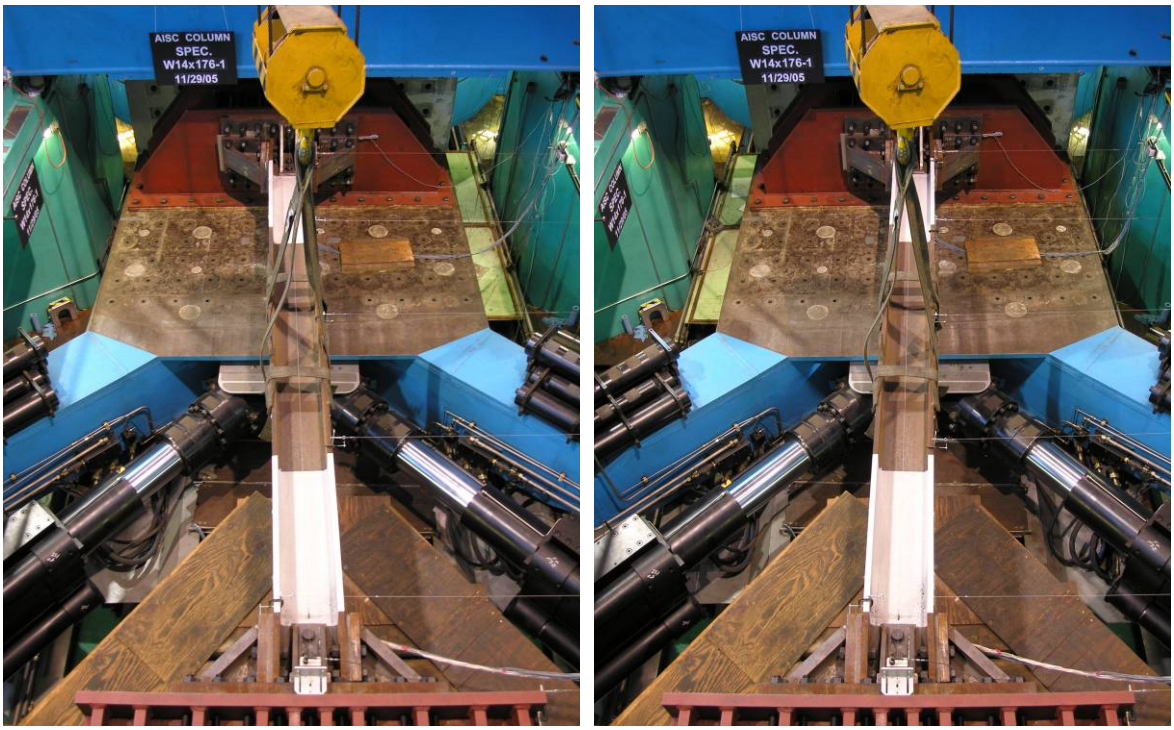

(a) 4% Drift

(b) 6% Drift

Figure 4.24 Specimen W14×176-35: Overall Deformed Configuration

Tension Excursion | Compression Excursion

(c) 8% Drift

(d) 10% Drift

Figure 4.24 Specimen W14×176-35: Overall Deformed Configuration

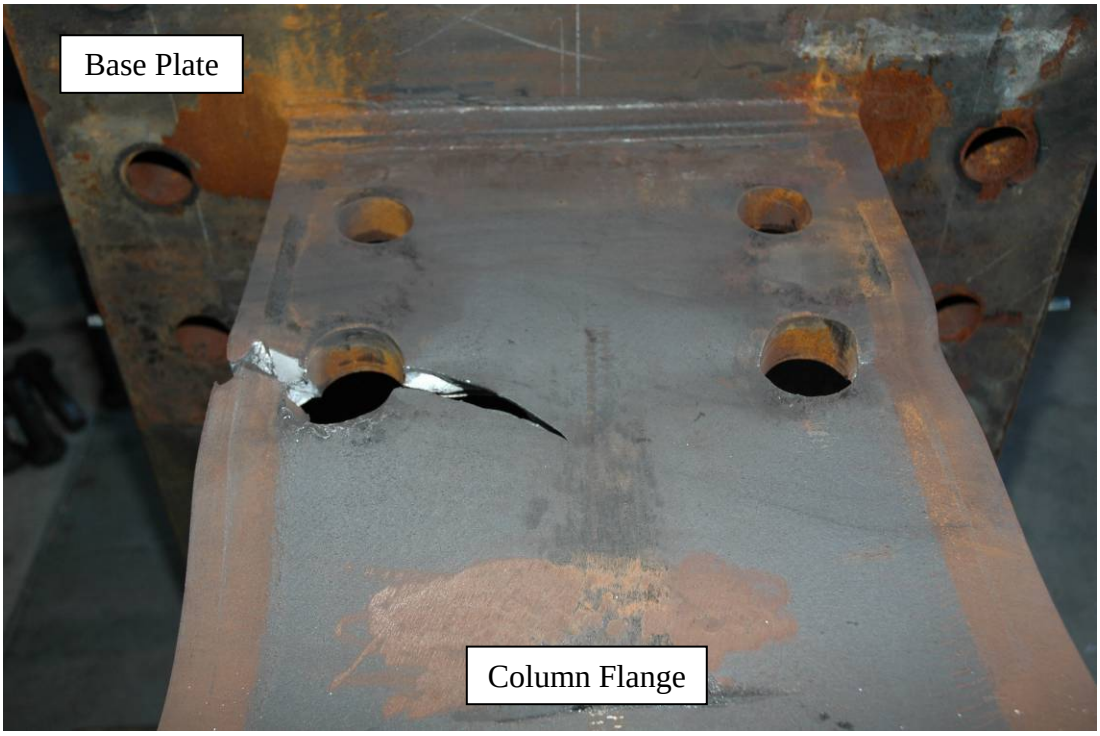

Figure 4.25 Specimen W14×176-35: Partial Column Flange Fracture (10% Drift)

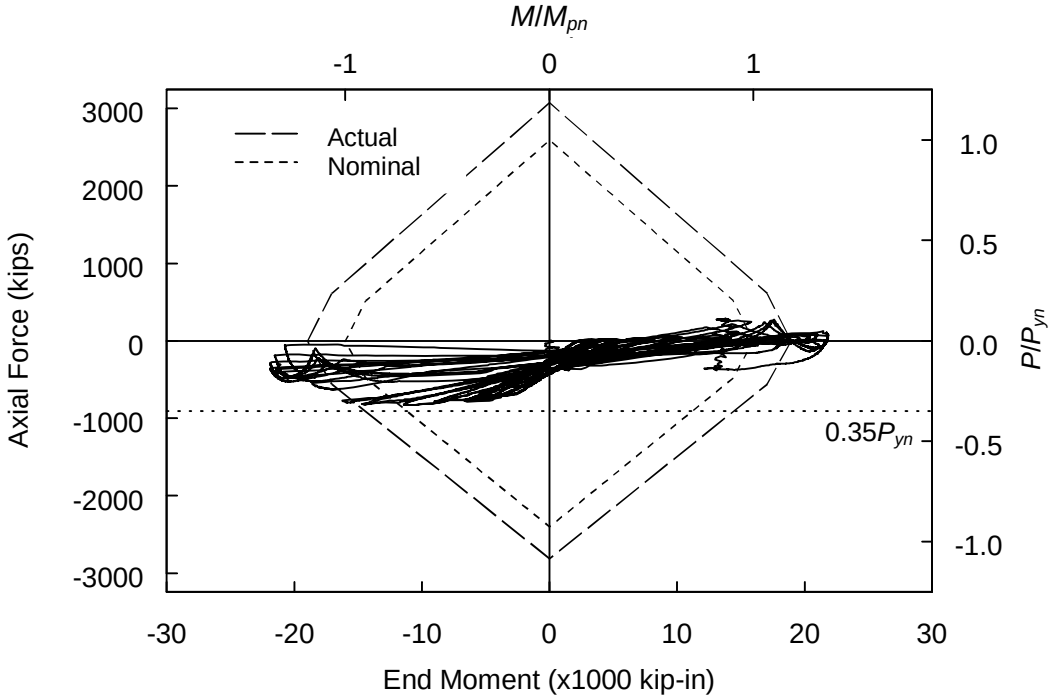

Figure 4.26 Specimen W14×176-35: *P-M* Interaction

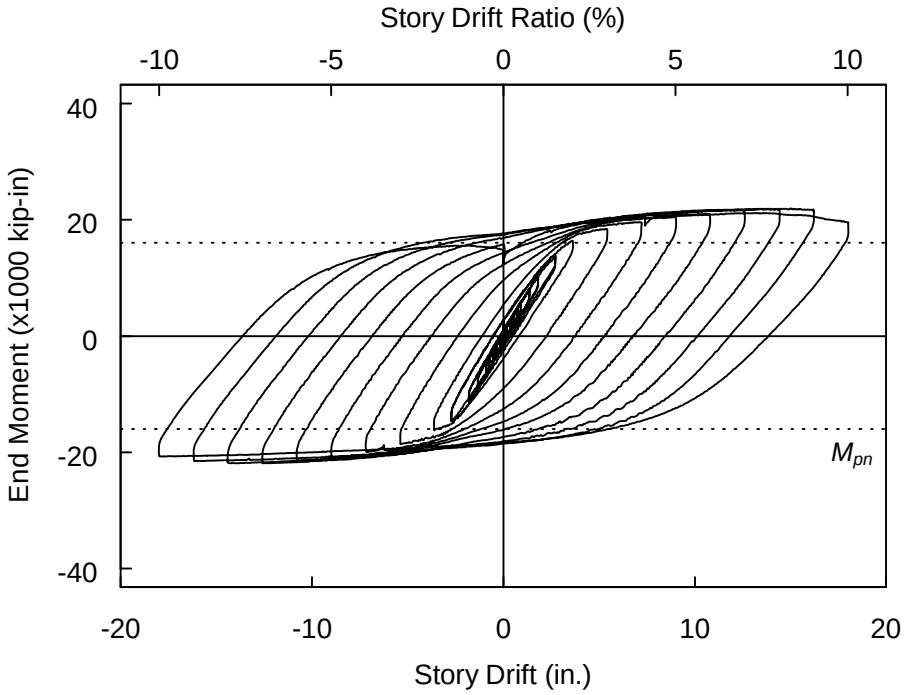

Figure 4.27 Specimen W14×176-35: End Moment versus Drift Response

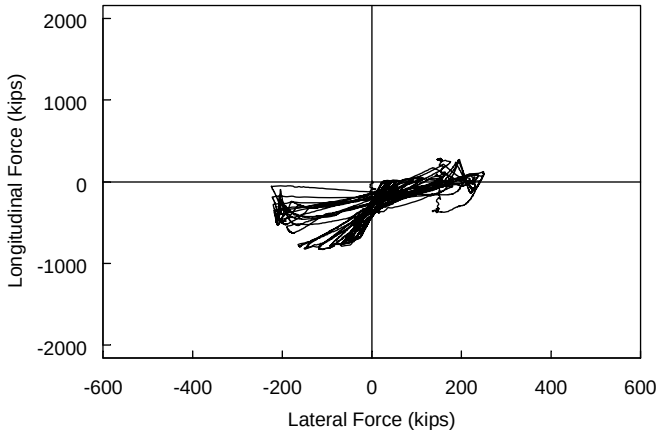

(a) Longitudinal Force versus Lateral Force

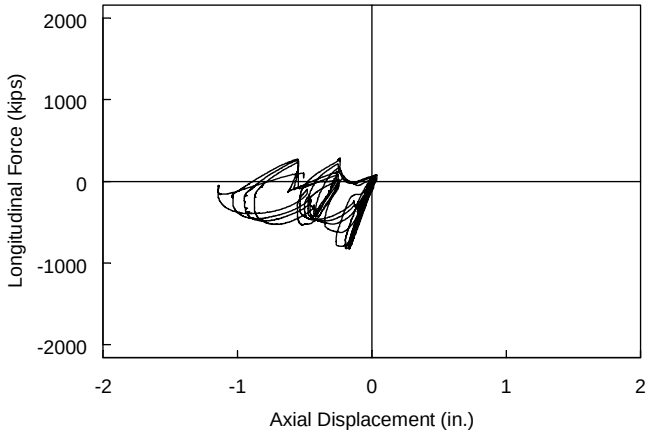

(b) Longitudinal Force versus Column Axial Displacement

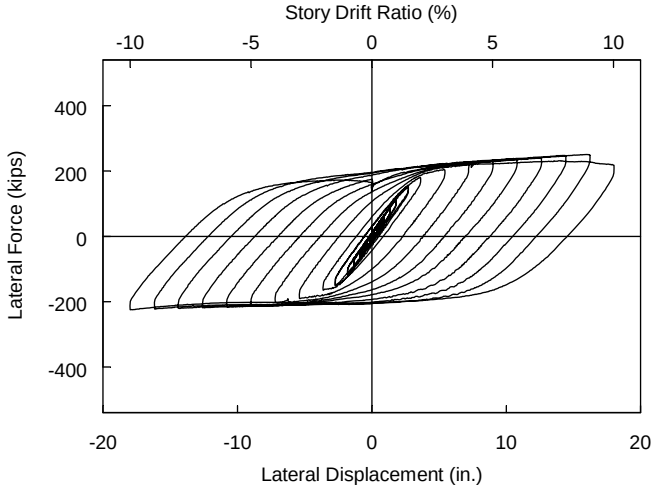

(c) Lateral Force versus Lateral Displacement

Figure 4.28 Specimen W14×176-35: Force-Displacement Response

East End West End

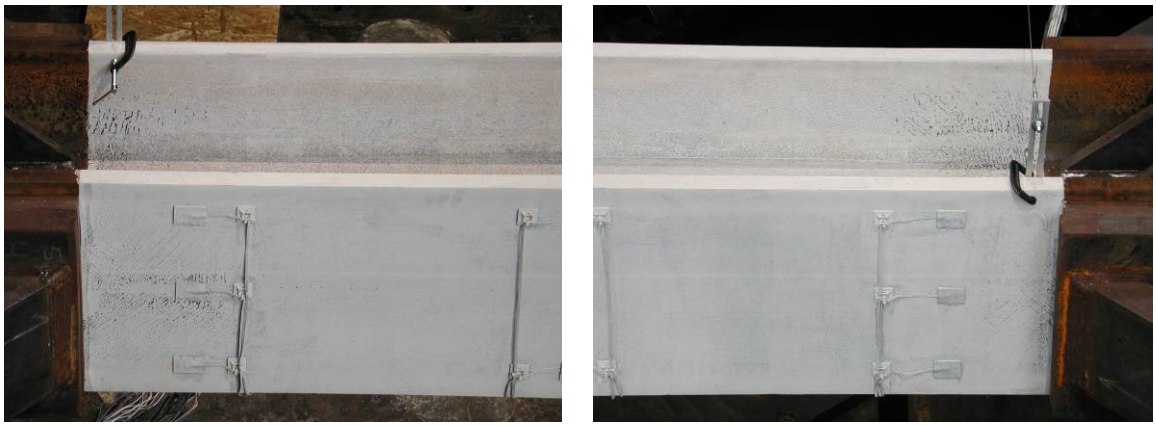

(a) 2% Drift

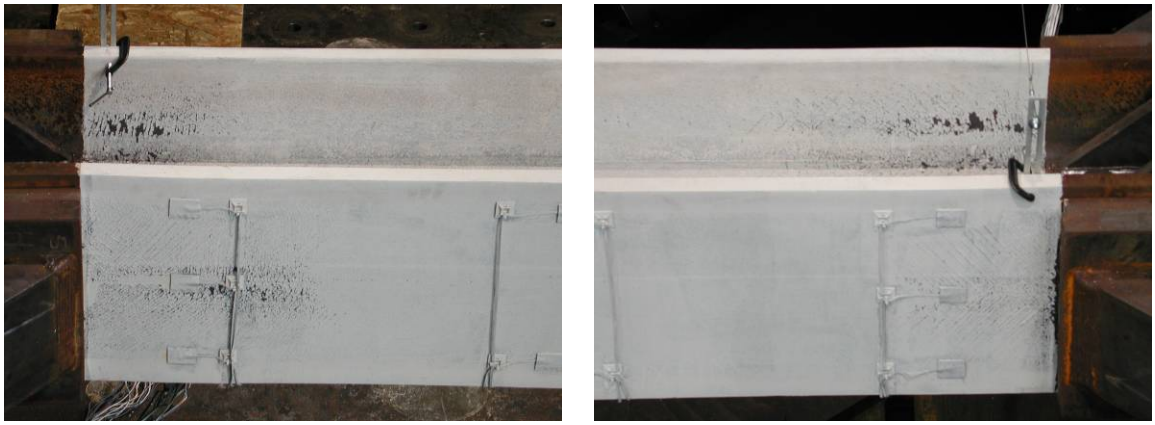

(b) 4% Drift

(c) 6% Drift

Figure 4.29 Specimen W14×176-55: Yielding Pattern

East End West End

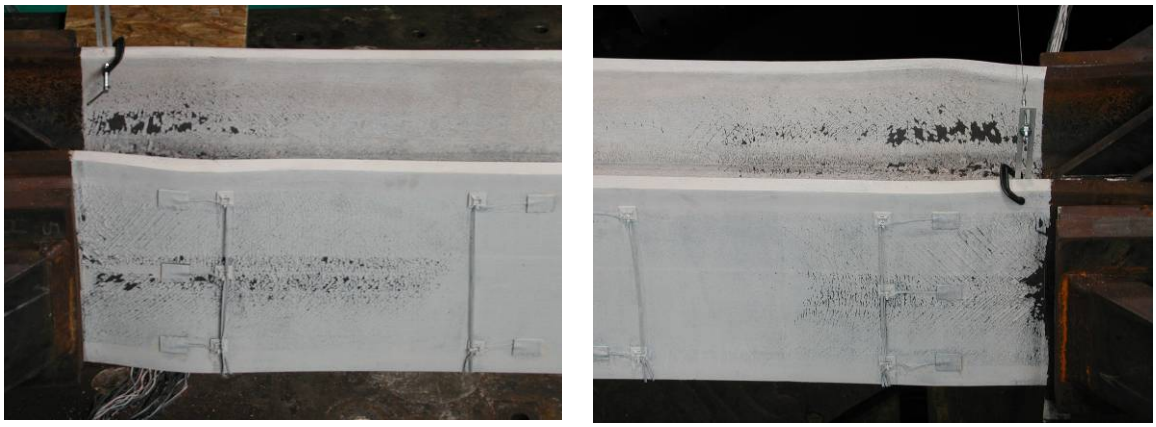

(d) 8% Drift

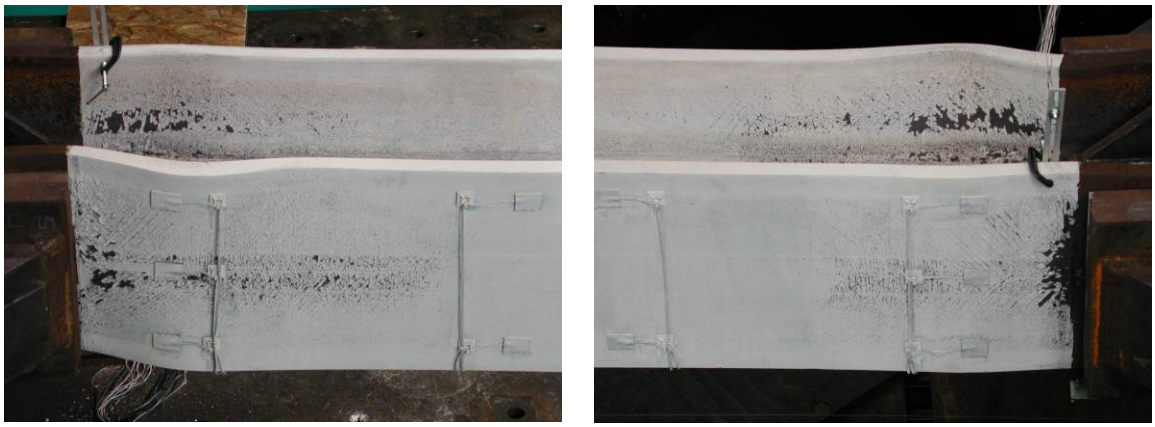

(e) 10% Drift

Figure 4.29 Specimen W14×176-55: Yielding Pattern (cont.)

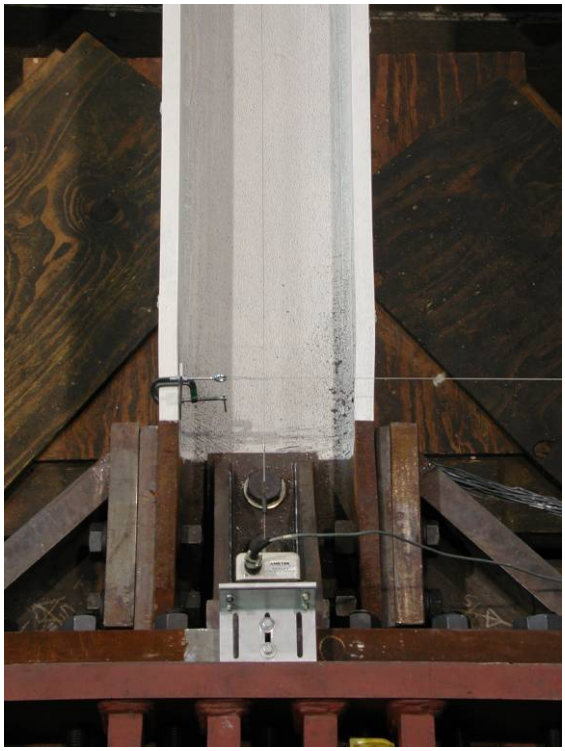

(a) -4% Drift

(b) -6% Drift

(c) -8% Drift

(d) -10% Drift

Figure 4.30 Specimen W14×176-55: Flange Local Buckling (West End)

Tension Excursion | Compression Excursion

(a) 4% Drift

(b) 6% Drift

Figure 4.31 Specimen W14×176-55: Overall Deformed Configuration

Tension Excursion | Compression Excursion

(c) 8% Drift

(d) 10% Drift

Figure 4.31 Specimen W14×176-55: Overall Deformed Configuration (cont.)

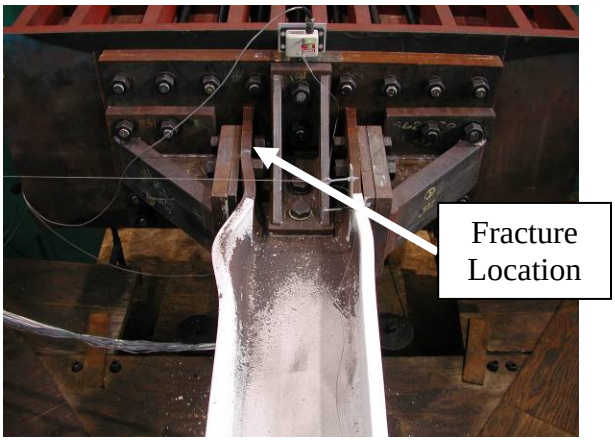

(a) Overall View of Fracture Location

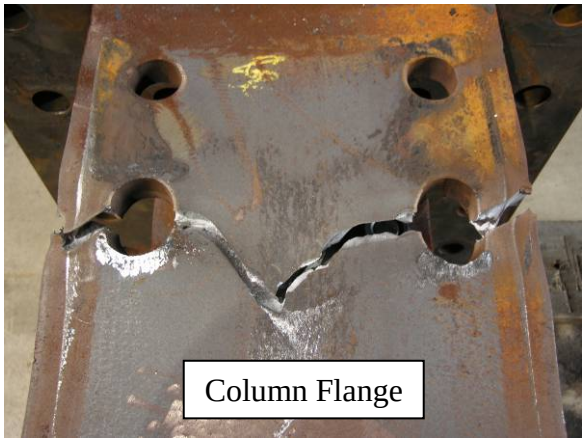

(b) View of Fracture from Exterior Side of Flange

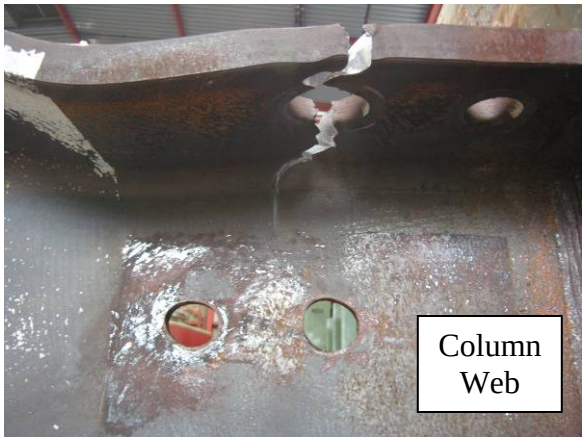

(c) View of Fracture from Interior Side of Flange

Figure 4.32 Specimen W14×176-55: Column Fracture (10% Drift)

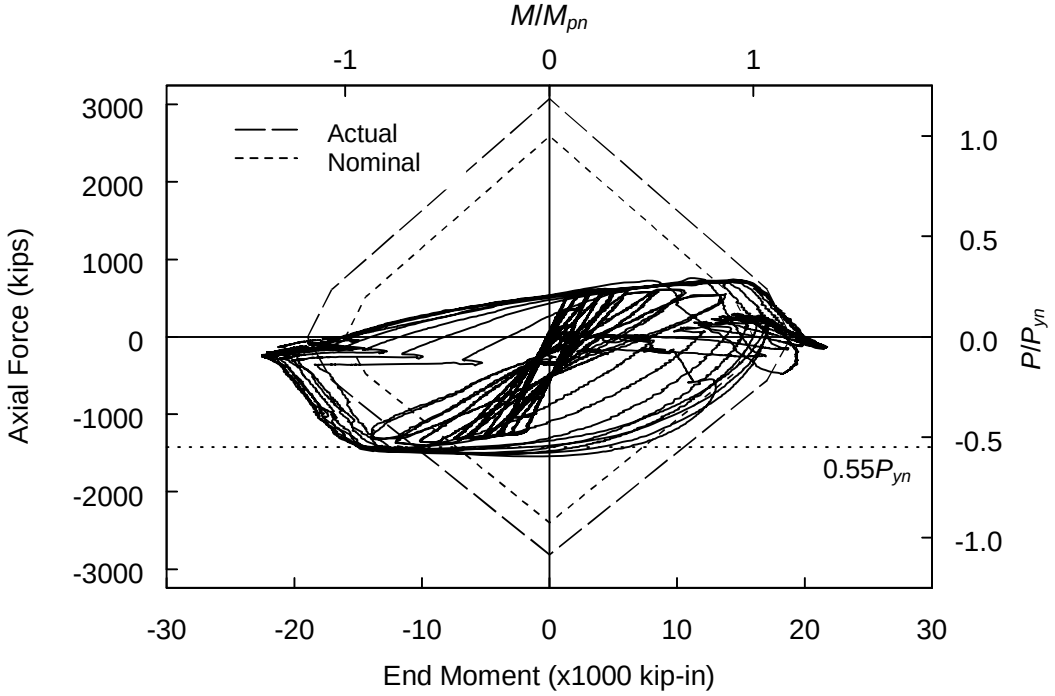

Figure 4.33 Specimen W14×176-55: *P-M* Interaction

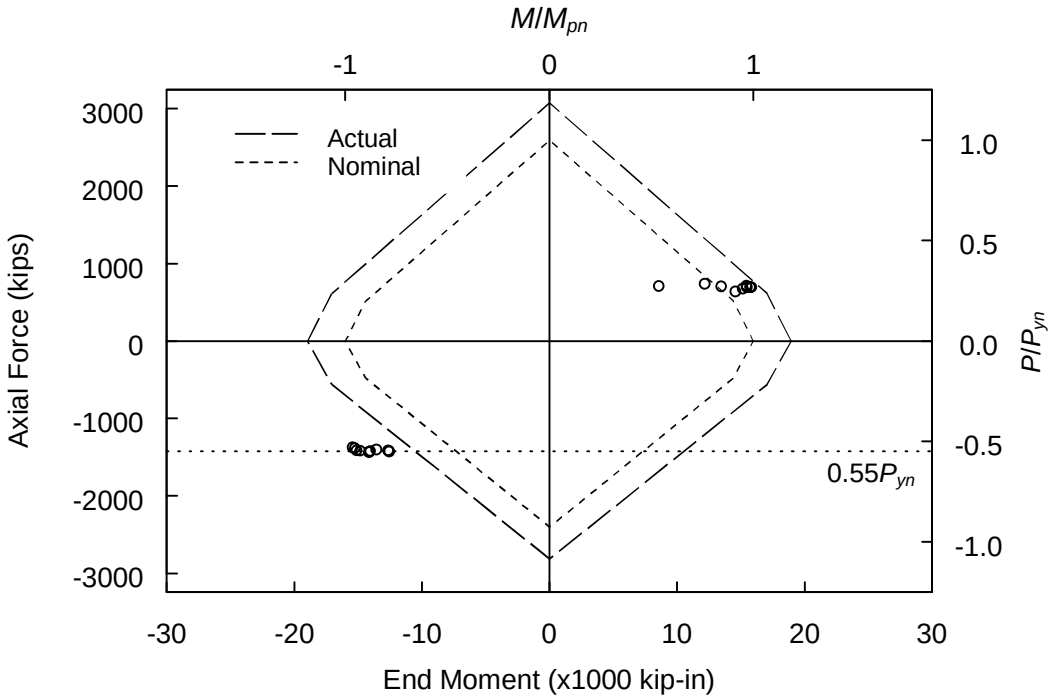

Figure 4.34 Specimen W14×176-55: *P-M* Interaction (Target Points)

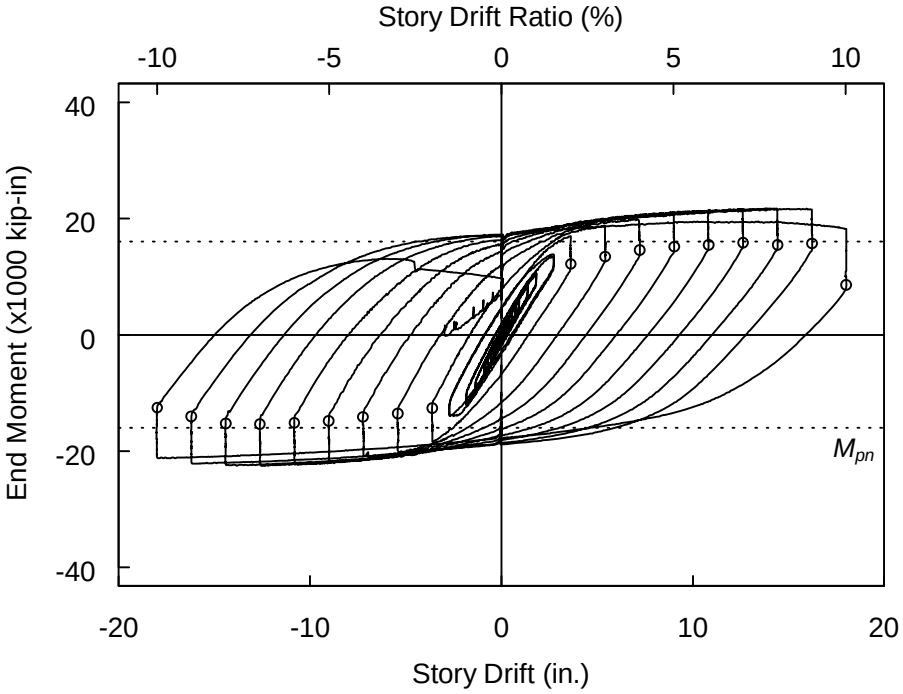

Figure 4.35 Specimen W14×176-55: End Moment versus Drift Response

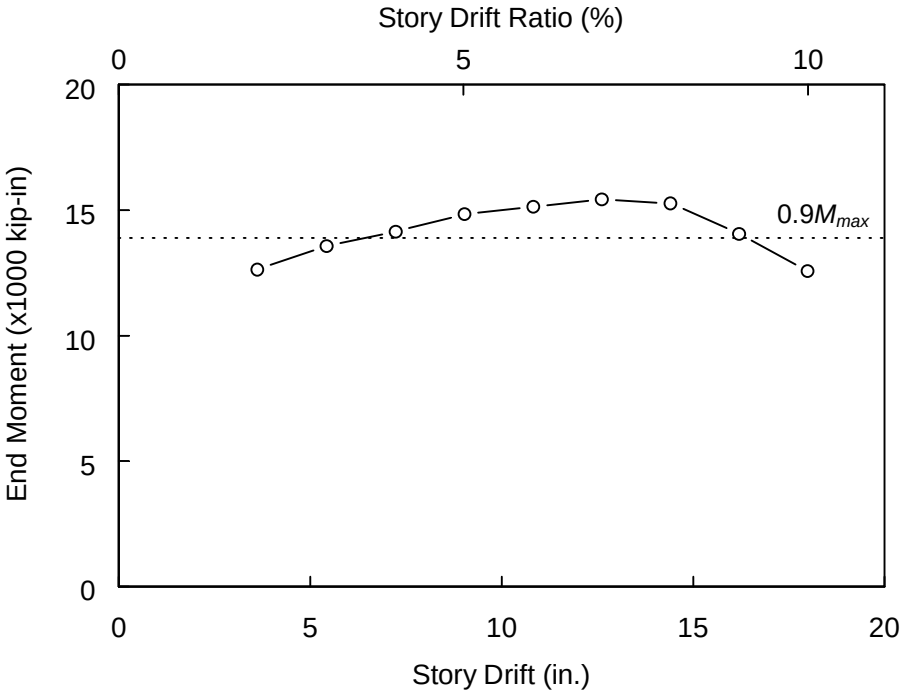

Figure 4.36 Specimen W14×176-55: Compression Side Target Points End Moment versus Drift Response

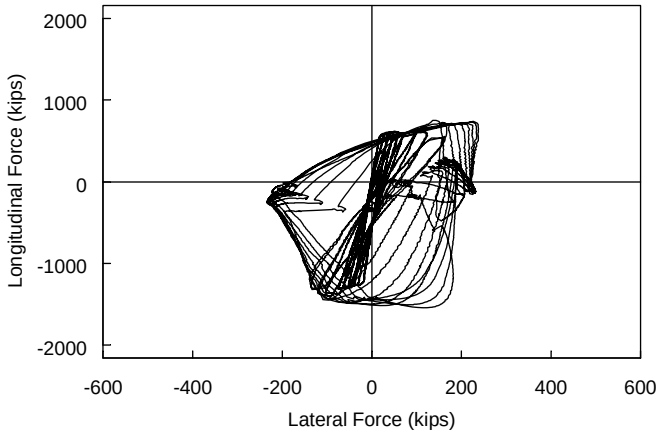

(a) Longitudinal Force versus Lateral Force

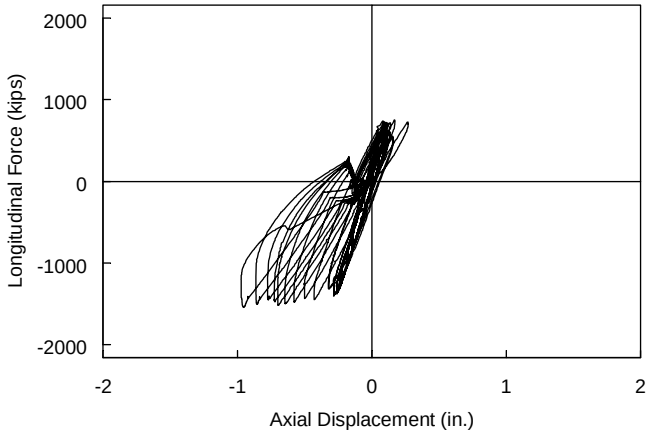

(b) Longitudinal Force versus Column Axial Displacement

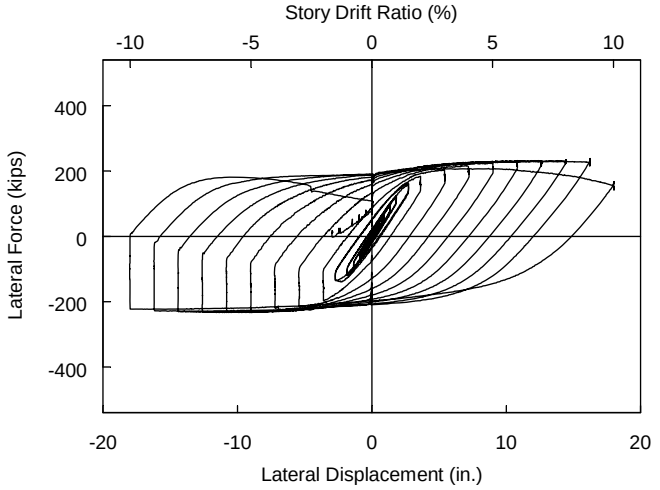

(c) Lateral Force versus Lateral Displacement

Figure 4.37 Specimen W14×176-55: Force-Displacement Response

East End West End

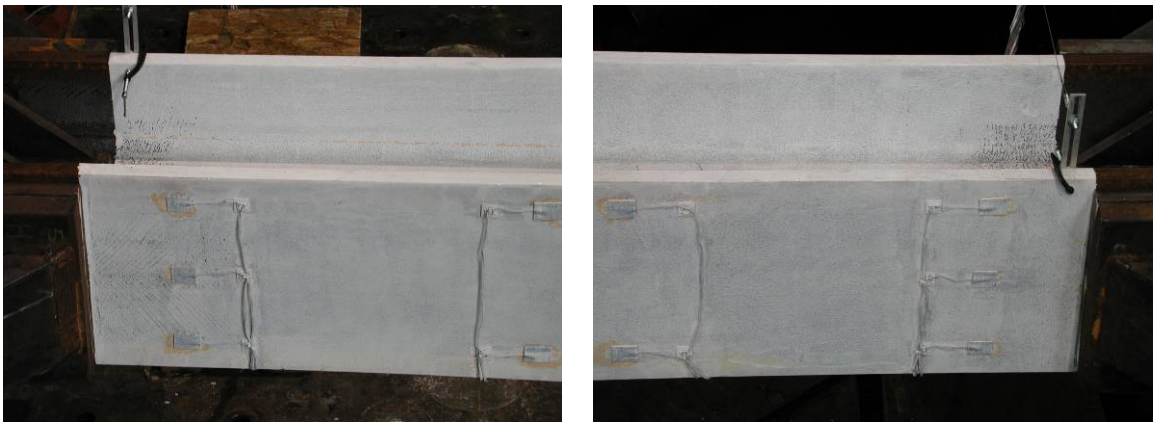

(a) 2% Drift

(b) 4% Drift

(c) 6% Drift

Figure 4.38 Specimen W14×176-75: Yielding Pattern

East End West End

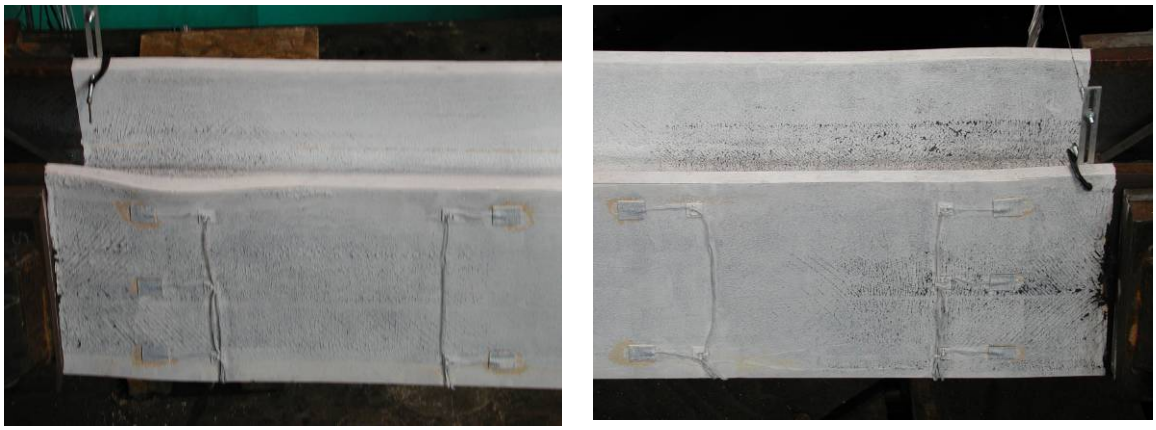

(d) 8% Drift

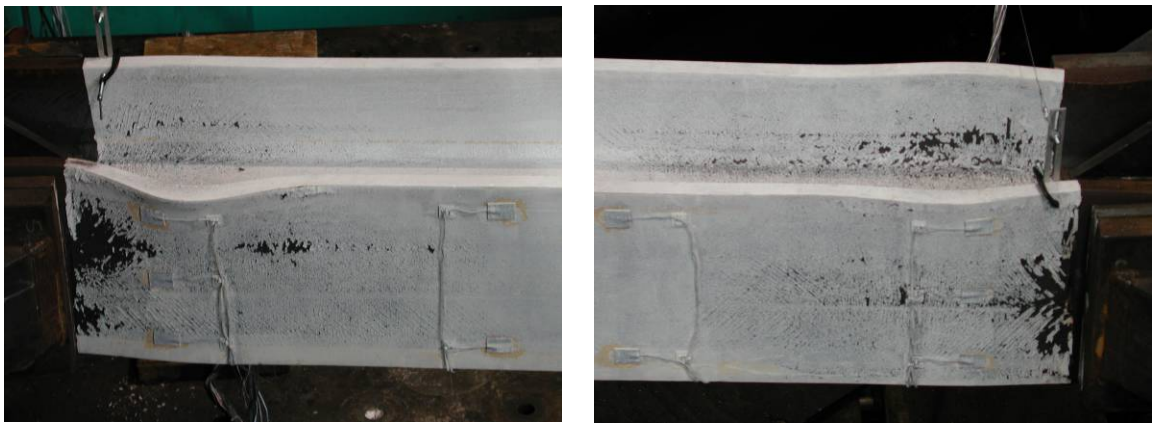

(e) 10% Drift

Figure 4.38 Specimen W14×176-75: Yielding Pattern (cont.)

(a) -4% Drift

(b) -6% Drift

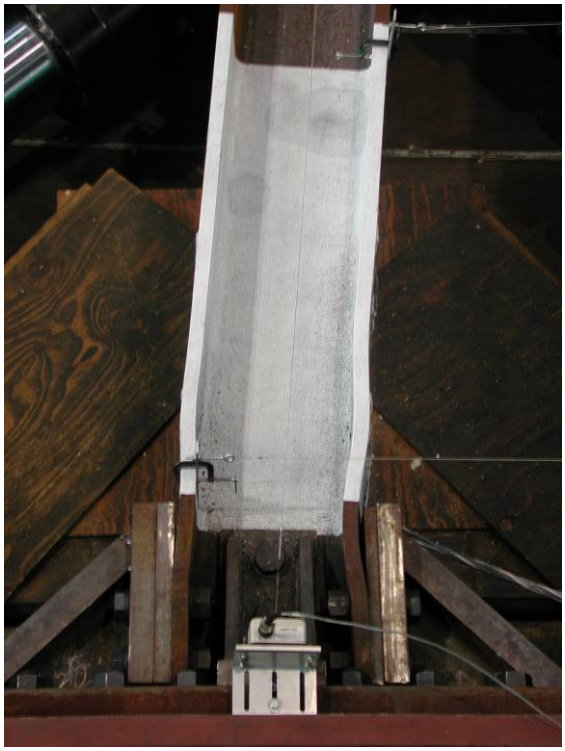

(c) -8% Drift

(d) -10% Drift

Figure 4.39 Specimen W14×176-75: Flange Local Buckling (West End)

Tension Excursion | Compression Excursion

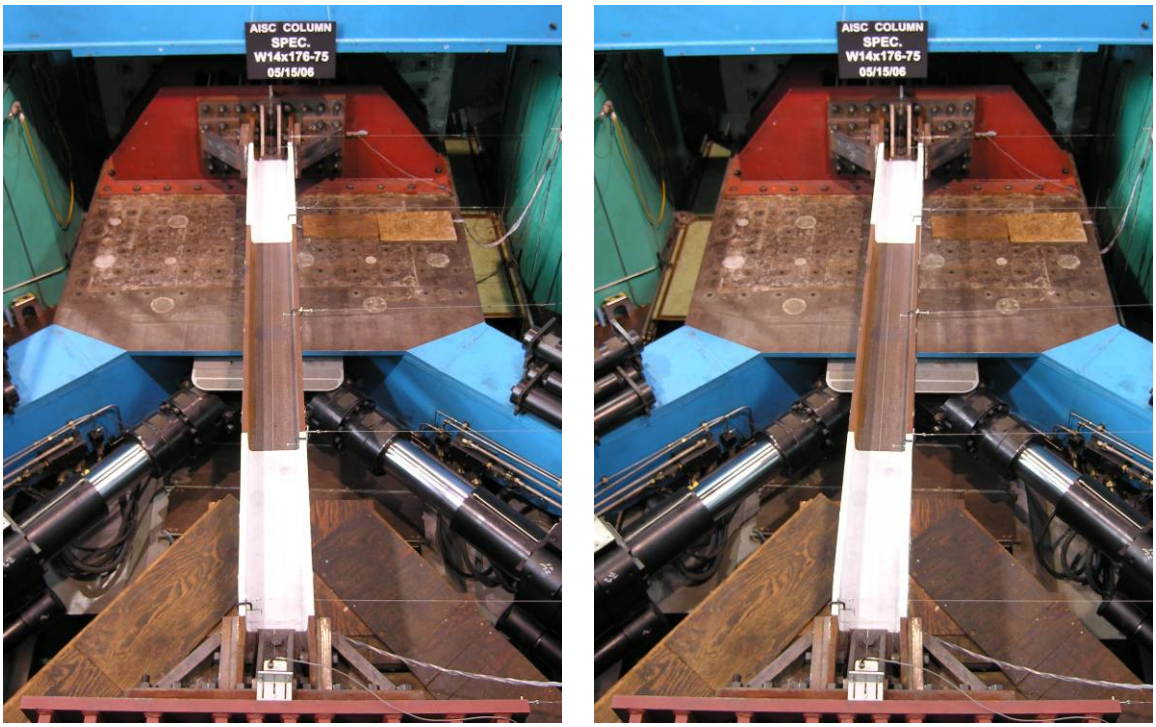

(a) 4% Drift

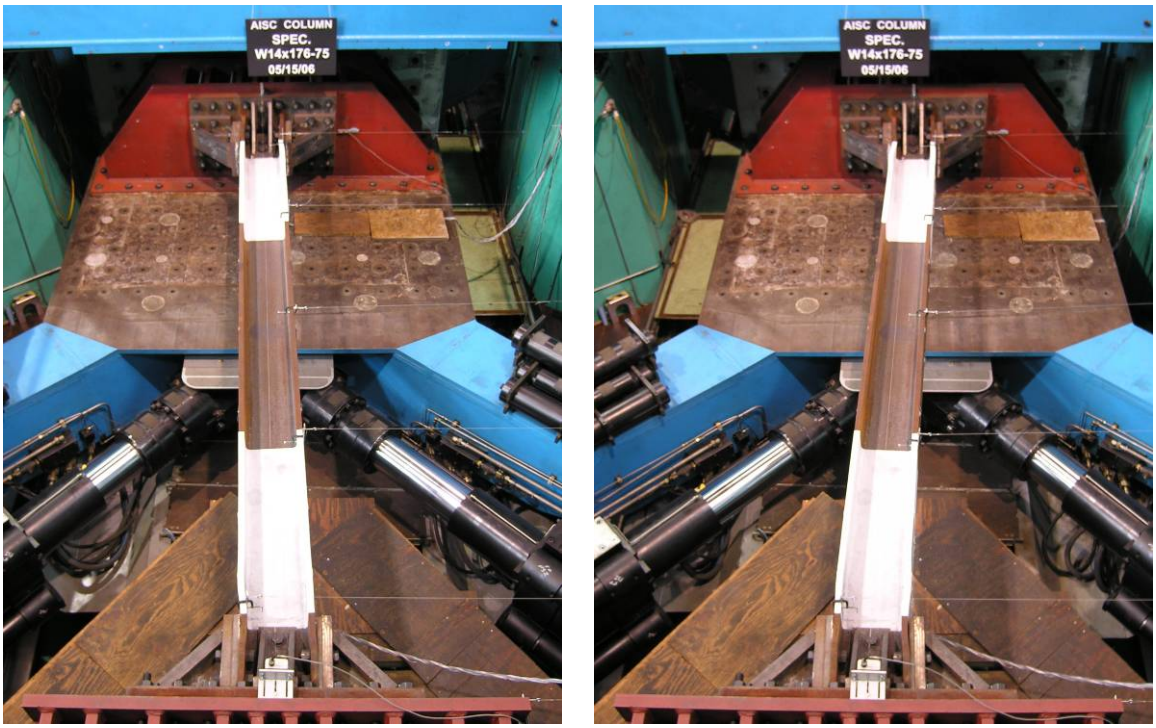

(b) 6% Drift

Figure 4.40 Specimen W14×176-75: Overall Deformed Configuration

Tension Excursion | Compression Excursion

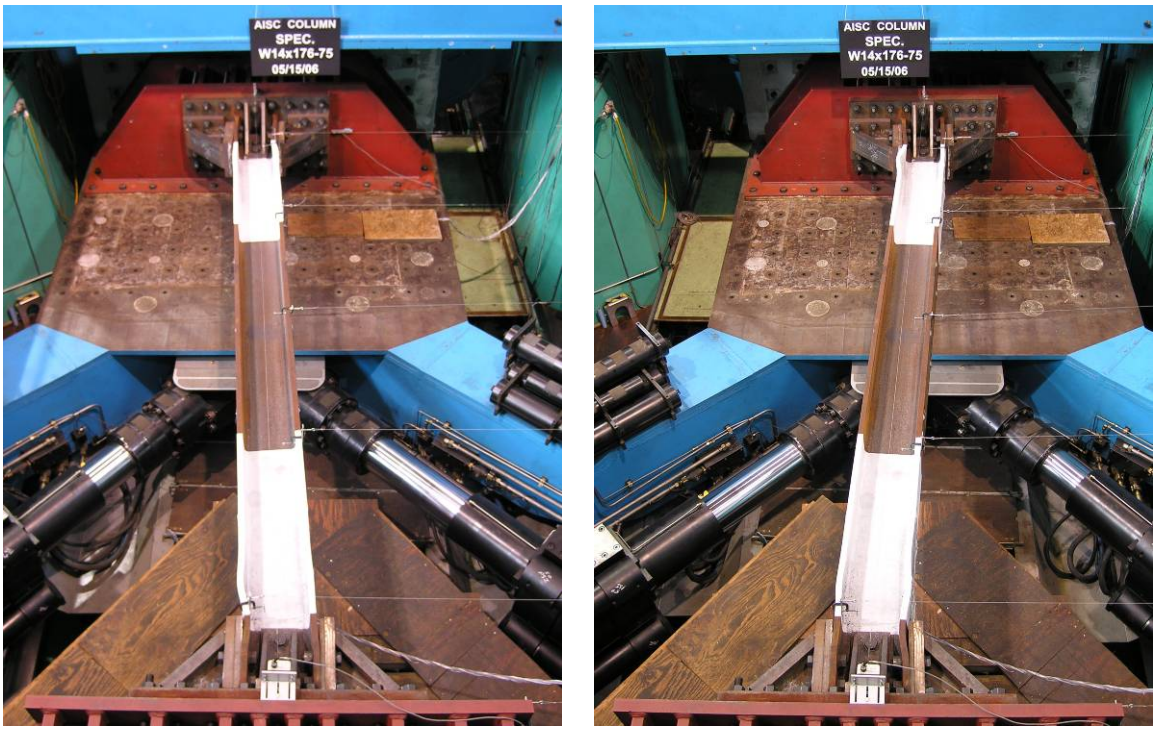

(c) 8% Drift

(d) 10% Drift

Figure 4.40 Specimen W14×176-75: Overall Deformed Configuration (cont.)

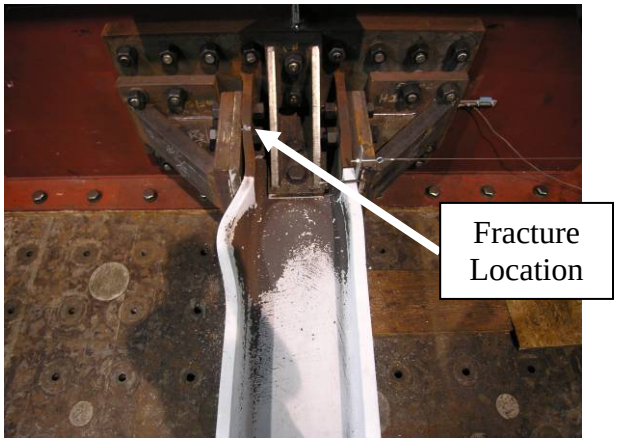

(a) Overall View of Fracture Location

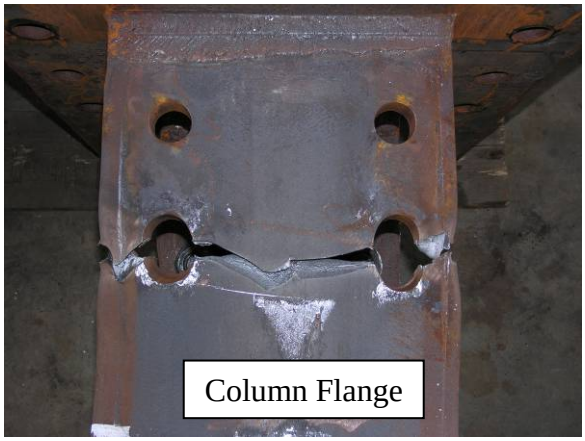

(b) View of Fracture from Exterior Side of Flange

(c) View of Fracture from Interior Side of Flange

Figure 4.41 Specimen W14×176-75: Column Fracture (10% Drift)

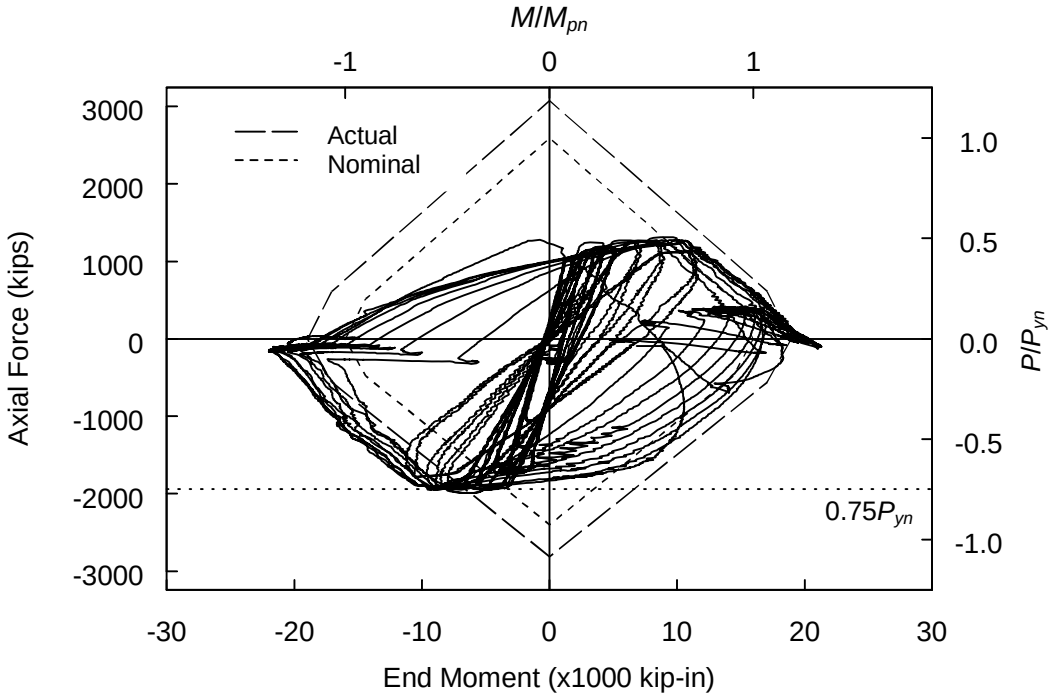

Figure 4.42 Specimen W14×176-75: *P*-*M* Interaction

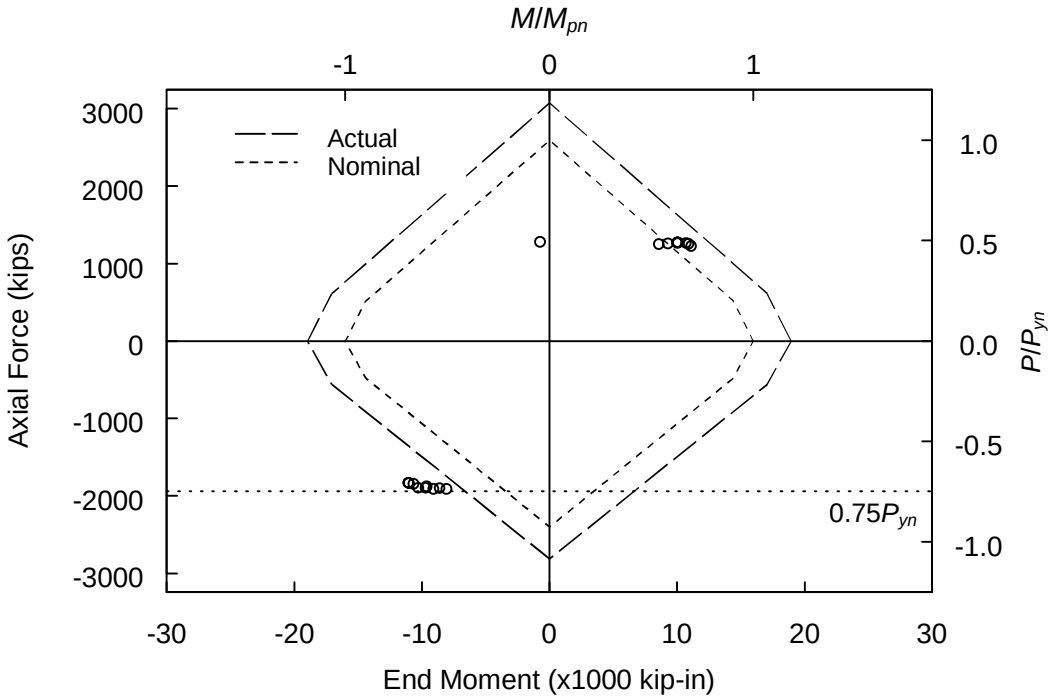

Figure 4.43 Specimen W14×176-75: *P*-*M* Interaction (Target Points)

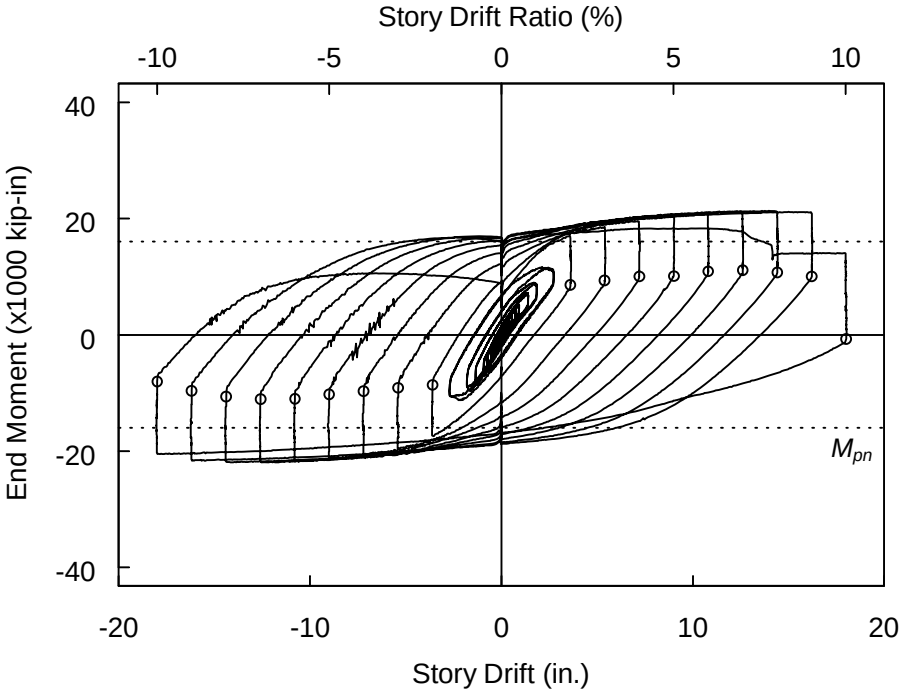

Figure 4.44 Specimen W14×176-75: End Moment versus Drift Response

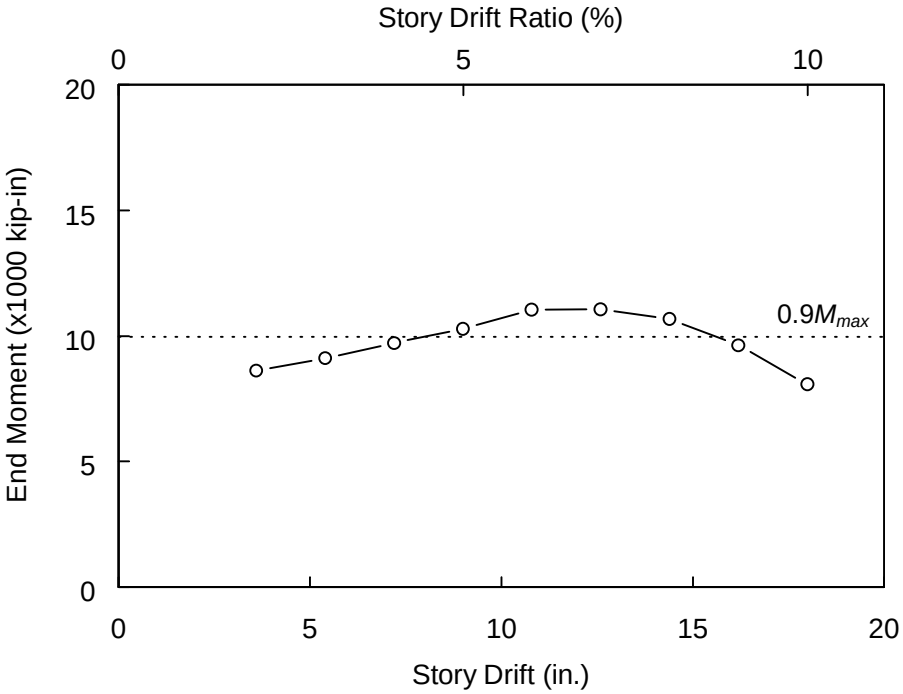

Figure 4.45 Specimen W14×176-75: Compression Side Target Points End Moment versus Drift Response

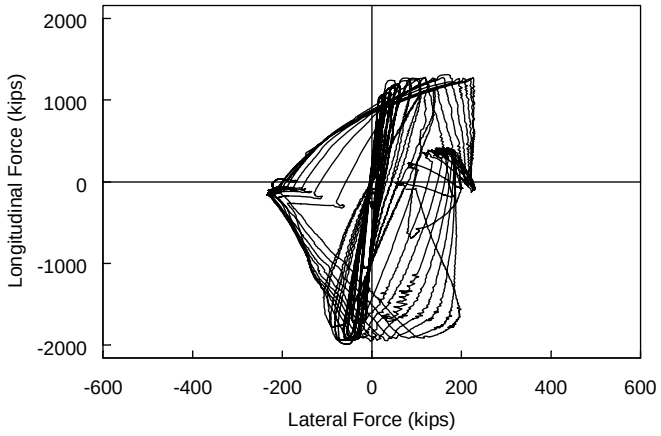

(a) Longitudinal Force versus Lateral Force

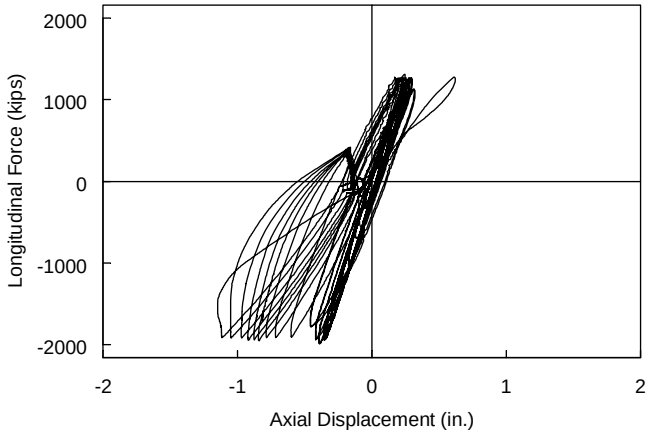

(b) Longitudinal Force versus Column Axial Displacement

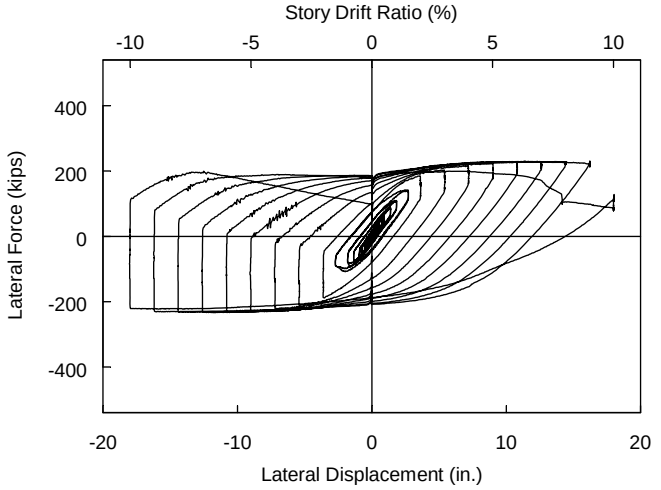

(c) Lateral Force versus Lateral Displacement

Figure 4.46 Specimen W14×176-75: Force-Displacement Response

East End West End

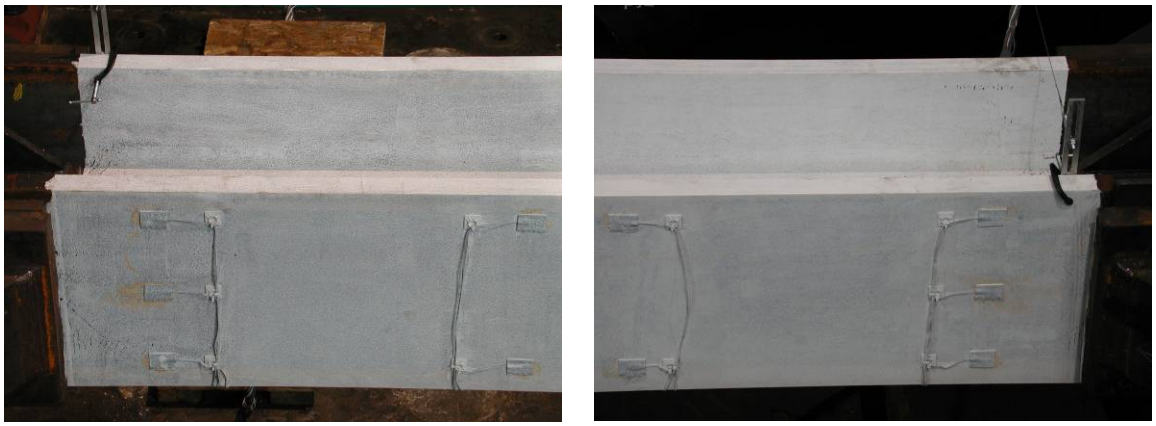

(a) 2% Drift

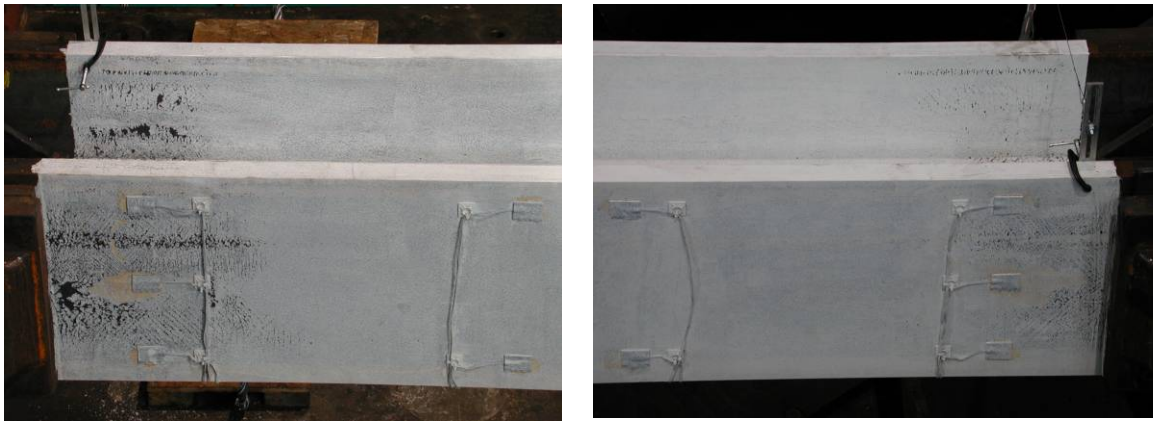

(b) 4% Drift

(c) 6% Drift

Figure 4.47 Specimen W14×233-35: Yielding Pattern

East End West End

(d) 8% Drift

Figure 4.47 Specimen W14×233-35: Yielding Pattern (cont.)

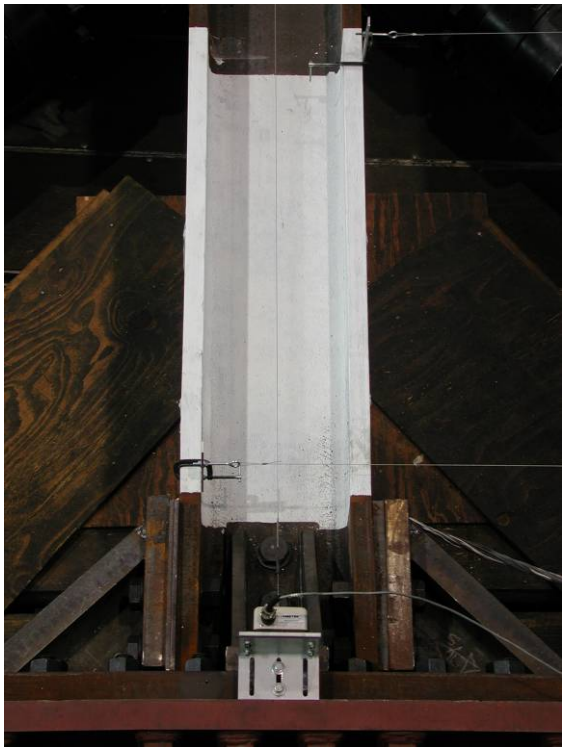

(a) -4% Drift

(b) -6% Drift

(c) -8% Drift

Figure 4.48 Specimen W14×233-35: Flange Local Buckling (West End)

Tension Excursion | Compression Excursion

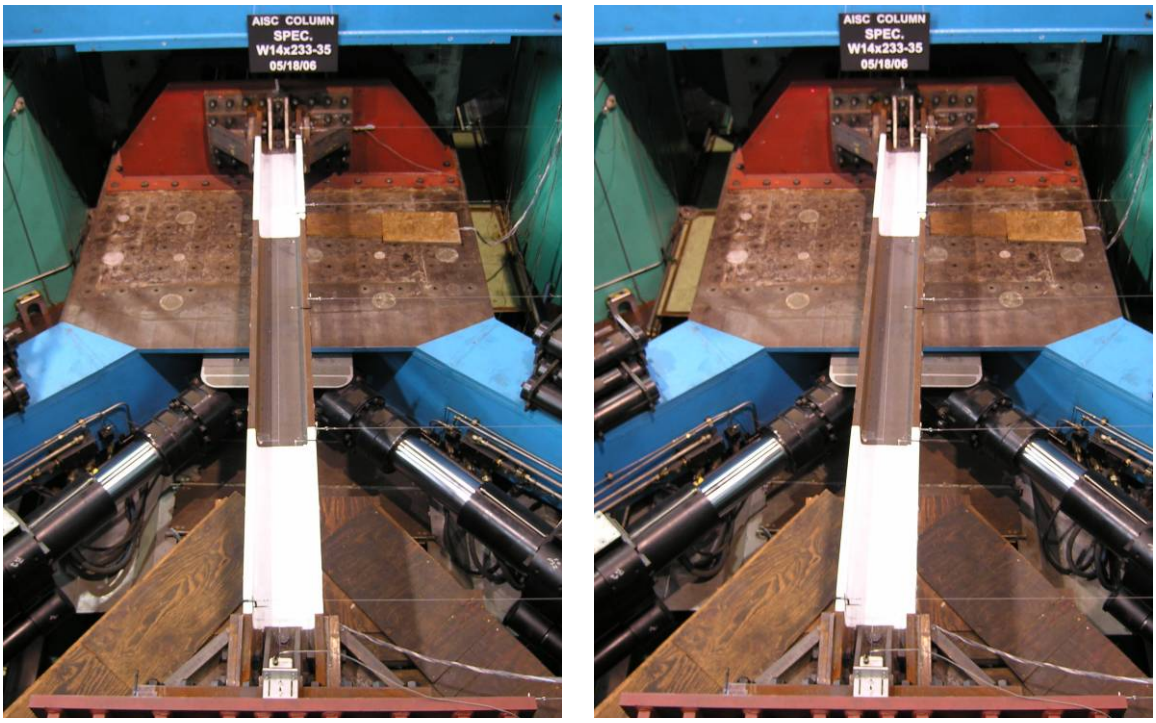

(a) 4% Drift

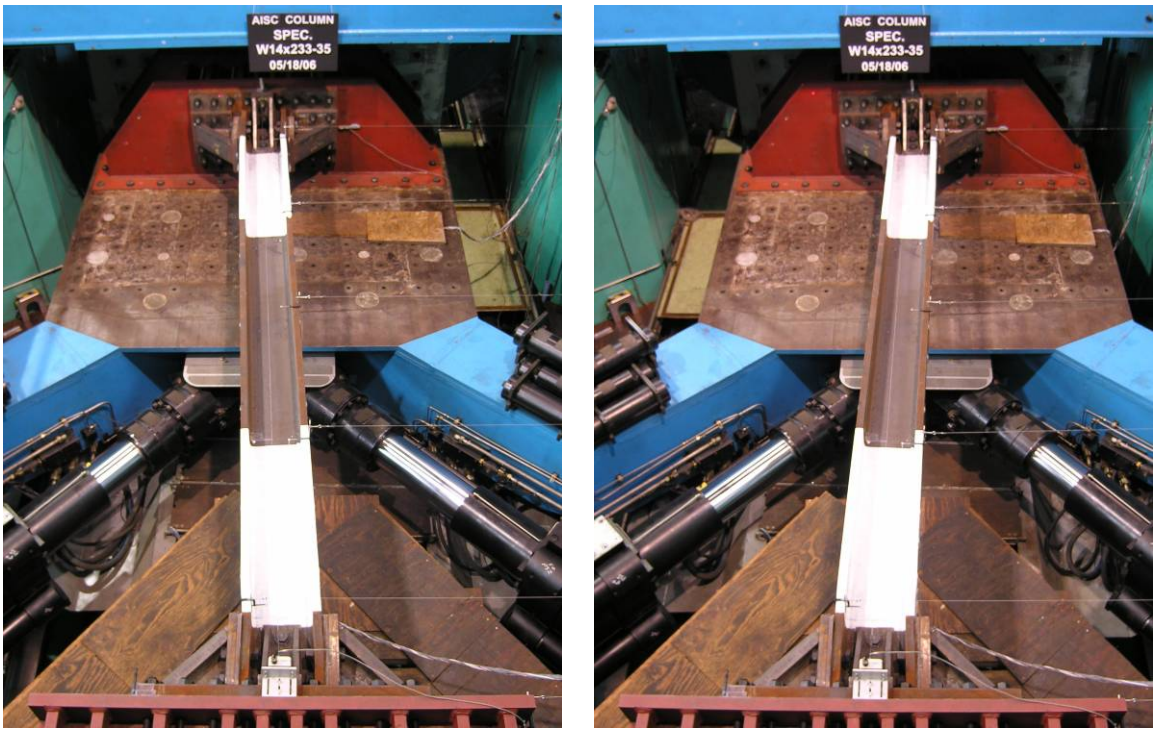

(b) 6% Drift

Figure 4.49 Specimen W14×233-35: Overall Deformed Configuration

Tension Excursion | Compression Excursion

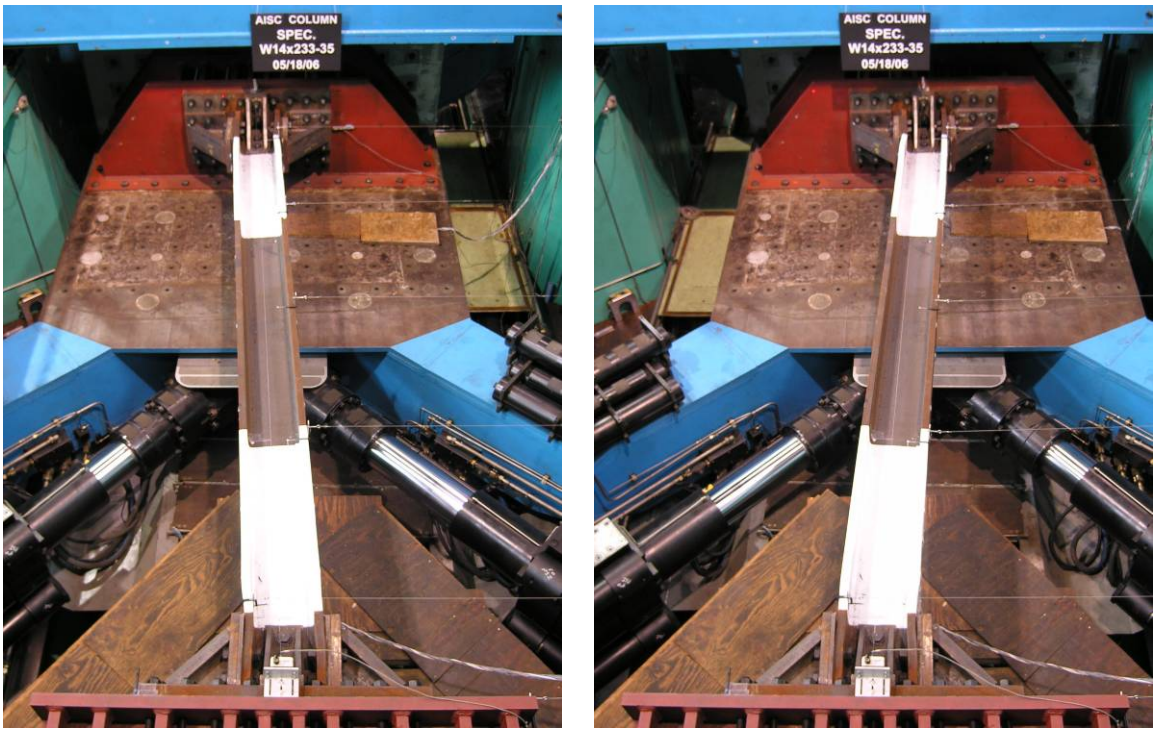

(c) 8% Drift

Figure 4.49 Specimen W14×233-35: Overall Deformed Configuration (cont.)

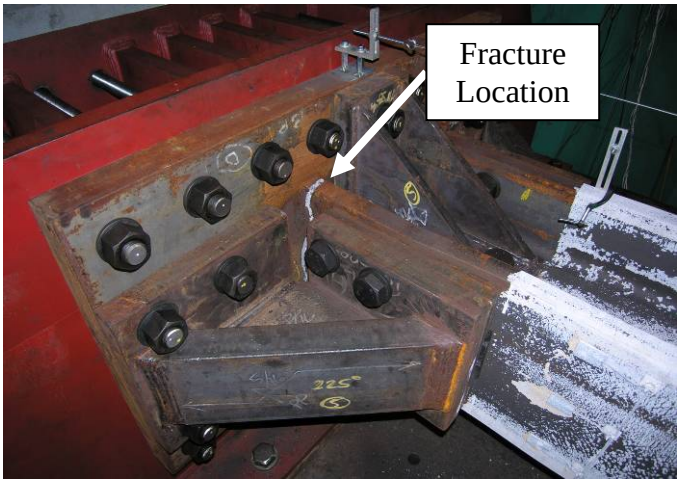

(a) Overall View of Fracture Location

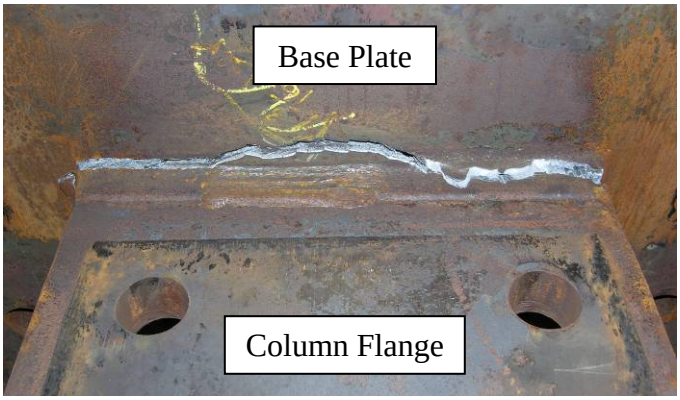

(b) View of Fracture from Exterior Side of Flange

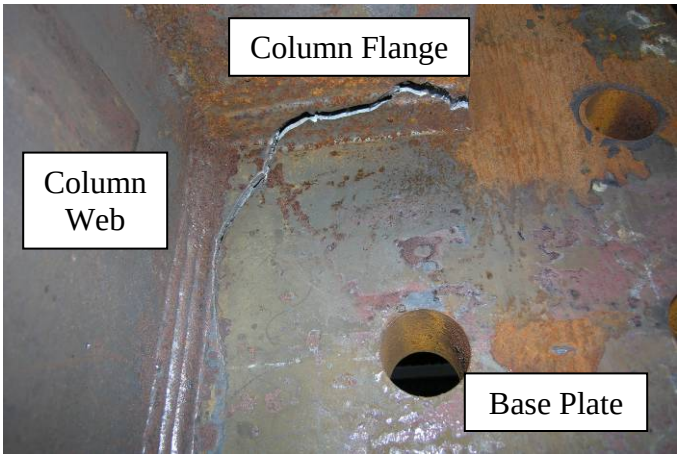

(c) View of Fracture from Interior Side of Flange

Figure 4.50 Specimen W14×233-35: Column-to-Base Plate Weld Fracture (9% Drift)

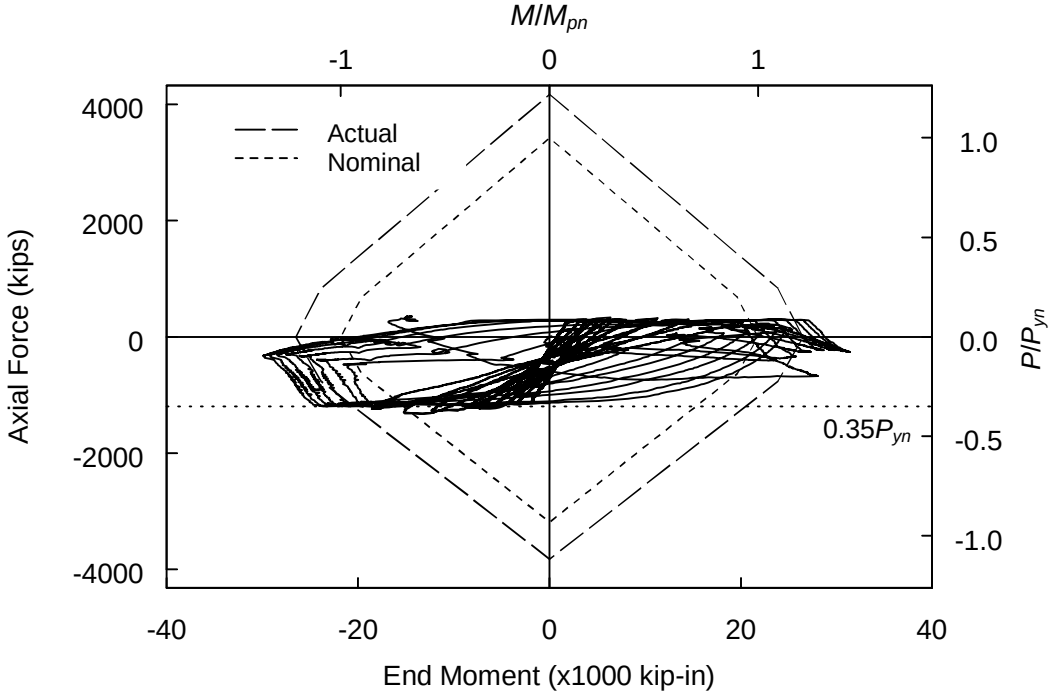

Figure 4.51 Specimen W14×233-35: *P-M* Interaction

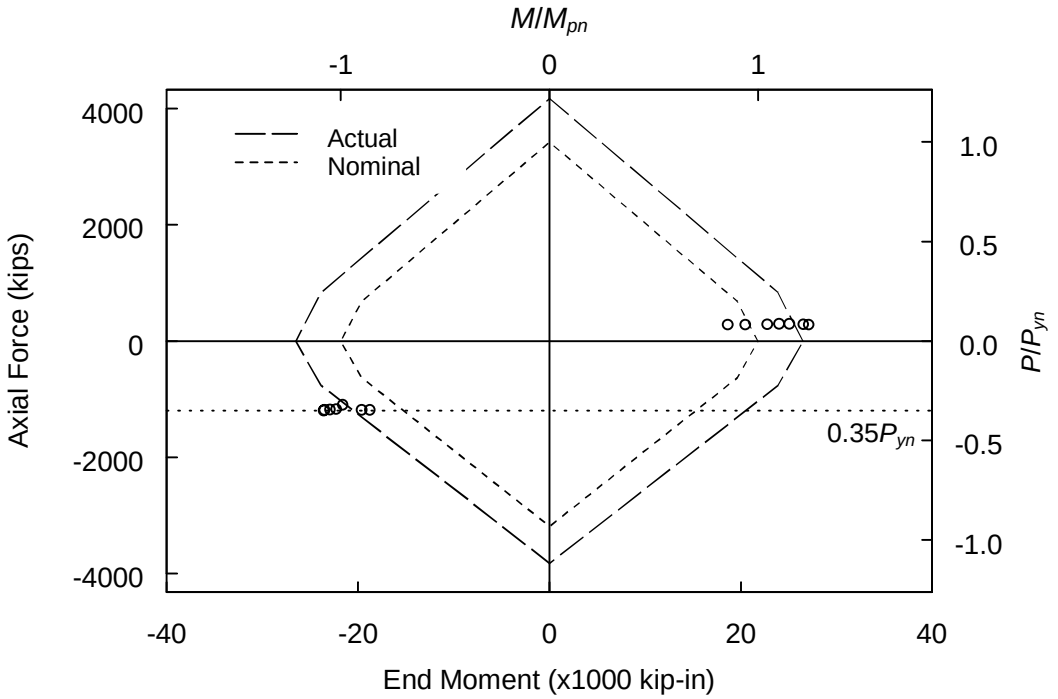

Figure 4.52 Specimen W14×233-35: *P-M* Interaction (Target Points)

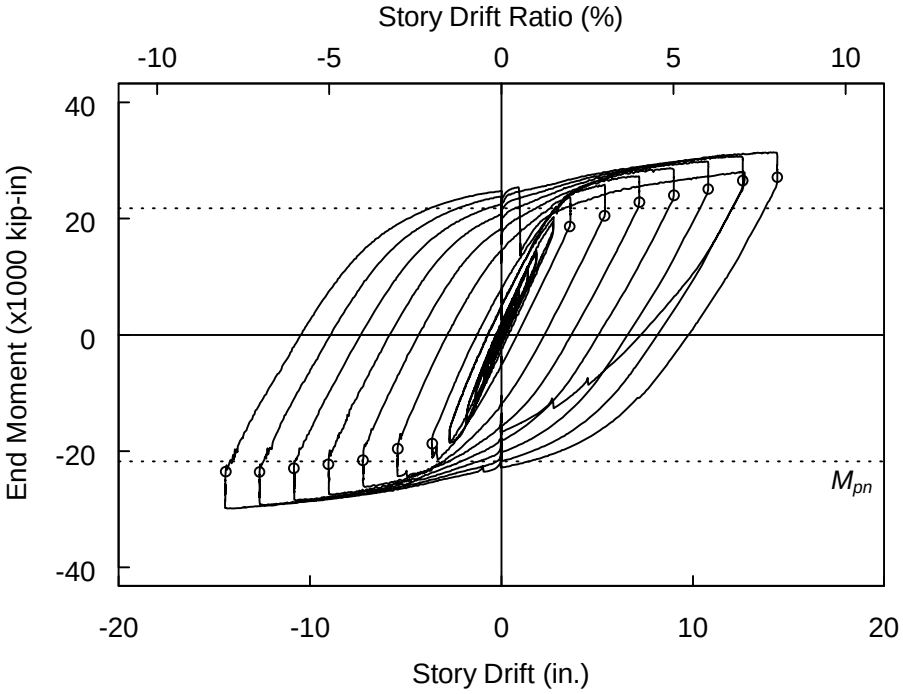

Figure 4.53 Specimen W14×233-35: End Moment versus Drift Response

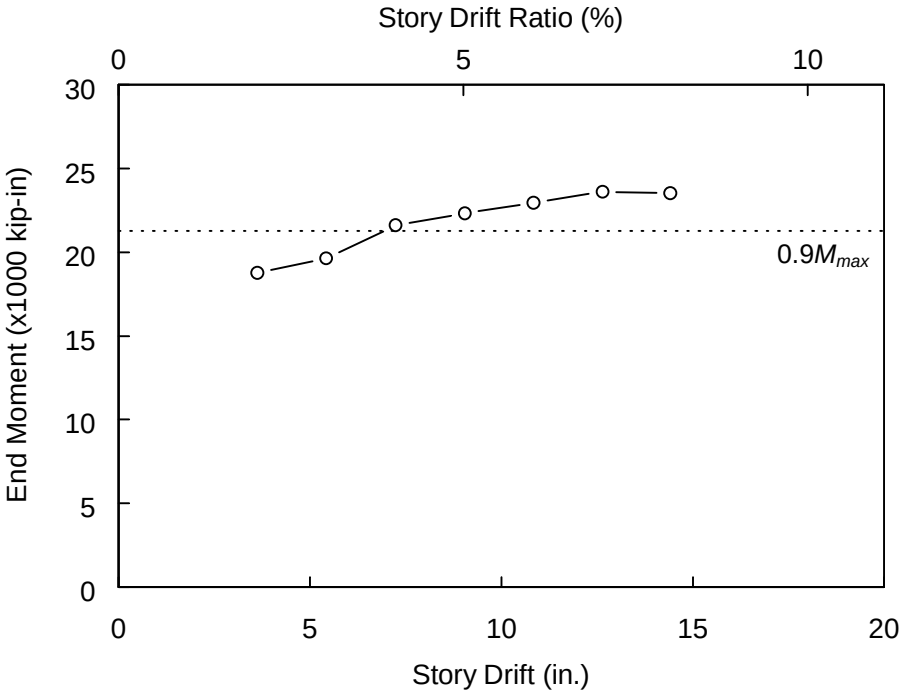

Figure 4.54 Specimen W14×233-35: Compression Side Target Points End Moment versus Drift Response

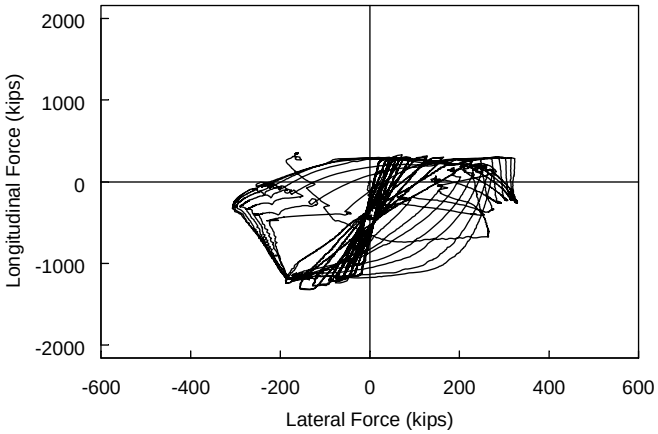

(a) Longitudinal Force versus Lateral Force

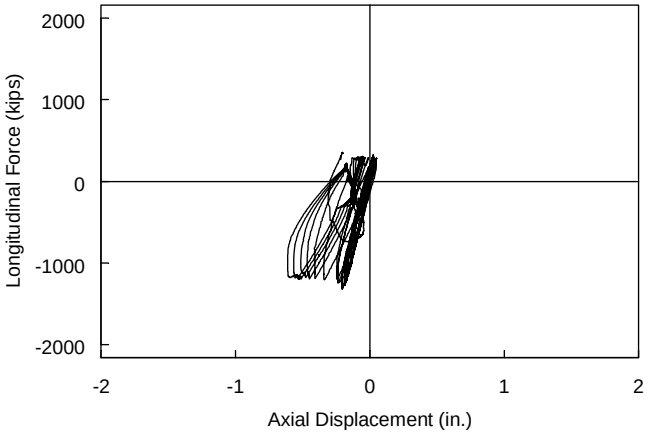

(b) Longitudinal Force versus Column Axial Displacement

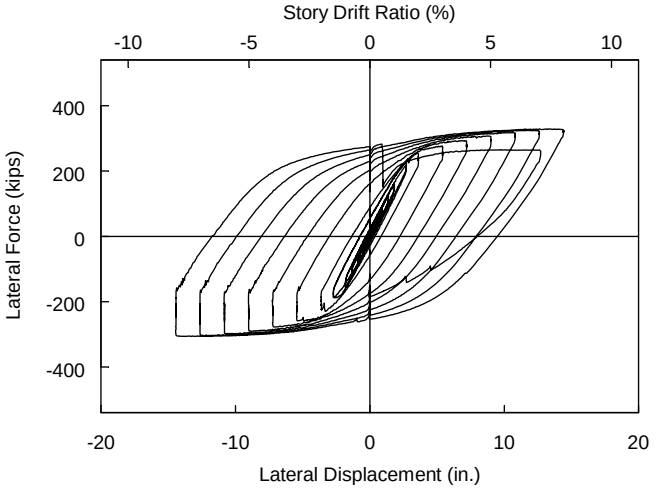

(c) Lateral Force versus Lateral Displacement

Figure 4.55 Specimen W14×233-35: Force-Displacement Response

East End West End

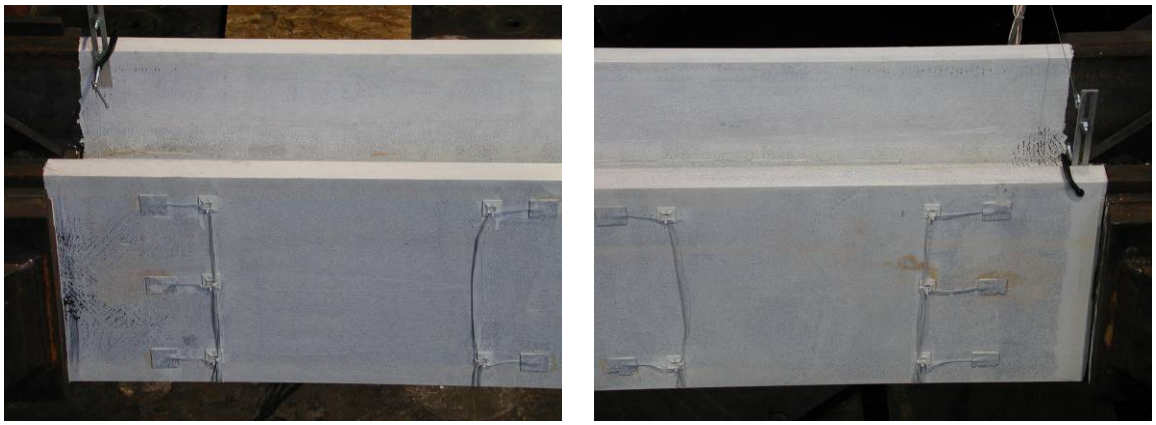

(a) 2% Drift

(b) 4% Drift

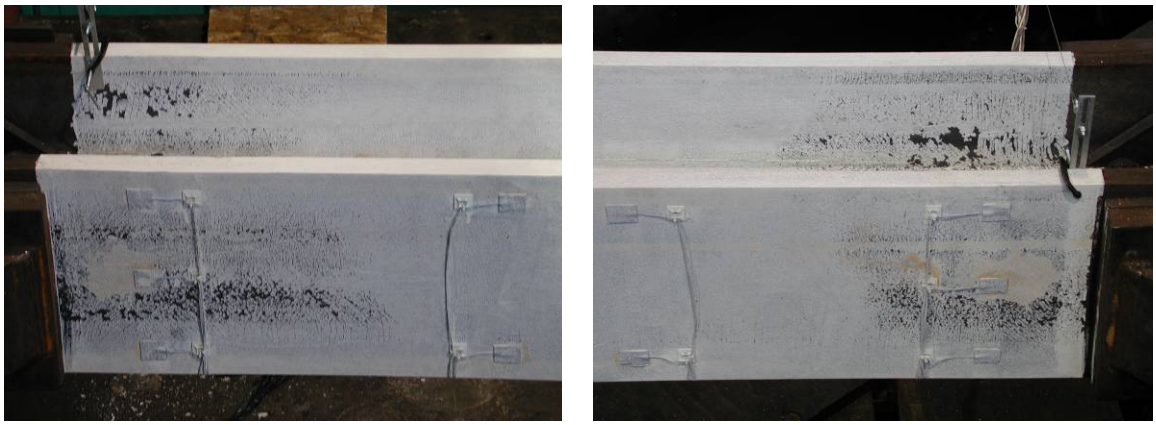

(c) 6% Drift

Figure 4.56 Specimen W14×233-55: Yielding Pattern

East End West End

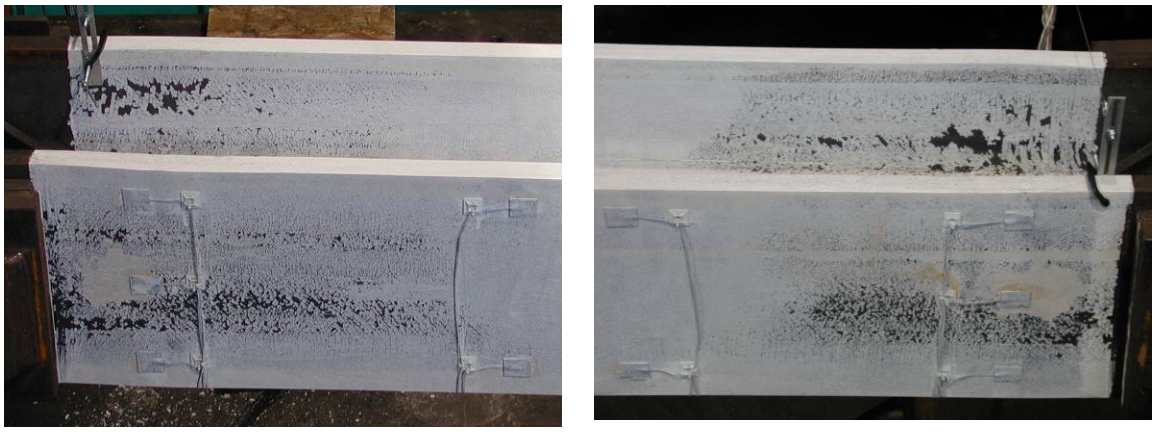

(d) 8% Drift

Figure 4.56 Specimen W14×233-55: Yielding Pattern (cont.)

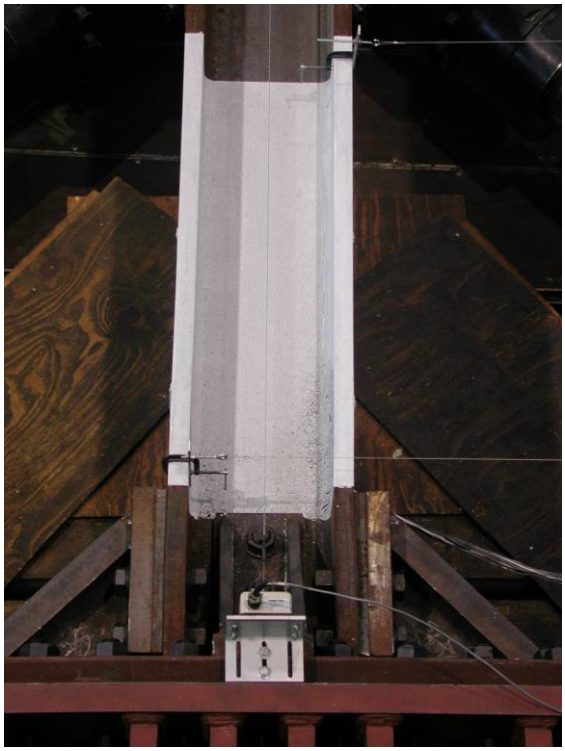

(a) -4% Drift

(b) -6% Drift

(c) -8% Drift

Figure 4.57 Specimen W14×233-55: Flange Local Buckling (West End)

Tension Excursion | Compression Excursion

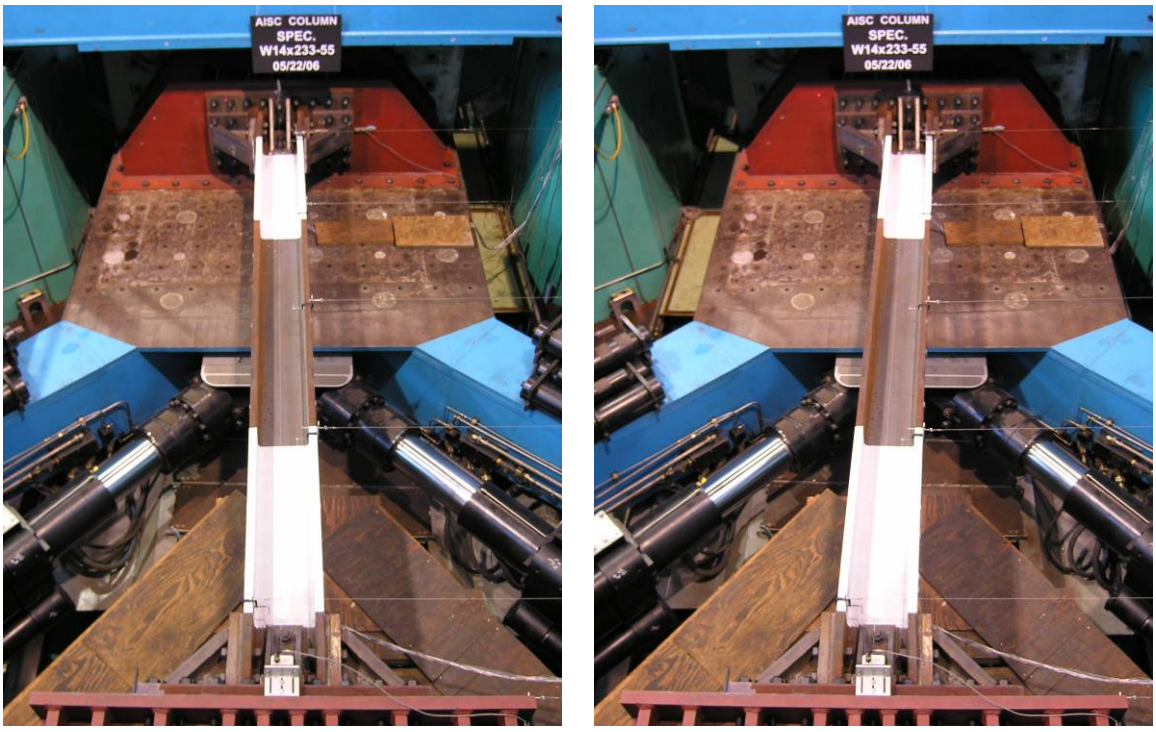

(a) 4% Drift

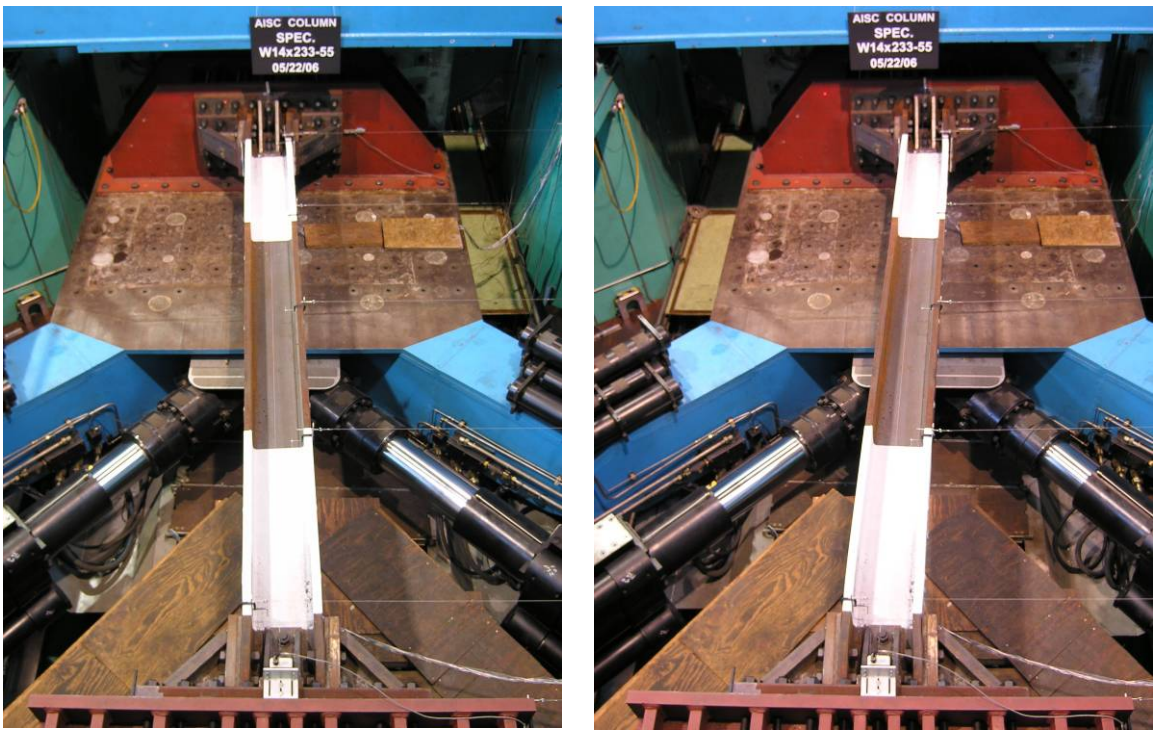

(b) 6% Drift

Figure 4.58 Specimen W14×233-55: Overall Deformed Configuration

Tension Excursion

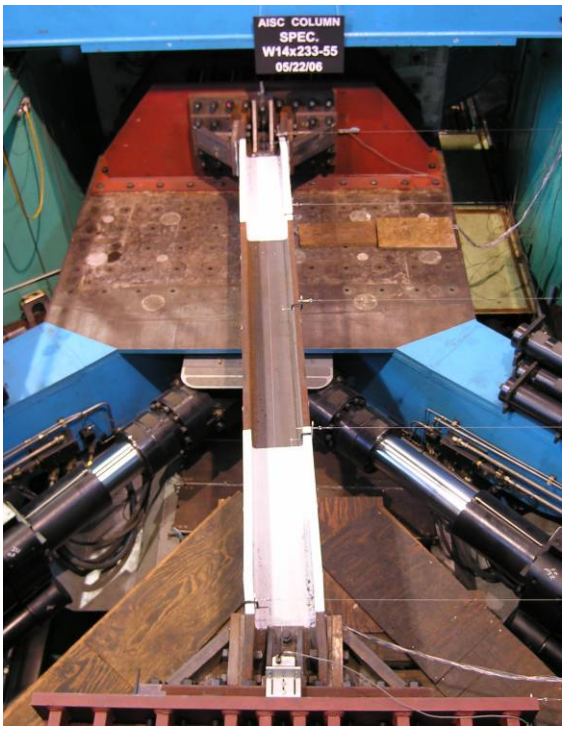

Compression Excursion

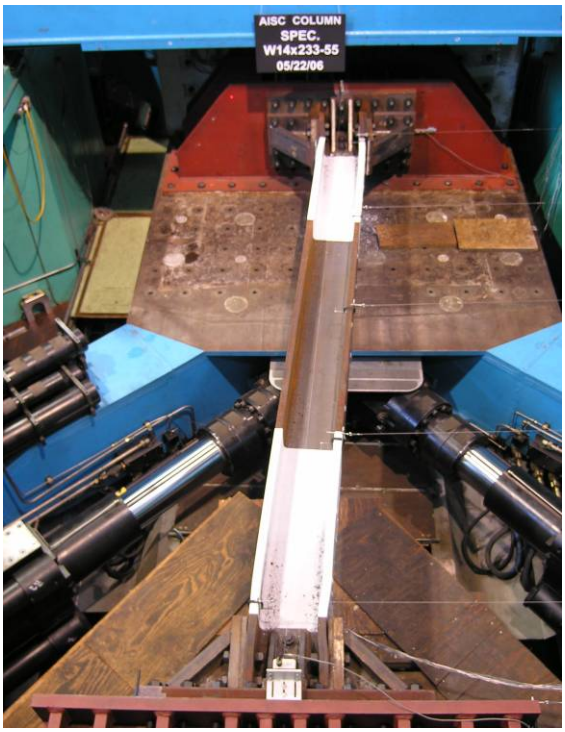

(c) 8% Drift

Figure 4.58 Specimen W14×233-55: Overall Deformed Configuration (cont.)

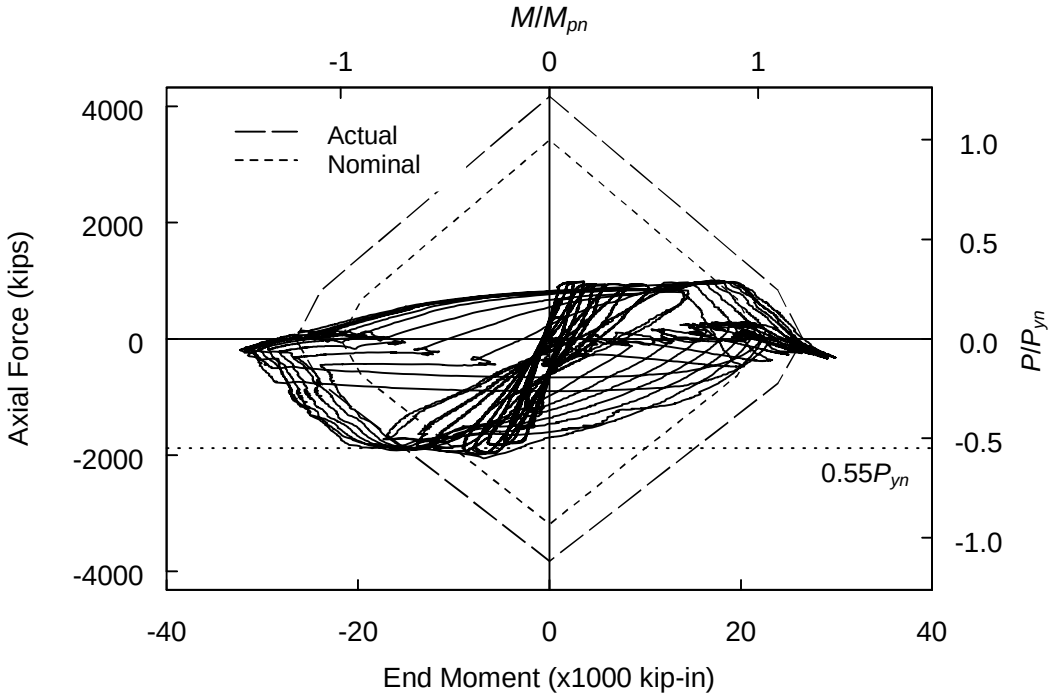

Figure 4.59 Specimen W14×233-55: *P-M* Interaction

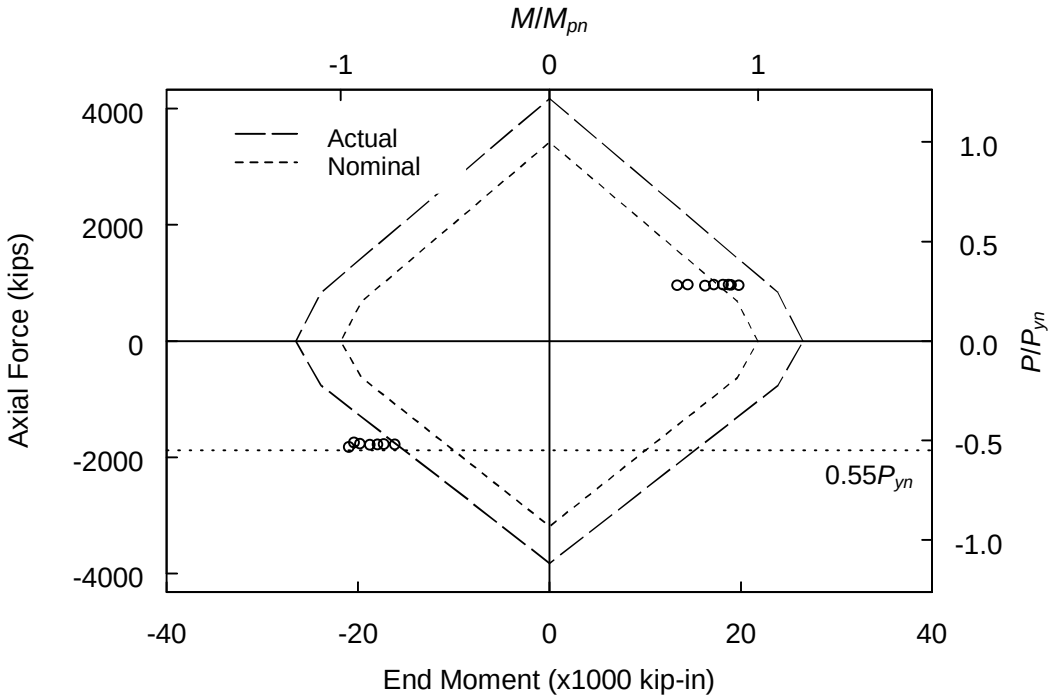

Figure 4.60 Specimen W14×233-55: *P-M* Interaction (Target Points)

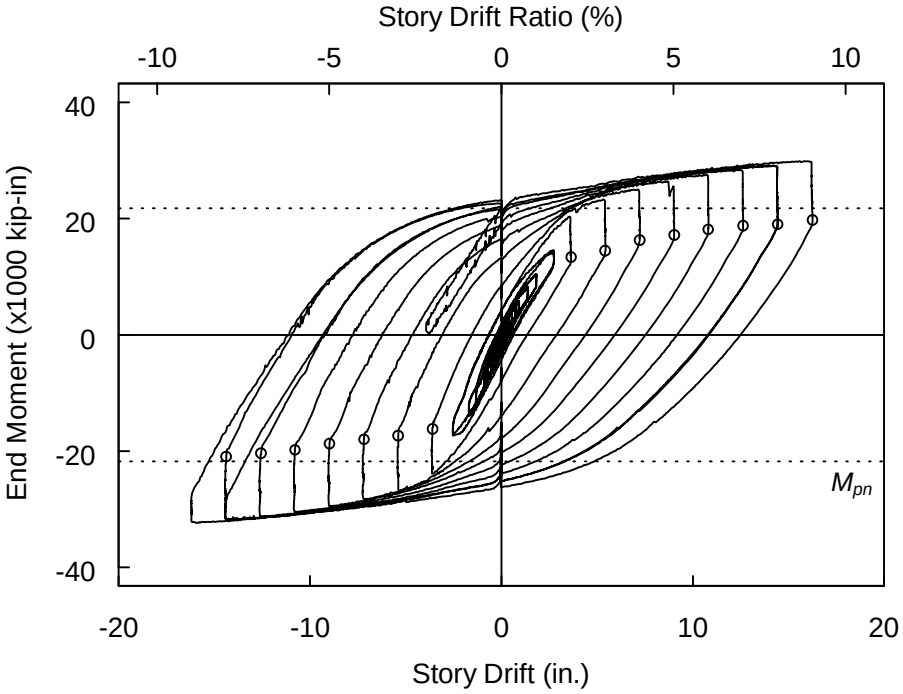

Figure 4.61 Specimen W14×233-55: End Moment versus Drift Response

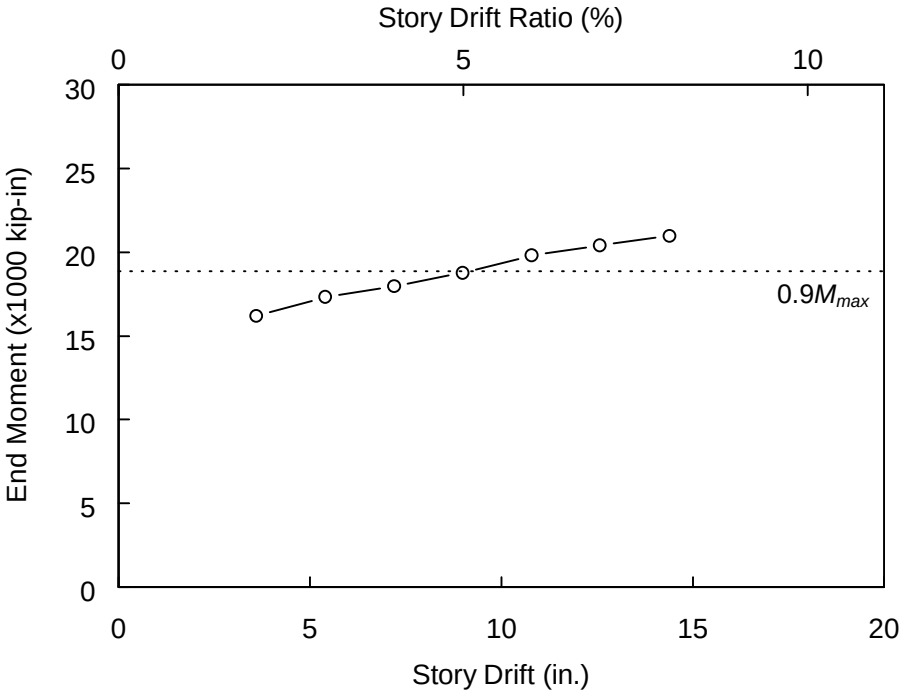

Figure 4.62 Specimen W14×233-55: Compression Side Target Points End Moment versus Drift Response

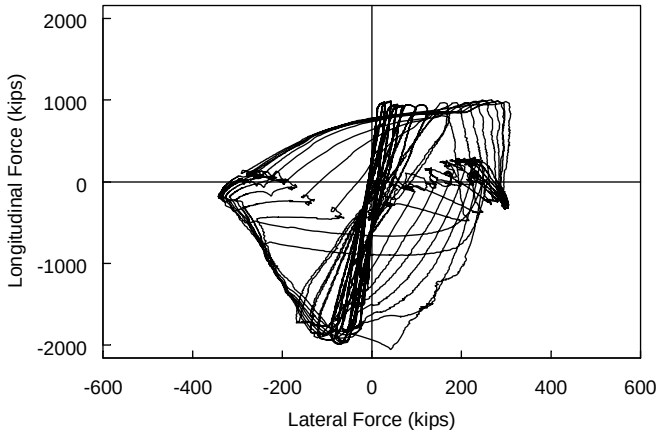

(a) Longitudinal Force versus Lateral Force

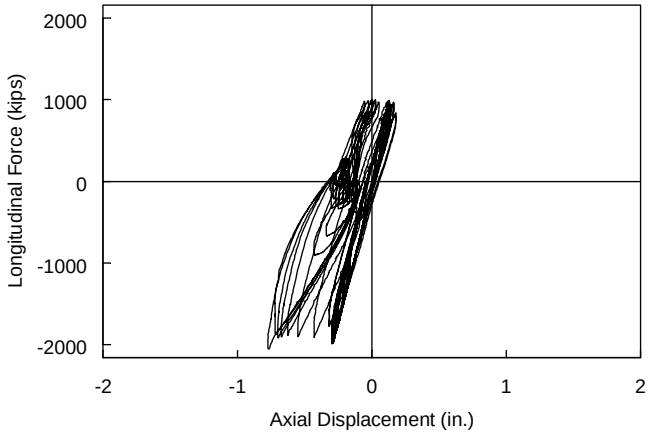

(b) Longitudinal Force versus Column Axial Displacement

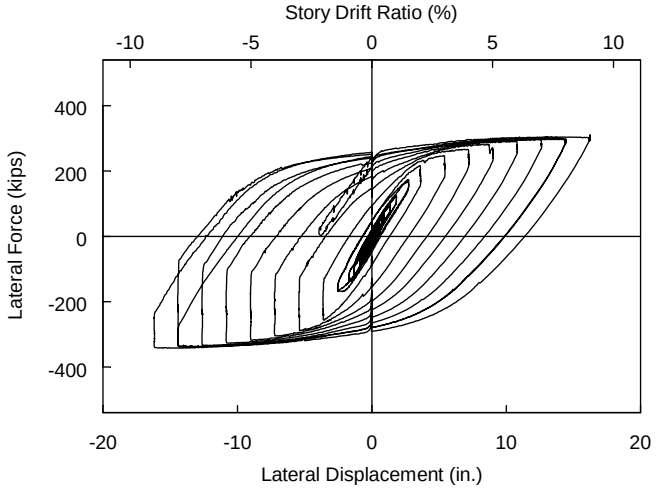

(c) Lateral Force versus Lateral Displacement

Figure 4.63 Specimen W14×233-55: Force-Displacement Response

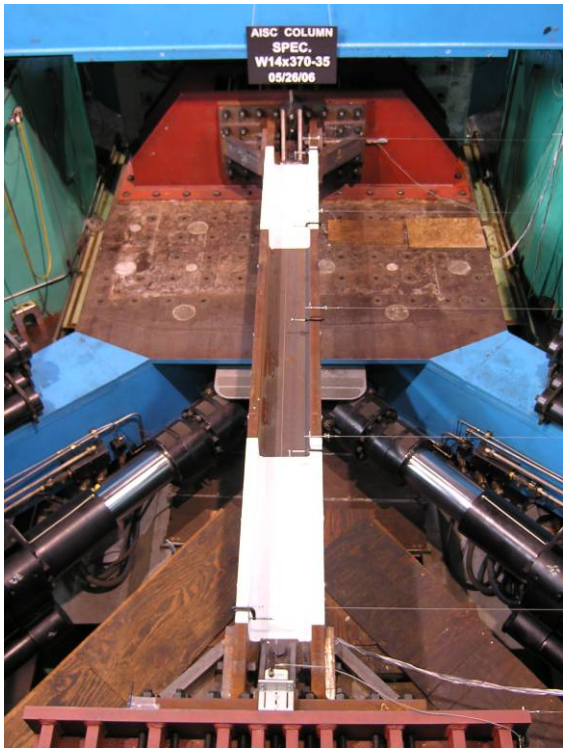

Figure 4.64 Specimen W14×370-35: Before Testing

East End

West End

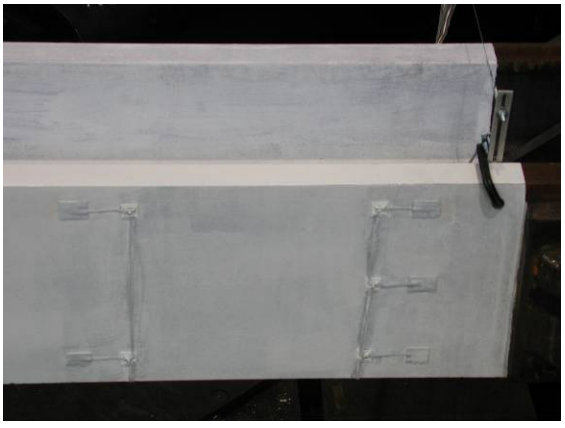

Figure 4.65 Specimen W14×370-35: Yielding Pattern at 2% Drift

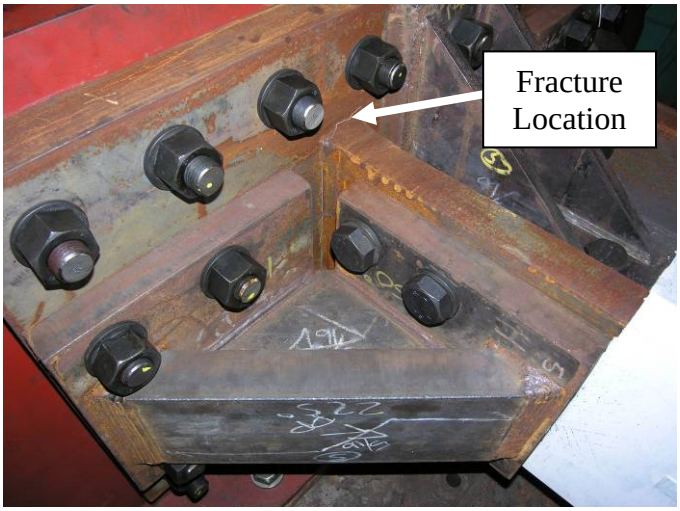

(a) Overall View of Fracture Location

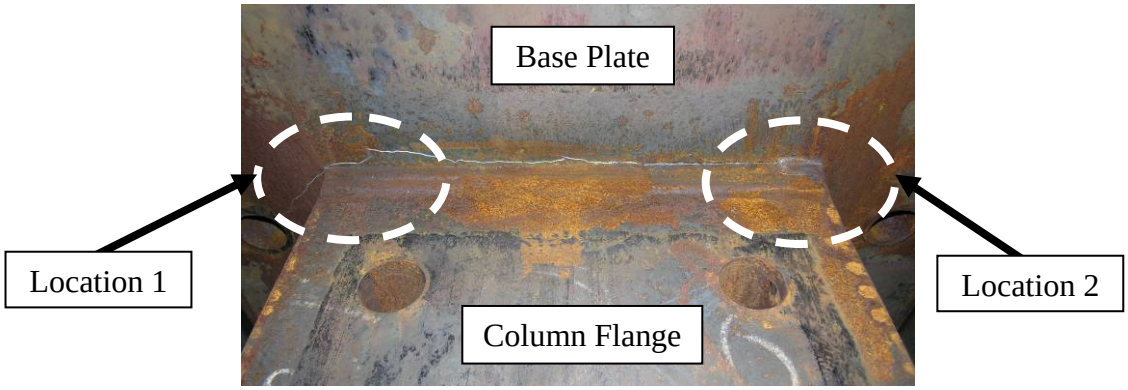

(b) View of Fracture from Exterior Side of Flange (with Haunches Removed)

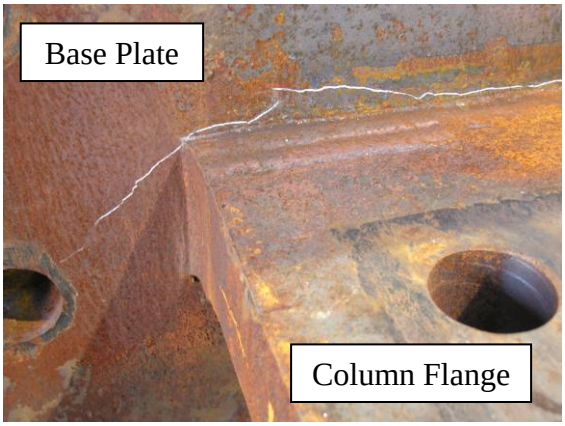

(c) View of Fracture Location 1
(with Haunches Removed)

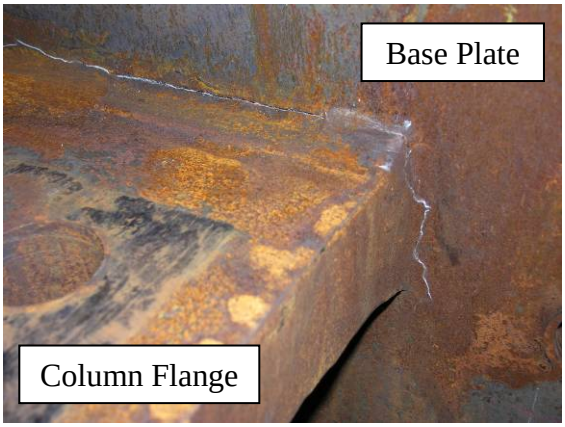

(d) View of Fracture Location 2
(with Haunches Removed)

Figure 4.66 Specimen W14×370-35: Column-to-Base Plate Weld Fracture (3% Drift)

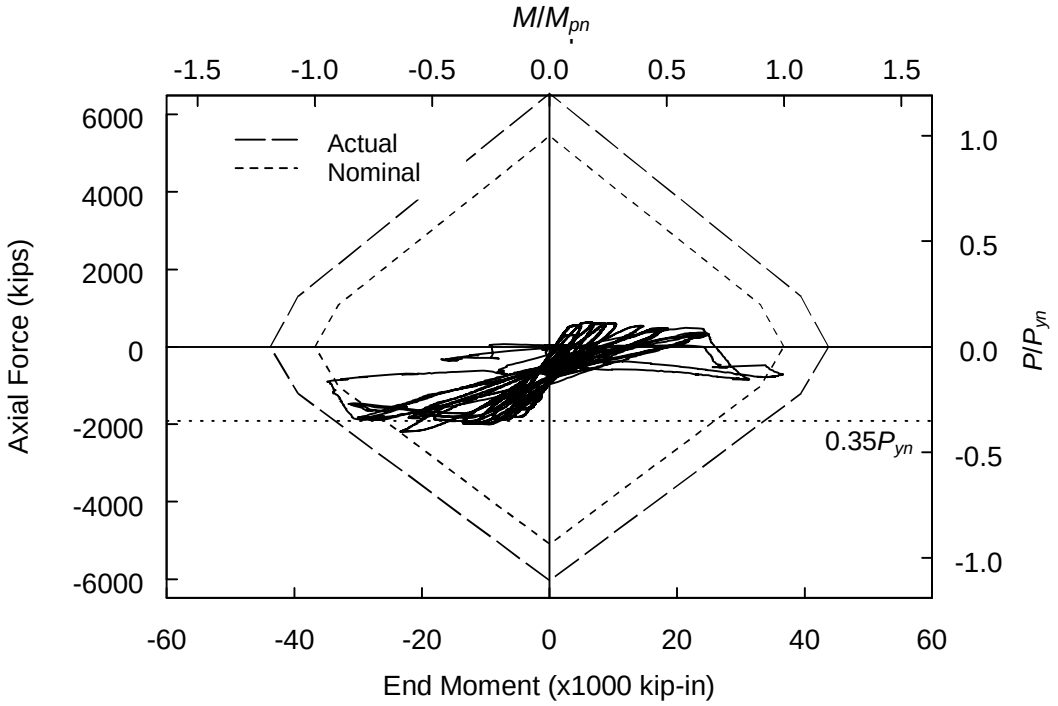

Figure 4.67 Specimen W14×370-35: *P*-*M* Interaction

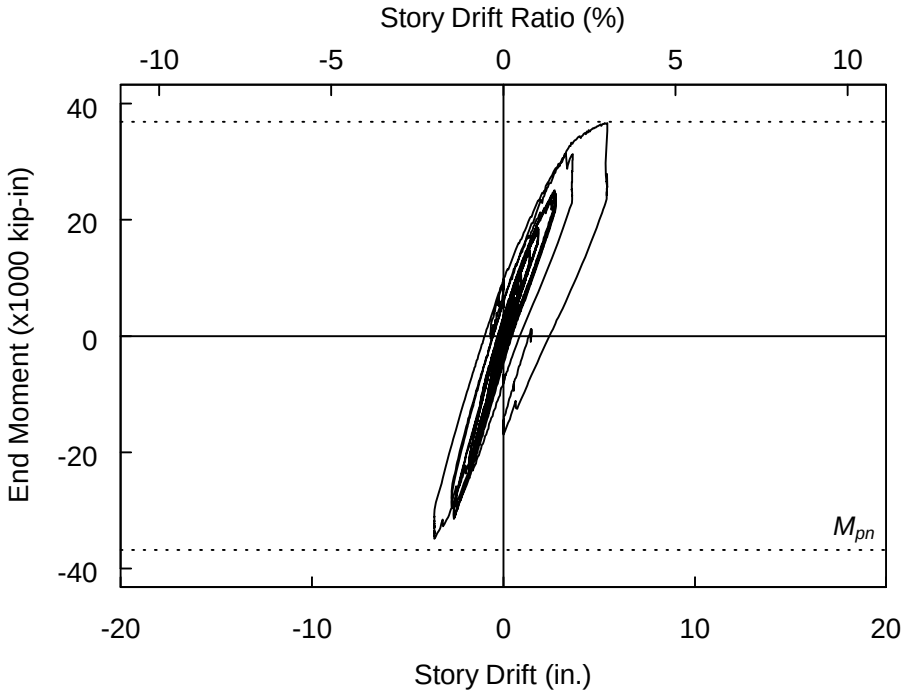

Figure 4.68 Specimen W14×370-35: End Moment versus Drift Response

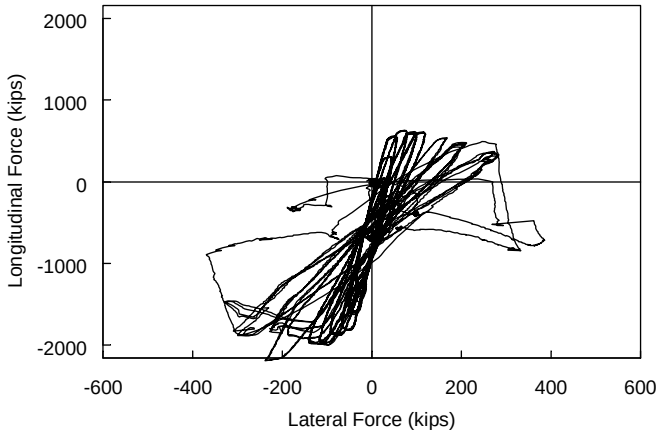

(a) Longitudinal Force versus Lateral Force

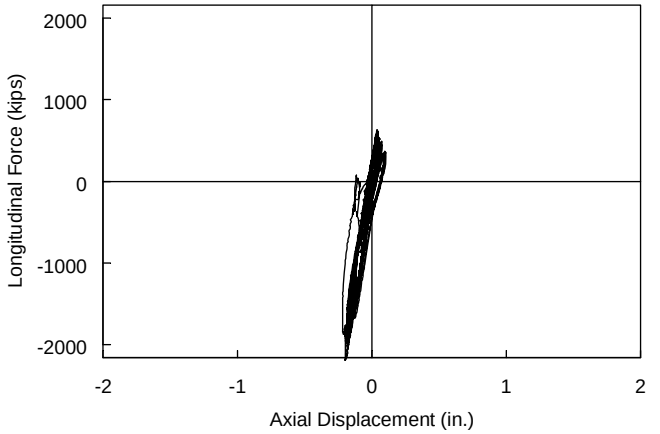

(b) Longitudinal Force versus Column Axial Displacement

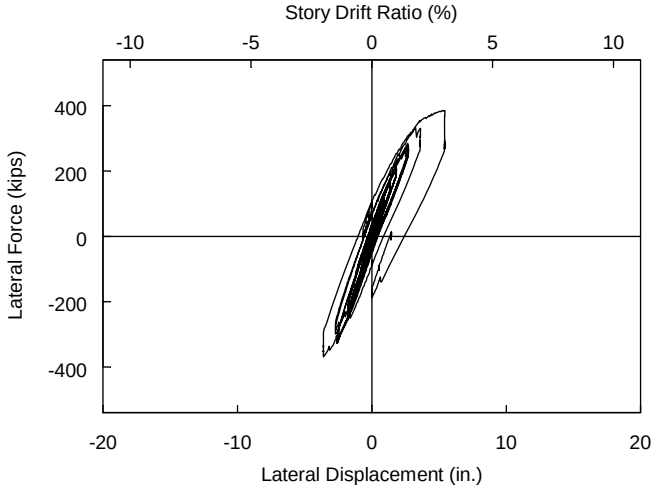

(c) Lateral Force versus Lateral Displacement

Figure 4.69 Specimen W14×370-35: Force-Displacement Response

5. COMPARISON OF EXPERIMENTAL RESULTS

5.1 Flange Yielding

For all specimens only minor yielding was observed at a story drift of 1.5%, the maximum expected drift from the nonlinear time-history analysis described in Chapter 2. The extent of flange yielding, as evidenced by flaking of the whitewash, measured after testing is shown in Figure 5.1 for all specimens. The combined compressive axial load and bending resulted in increased compressive stresses on one flange (referred to as the compression flange) and the tensile axial load and bending resulted in increased tensile stresses on the opposite flange. For this testing the compressive axial load was greater than the tensile axial load due to the gravity load offset. Consistent with this applied loading the compression flange yielded length was observed to be greater than the tension flange yielded length. For the $0.75P_y$ specimens the compression flange yielded length was approximately two times the column depth. It is noted that this is two times the normally assumed plastic hinge length for moment frame beams.

5.2 Local Buckling

Flange local buckling was observed for all specimens with the exception of Specimen W14×370-35 (which failed at 3% drift before any local buckling could occur). This flange local buckling was observed to occur in a symmetric mode (i.e. deformation of the flange on opposite sides of the web was in the same direction). No web local buckling was observed for any of the specimens. During testing it was observed that flange local buckling forming on the negative drift excursion would fully straighten on the following positive drift excursion and visa-versa. This cyclic straightening continued to occur until about 8% drift when the buckled amplitude would only partially straighten on the subsequent opposite drift excursion. Figure 5.2 shows a comparison of flange local buckling photos for the different specimens at -6% drift and Figure 5.3 at -8% drift. The relatively small amplitude of flange local buckling at -6% drift (more than three times the maximum drift from the analysis of Chapter 2) provided an indication that column strength degradation due to local buckling is not expected to be of critical importance for the seismic design of the tested column sections. This may not be the

case, however, for deep columns which have higher web slenderness than the W14 sections tested.

5.3 *P-M* Interaction and Moment versus Drift Response

Figures 5.4 to 5.7 show a comparison of the *P-M* interaction for all tested specimens. The *P-M* test data and the established *P-M* interaction surface agreed well with each other. Significant cyclic overstrength was observed between the test data and the *P-M* interaction surface based on nominal material properties. The overstrength tended to be higher for heavier sections with a smaller width-thickness ratio.

The moment versus drift response for all specimens is compared in Figures 5.8 to 5.11. Recall that the discrete points on the figures indicate where the combined axial load and drift targets were reached. The points on the positive drift side that show a significantly reduced capacity occurred after partial or complete fracture of the specimen. The overall moment versus drift response was very similar for each specimen due to the sequence in which the load was applied. Recall that for 2% drift and beyond in Loading Scheme C lateral displacement was first applied until the target drift was reached and then axial load was increased to the target value. The points included in the moment versus drift plots represent the actual behavior of interest in this study. By comparing the results from, for example, Figure 5.9(b and c) the reduced moment capacity due to increased axial load is evident.

5.4 Drift Capacity

Figure 5.12 provides a comparison of moment versus drift response for the compressive axial load target points for the five specimens tested using Loading Scheme C. The reduced moment capacity from increased axial load is evident from Figure 5.12(b and c) and (d and e). It was also observed that increasing the column section weight increased the story drift at which degradation in moment capacity occurred. It is assumed that this was due to reduced influence of local buckling for the stockier column sections. Table 5.1 provides the drift capacities defined assuming an allowable 10% reduction from peak moment resistance. Drift capacities of 7% to 9% were more than four times

the expected BRBF story drift from earthquake nonlinear time-history analysis. These drift capacities correspond to a ductility of approximately 10.

Table 5.1 Drift Capacity

Specimen Designation	Drift Capacity
W14×132-75	7%
W14×176-55	9%
W14×176-75	8%
W14×233-35	8%
W14×233-55	>8%

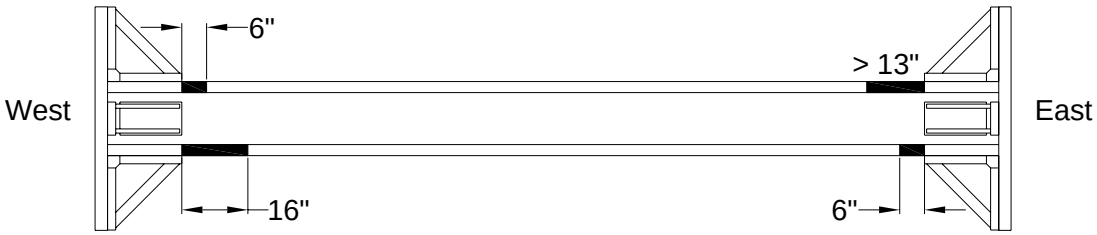

(a) W14×132-35 (6% Drift)

(b) W14×132-55 (8% Drift)

(c) W14×132-75 (10% Drift)

Figure 5.1 Extent of Flange Yielding

(d) W14×176-35 (10% Drift)

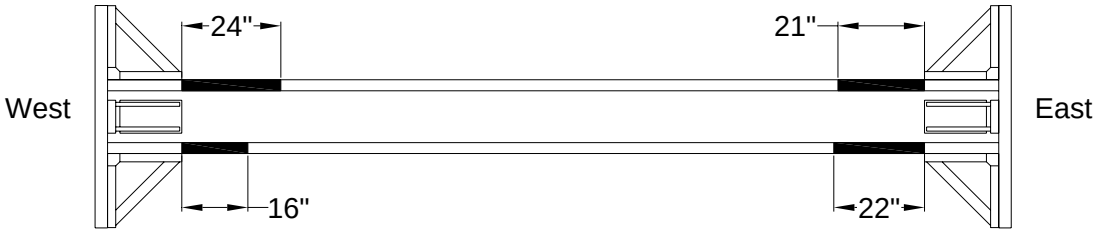

(e) W14×176-55 (10% Drift)

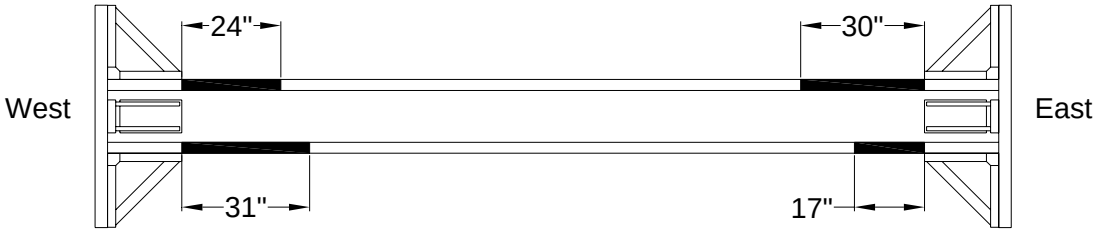

(f) W14×176-75 (10% Drift)

Figure 5.1 Extent of Flange Yielding (cont.)

(g) W14×233-35 (8% Drift)

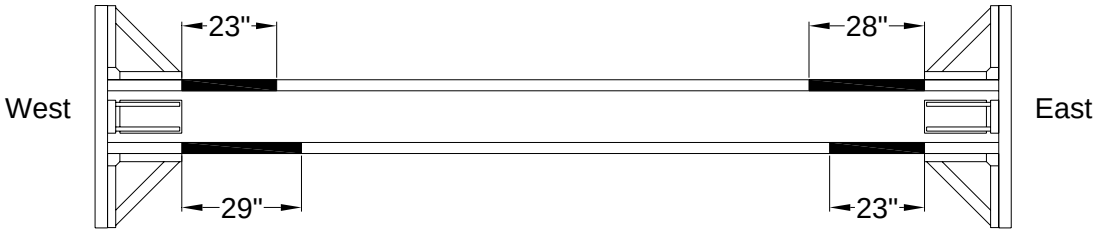

(h) W14×233-55 (8% Drift)

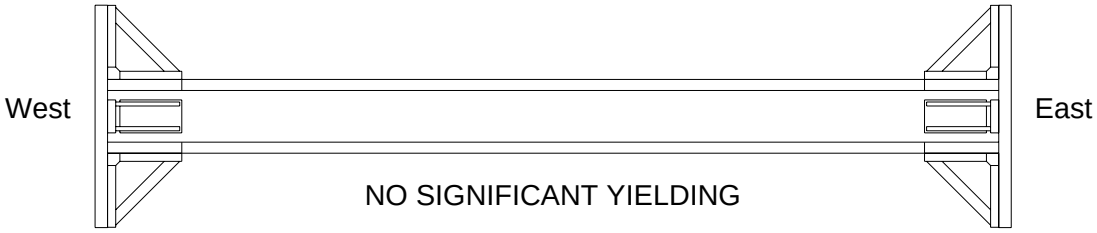

(i) W14×370-35 (2% Drift)

Figure 5.1 Extent of Flange Yielding (cont.)

$0.35P_y$ $0.55P_y$ $0.75P_y$

(a) W14×135-35

(b) W14×135-55

(c) W14×135-75

(d) W14×176-35

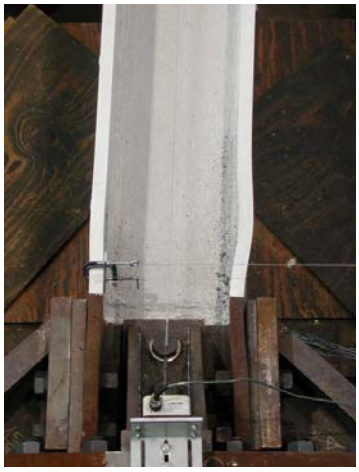

(e) W14×176-55

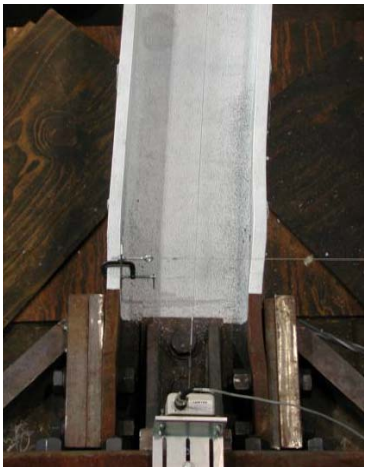

(f) W14×176-75

(g) W14×233-35

(h) W14×233-55

Figure 5.2 Comparison of Flange Local Buckling at -6% Drift

$0.35P_y$ $0.55P_y$ $0.75P_y$

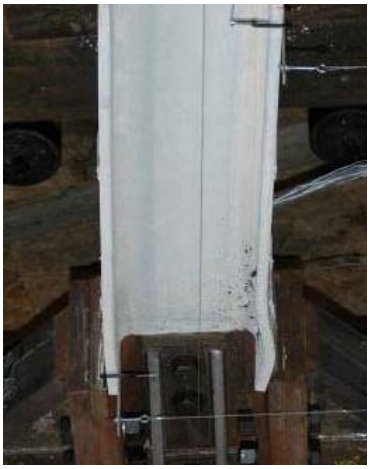

(a) W14×135-55

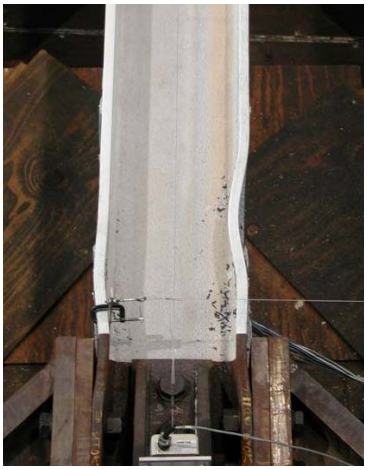

(b) W14×135-75

(c) W14×176-35

(d) W14×176-55

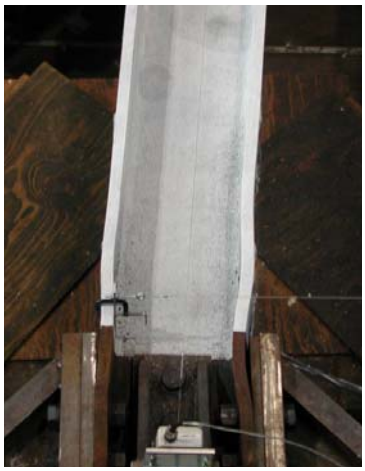

(e) W14×176-75

(f) W14×233-35

(g) W14×233-55

Figure 5.3 Comparison of Flange Local Buckling at -8% Drift

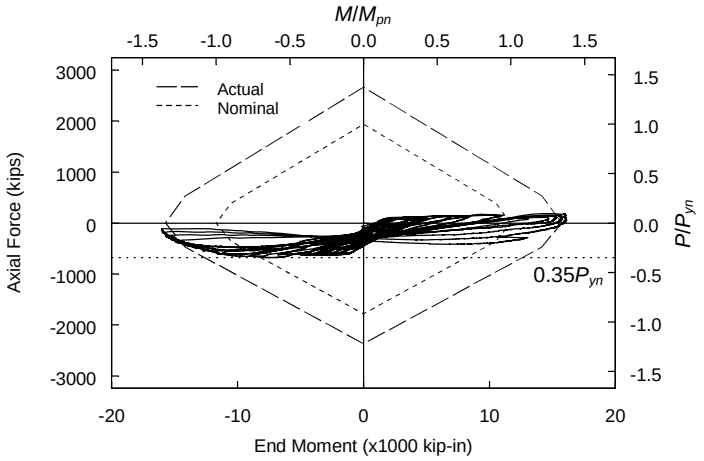

(a) 35%P_y

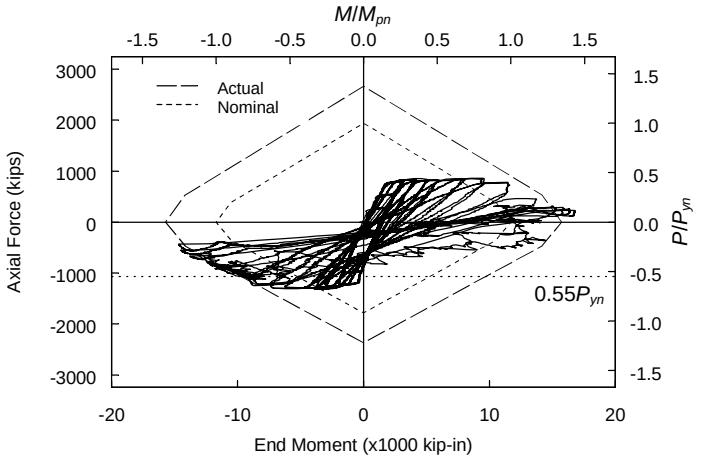

(b) 55%P_y

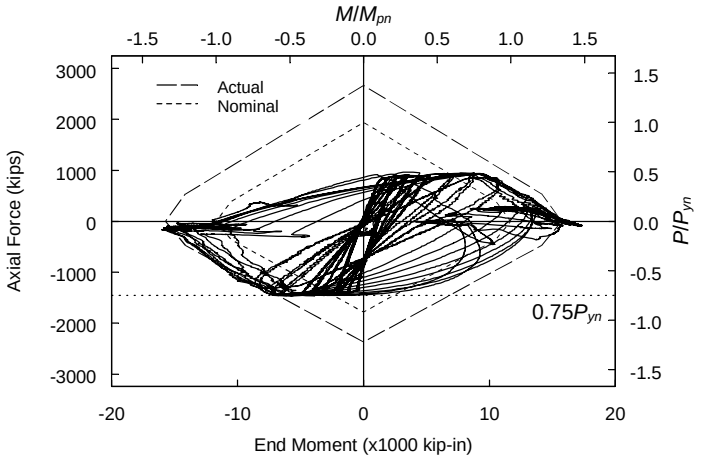

(c) 75%P_y

Figure 5.4 Specimen W14×132: Comparison of *P*-*M* Interaction

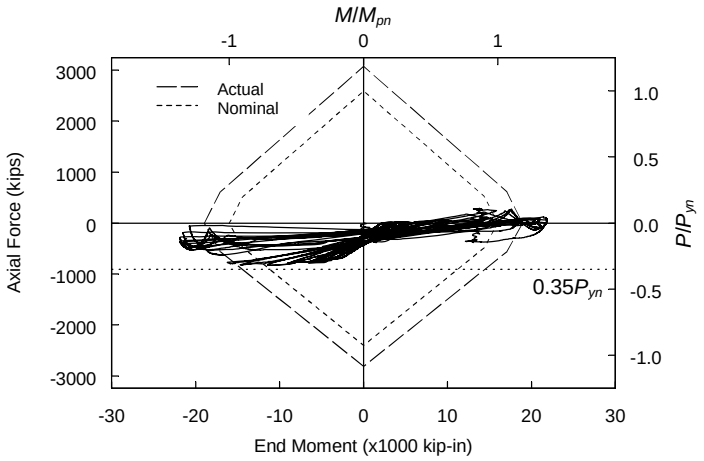

(a) 35%P_y

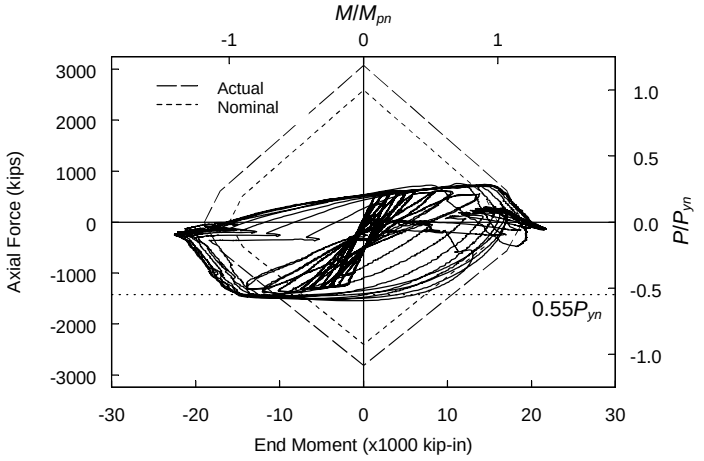

(b) 55%P_y

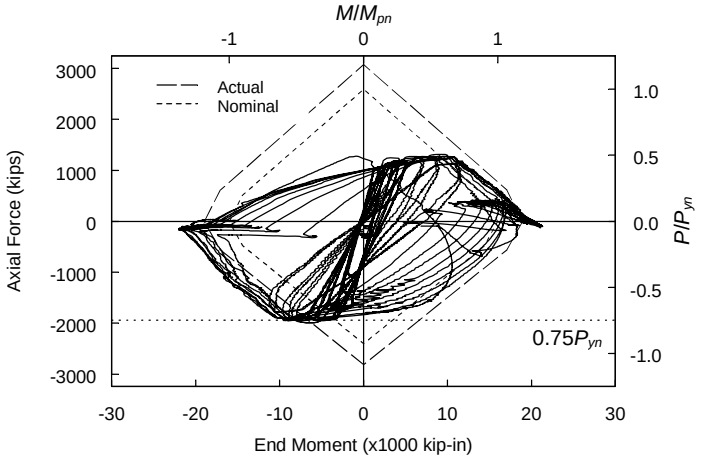

(c) 75%P_y

Figure 5.5 Specimen W14×176: Comparison of *P*-*M* Interaction

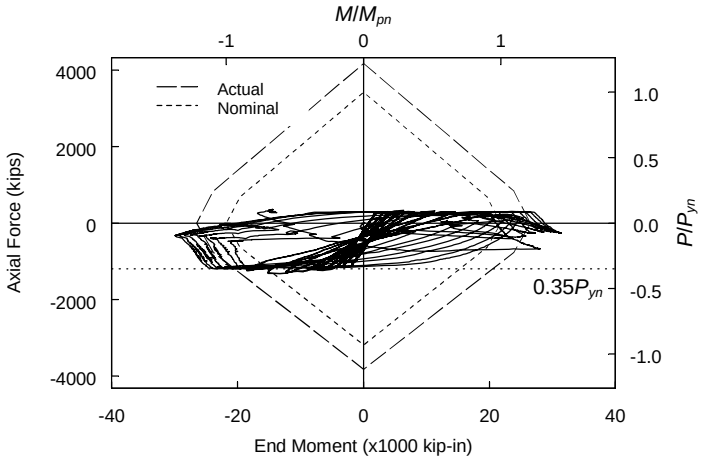

(a) 35%P_y

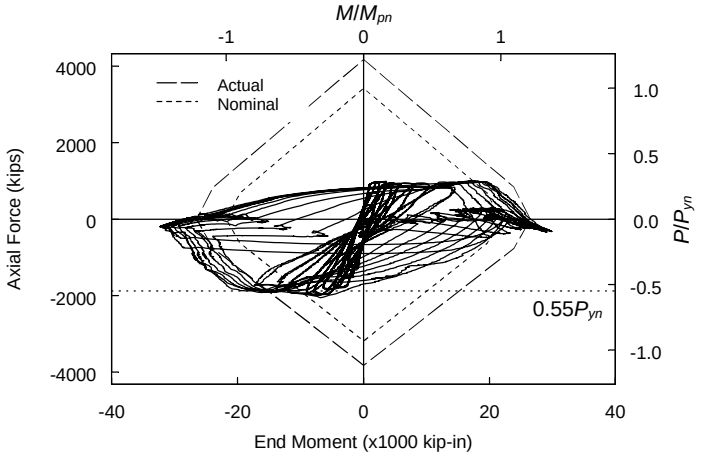

(b) 55%P_y

Figure 5.6 Specimen W14×233: Comparison of *P*-*M* Interaction

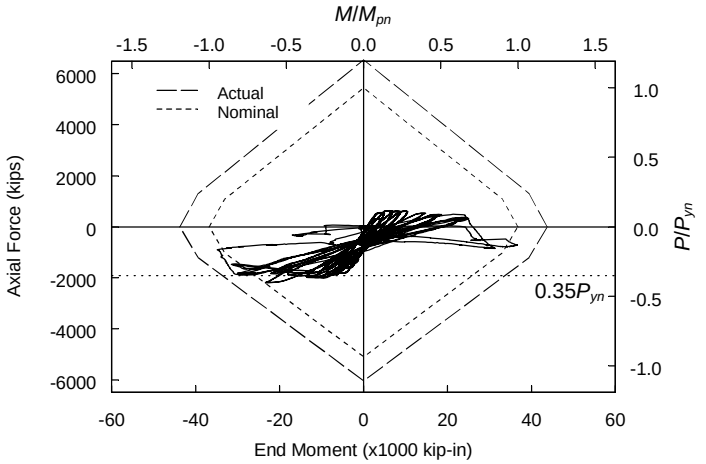

Figure 5.7 Specimen W14×370-35: *P*-*M* Interaction

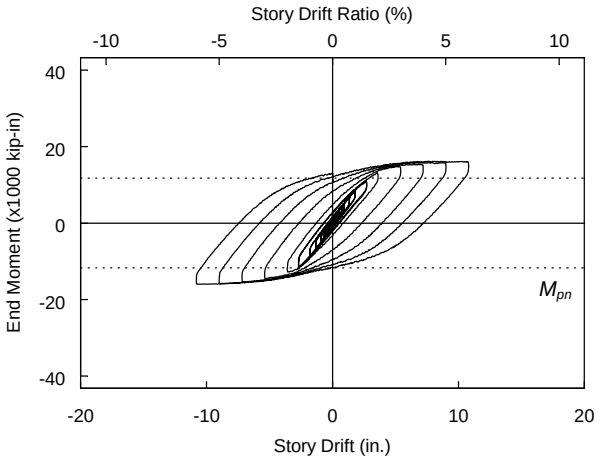

(a) 35%P_y

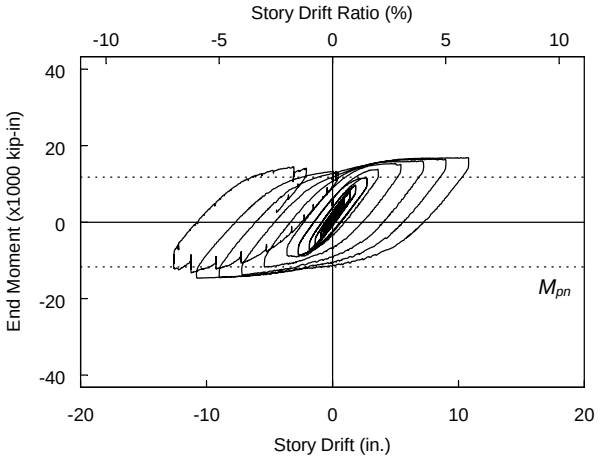

(b) 55%P_y

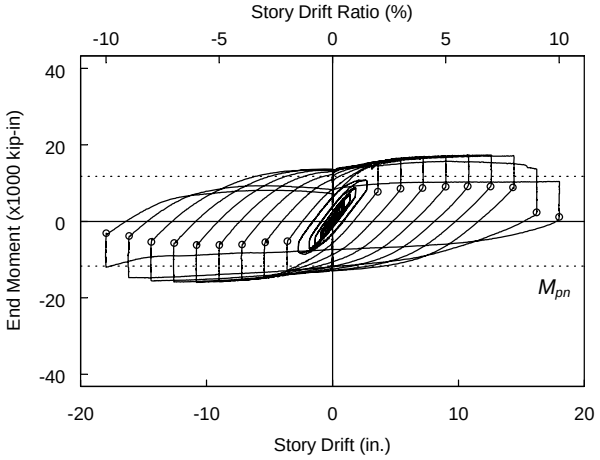

(c) 75%P_y

Figure 5.8 Specimen W14×132: Comparison of End Moment versus Drift Response

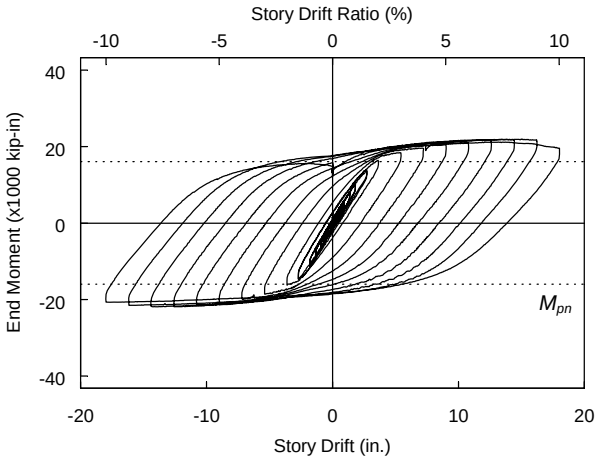

(a) 35%P_y

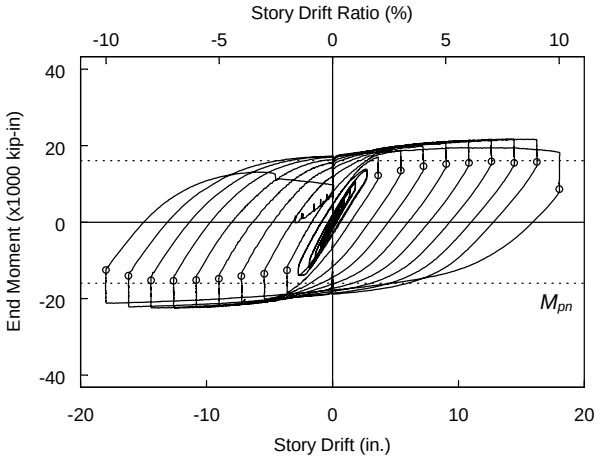

(b) 55%P_y

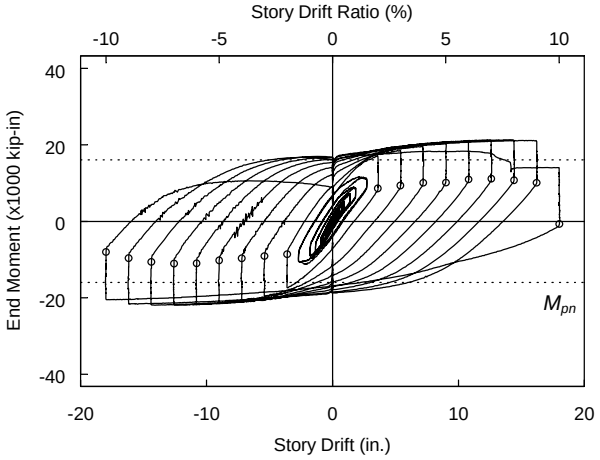

(c) 75%P_y

Figure 5.9 Specimen W14×176: Comparison of End Moment versus Drift Response

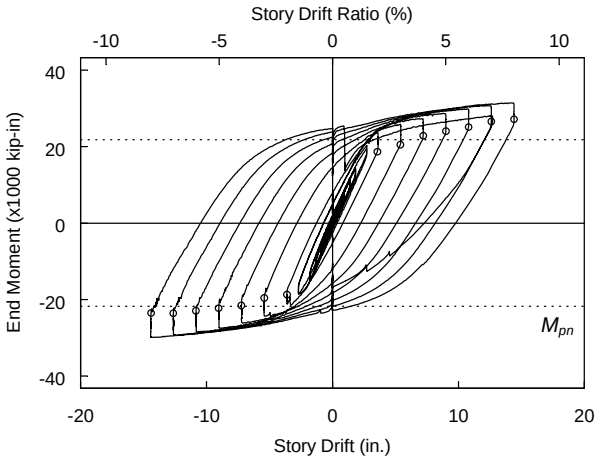

(a) 35%P_y

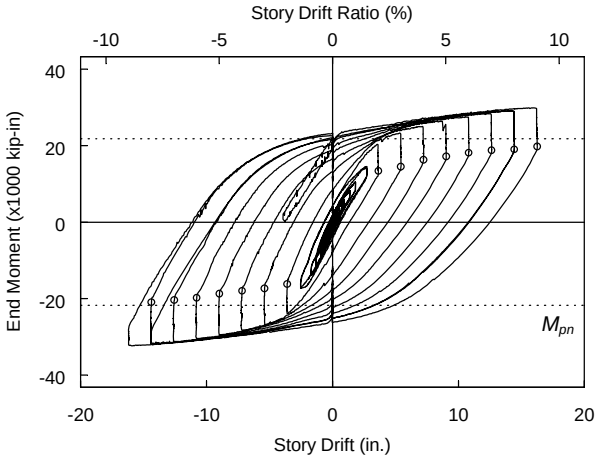

(b) 55%P_y

Figure 5.10 Specimen W14×233: Comparison of End Moment versus Drift Response

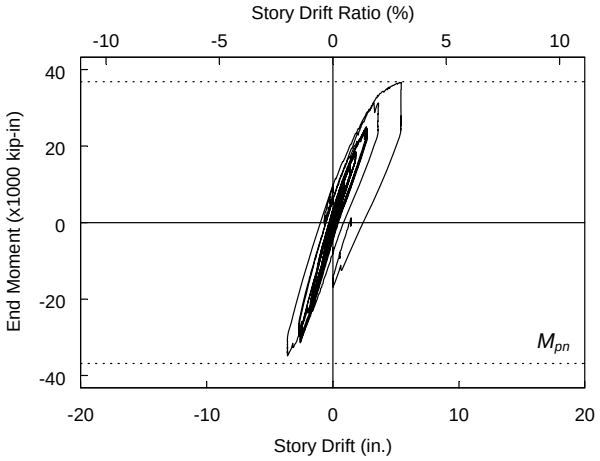

Figure 5.11 Specimen W14×370-35: End Moment versus Drift Response

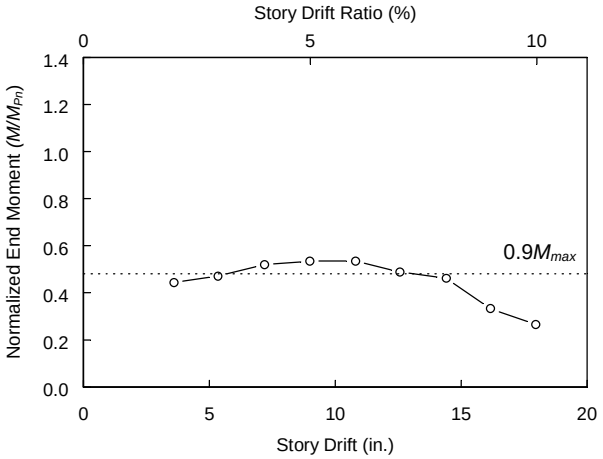

(a) W14×132-75

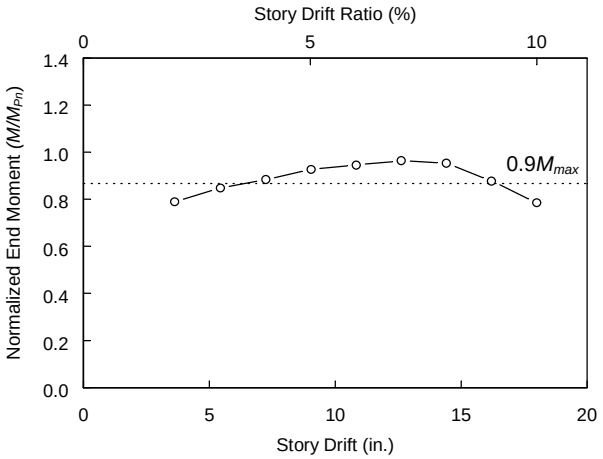

(b) W14×176-55

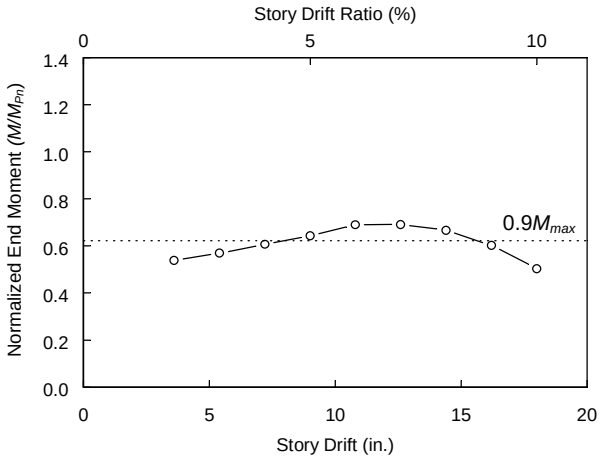

(c) W14×176-75

Figure 5.12 Comparison of Target Points End Moment versus Drift Response

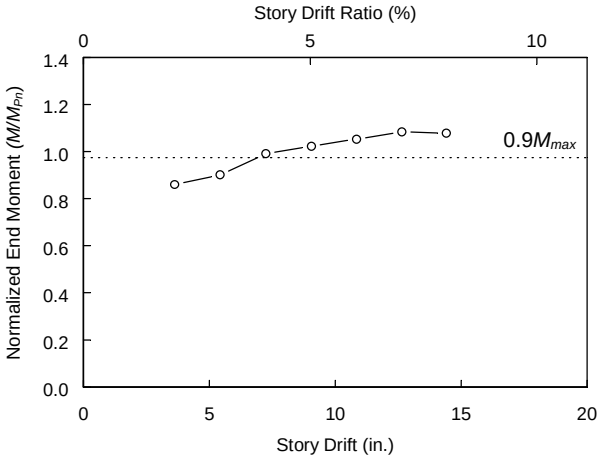

(d) W14×233-35

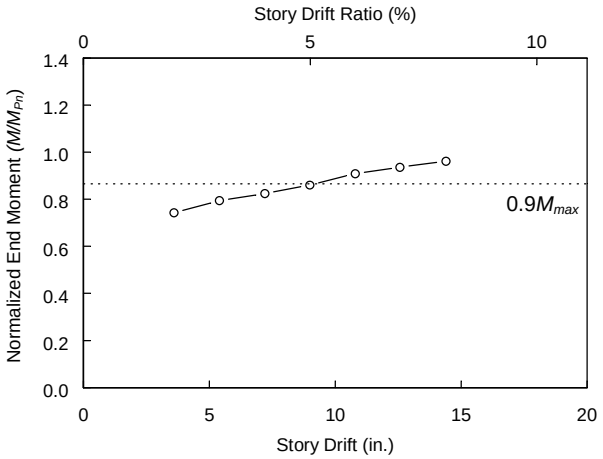

(e) W14×233-55

Figure 5.12 Comparison of Target Points End Moment versus Drift Response (cont.)

6. ANALYTICAL STUDY OF TEST SPECIMENS

6.1 Modeling Techniques

The finite element program ABAQUS (ABAQUS Inc. 2005) was used to model the steel column specimens. Models predict global behavior, yielding, and strength degradation resulting from local buckling at large drifts. Standard shell elements were used in the models. The general-purpose shell element type used (ABAQUS S4R) has four nodes with six degrees of freedom per node, 3 translational and 3 rotational. This element allows for transverse shear deformations, accounts for finite membrane strains, and will allow for changes in thickness, making it suitable for large-strain analysis.

6.2 Boundary Conditions and Column Geometry

The boundary conditions simulated those used for experimental testing of the steel column specimens. Only the 15 ft clear length of the specimens was modeled. A fixed connection was used at both ends of the column to simulate the restraint provided by the column base plate and the flange and web haunches (see Figure 3.1). Consistent with the test set-up no additional lateral bracing was provided. Figure 6.1 shows the column model boundary conditions and finite element mesh.

6.3 Material Properties

A992 steel was specified for the test specimen column sections. In the analysis, it was assumed that the yield strength for all the steel material was 54 ksi. An elastic modulus of 29,000 ksi and a Poisson's ratio of 0.3 were specified for the elastic material properties. The plasticity in the models was based on a von Mises yield surface and associated flow rule. The plastic hardening was defined by a nonlinear kinematic hardening law.

Data from cyclic coupon testing performed at Lehigh University (Kaufmann et al. 2001) was used to determine appropriate values for the plasticity material model parameters. Steel C from the Lehigh study was selected as the prototype material. Steel C had a yield strength of 54 ksi and an ultimate strength of 72 ksi under monotonic testing, which was judged to be representative of the A992 steel members used for laboratory specimen fabrication. Figure 6.2 shows results of cyclic coupon testing of the

prototype material performed at ±4% strain. The shape of the stabilized curve was used to determine the parameters that define the plasticity model.

6.4 Loading Protocol and Computational Algorithm

Models were subjected to one of three loading sequences. The first loading sequence was a monotonic loading consisting of an initial application of the target axial load followed by lateral displacement to the target drift. Separate monotonic loading cases were run for both the tension and compression target axial loads. The second loading sequence was cyclic and consisted of using recorded axial load and lateral displacement from experimental testing as the input loading for analysis. The third loading sequence, termed the ideal loading sequence consisted of application of simultaneous, in-phase axial load and lateral displacement, which achieved the targets at the same time. This type of loading sequence controlling the axial load and lateral displacement would have been ideal for experimental testing but load control for such a specimen is considered unsafe for the equipment and personnel.

Lateral displacement and axial load were imposed at the column end loading point. A rigid constraint was imposed on edges at the column ends to prevent stress concentrations at the loading and reaction points. The forces, moments, and displacements associated with the applied loading along with various stress and strain components and the deformed shape were obtained from the computer analysis.

6.5 Effect of Residual Stresses

Model W14×132 was used to investigate the effect of residual stresses on the performance of the column specimens subjected to combined high axial load and lateral drift. Residual stresses exist in an non-loaded wide-flange steel section and primarily result from uneven cooling after hot rolling of the section. A simplified linear residual stress distribution is shown in Figure 6.3(a). The maximum residual stress was assumed to be 12 ksi (Salmon and Johnson 1996). This self-equilibrating residual stress distribution was applied to the model as an initial stress condition as shown in the axial stress contour plot in Figure 6.3(b).

A comparison of the monotonic moment versus drift response for Model W14×132 at the three target axial load levels with and without residual stresses is shown in Figure 6.4. It was observed that residual stresses did not have a significant effect on the monotonic behavior of this model. Model W14×132-75 with and without residual stresses was subjected to the loading history from experimental test data. Figure 6.5 provides a comparison of the *P-M* interaction and moment versus drift response and again shows that the effect of residual stresses on the performance of this model was negligible.

6.6 Analysis Results of W14 Column Models

6.6.1 Monotonic Loading Sequence Results

Monotonic loading of the models was conducted to provide a simple approximation of cyclic behavior before performing a more computationally intensive cyclic analysis. Moment versus drift response (see Figure 6.6) was in general agreement with behavior observed during testing. Increase of the axial load level caused a corresponding decrease in moment capacity. Also, consistent with observations from the experimental results Figure 6.6(a and b) shows a softening of the moment versus drift at large negative drifts for Models W14×132 and W14×176. This softening behavior was not observed for Specimens W14×233 and was not observed in the monotonic response of Model W14×233 or Model W14×370.

6.6.2 Comparison of Specimen and Model Results

A comparison of test specimen and model *P-M* interaction is provided in Figures 6.7 to 6.10. The model response was from the loading sequence using recorded axial load and lateral displacement from experimental testing as the input loading for analysis. In general, good agreement was observed between the specimen and model responses. Models did tend to slightly overpredict the moment as compared with experimental results. Figures 6.11 to 6.14 compare the experimental and analytically predicted moment versus drift response. Discrete points shown on these figures again represent points where both the target axial load and drift were achieved. Good agreement was observed between the specimen and model moment versus drift response. Figures 6.15 to

6.18 show axial stress contour plots and the model deformed shapes at -5% drift for the loading history generated from test results. The figures show symmetric flange local buckling, which was consistent with tests. No web local buckling was observed (consistent with experimental results). The amplitude of flange local buckling was observed to decrease as the section weight increased. For Model W14×233 and Model W14×370 only very minor local buckling was observed.

6.6.3 Comparison of Results for Two Cyclic Loading Sequences

Figures 6.19 to 6.22 show a comparison of *P-M* interaction for models loaded with the loading history from test data and the ideal loading history (in-phase axial load and lateral displacement). Both loading sequences were observed to result in very similar *P-M* interaction response. The moment versus drift for the two loading sequences is shown in Figures 6.23 to 6.26. At first the results from the two different loading sequences did not appear to be well correlated. However, when the discrete points on the loading history from test plots were compared with the ideal loading history response plots reasonable agreement was observed. The correlation in response between models subjected to the two different cyclic loading histories provided an indication that Loading Scheme C, used for experimental testing, was a reasonable approximation of the more ideal in-phase axial load and lateral displacement loading sequence. The correlation also enabled extrapolation to other axial load levels and other column sections using the ideal loading sequence and confidence gained in the modeling techniques to reasonably predict experimentally observed behavior.

6.7 Analysis Results of W27 Column Models

The W14 columns tested were in general very stocky sections. Figure 6.27(a) shows that the flange slenderness for the W14×132 section was very close to the limiting value of 7.2 (AISC 2005a) but the web slenderness was less than half of the allowable value for a column with an axial load ratio, P/P_y equal to 0.75. In order to investigate the performance of columns with web slenderness closer to the limiting value a W27×146, W27×194, and W27×281 section were modeled and subjected to loading sequences similar to the W14 section models. Figure 6.27(b) shows that the flange and web

slenderness for the W27×146 section were very close to the current seismically compact limit.

6.7.1 Monotonic Loading Sequence Results

The monotonic moment versus drift for the W27 deep column models, shown in Figure 6.28, indicates more severe degradation in response than for the W14 column models (Figure 6.6). Increasing the section weight (reducing λ_{ps}) tended to reduce the degradation observed at large drifts. Figure 6.28 also shows softening of the response for large positive drifts, which was not observed for the W14 models.

6.7.2 Cyclic Loading Sequence Results

The cyclic loading sequence applied to these models was the ideal loading sequence, with in-phase axial load and lateral displacement. The *P-M* interaction along with the *P-M* interaction surface based on nominal material properties is shown in Figures 6.29 to 6.31 for Models W27×146, W27×194, and W27×281. It is noted that the shape of the *P-M* interaction appears to be somewhat inconsistent with the shape of the *P-M* interaction surface. Much larger moments were observed at high axial loads than would have been predicted by the interaction surface.

Figures 6.32 to 6.34 show the moment versus drift response for the W27 models. Six of the models did not complete the loading sequence to 10% drift due to severe local buckling and associated computational instability. The response of the W27 deep column models showed more significant degradation than for the W14 column sections tested. The reliability of deep columns under combined high axial load and drift demand should be the subject of further analytical and experimental investigation.

Figures 6.35 to 6.37 show axial stress contour plots and the model deformed shapes at -5% drift. Significant flange and web local buckling was observed for the W27×146 and W27×194 sections. Flange and web local buckling observed for Model W27×281 was much less severe. This is consistent with the improved moment versus drift response of this model as compared with the two lighter W27 sections modeled. Unlike the symmetric flange local buckling observed for the W14 test specimens and models the W27 models showed antisymmetric flange local buckling.

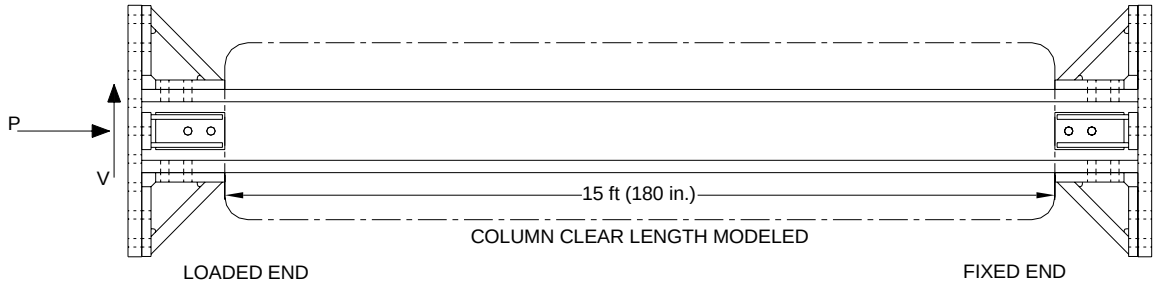

(a) Specimen Plan View

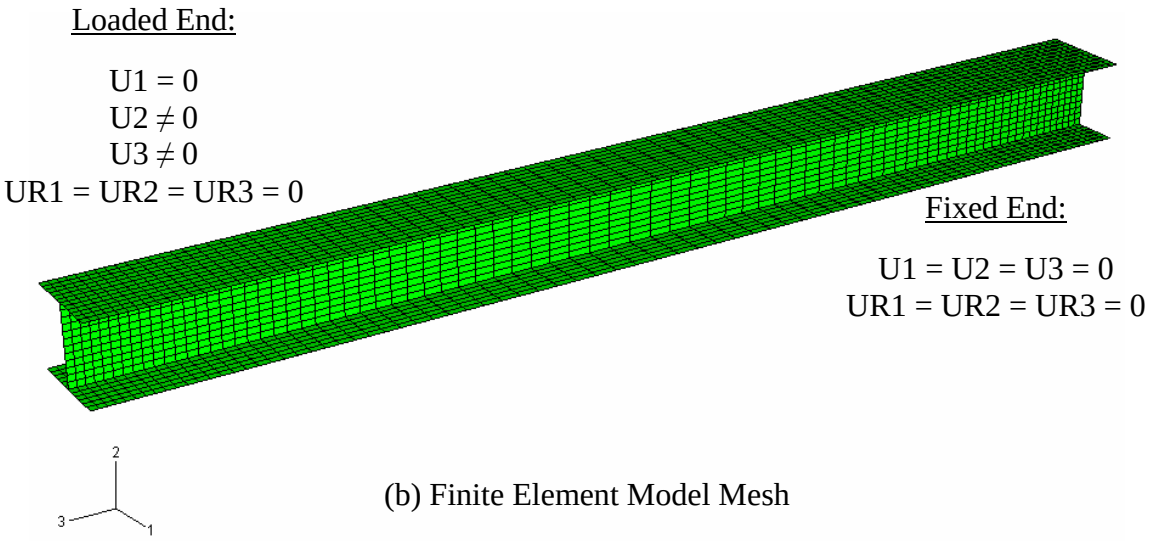

(b) Finite Element Model Mesh

Figure 6.1 Model Boundary Conditions and Geometry

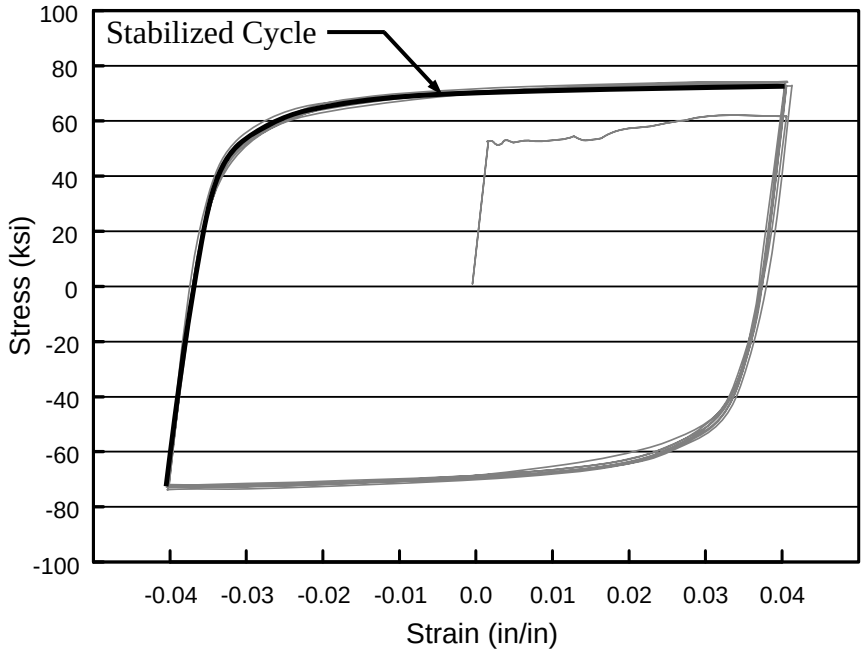

Figure 6.2 Cyclic Material Test Results (Kaufmann et al. 2001)

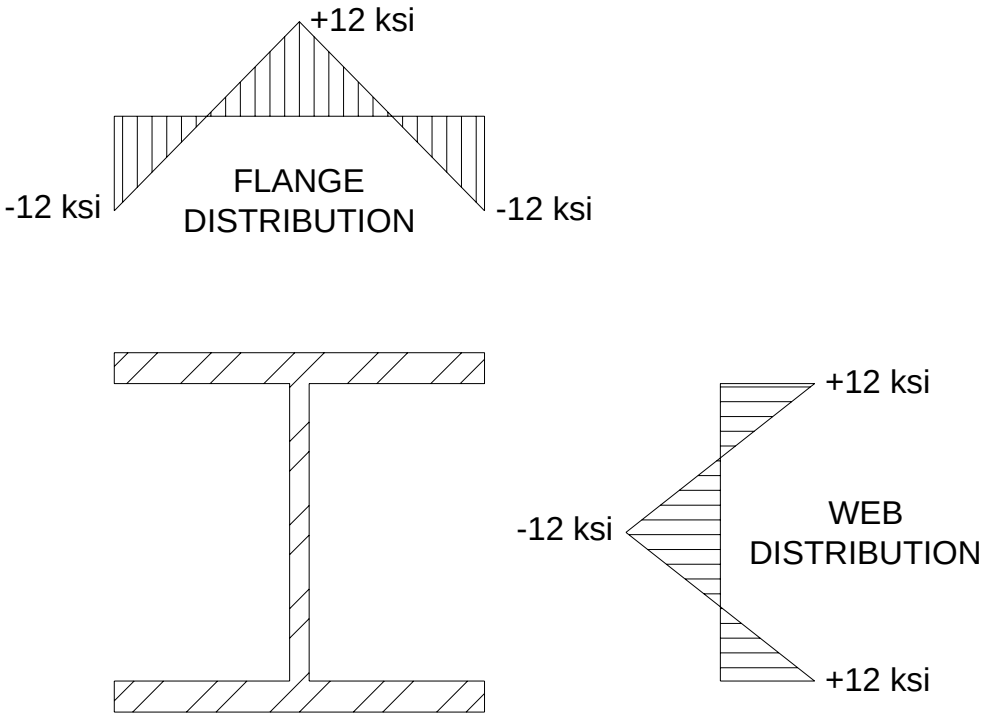

(a) Assumed Residual Stresses

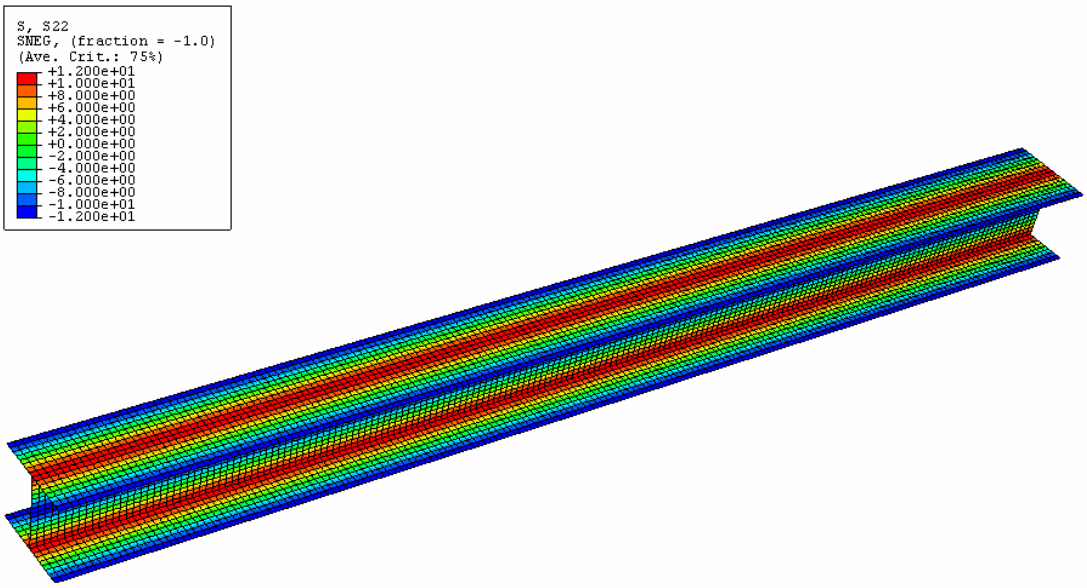

(b) Initial Model Residual Stresses

Figure 6.3 Residual Stress Distribution

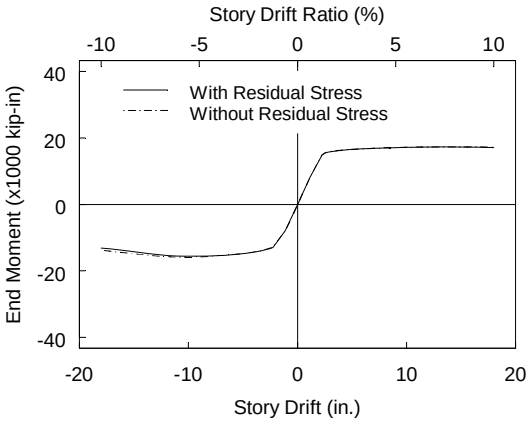

(a) 35%P_y

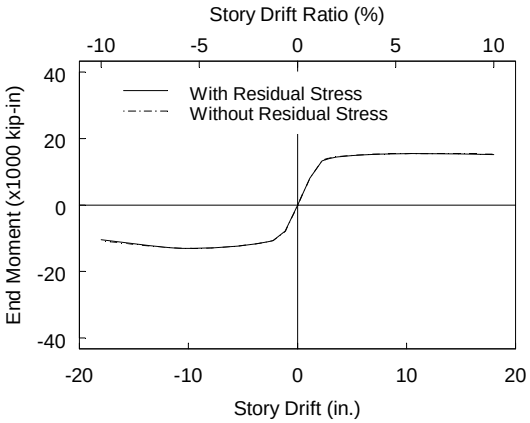

(b) 55%P_y

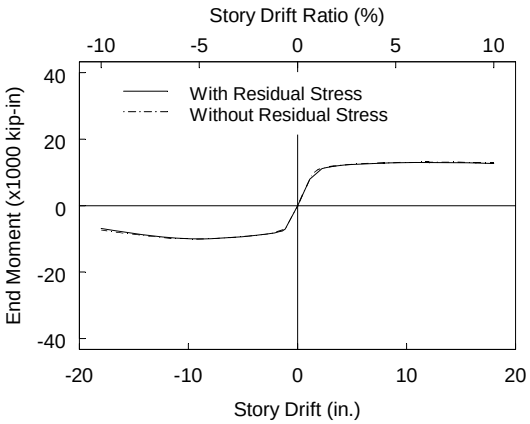

(c) 75%P_y

Figure 6.4 Comparison of the W14×132 Models Monotonic End Moment versus Drift Response with and without Residual Stresses

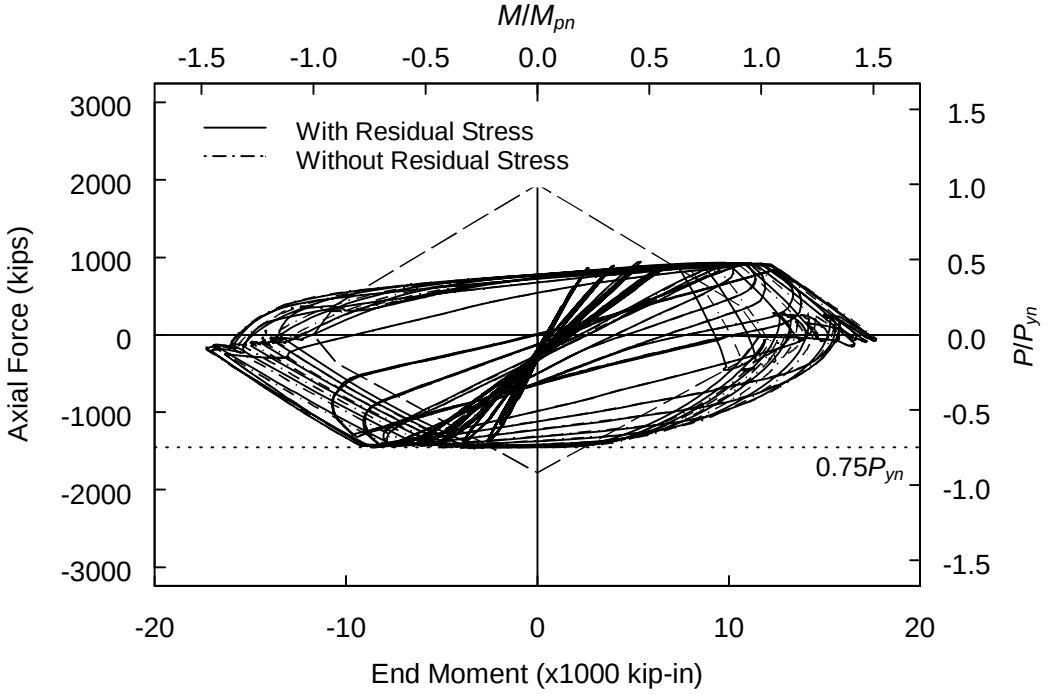

(a) *P*-*M* Interaction

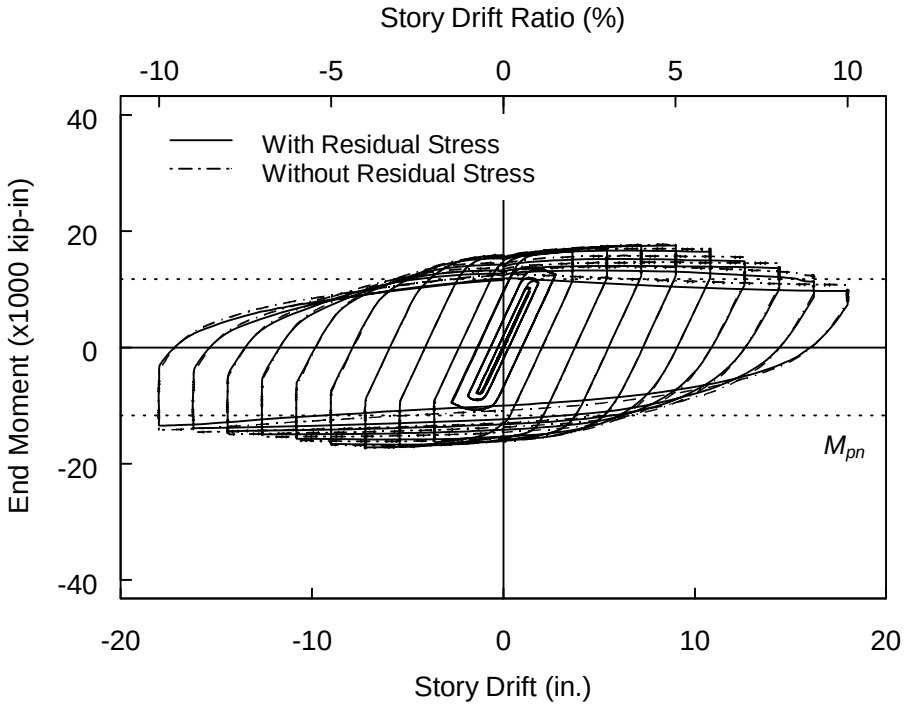

(b) End Moment versus Drift Response

Figure 6.5 Comparison of Model W14×132-75 Response with and without Residual Stresses

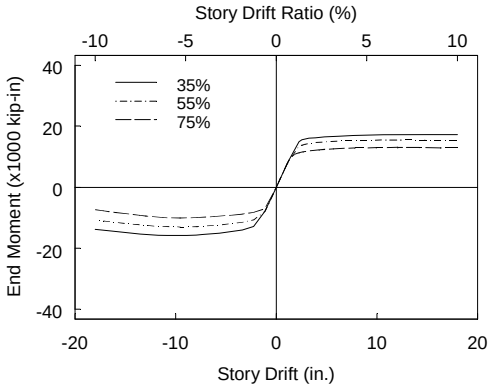

(a) W14×132

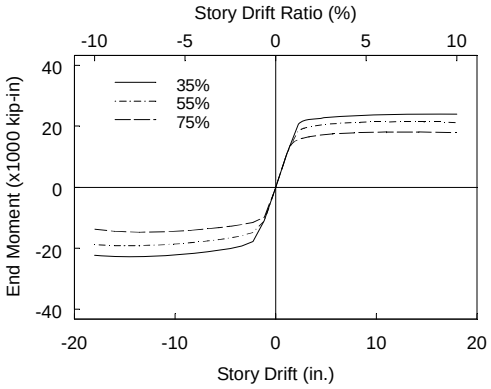

(b) W14×176

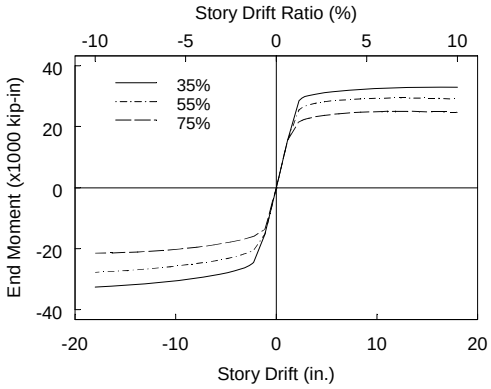

(c) W14×233

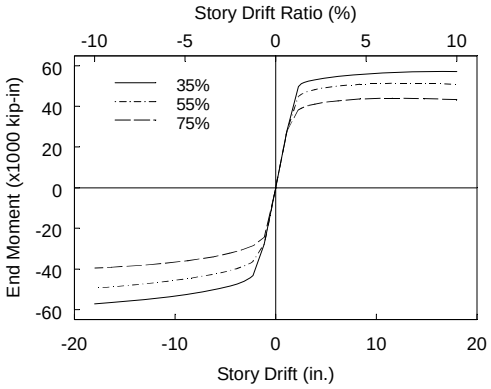

(d) W14×370

Figure 6.6 Comparison of W14 Column Models Monotonic End Moment versus Drift Response

Specimen Model

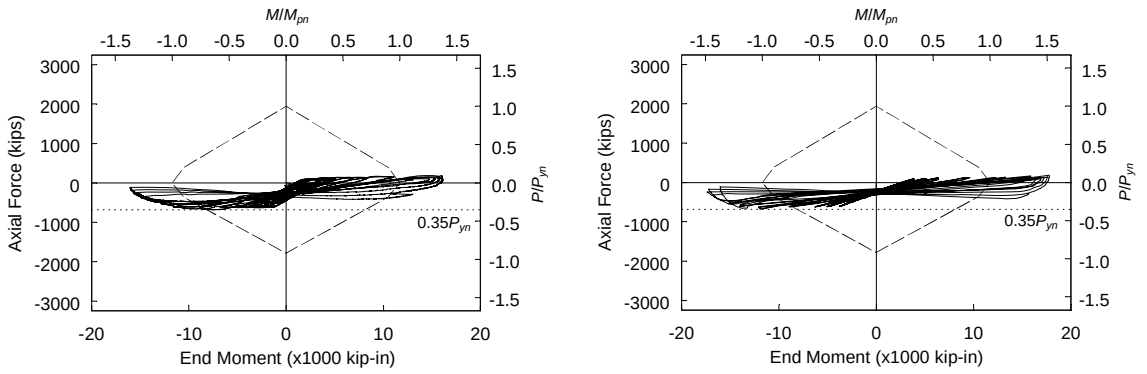

(a) 35%P_y

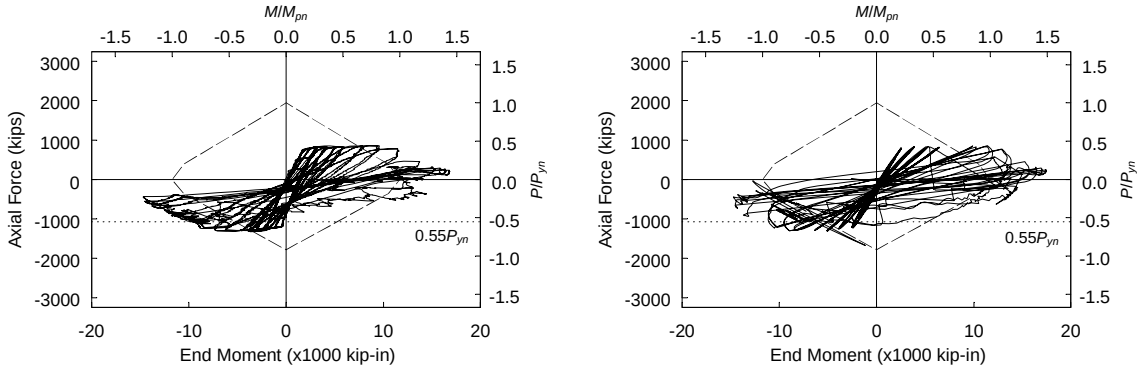

(b) 55%P_y

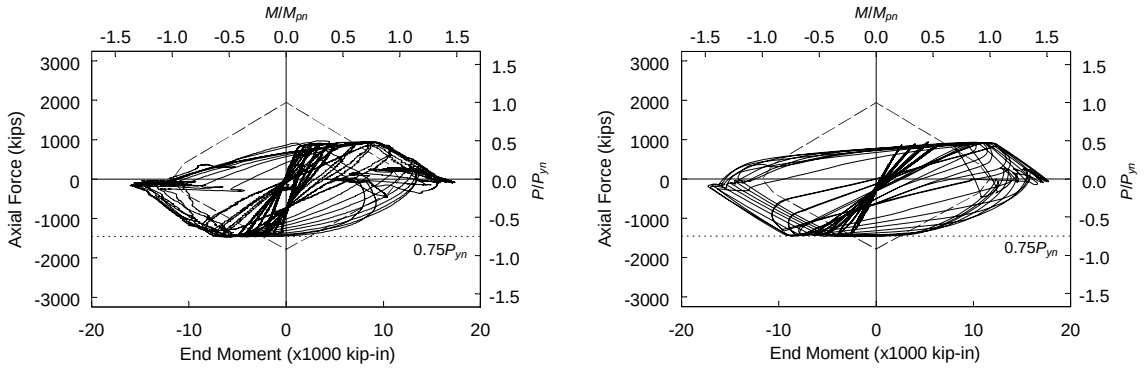

(c) 75%P_y

Figure 6.7 Model W14×132: Comparison of Specimen and Model *P*-*M* Interaction

Specimen Model

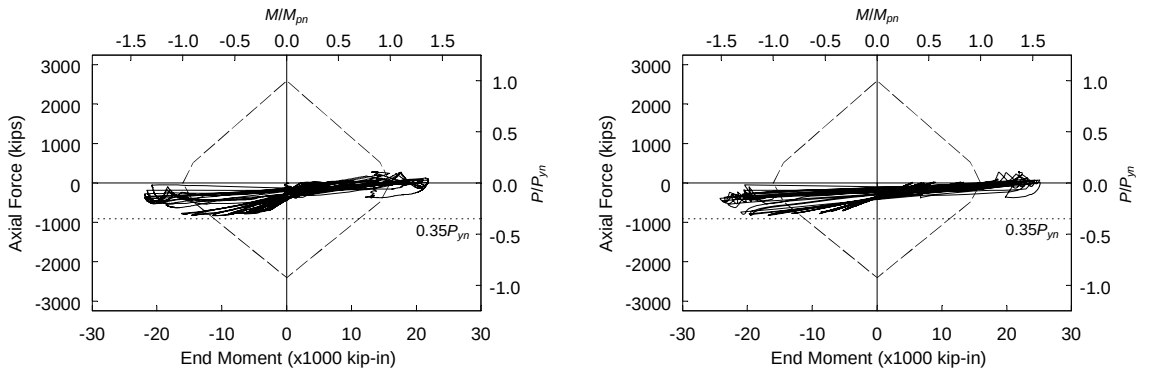

(a) 35%P_y

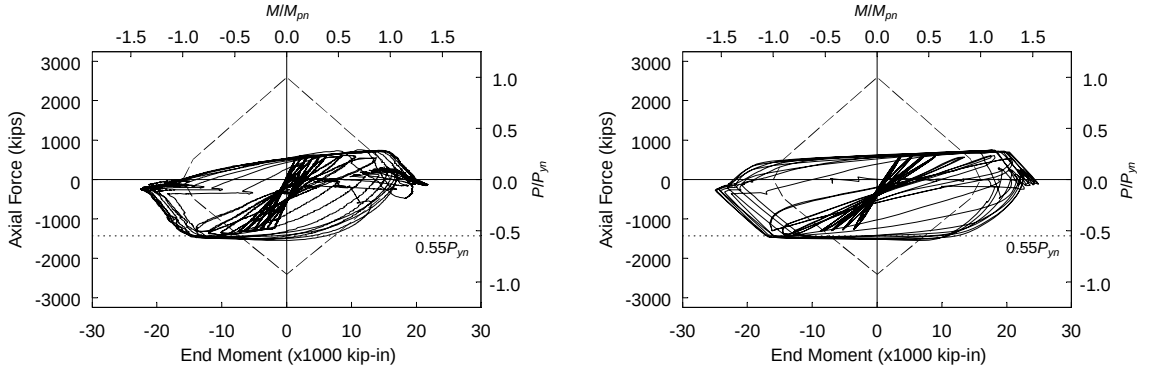

(b) 55%P_y

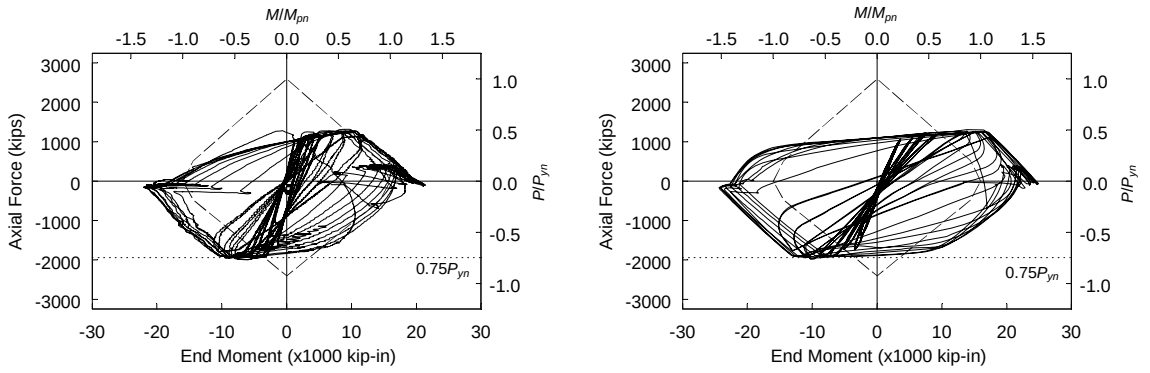

(c) 75%P_y

Figure 6.8 Model W14×176: Comparison of Specimen and Model *P*-*M* Interaction

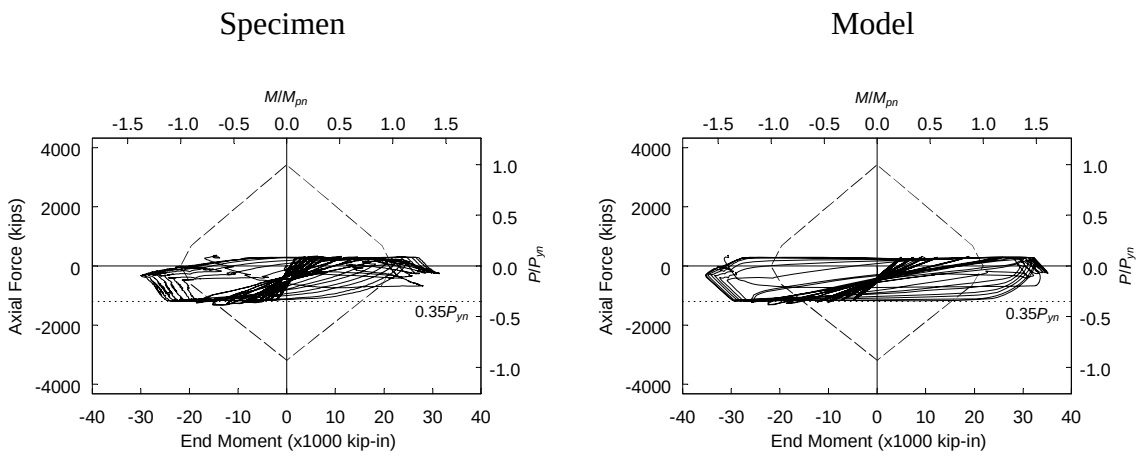

(a) 35%P_y

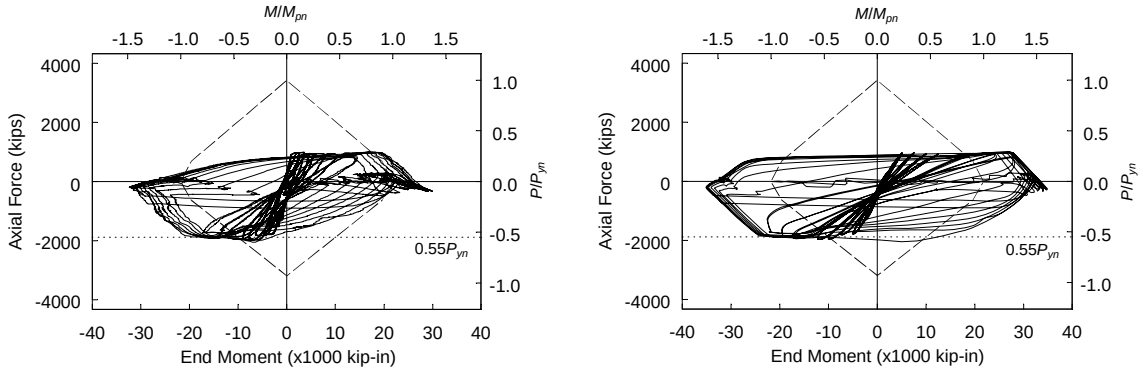

(b) 55%P_y

Figure 6.9 Model W14×233: Comparison of Specimen and Model *P-M* Interaction

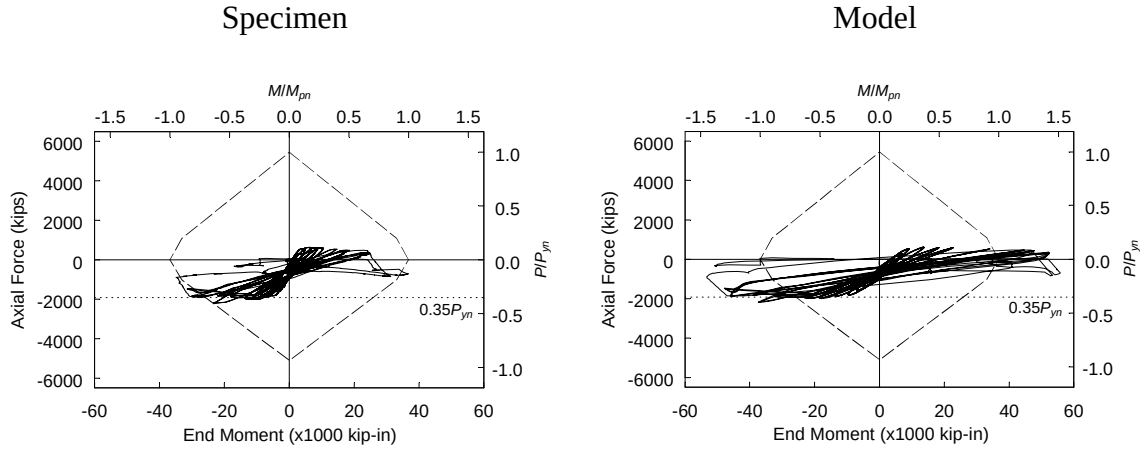

Figure 6.10 Model W14×370-35: Comparison of Specimen and Model *P-M* Interaction

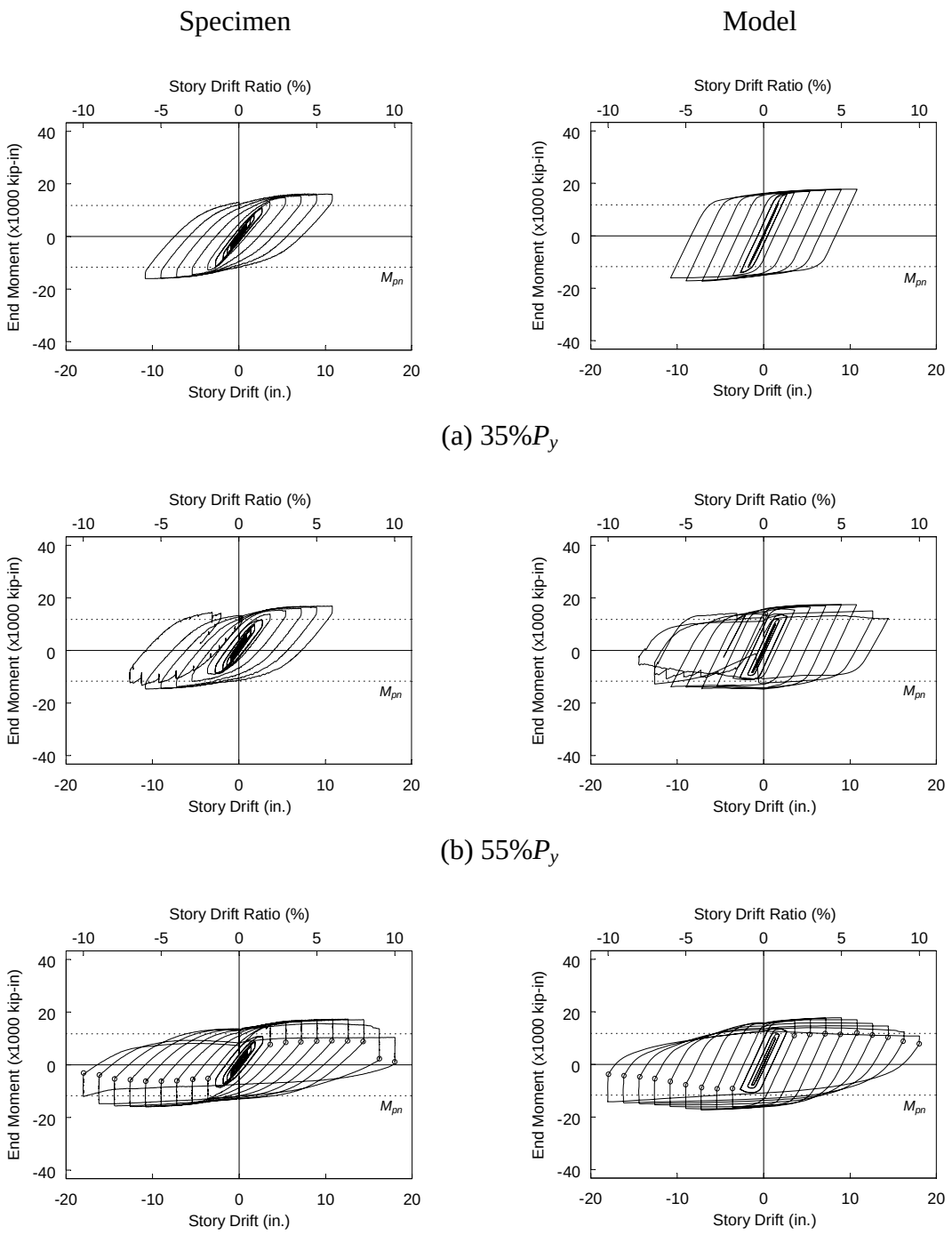

(a) 35%P_y

(b) 55%P_y

(c) 75%P_y

Figure 6.11 Model W14×132: Comparison of Specimen and Model End Moment versus Drift Response

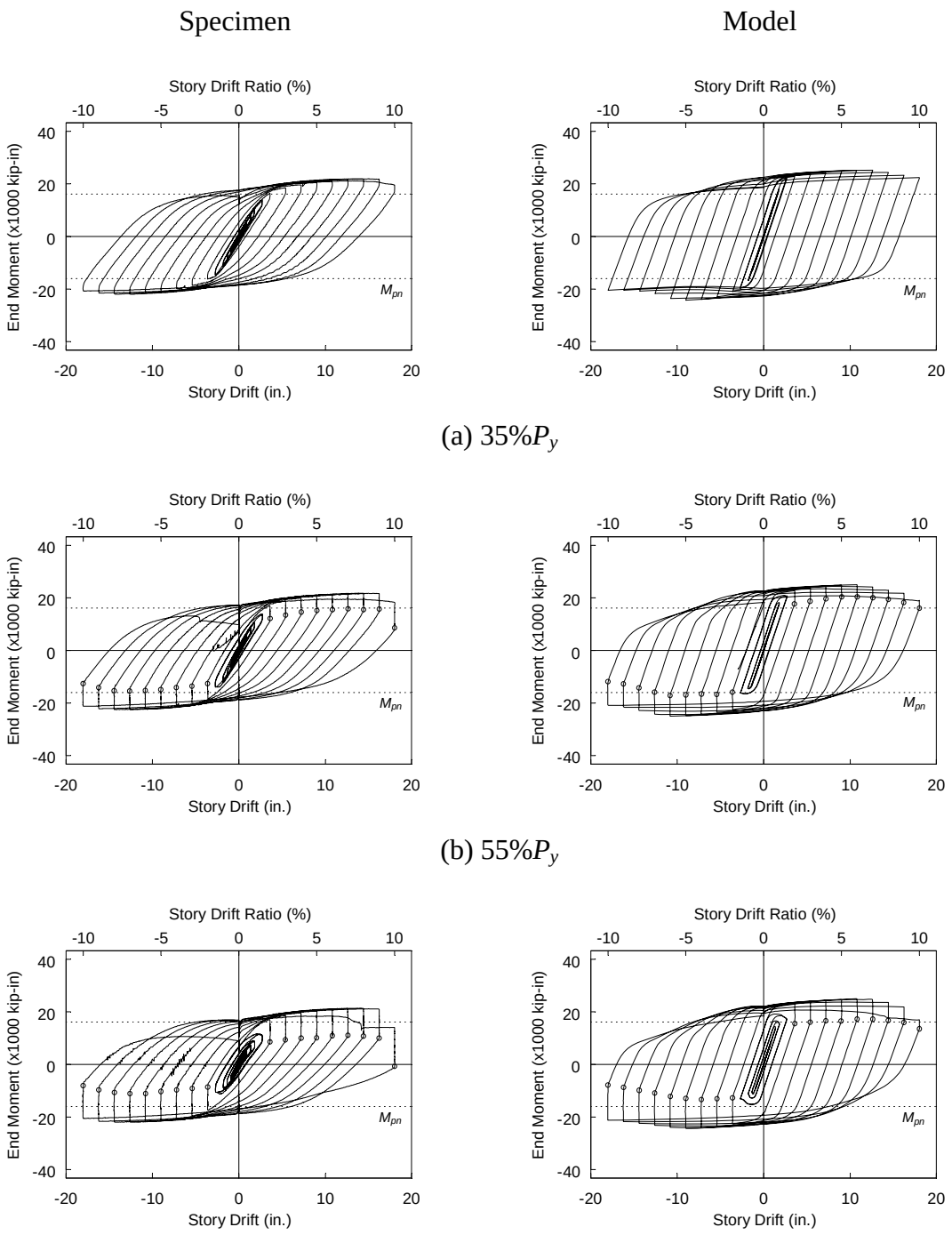

(a) 35%P_y

(b) 55%P_y

(c) 75%P_y

Figure 6.12 Model W14×176: Comparison of Specimen and Model End Moment versus Drift Response

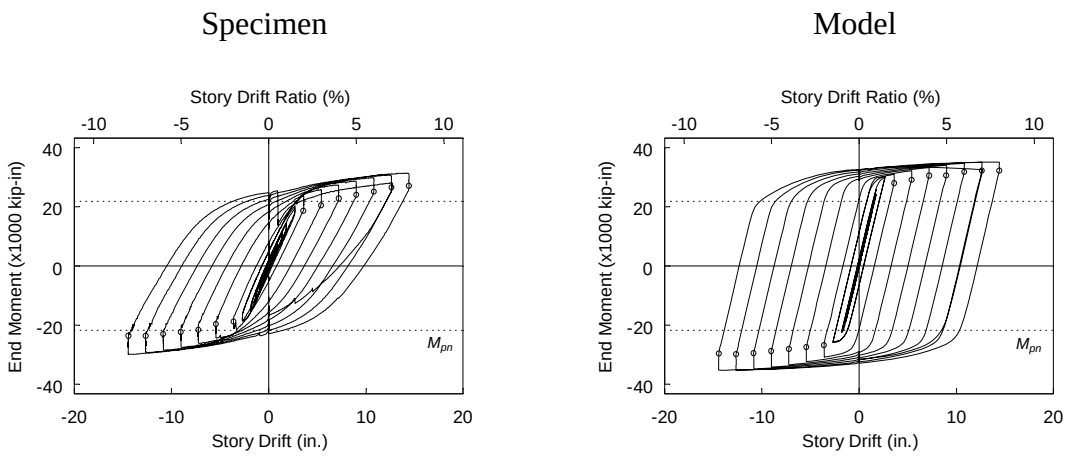

(a) 35%P_y

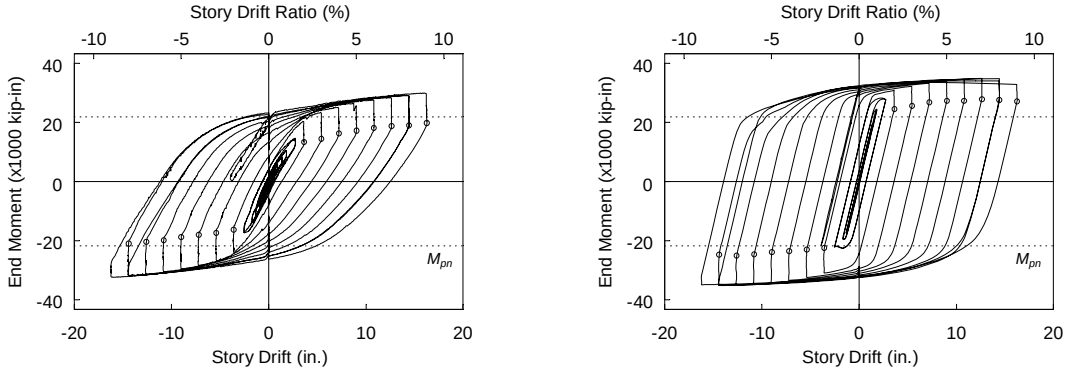

(b) 55%P_y

Figure 6.13 Model W14×233: Comparison of Specimen and Model End Moment versus Drift Response

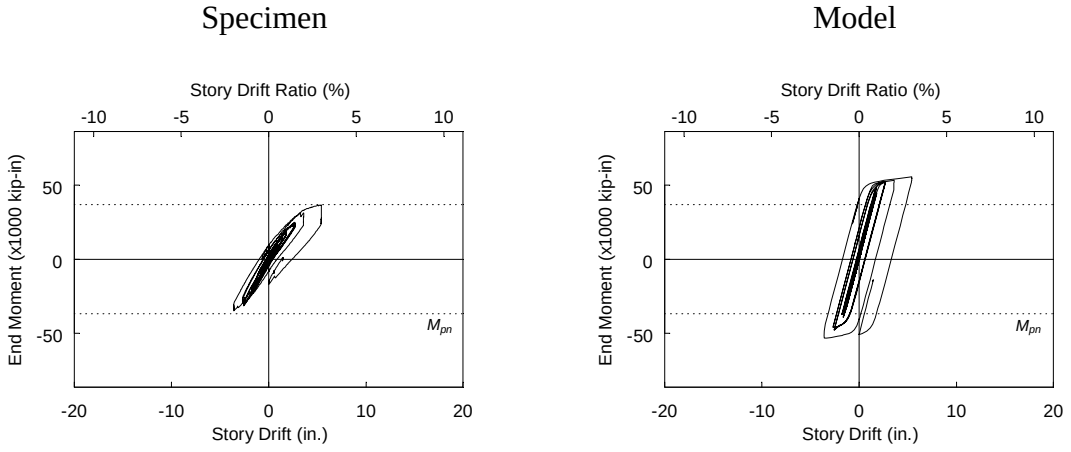

Figure 6.14 Model W14×370-35: Comparison of Specimen and Model End Moment versus Drift Response

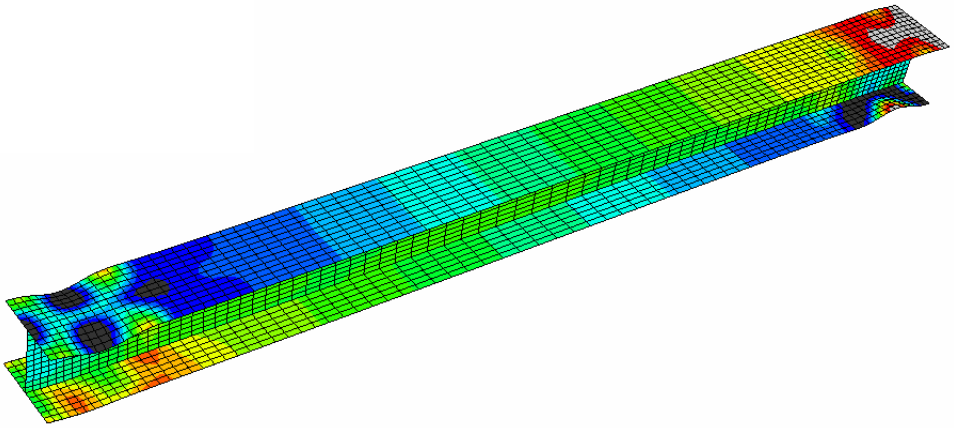

(a) 35%P_y

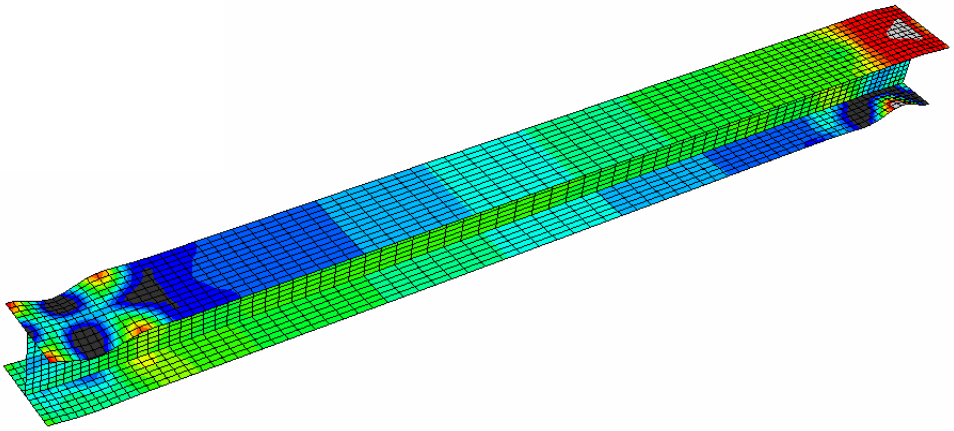

(b) 55%P_y

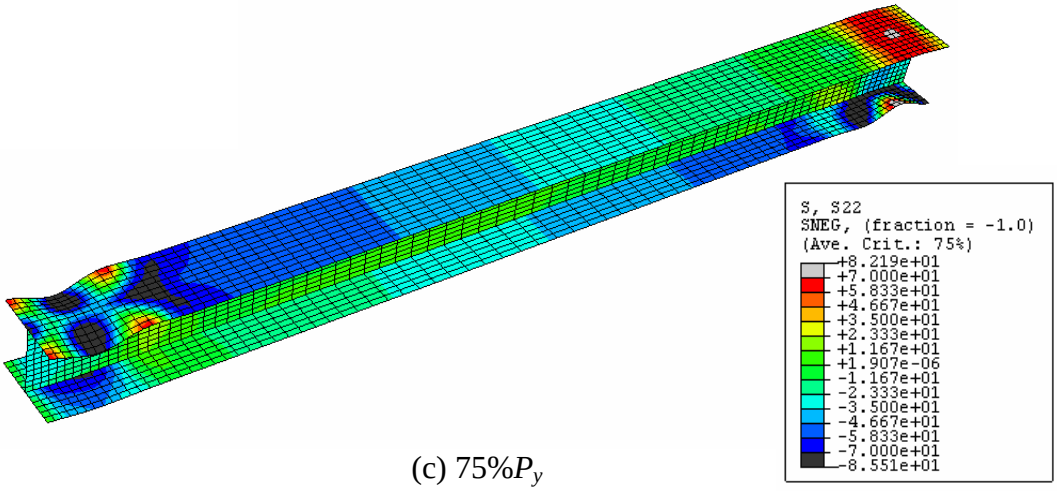

(c) 75%P_y

Figure 6.15 Model W14×132: 5% Drift

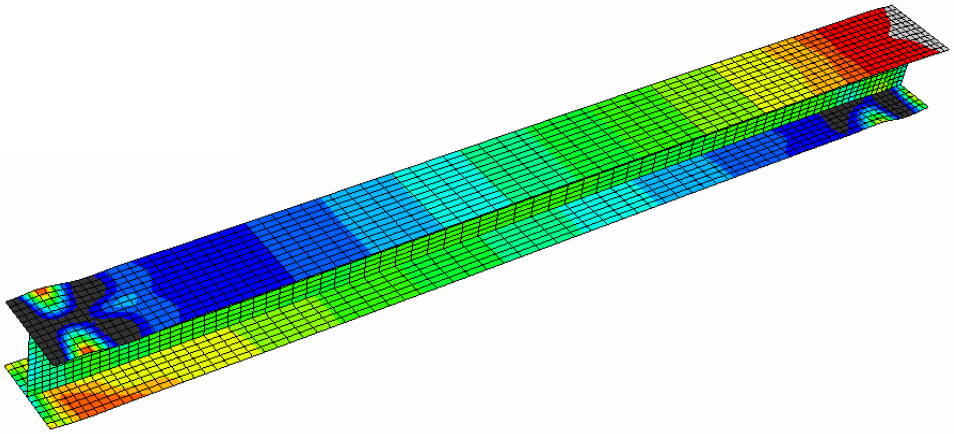

(a) 35%P_y

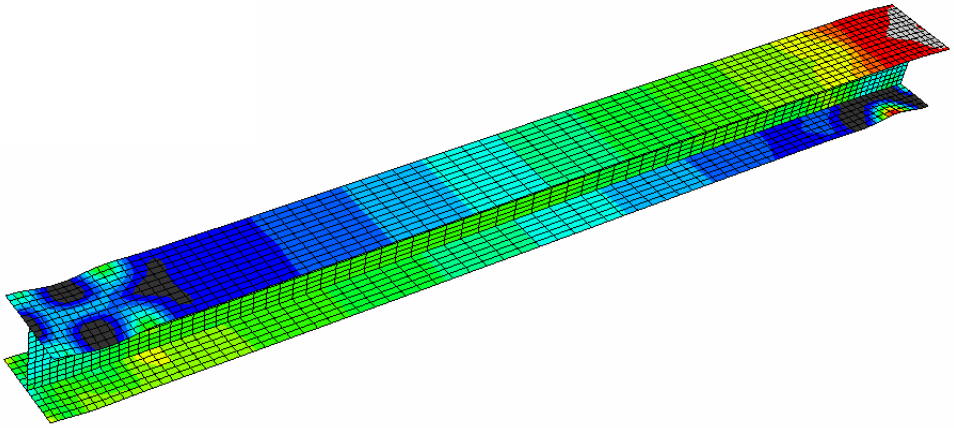

(b) 55%P_y

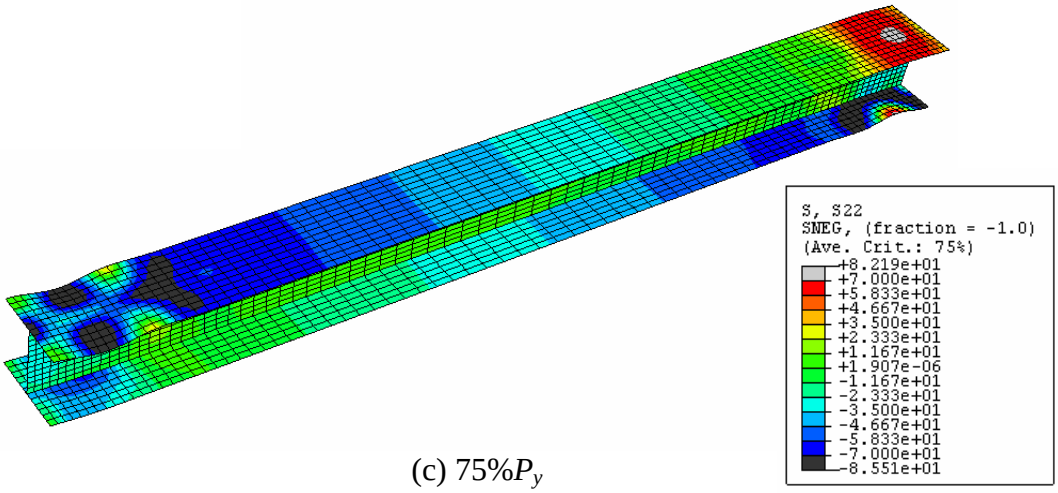

(c) 75%P_y

Figure 6.16 Model W14×176: 5% Drift

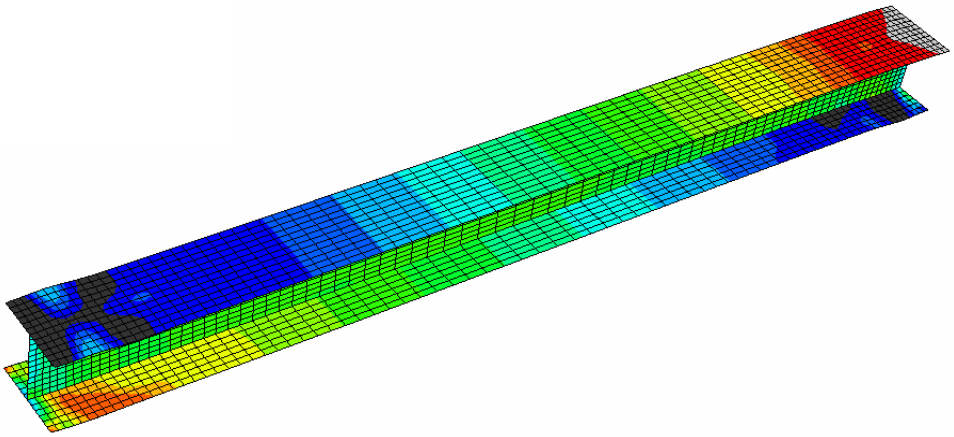

(a) 35%P_y

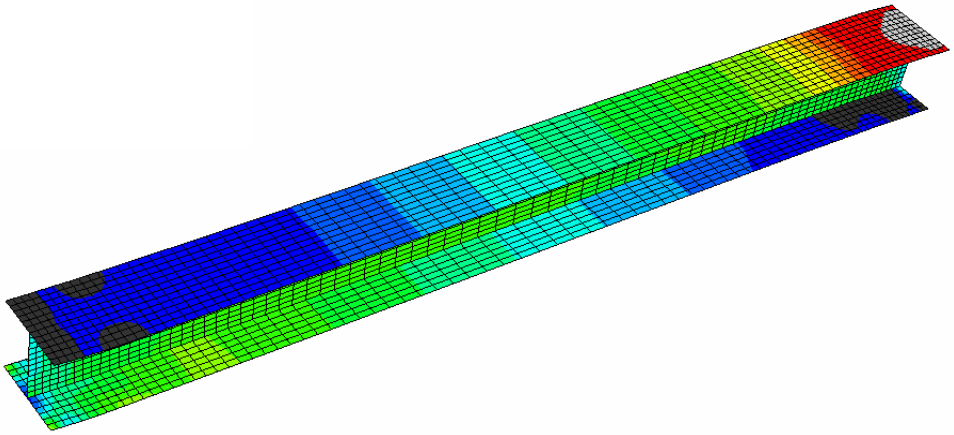

(b) 55%P_y

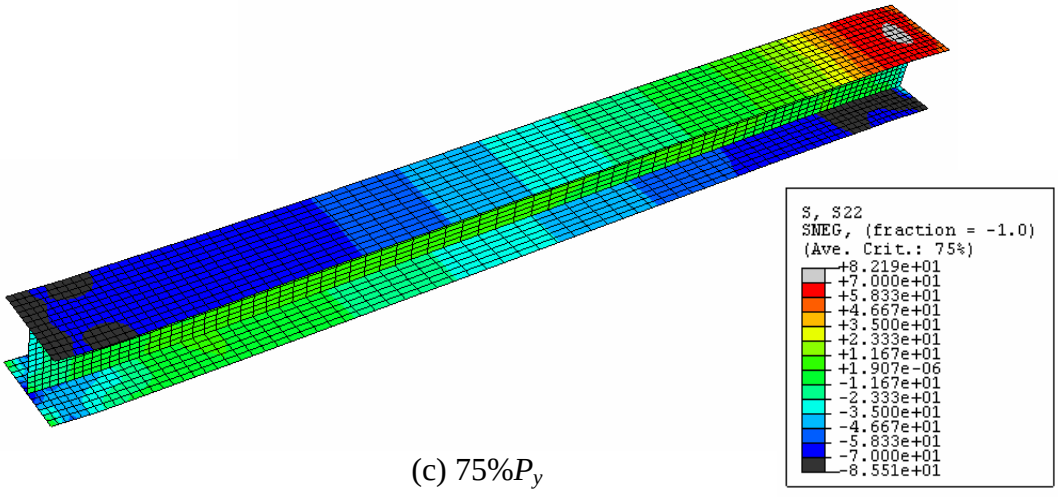

(c) 75%P_y

Figure 6.17 Model W14×233: 5% Drift

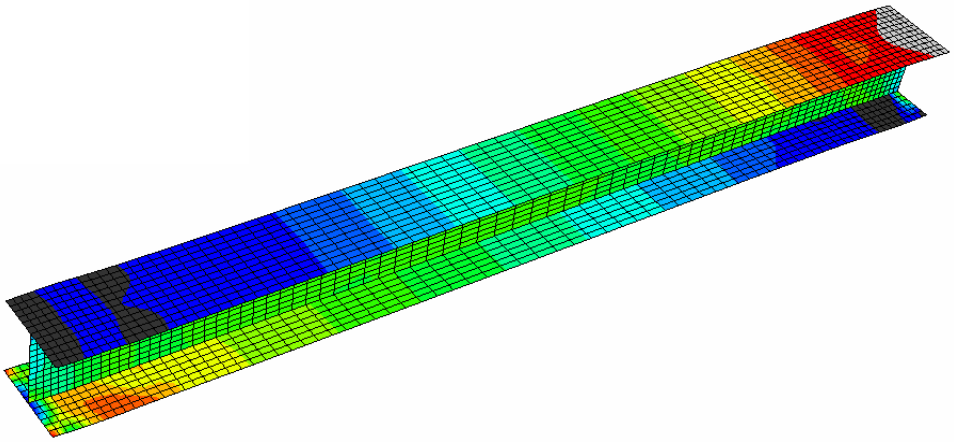

(a) 35%P_y

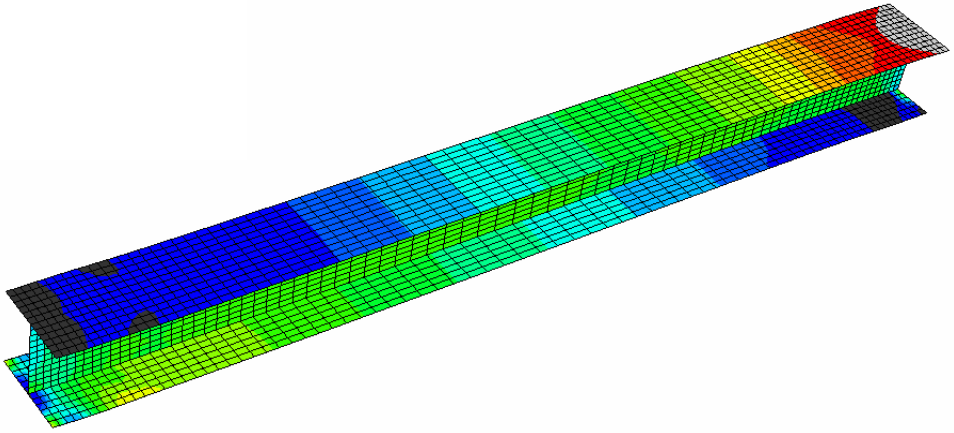

(b) 55%P_y

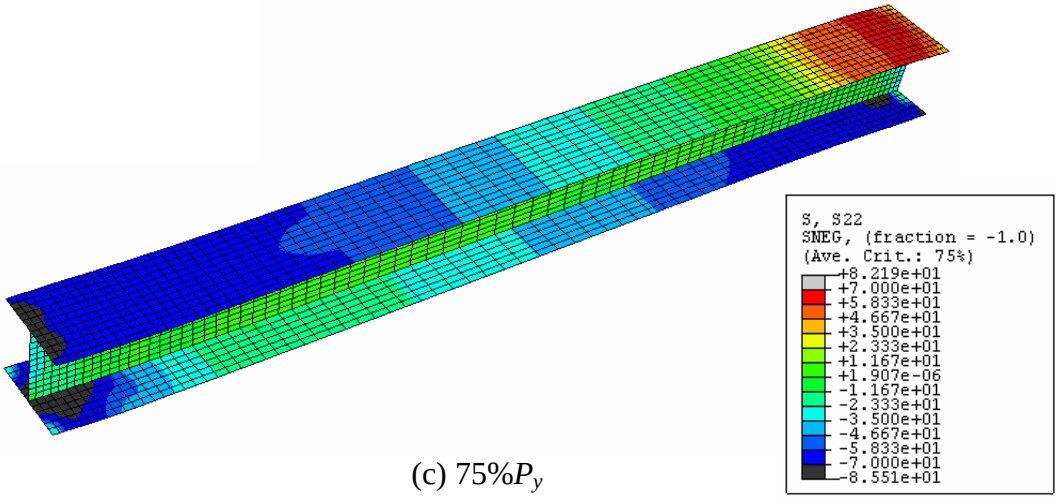

(c) 75%P_y

Figure 6.18 Model W14×370: 5% Drift

Loading History from Test | Ideal Loading History

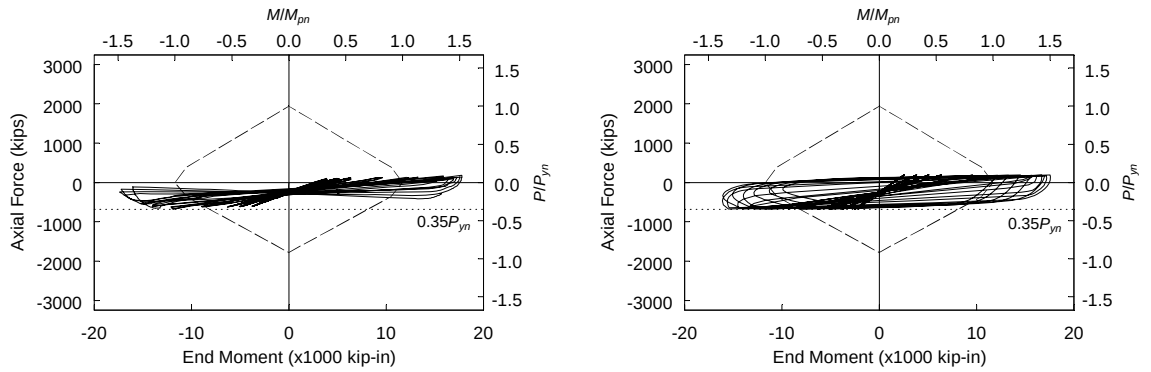

(a) 35%P_y

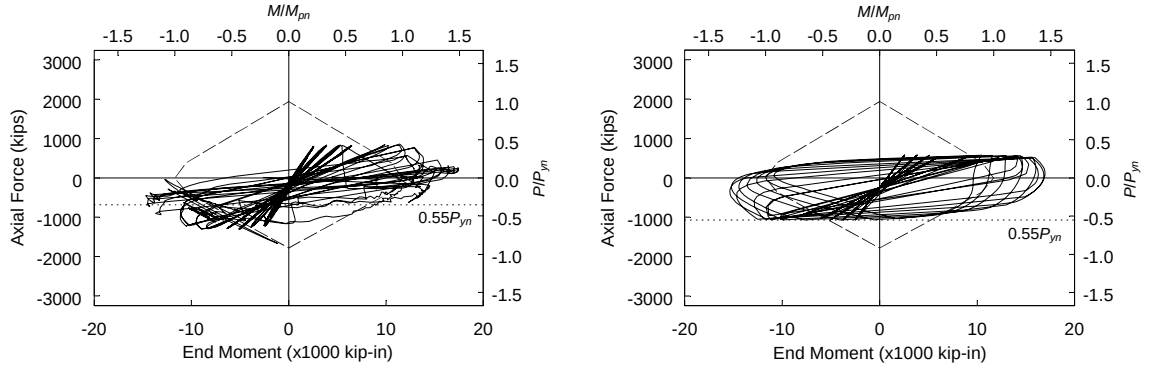

(b) 55%P_y

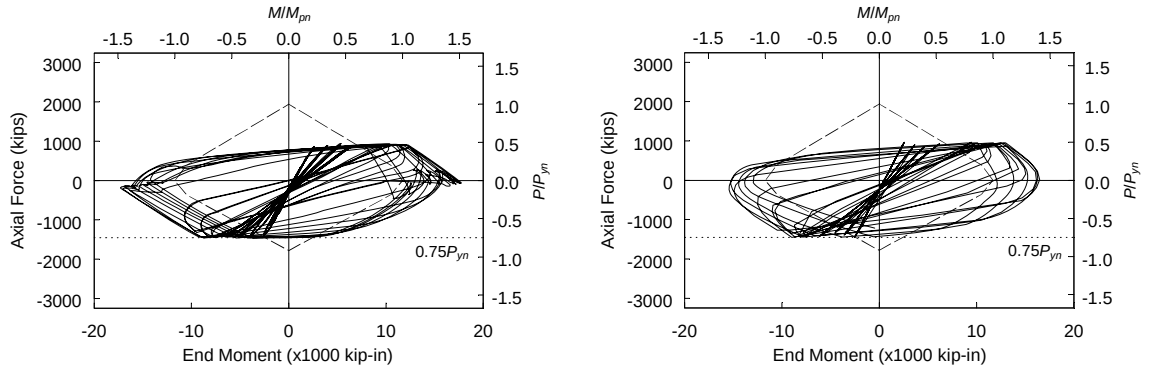

(c) 75%P_y

Figure 6.19 Model W14×132: Comparison of *P*-*M* Interaction

Loading History from Test | Ideal Loading History

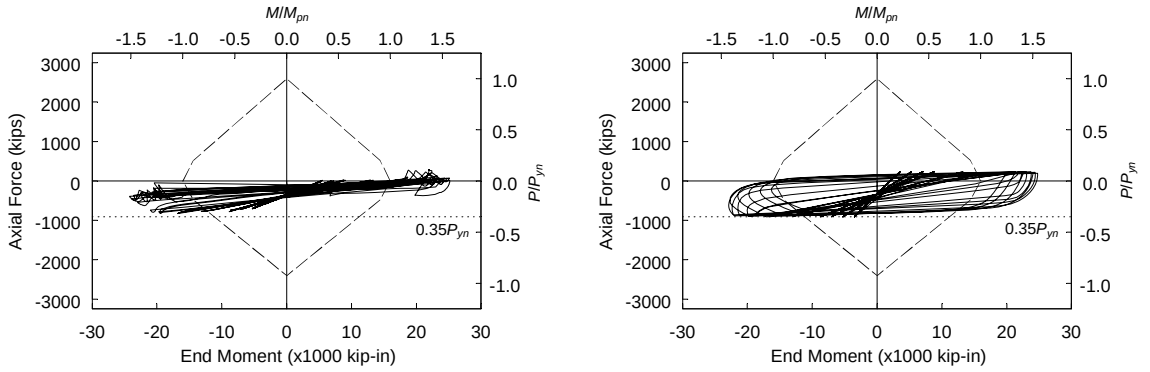

(a) 35%P_y

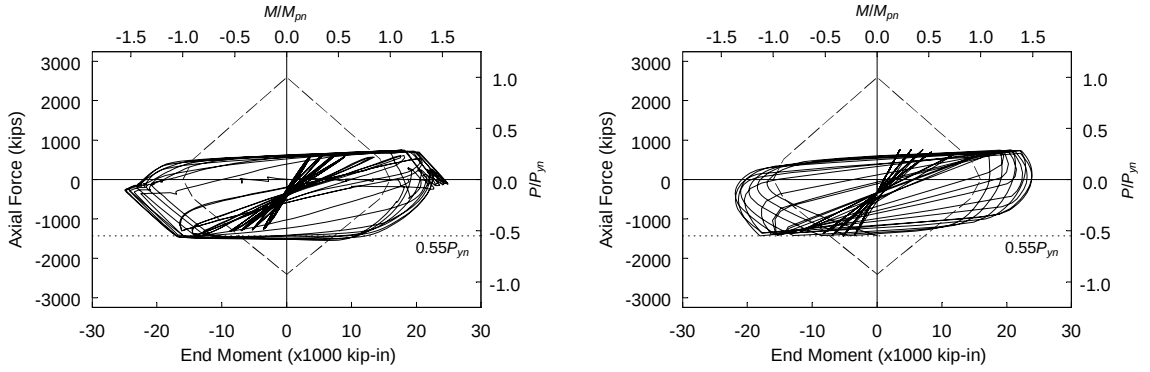

(b) 55%P_y

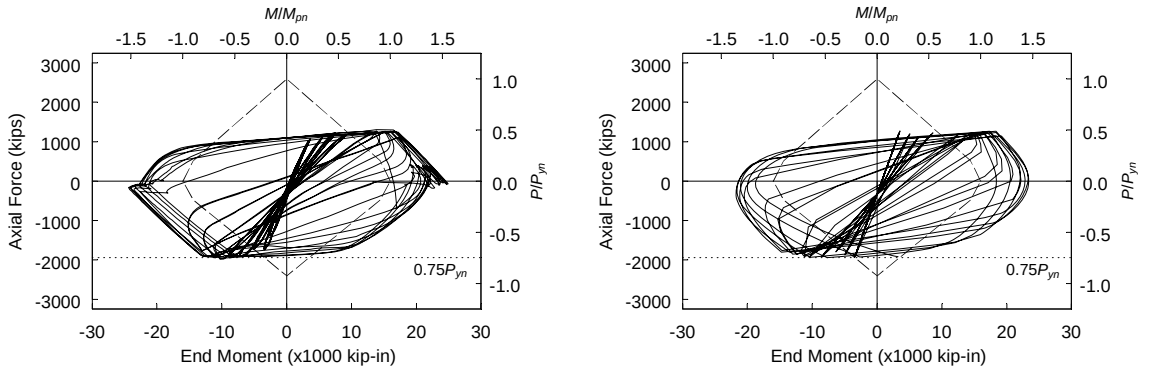

(c) 75%P_y

Figure 6.20 Model W14×176: Comparison of *P*-*M* Interaction

Loading History from Test

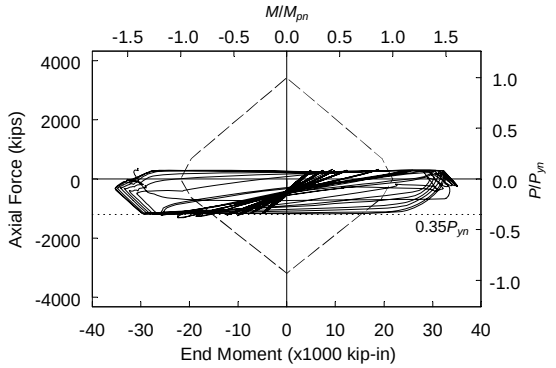

Ideal Loading History

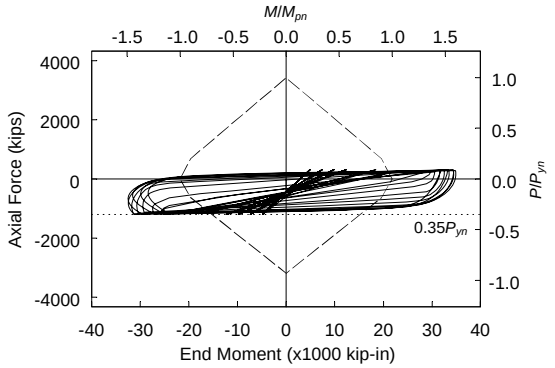

(a) 35%P_y

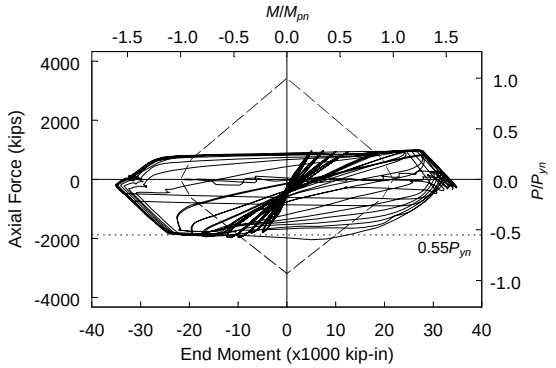

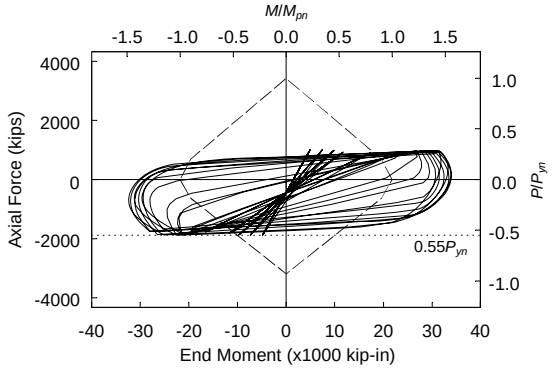

(b) 55%P_y

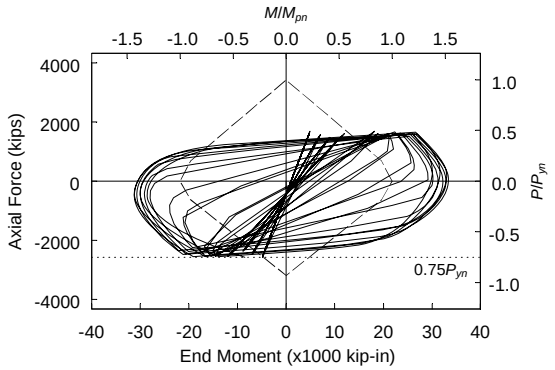

(c) 75%P_y

Figure 6.21 Model W14×233: Comparison of *P*-*M* Interaction

Loading History from Test

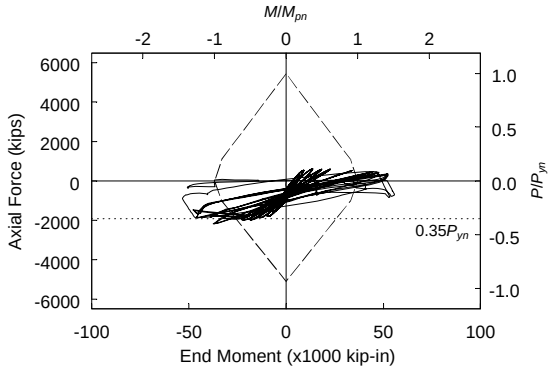

Ideal Loading History

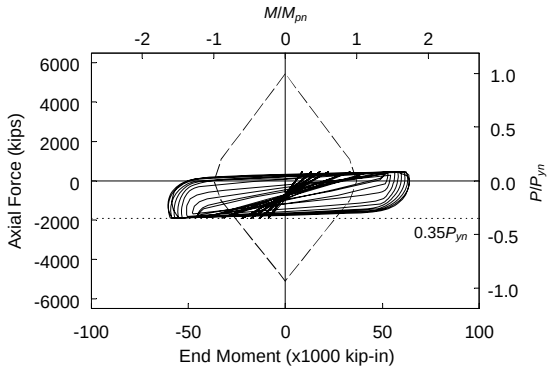

(a) 35%P_y

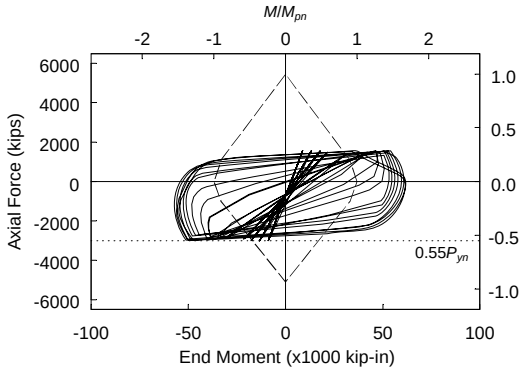

(b) 55%P_y

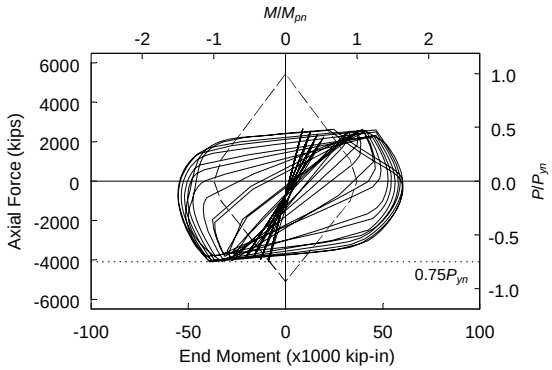

(c) 75%P_y

Figure 6.22 Model W14×370: Comparison of *P*-*M* Interaction

Loading History from Test | Ideal Loading History

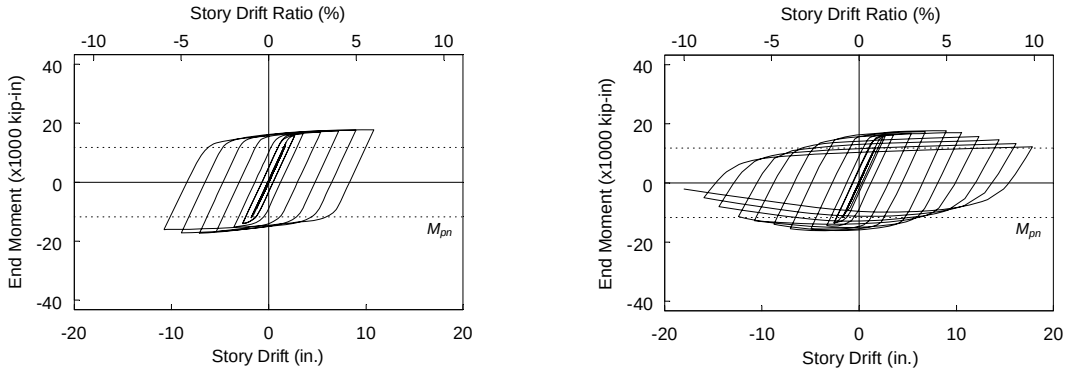

(a) 35%P_y

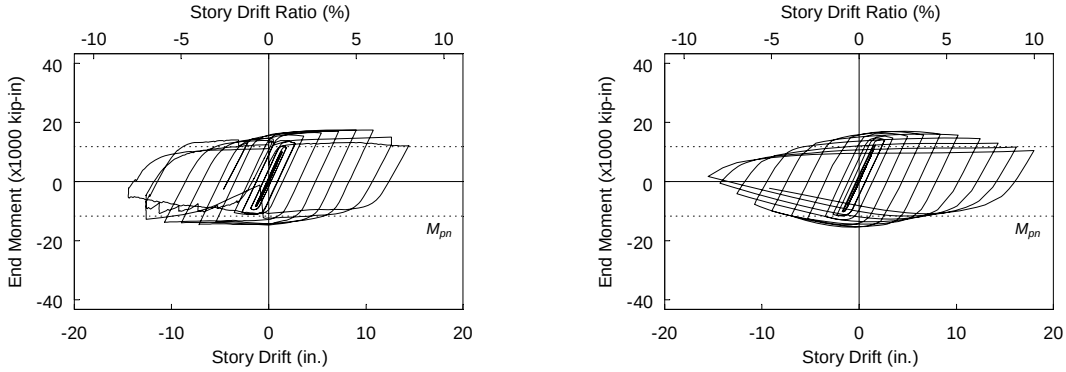

(b) 55%P_y

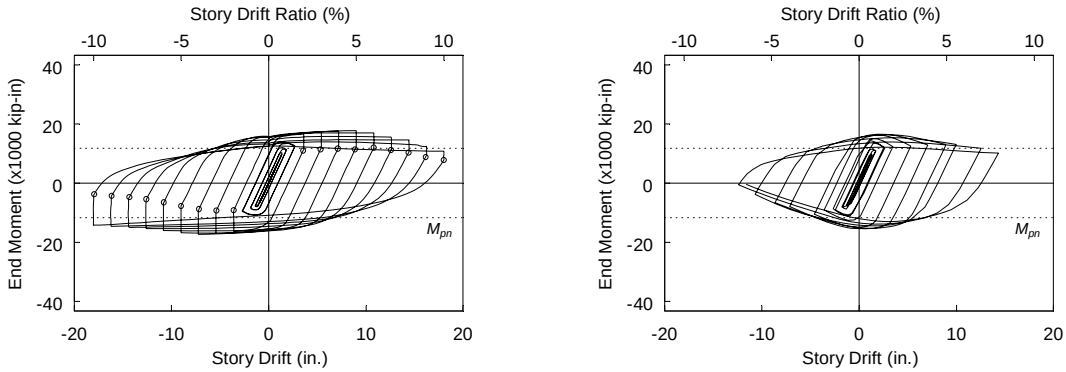

(c) 75%P_y

Figure 6.23 Model W14×132: Comparison of End Moment versus Drift Response

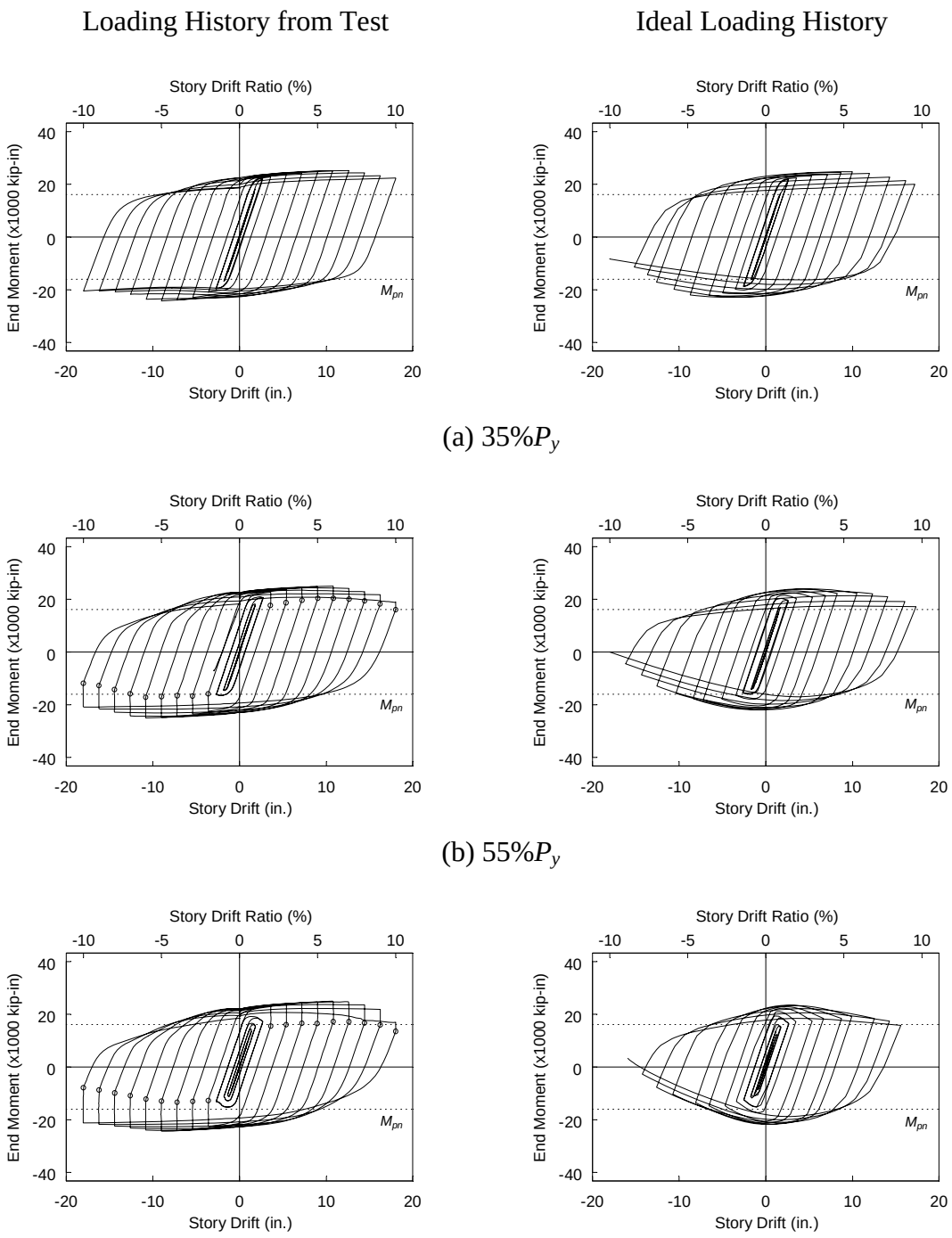

(a) 35%P_y

(b) 55%P_y

(c) 75%P_y

Figure 6.24 Model W14×176: Comparison of End Moment versus Drift Response

Loading History from Test

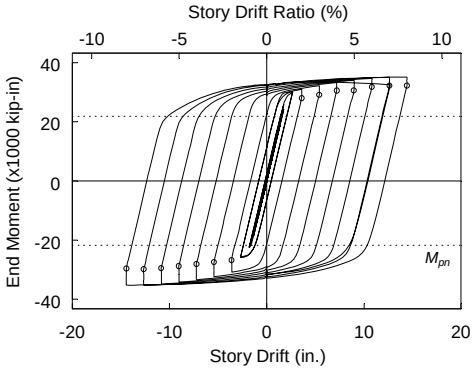

Ideal Loading History

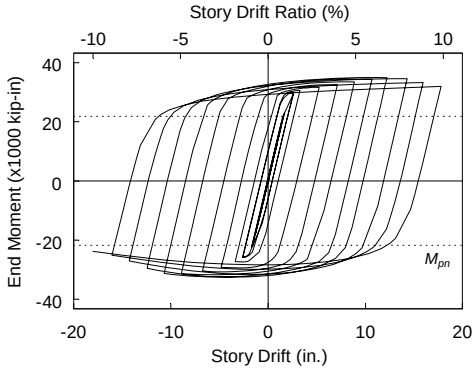

(a) 35%P_y

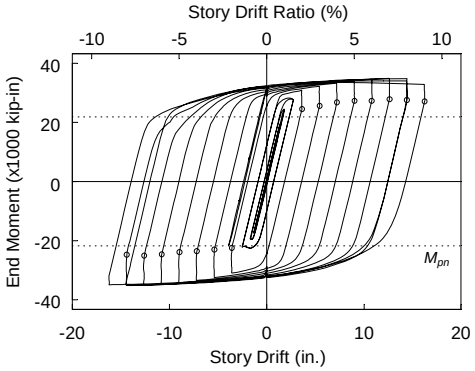

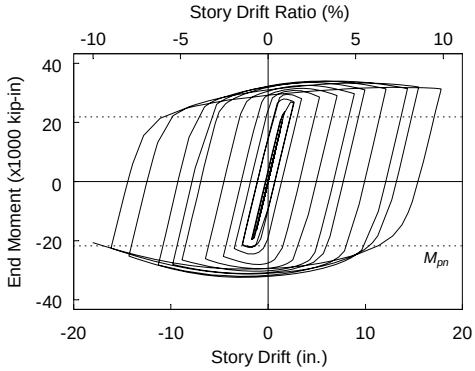

(b) 55%P_y

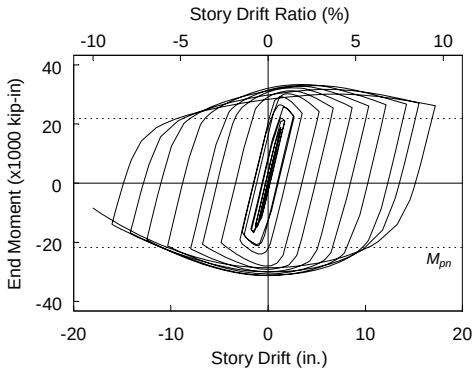

(c) 75%P_y

Figure 6.25 Model W14×233: Comparison of End Moment versus Drift Response

Loading History from Test

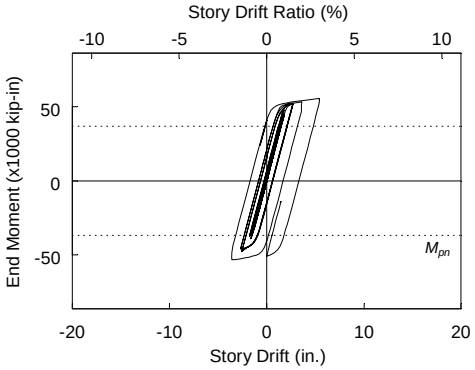

Ideal Loading History

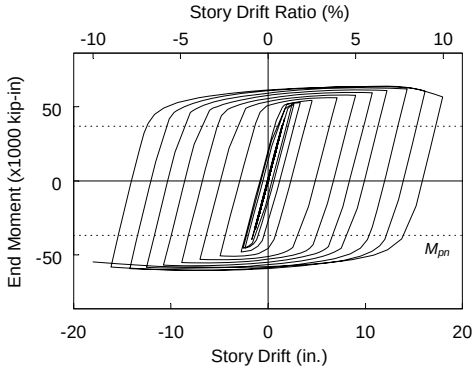

(a) 35%P_y

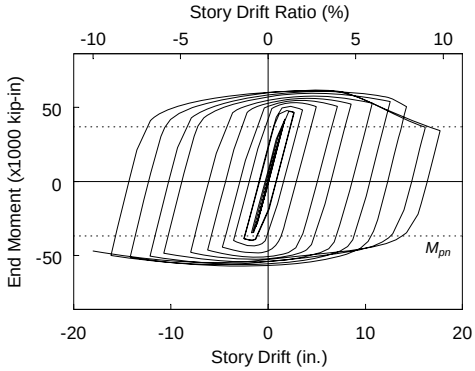

(b) 55%P_y

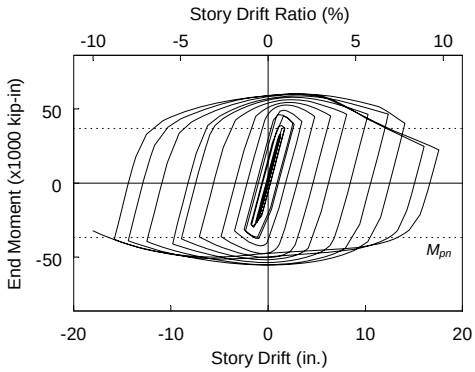

(c) 75%P_y

Figure 6.26 Model W14×370: Comparison of End Moment versus Drift Response

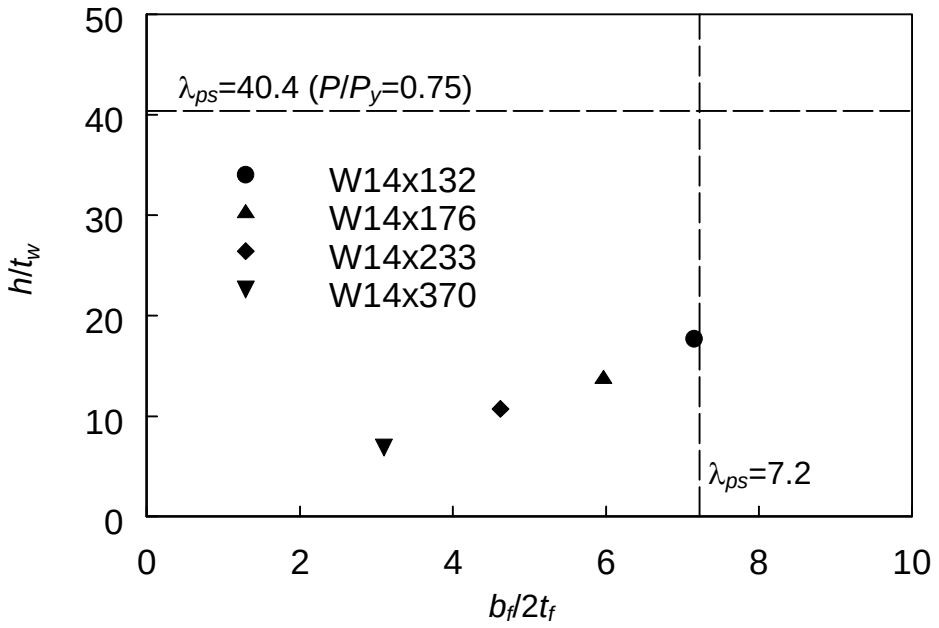

(a) Specimen and Model W14 Sections

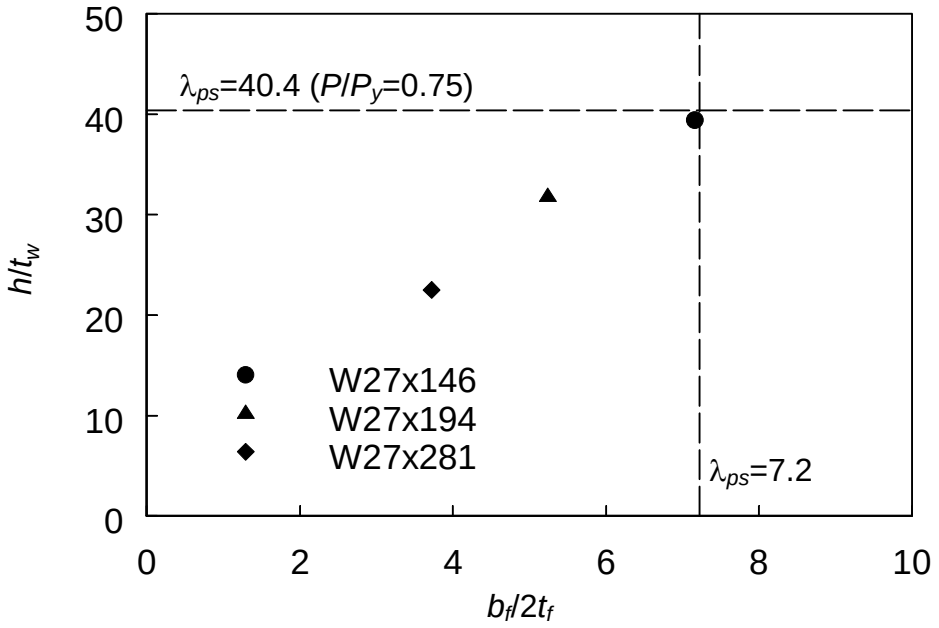

(b) Model W27 Sections

Figure 6.27 Comparison of Width-Thickness Ratios with λ_{ps} for Investigated W-Shapes

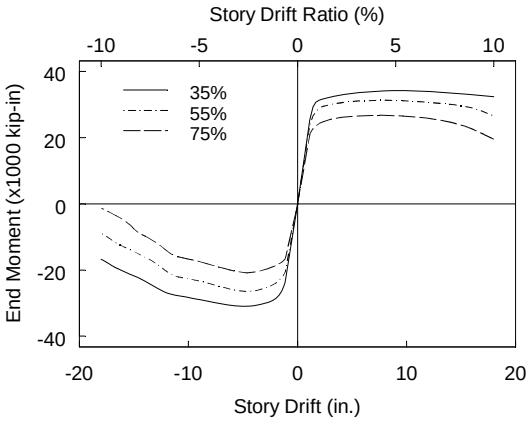

(a) W27×146

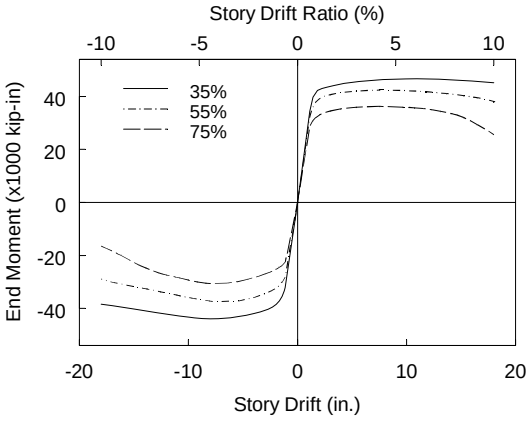

(b) W27×194

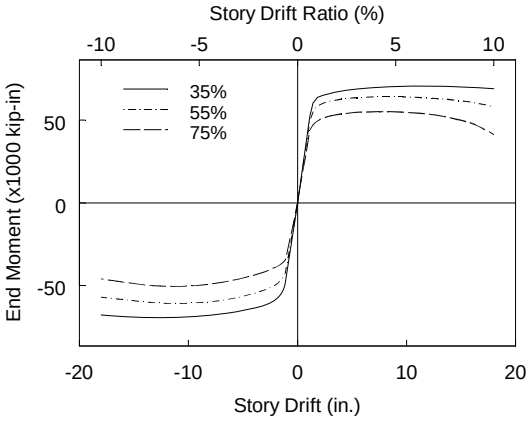

(c) W27×281

Figure 6.28 Comparison of Deep Column Models Monotonic End Moment versus Drift Response

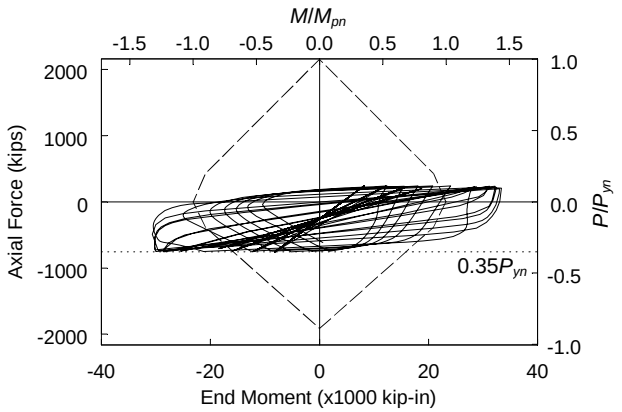

(a) 35%P_y

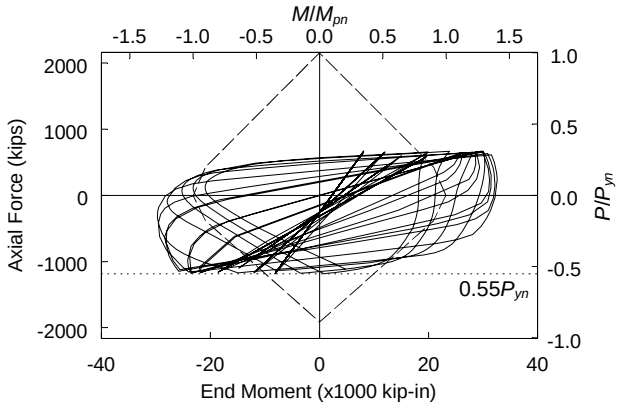

(b) 55%P_y

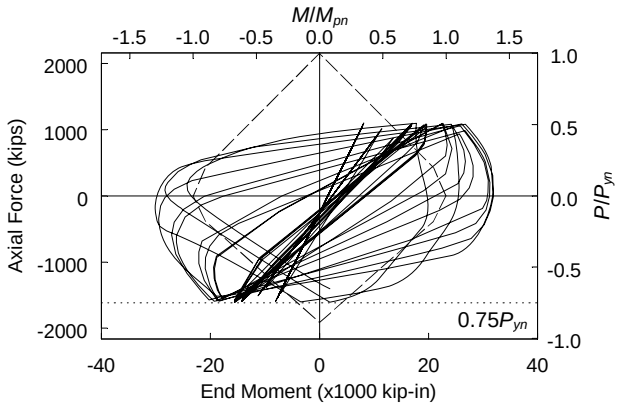

(c) 75%P_y

Figure 6.29 Model W27×146: Comparison of *P-M* Interaction

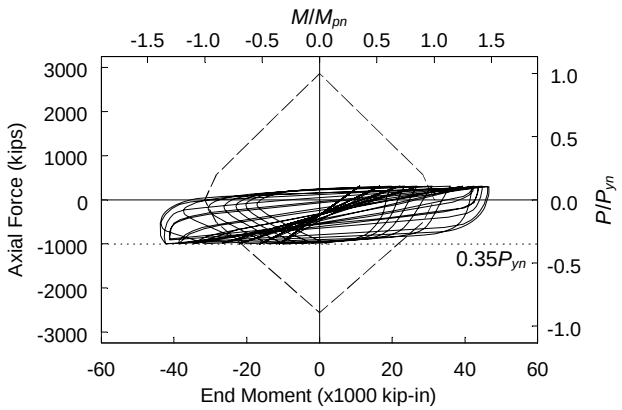

(a) 35%P_y

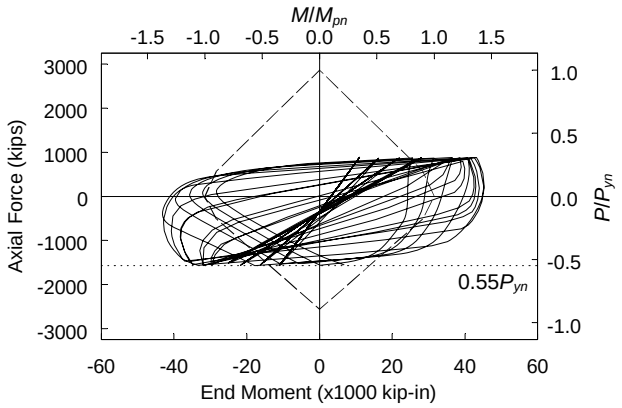

(b) 55%P_y

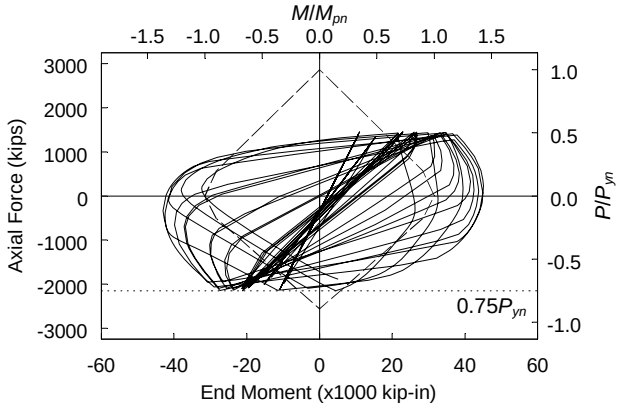

(c) 75%P_y

Figure 6.30 Model W27×194: Comparison of *P*-*M* Interaction

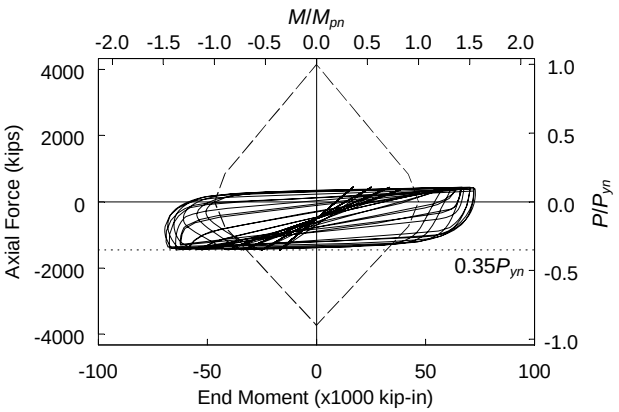

(a) 35%P_y

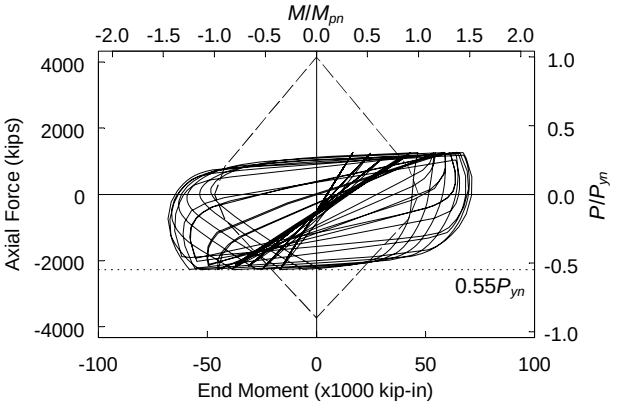

(b) 55%P_y

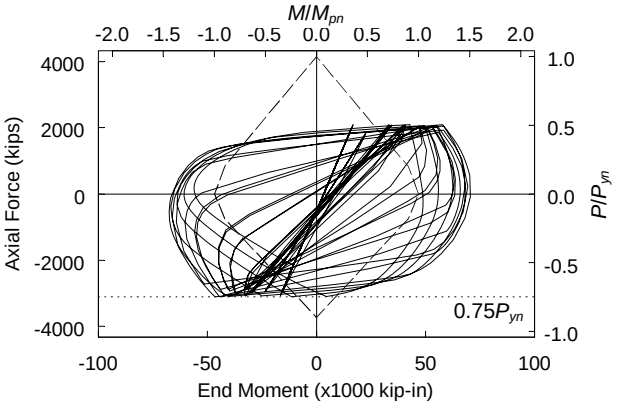

(c) 75%P_y

Figure 6.31 Model W27×281: Comparison of *P*-*M* Interaction

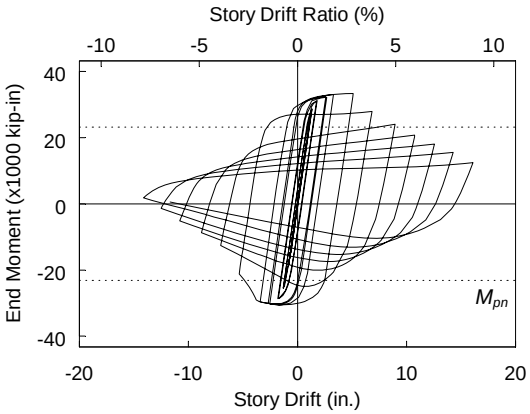

(a) 35%P_y

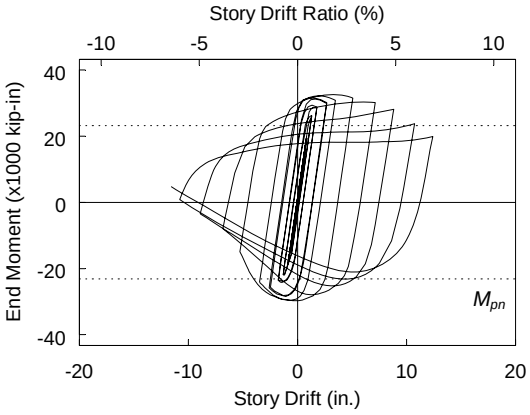

(b) 55%P_y

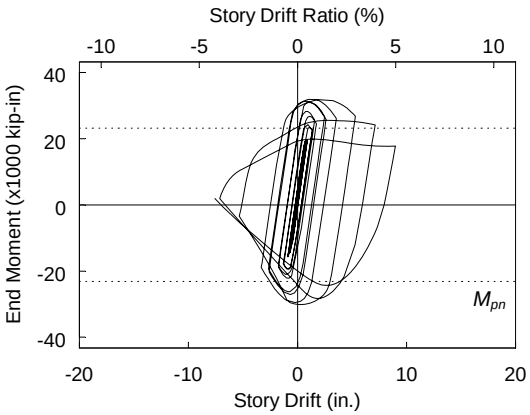

(c) 75%P_y

Figure 6.32 Model W27×146: Comparison of End Moment versus Drift Response

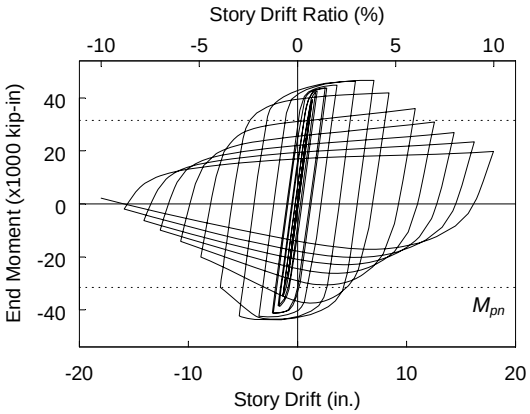

(a) 35%P_y

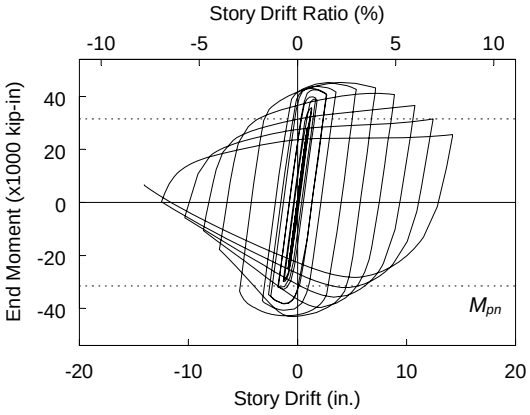

(b) 55%P_y

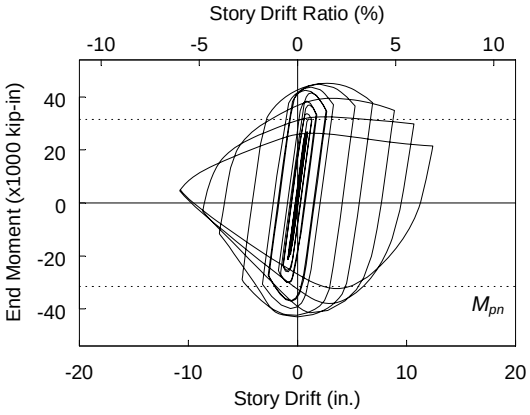

(c) 75%P_y

Figure 6.33 Model W27×194: Comparison of End Moment versus Drift Response

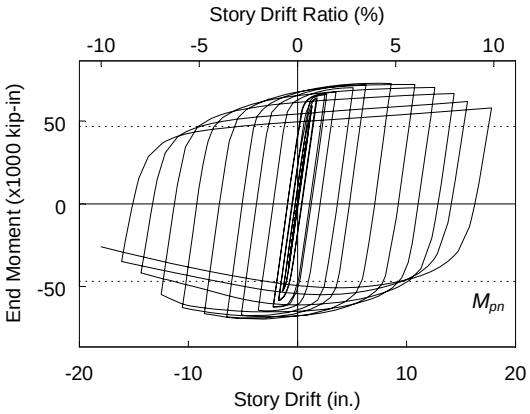

(a) 35%P_y

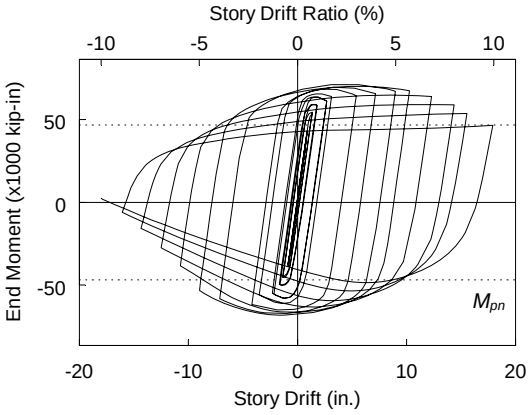

(b) 55%P_y

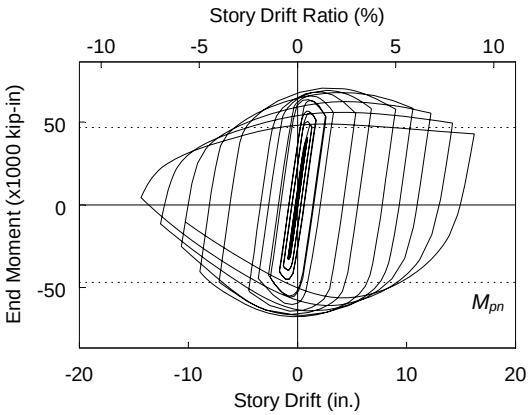

(c) 75%P_y

Figure 6.34 Model W27×281: Comparison of End Moment versus Drift Response

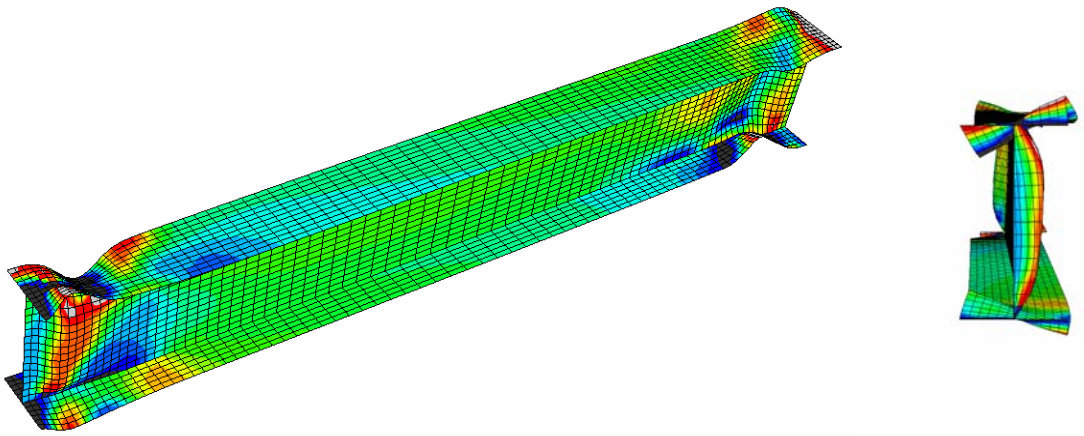

(a) 35%P_y

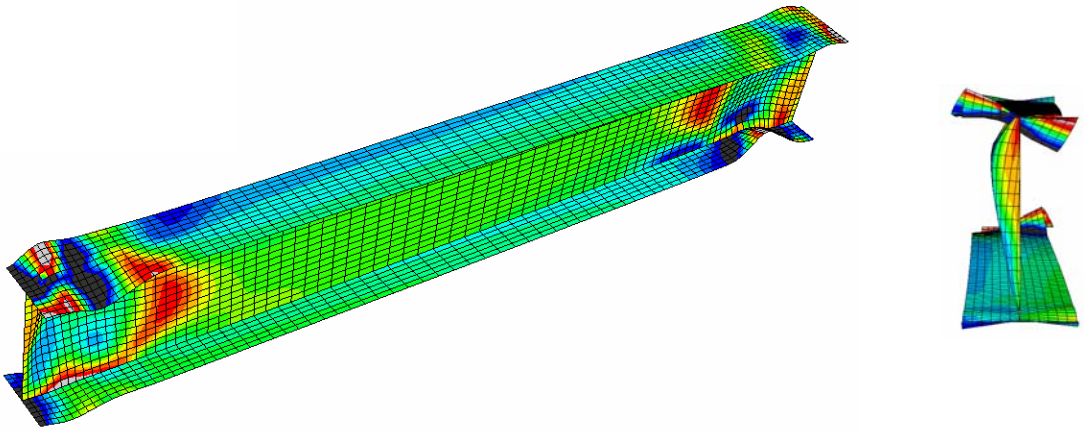

(b) 55%P_y

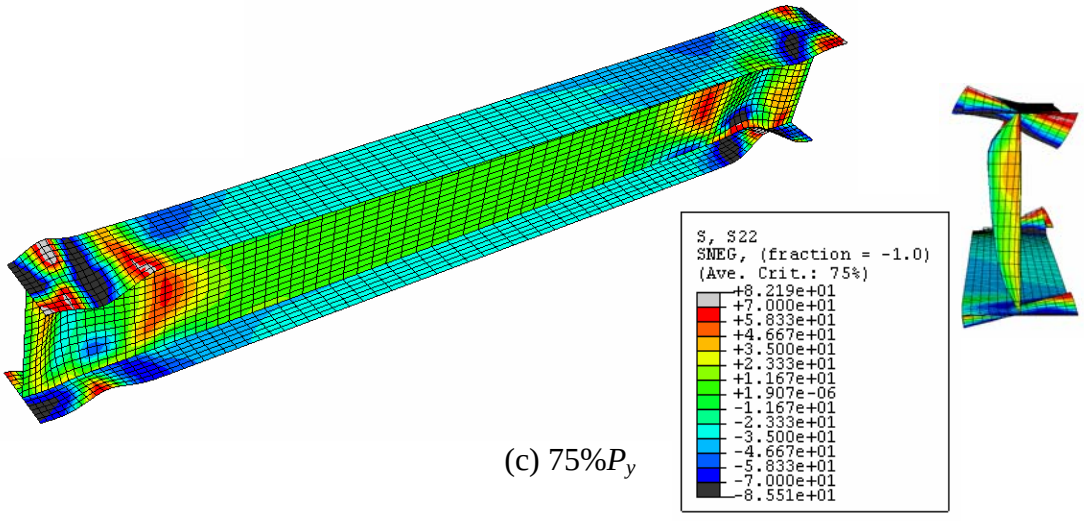

(c) 75%P_y

Figure 6.35 Model W27×146: 5% Drift

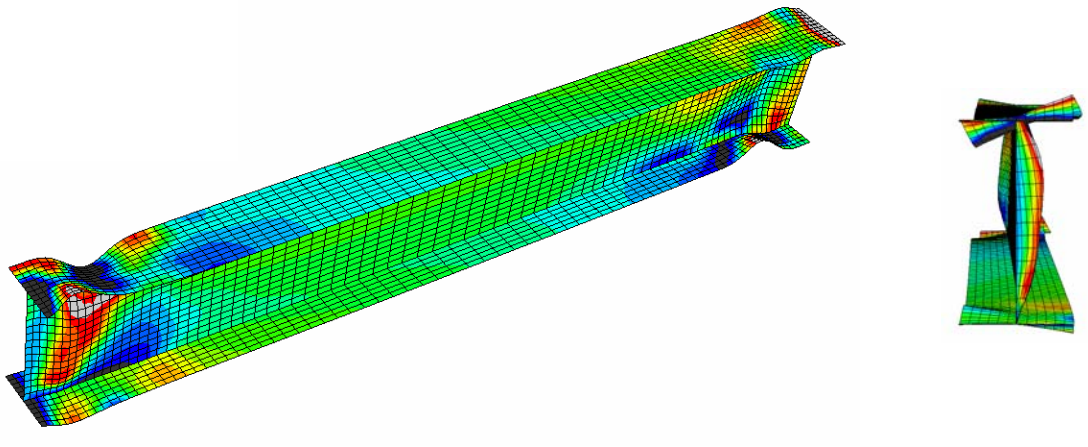

(a) 35%P_y

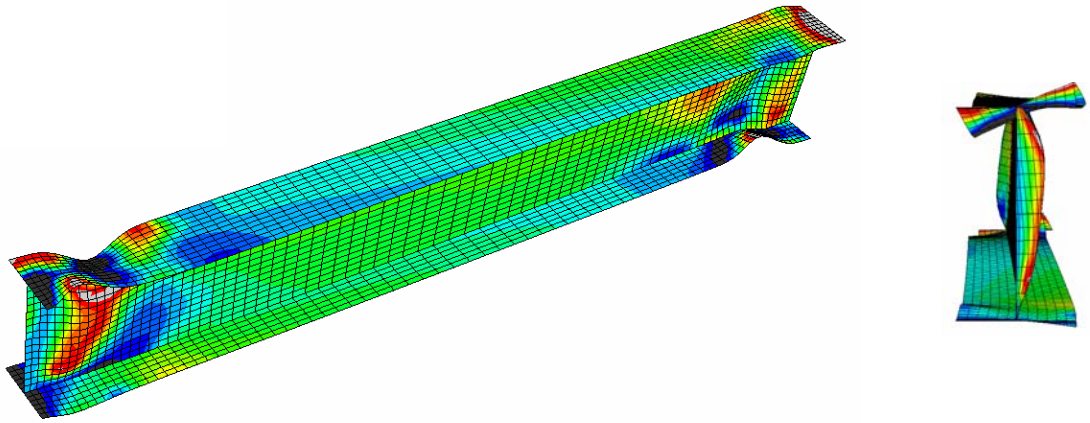

(b) 55%P_y

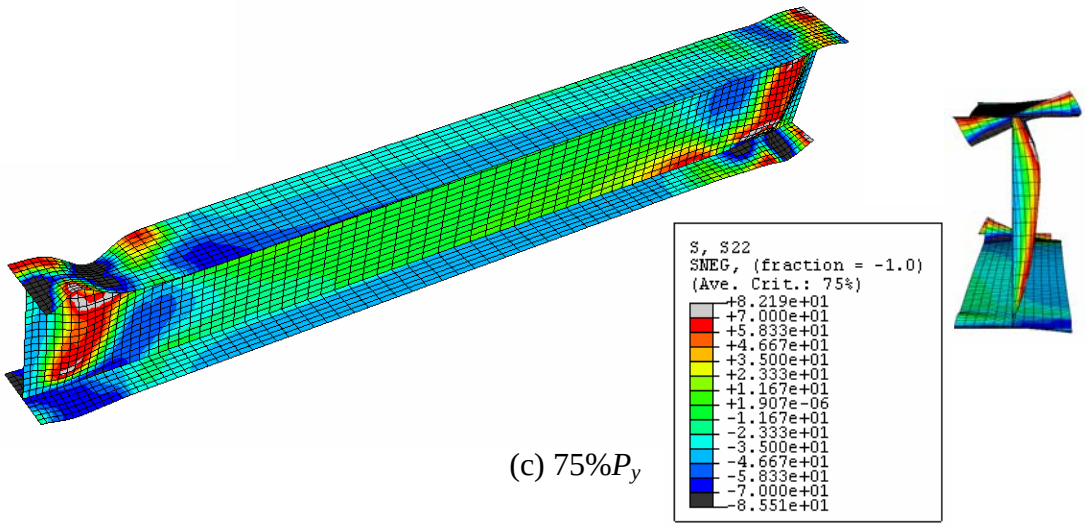

(c) 75%P_y

Figure 6.36 Model W27×194: 5% Drift

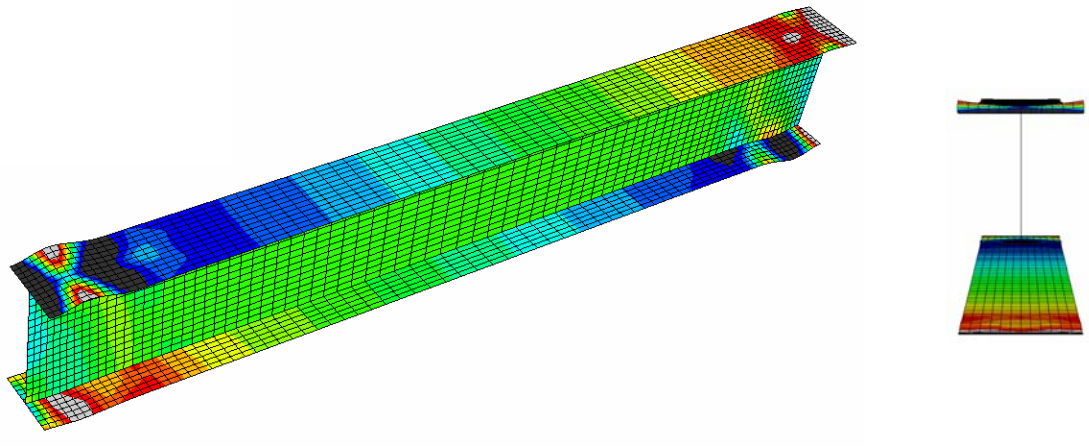

(a) 35%P_y

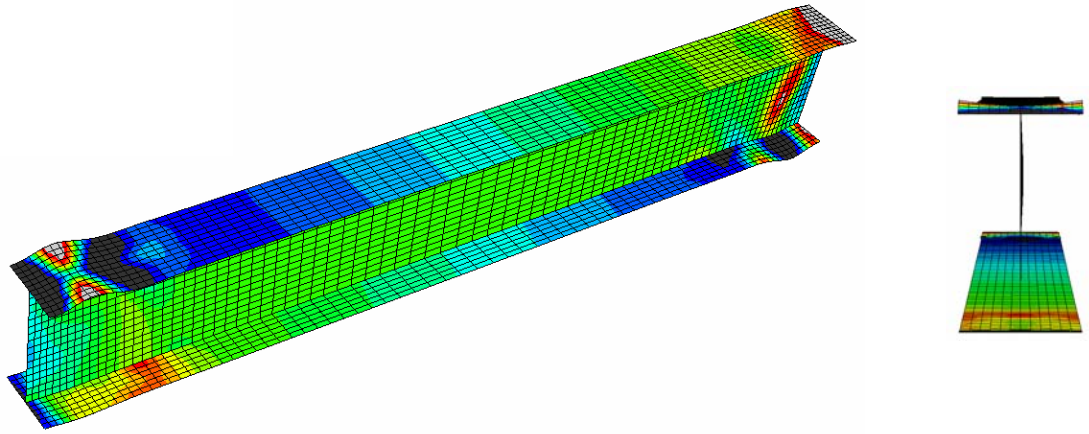

(b) 55%P_y

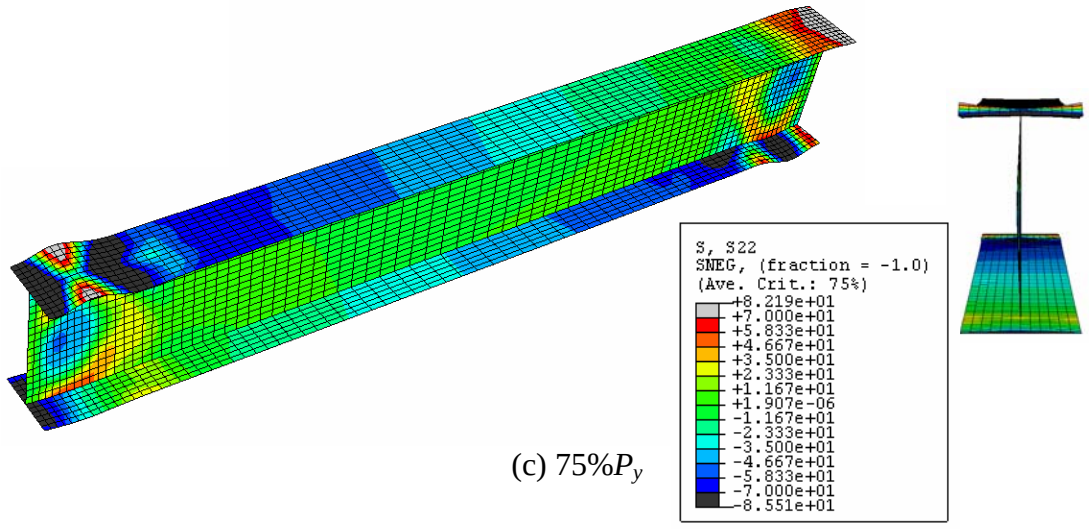

(c) 75%P_y

Figure 6.37 Model W27×281: 5% Drift

7. SUMMARY AND CONCLUSIONS

7.1 Summary

To develop a rational loading sequence for cyclic testing of braced frame columns, 3-story and 7-story BRBF prototype building models were designed and analyzed. Nonlinear time-history analysis of frame models, subjected to a suite of 20 ground motion records, was conducted. First-story column axial load and story drift ratio time-histories for the 20 records were processed using a rainflow cycle counting procedure. Statistical analysis was used to quantify maximum and cumulative column demands and a loading sequence for experimental testing was developed. The loading sequence was controlled by story drift ratio, and column axial loads were calculated based on idealized brace demand on the columns.

The experimental program consisted of testing nine full-scale fixed-base columns. ASTM A992 steel wide-flange sections typical of braced frame columns, representing a practical range of flange and web width-to-thickness ratios, and 15 ft story height were subjected to different levels of axial force demand ($0.35P_y$, $0.55P_y$, and $0.75P_y$) combined with story drift demand for these simulated first-story columns. Column specimens were tested in a horizontal configuration with one end of the specimen attached to a reaction fixture that was attached to a strong-wall. The other end of the specimen was attached to a reaction fixture attached to the SRMD shake table platen. Longitudinal and lateral movement of the shake table platen imposed load in both directions. Since the objective of this research was focused on strength and ductility capacities of steel columns, not the column base connection to surrounding members, both ends of the column specimen were strengthened by stiffeners or re-usable haunches to simulate the fixed-end condition. Except for both ends, specimens were not braced laterally to inhibit weak-axis buckling. Three different loading schemes were used during testing to overcome difficulties encountered in simultaneously controlling the SRMD input longitudinal and lateral displacements to achieve both the desired column axial load targets and story drift targets. The final Loading Scheme C consisted of in-phase story drift and column axial load to represent realistic frame action through the 1.5% drift cycles. Calculation of column axial loads at the protocol drift levels were based on reaching the target column compressive axial load (e.g., $0.35P_y$, $0.55P_y$, $0.75P_y$) at 0.002 rad. story drift ratio (yield

drift) and axial loads for all excursions larger than the yield drift were equal to the maximum level for that specimen. For cycles at 2% drift and beyond the drift component of displacement was applied first, followed by application of longitudinal displacement until the target axial load was achieved. By loading in this manor the tests were safely conducted in displacement control and the combined target axial loads and story drifts could be achieved.

7.2 Conclusions

The test data agreed well with the established *P-M* interaction surface. Significant overstrength was observed between the test data and the *P-M* interaction surface based on nominal material properties. Drift capacities of 7% to 9% were calculated assuming a 10% reduction from peak moment resistance is used to define the drift capacity. These drift capacities correspond to a ductility of approximately 10 and were more than four times the expected BRBF story drift from earthquake nonlinear time-history analysis. For all specimens only minor yielding was observed at a story drift of 1.5%, the maximum expected drift from nonlinear time-history analysis.

Flange local buckling was observed for all specimens with the exception of Specimen W14×370-35, which failed prematurely due to fracture of the column flange-to-base plate welded joint. No web local buckling was observed. Cyclic straightening of flange local buckling occurred until about 8% drift when the buckled amplitude formed on one drift excursion would only partially straighten on the subsequent opposite drift excursion. The relatively small amplitude of flange local buckling observed at 6% drift (more than three times the maximum expected drift) provided an indication that strength degradation due to flange local buckling is not expected to present a problem for the seismic design of the tested W14 column sections.

No fracture was observed for Specimens W14×132-35, W14×132-55, and W14×233-55. Specimens W14×132-75, W14×176-35, W14×176-55, and W14×176-75 experienced partial or complete fracture of the column flange through the haunch bolt hole net section. Specimens W14×233-35, and W14×370-35 failed by fracture of the column flange-to-base plate electroslag complete joint penetration groove welded joint. With the exception of Specimen W14×370-35, which failed at 3% drift, the fracture of

the other specimens occurred at 8% drift or larger, which was well beyond the expected earthquake drift demand on these columns.

The finite element program ABAQUS was used to model the steel column specimens. Models predicted global behavior, yielding, and strength degradation resulting from local buckling at large drifts. Models were subjected to both monotonic and cyclic loading sequences. Analysis results were observed to be well correlated with experimental results. It was determined that a typical initial residual stress distribution did not significantly effect the *P-M* interaction or moment versus drift response. The behavior of deep columns with higher width/thickness ratios than the tested W14 sections was also investigated. Finite element analysis of three W27 column models similar to tested specimens revealed a potential vulnerability of deep columns to combined high axial load and drift demand. Significant degradation from flange and web local buckling was accelerated by the presence of high axial load.

REFERENCES

(1) ABAQUS Inc. (2005), *ABAQUS/CAE Users Manual*, Electronic Version 6.4-5, Pawtucket, RI.

(2) Aiken, I., Clark, P., Tajirian, F., Kasai, K., Kimura, I. and Ko, E. (2000). "Unbonded Braces in the United States-Design Studies, Large-Scale Testing and the First Building Application." *Proceedings of International Symposium on Passive Control*, Tokyo Institute of Technology, Tokyo, Japan, pp. 203-217.

(3) American Institute of Steel Construction and Structural Engineers Association of California. (2001). *Recommended Buckling-Restrained Braced Frame Provisions*. Chicago, IL.

(4) American Institute of Steel Construction. (2005a). *Seismic Provisions for Structural Steel Buildings*. Chicago, IL.

(5) American Institute of Steel Construction. (2005b). *Thirteenth Edition Steel Construction Manual*. Chicago, IL.

(6) Black, C., Makris, N. and Aiken, I. (2002). "Component Testing, Stability Analysis and Characterization of Buckling Restrained Braces." *Report No. PEER-2002/08*, Pacific Earthquake Engineering Research Center, University of California, Berkeley, CA.

(7) International Code Council Inc. (2006). *International Building Code*. Whittier, CA.

(8) Kaufmann, E., Metrovich, B. and Pense, A. (2001), "Characterization of Cyclic Inelastic Strain Behavior on Properties of A572 Gr. 50 and A913 Rolled Sections." *ATLASS Report No. 01-13*, National Center for Engineering Research on Advanced Technology for Large Structural Systems, Lehigh University, Bethlehem, PA.

(9) Krawinkler, H. (1996). "Cyclic Loading Histories for Seismic Experimentation on Strucutural Components." *Earthquake Spectra*, 12(1).

(10) Krawinkler, H., Gupta, A., Medina, R. and Luco, N. (2000). "Loading Histories for Seismic Performance Testing of SMRF Components and Assemblies." *Report No. SAC/BD-00/10.* SAC Joint Venture.

(11) Krawinkler, H., Parisi, F., Ibarra, L., Ayoub, A. and Medina, R. (2001). "Development of a Testing Protocol for Wood Frame Structures." *Report No. W-02*, CUREE-Caltech Woodframe Project, Stanford University, Palo Alto, CA.

(12) Krawinkler, H., Medina, R. and Alavi, B. (2003). "Seismic Drift and Ductility Demands and their Dependence on Ground Motions." *Engineering Structures*, 25(5), pp. 637-653.

(13) Lopez, W. and Sabelli, R. (2004). “Seismic Design of Buckling-Restrained Braced Frames.” Structural Steel Education Council Technical Information & Product Services, Moraga, CA.

(14) Medina, R.A. (2003). “Seismic Demands for Nondeteriorating Frame Structures and their Dependence on Ground Motions.” *Ph.D. Dissertation*, Department of Civil and Environmental Engineering, Stanford University, Palo Alto, CA.

(15) Merritt, S., Uang, C.M., Benzoni, G. (2003a). “Subassemblage Testing of Corebrace Buckling-Restrained Braces.” *Report No. TR-2003/01*, University of California, San Diego, La Jolla, CA.

(16) Merritt, S., Uang, C.M., Benzoni, G. (2003b). “Subassemblage Testing of Star Seismic Buckling-Restrained Braces.” *Report No. TR-2003/04*, University of California, San Diego, La Jolla, CA.

(17) Merritt, S., Uang, C.M., Benzoni, G. (2003c). “Uniaxial Testing of Associated Buckling-Restrained Braces.” *Report No. TR-2003/05*, University of California, San Diego, La Jolla, CA.

(18) Newell, J., Uang, C.M., Benzoni, G. (2005). “Subassemblage Testing of Corebrace Buckling-Restrained Braces (F Series).” *Report No. TR-2005/01*, University of California, San Diego, La Jolla, CA.

(19) Newell, J., Uang, C.M., Benzoni, G. (2006). “Subassemblage Testing of Corebrace Buckling-Restrained Braces (G Series).” *Report No. TR-2006/01*, University of California, San Diego, La Jolla, CA.

(20) Prakash, V., Powell, G.H., and Campbell, S. (1993). “DRAIN-2DX: Base Program Description and User Guide.” *Report No. UCB/SEMM-93/17*, Department of Civil Engineering, University of California, Berkeley, CA.

(21) Richards, P. and Uang, C.-M. (2003). “Development of Testing Protocol for Short Links in Eccentrically Braced Frames.” *Report No. SSRP-2003/08*, University of California, San Diego, La Jolla, CA.

(22) Sabelli, R. (2001). “Research of Improving the Design and Analysis of Earthquake-Resistant Steel-Braced Frames.” *2000 NEHRP Professional Fellowship Report.* EERI, Oakland, CA.

(23) Salmon, C. and Johnson, J. (1996). *Steel Structures: Design and Behavior, Emphasizing Load and Resistance Factor Design.* 4th Ed. HarperCollins College Publishers, New York.

(24) Structural Engineering Institute and American Society of Civil Engineers. (2005). *Minimum Design Loads for Buildings and Other Structures*, ASCE 7-05. Reston, Va.

(25) Uang, C.M. and Nakashima, M. (2004). “Steel Buckling-Restrained Braced Frames.” (Chapter 16) in *Earthquake Engineering: Recent Advances and Applications*, editors: Y. Bozorgnia and V. V. Bertero, CRC Press, Boca Raton.

(26) Watanabe, A. (1992). “Development of Composite Brace with a Large Ductility.” *US-Japan Workshop on Composite and Hybrid Structures*, San Francisco, CA.

(27) Watanabe, A., Hitomi, Y., Saeki, E., Wada, A., Fujimoto, M. (1988). “Properties of Brace Encased in Buckling-Restraining Concrete and Steel Tube.” *Proceedings of Ninth World Conference on Earthquake Engineering*, Tokyo-Kyoto, Japan. Paper No. 6-7-4. Vol. IV, pp. 719-724.

APPENDIX A: Time-History Analysis Results

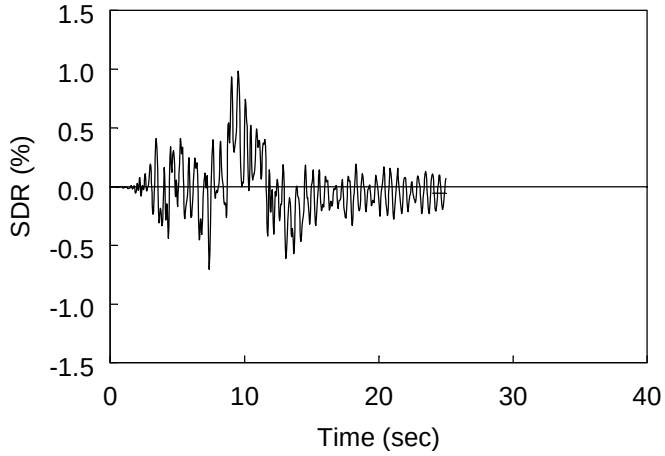

(a) Third Story

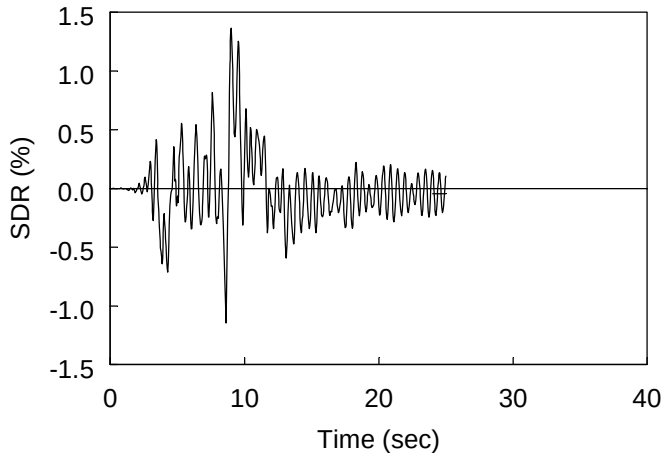

(b) Second Story

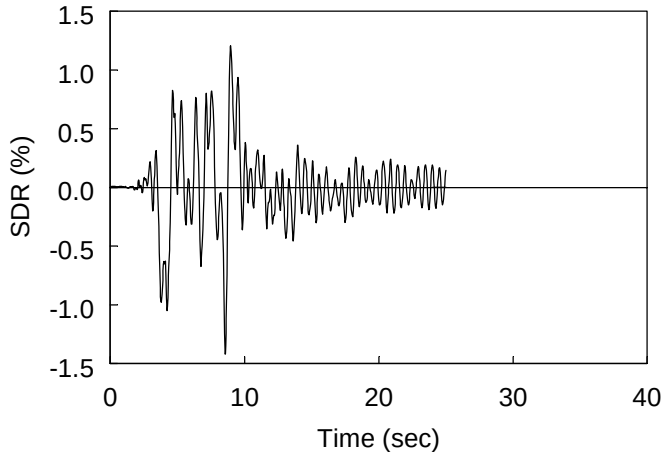

(c) First Story

3-Story BRBF: Story Drift Ratio Time-Histories (Record P09)

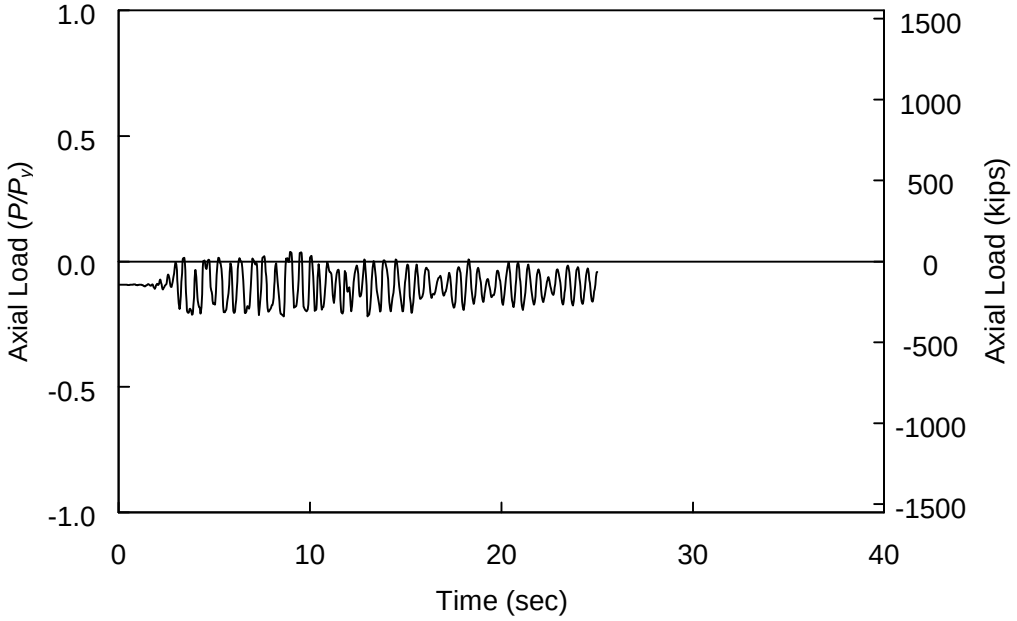

(a) Axial Load

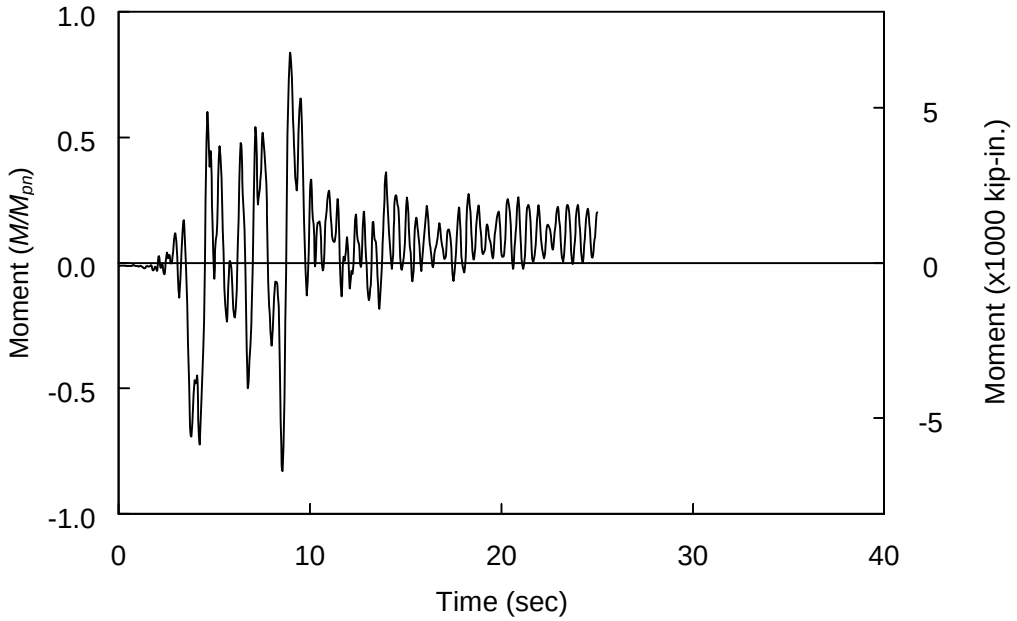

(b) Moment at Column Base

3-Story BRBF: Column Response Time-Histories (Record P09)

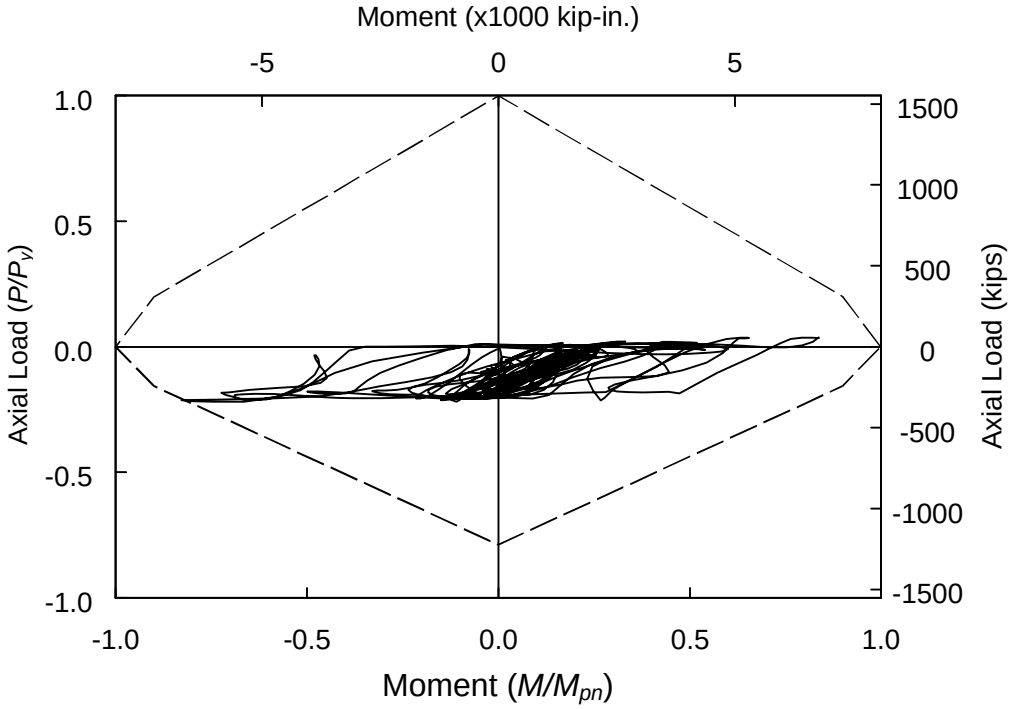

3-Story BRBF: Axial Load-Moment Interaction (Record P09)

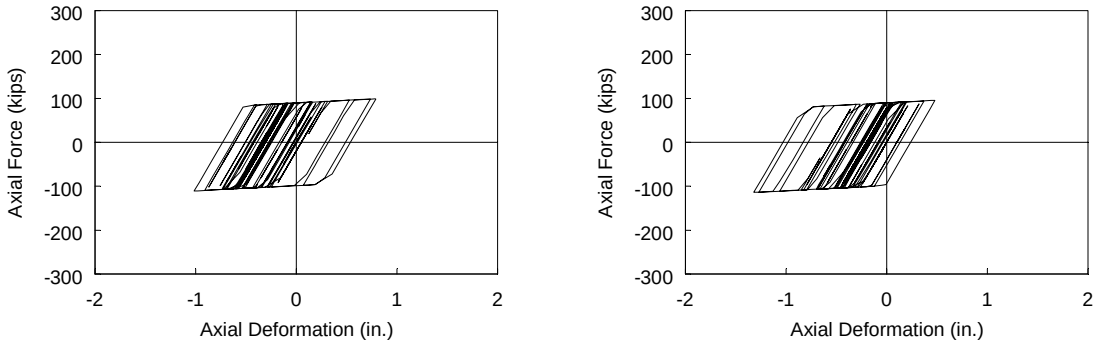

(a) Third Story

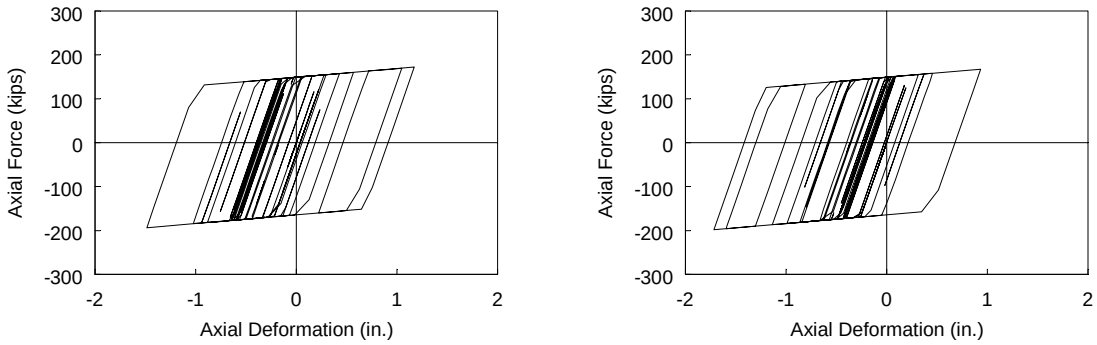

(b) Second Story

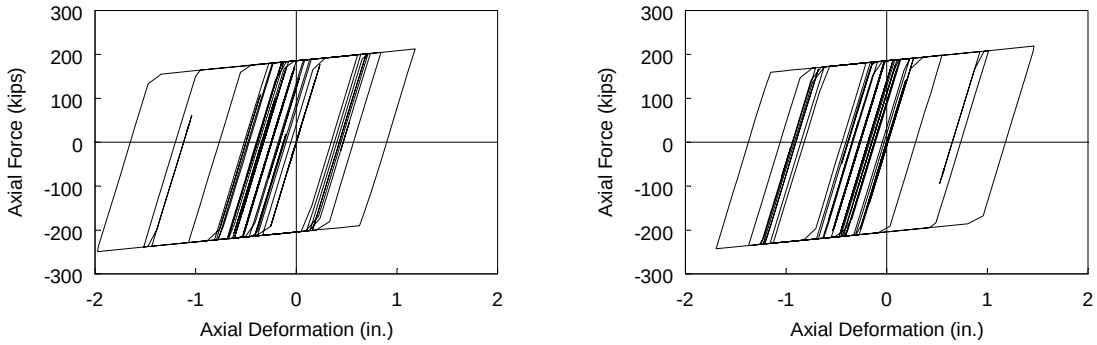

(c) First Story

3-Story BRBF: Brace Axial Load versus Axial Deformation Relationship (Record P09)

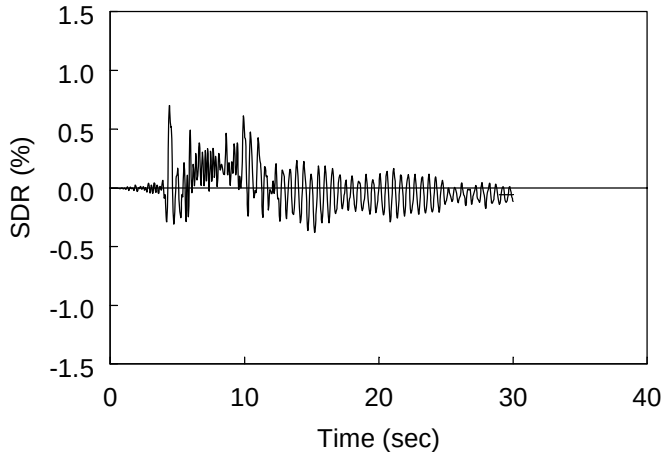

(a) Third Story

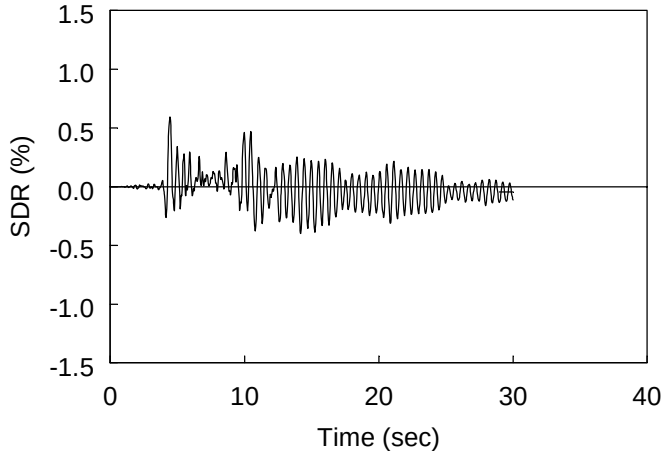

(b) Second Story

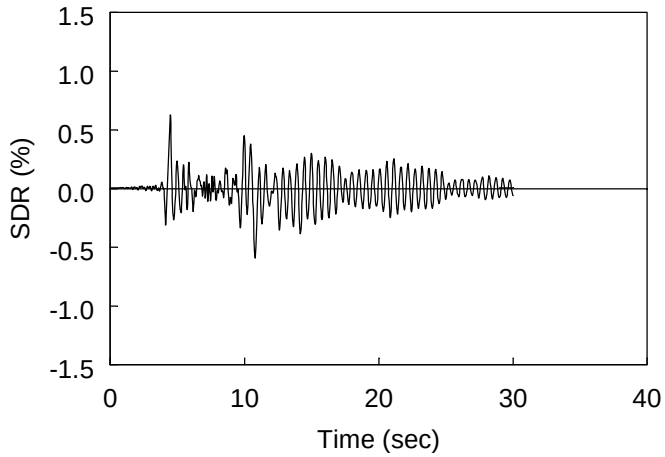

(c) First Story

3-Story BRBF: Story Drift Ratio Time-Histories (Record P14)

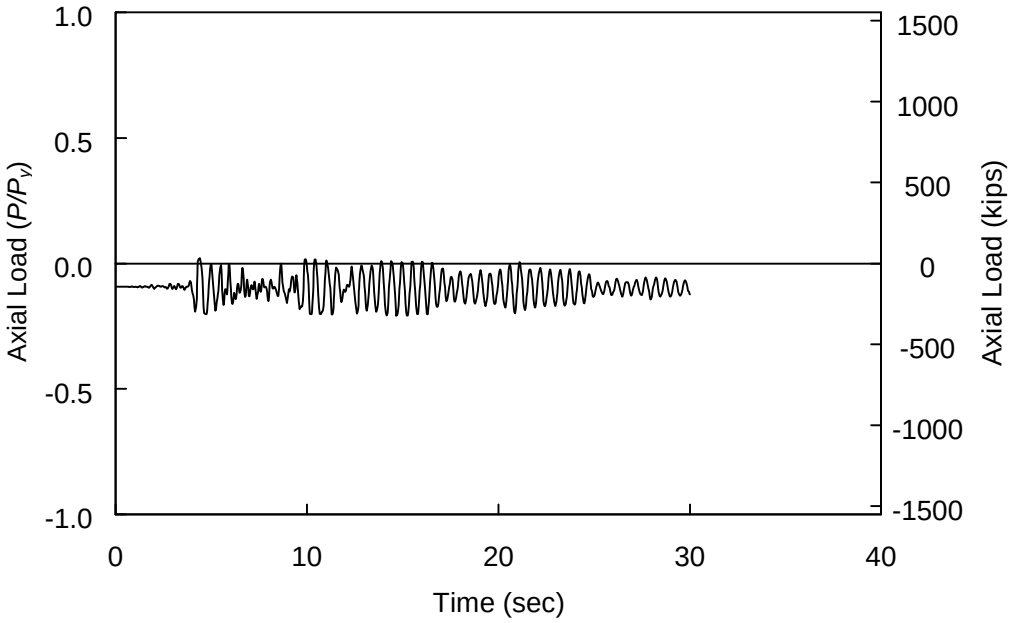

(a) Axial Load

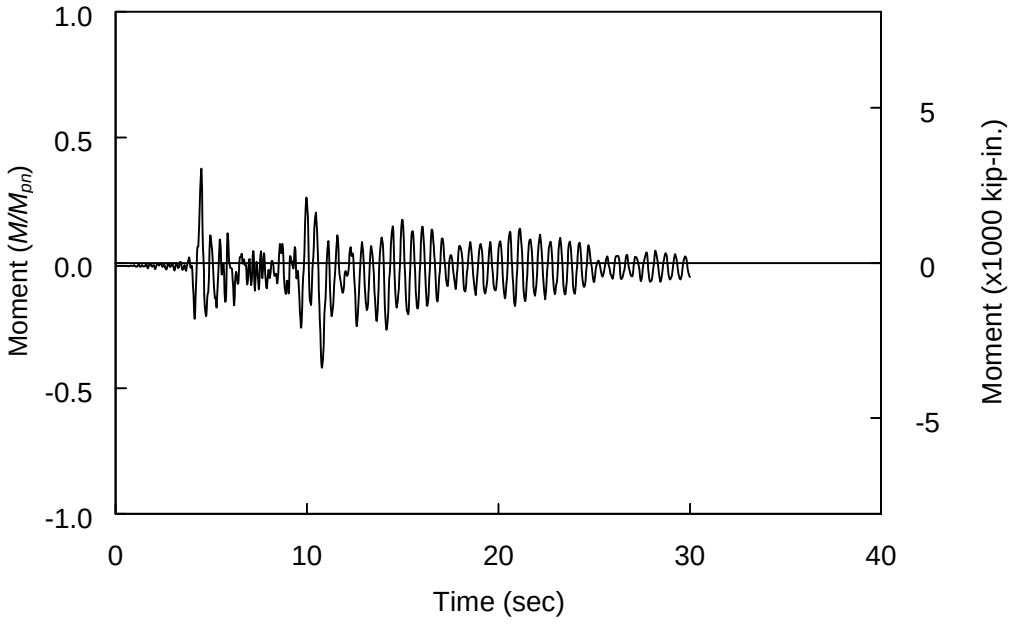

(b) Moment at Column Base

3-Story BRBF: Column Response Time-Histories (Record P14)

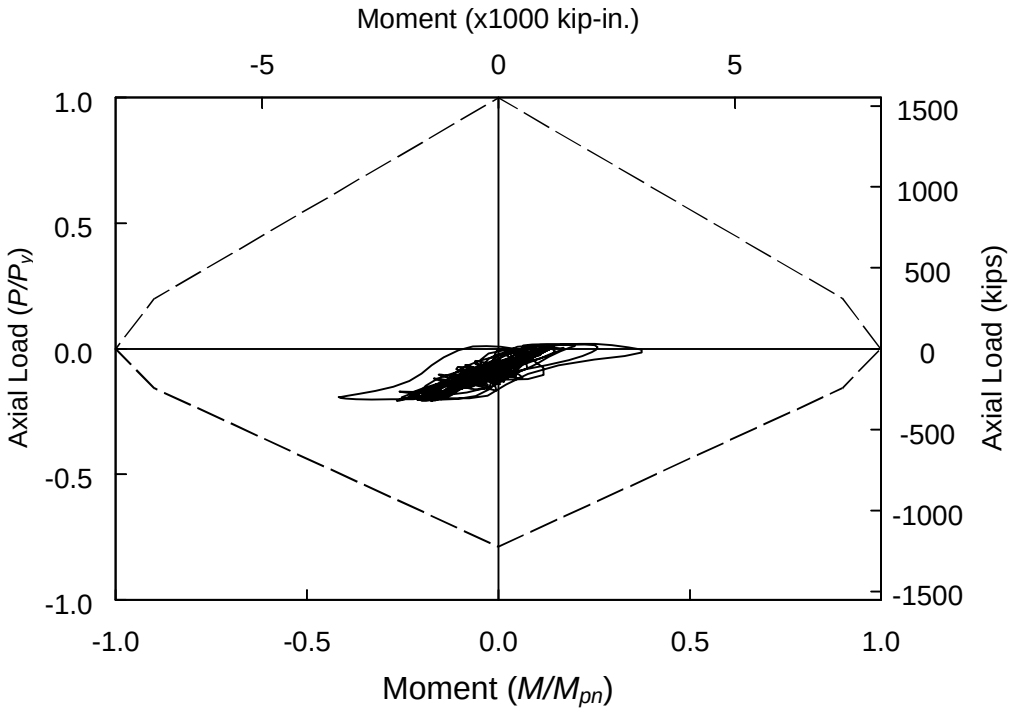

3-Story BRBF: Axial Load-Moment Interaction (Record P14)

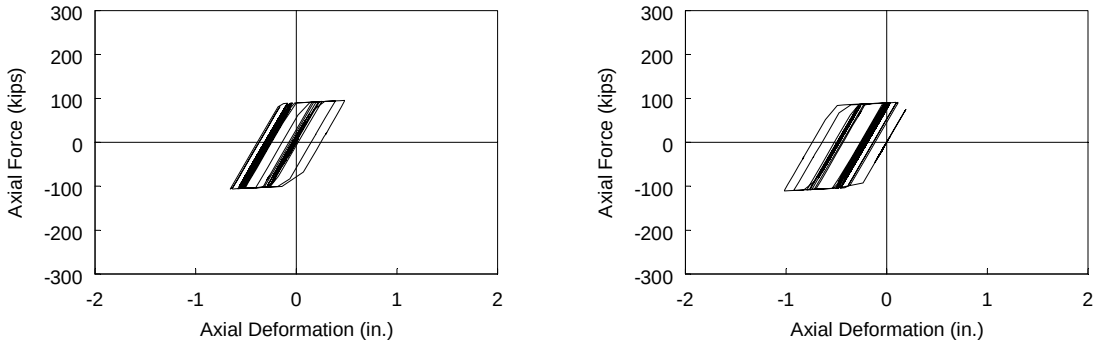

(a) Third Story

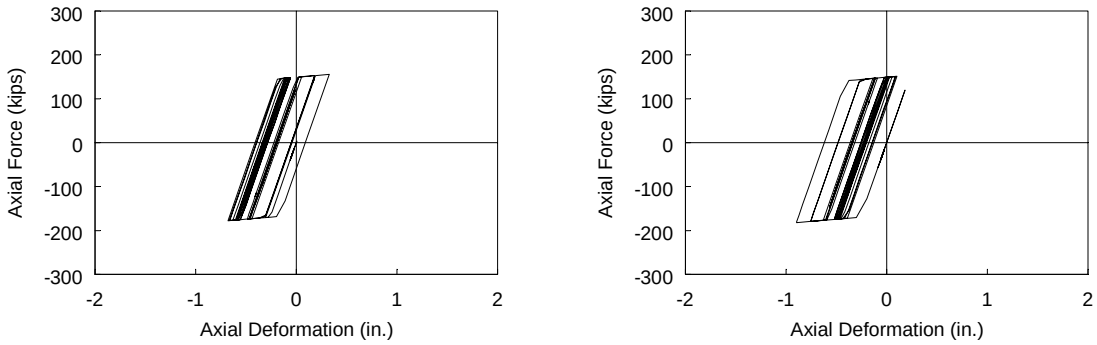

(b) Second Story

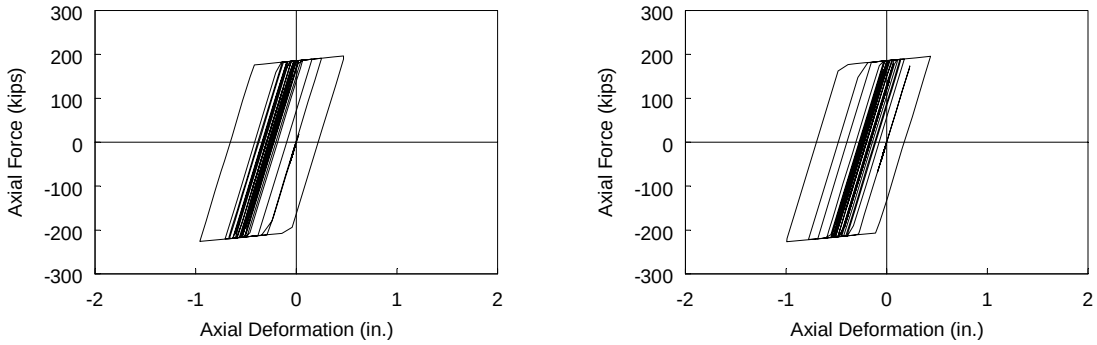

(c) First Story

3-Story BRBF: Brace Axial Load versus Axial Deformation Relationship (Record P14)

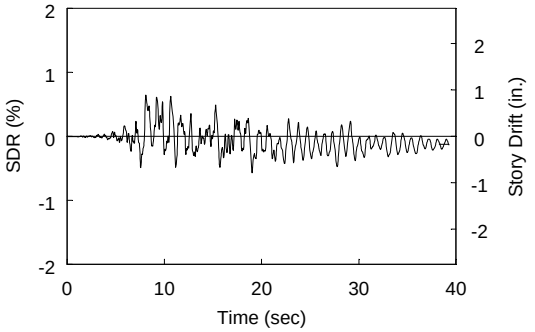

(a) Seventh Story

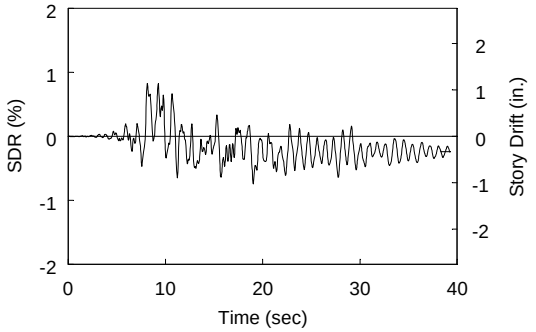

(b) Sixth Story

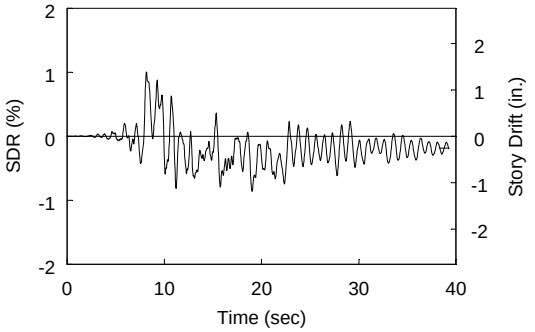

(c) Fifth Story

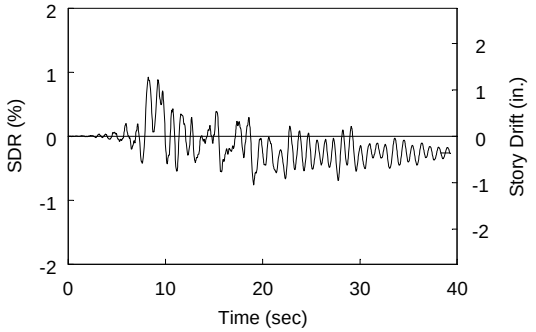

(d) Fourth Story

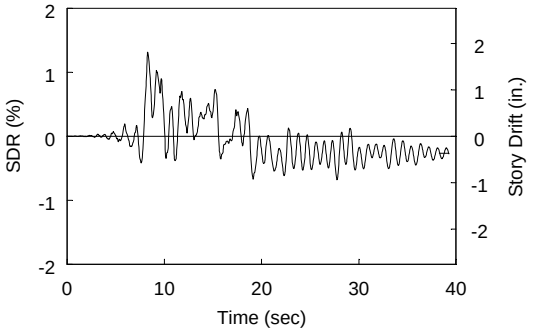

(e) Third Story

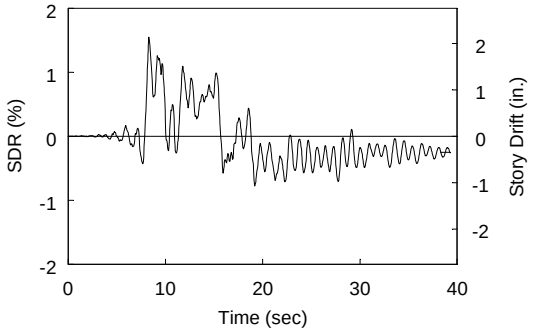

(f) Second Story

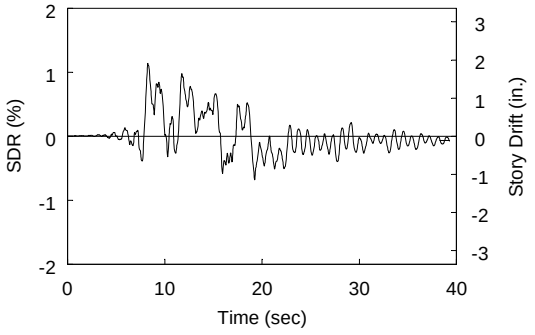

(g) First Story

7-Story BRBF: Story Drift Ratio Time-Histories (Record P08)

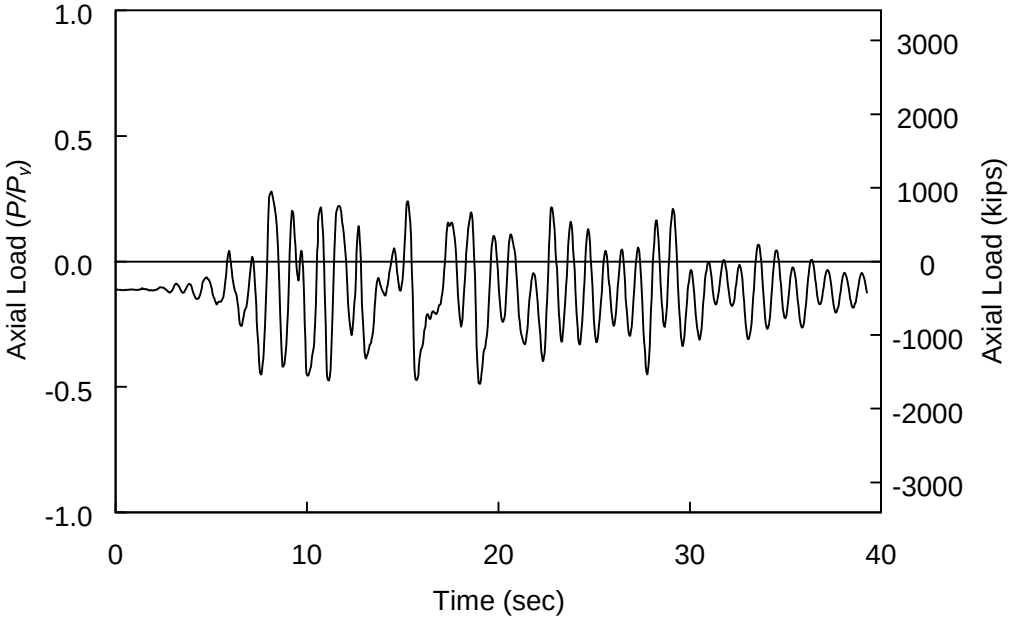

(a) Axial Load

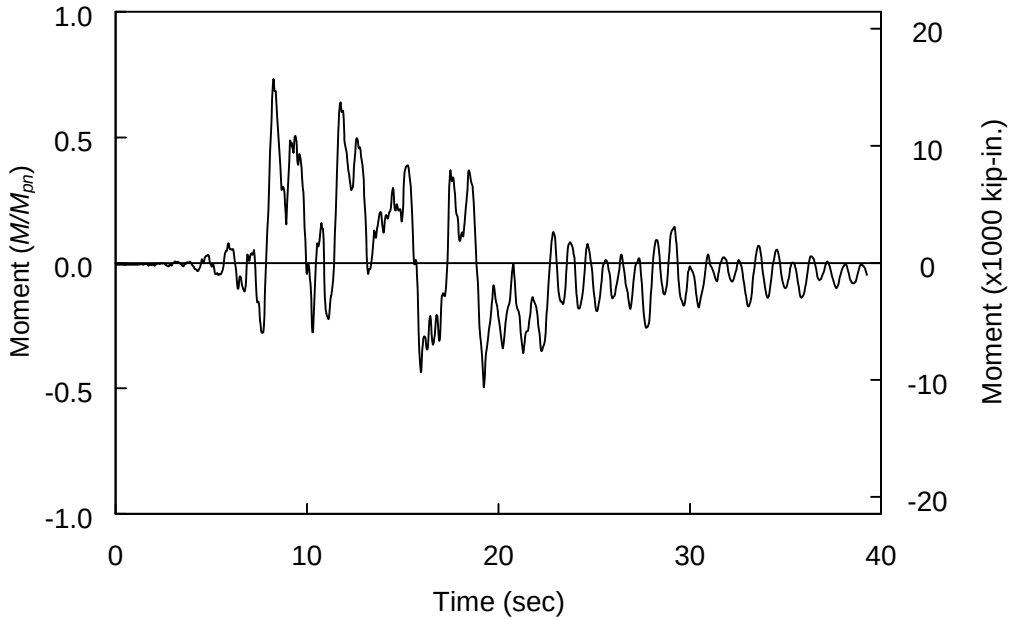

(b) Moment at Column Base

7-Story BRBF: Column Response Time-Histories (Record P08)

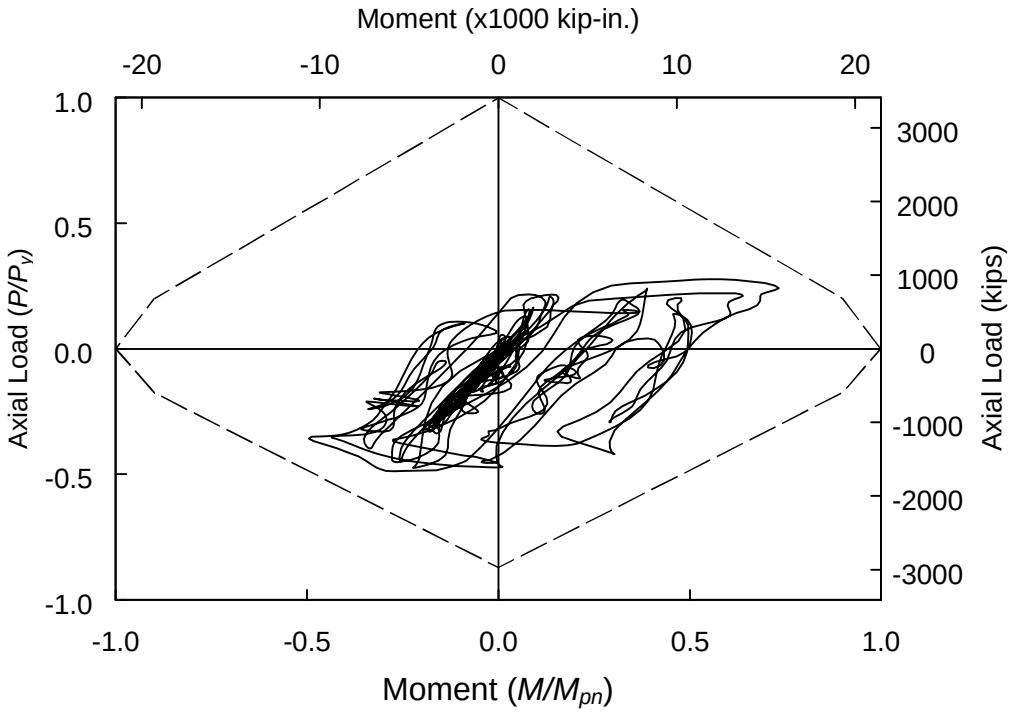

7-Story BRBF: Axial Load-Moment Interaction (Record P08)

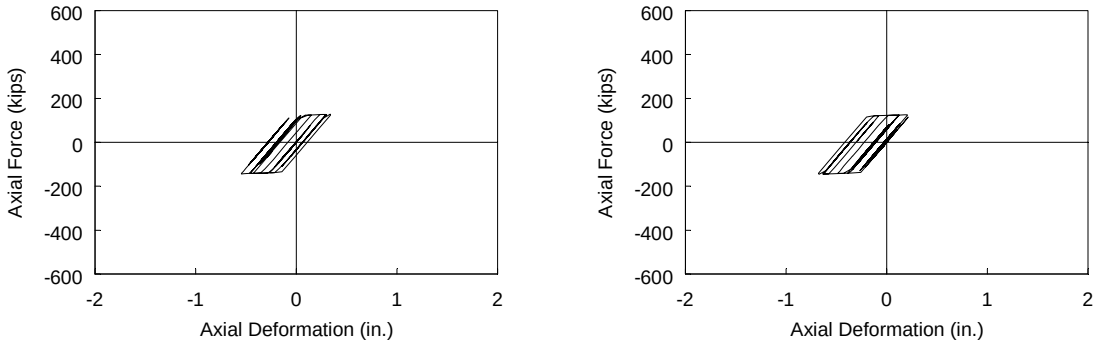

(a) Seventh Story

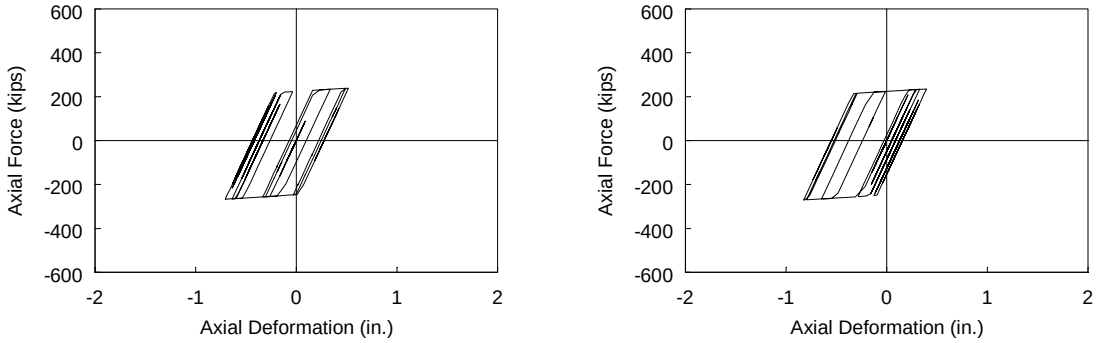

(b) Sixth Story

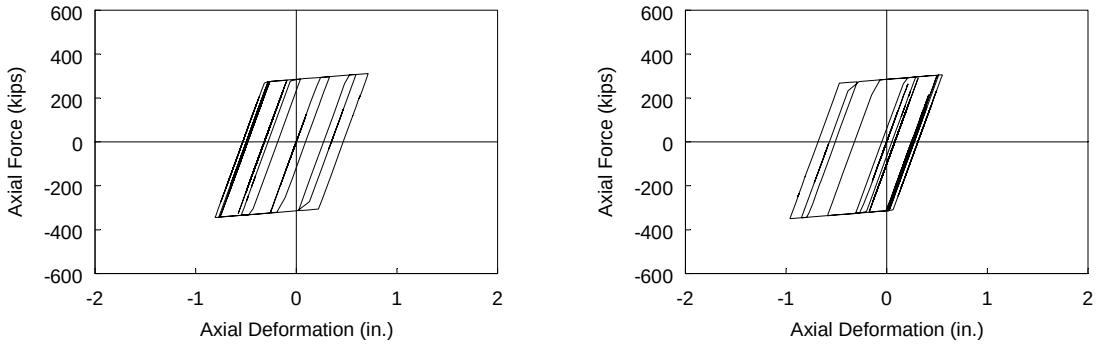

(c) Fifth Story

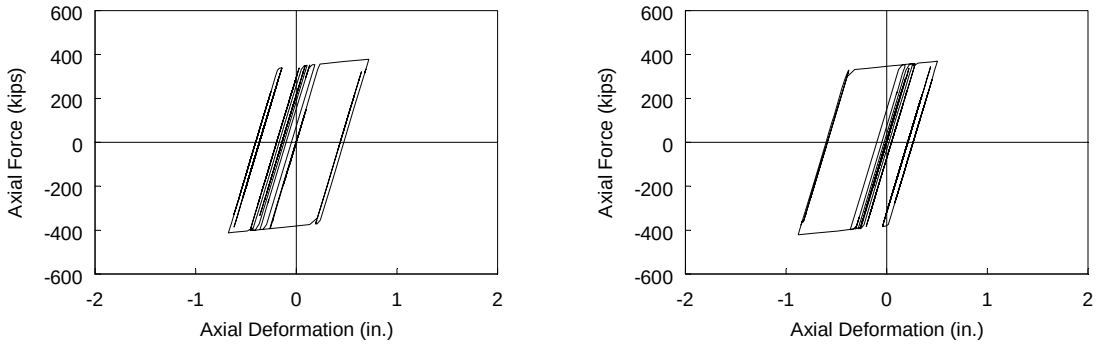

(d) Fourth Story

7-Story BRBF: Brace Axial Load versus Axial Deformation Relationship for Record P08

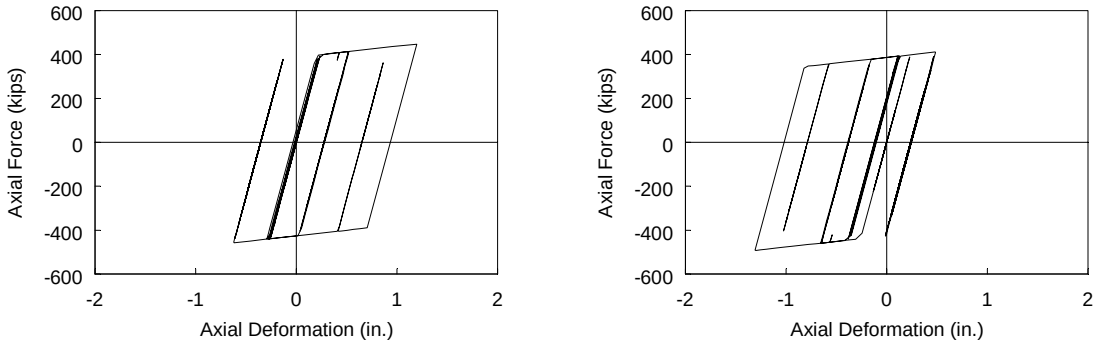

(e) Third Story

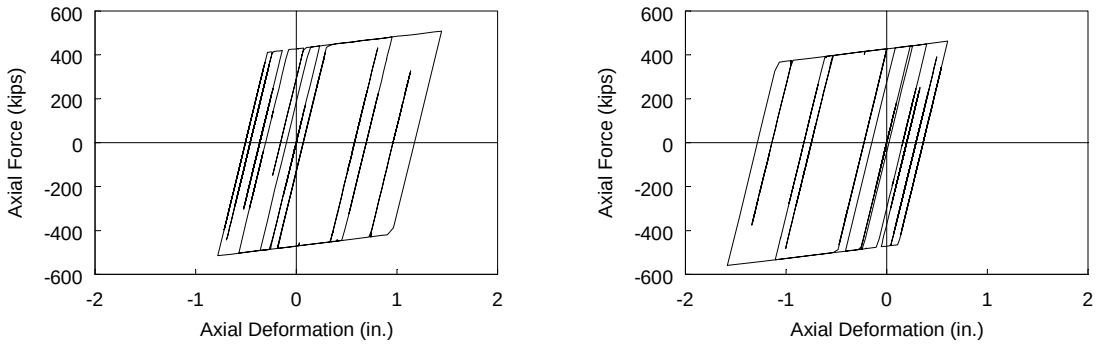

(f) Second Story

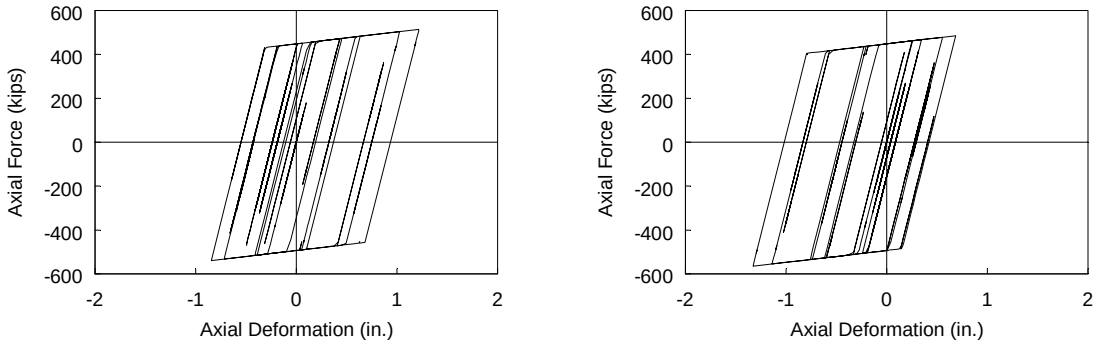

(g) First Story

7-Story BRBF: Brace Axial Load versus Axial Deformation Relationship for Record P08 (cont.)

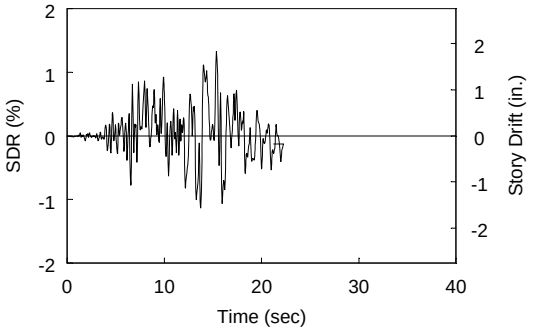

(a) Seventh Story

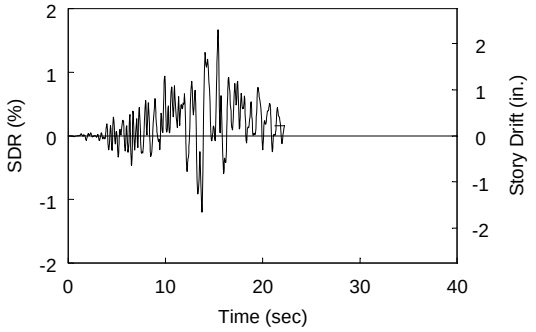

(b) Sixth Story

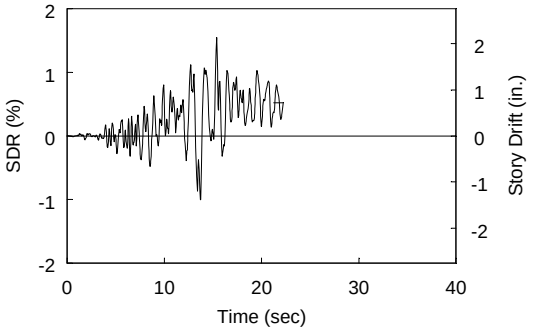

(c) Fifth Story

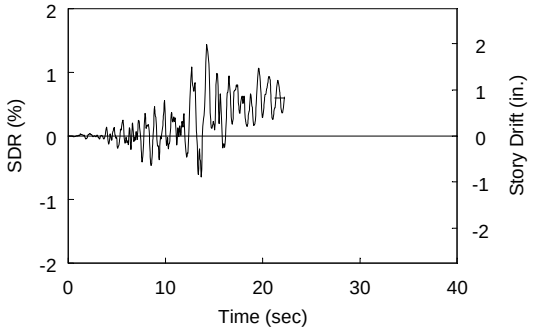

(d) Fourth Story

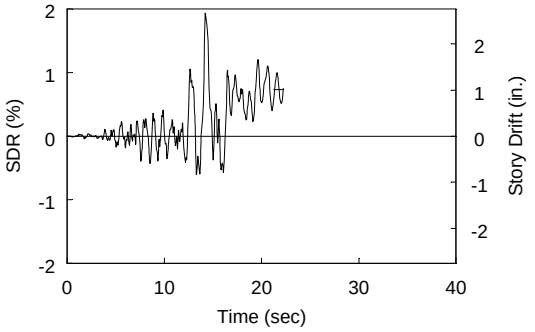

(e) Third Story

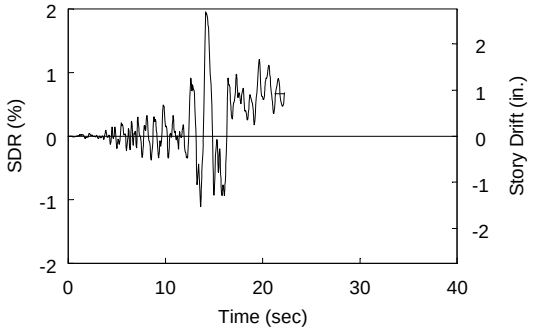

(f) Second Story

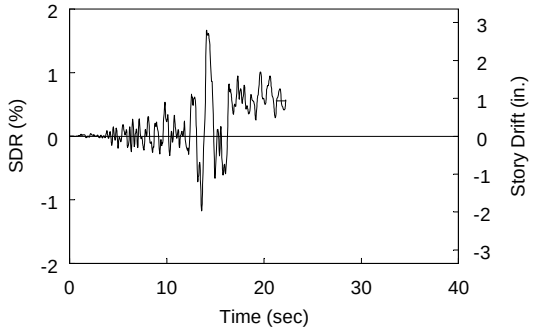

(g) First Story

7-Story BRBF: Story Drift Ratio Time-Histories (Record P19)

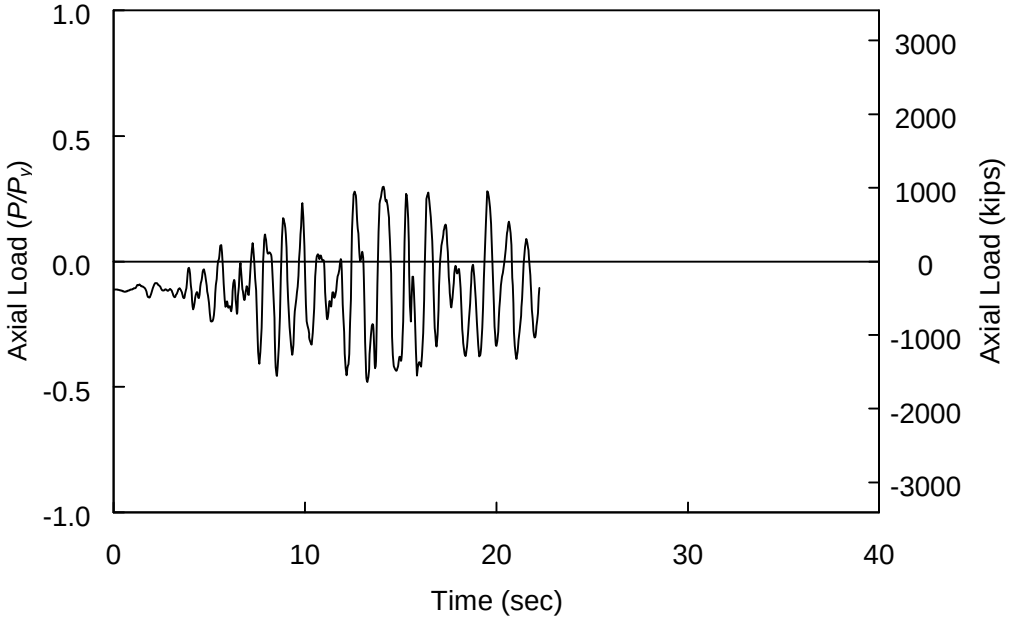

(a) Axial Load

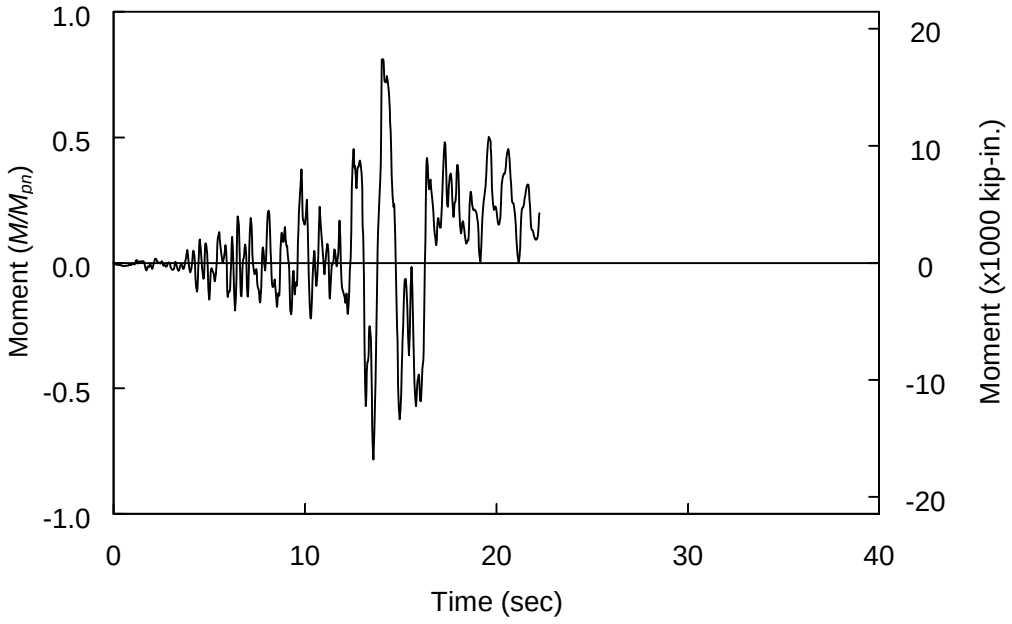

(b) Moment at Column Base

7-Story BRBF: Column Response Time-Histories (Record P19)

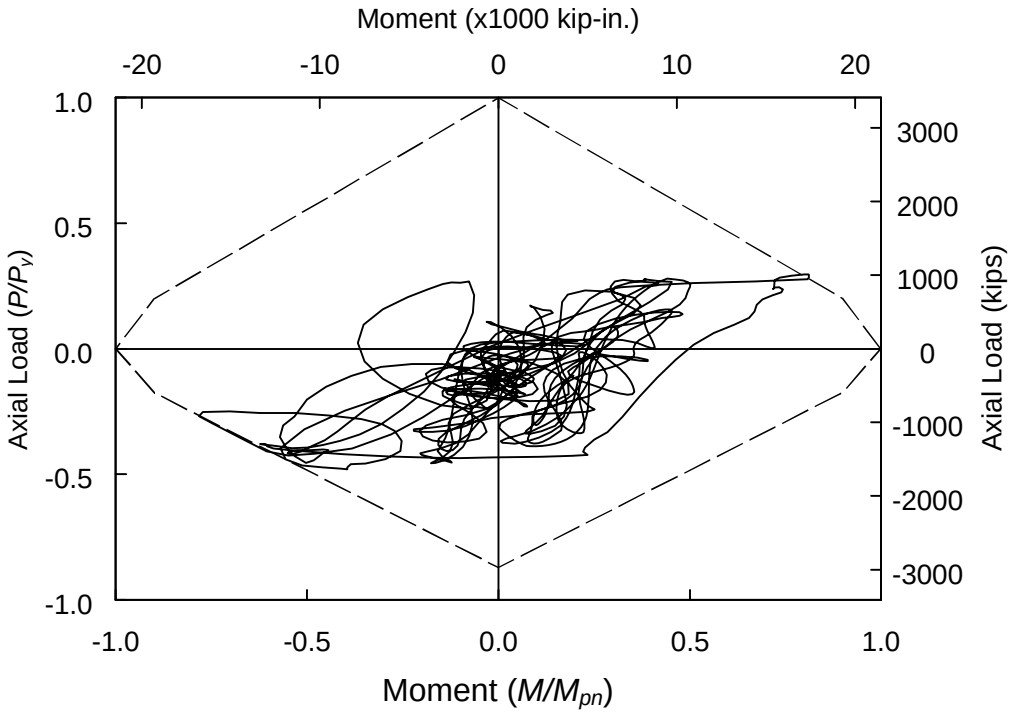

7-Story BRBF: Axial Load-Moment Interaction (Record P19)

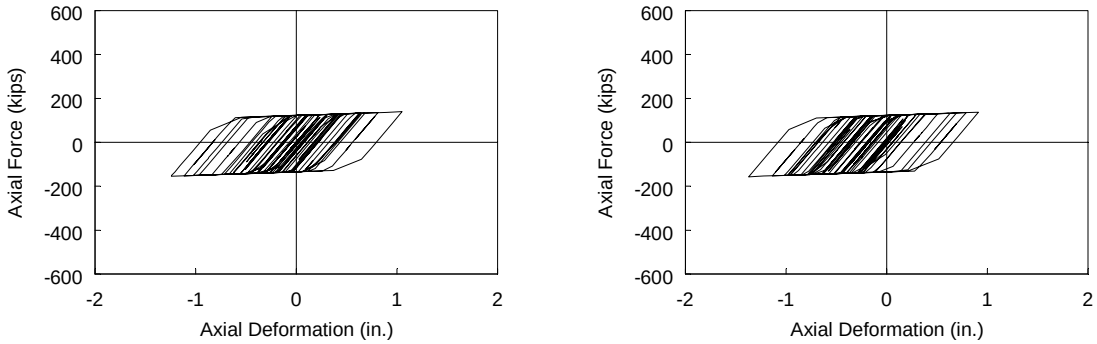

(a) Seventh Story

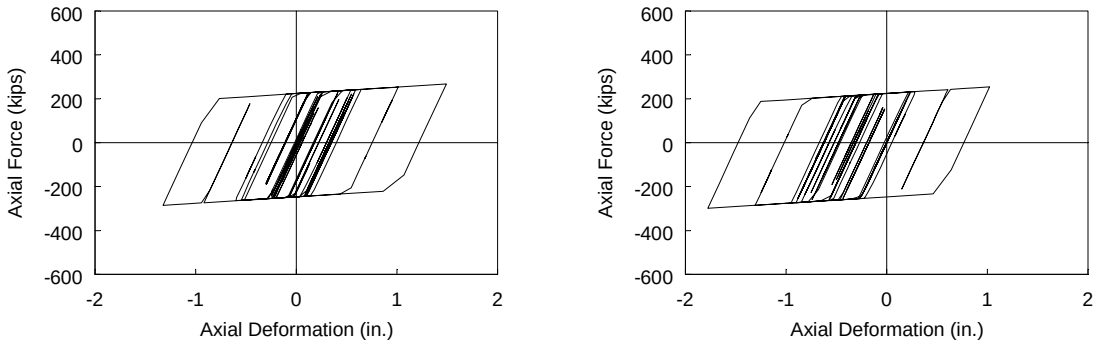

(b) Sixth Story

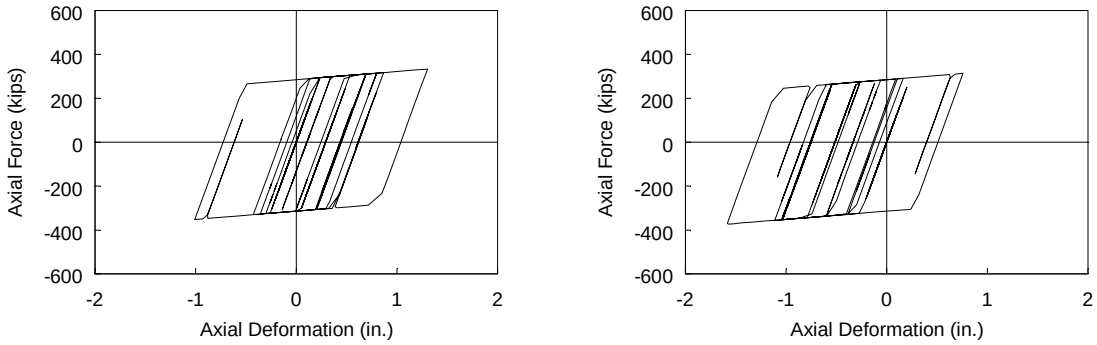

(c) Fifth Story

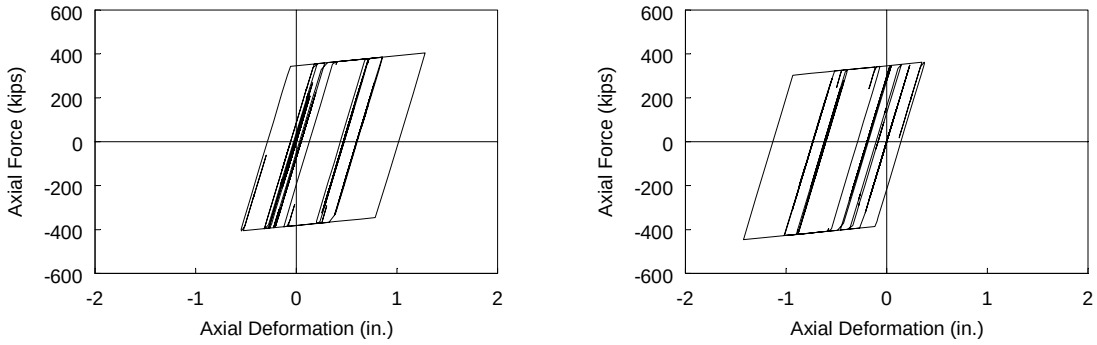

(d) Fourth Story

7-Story BRBF: Brace Axial Load versus Axial Deformation Relationship for Record P19

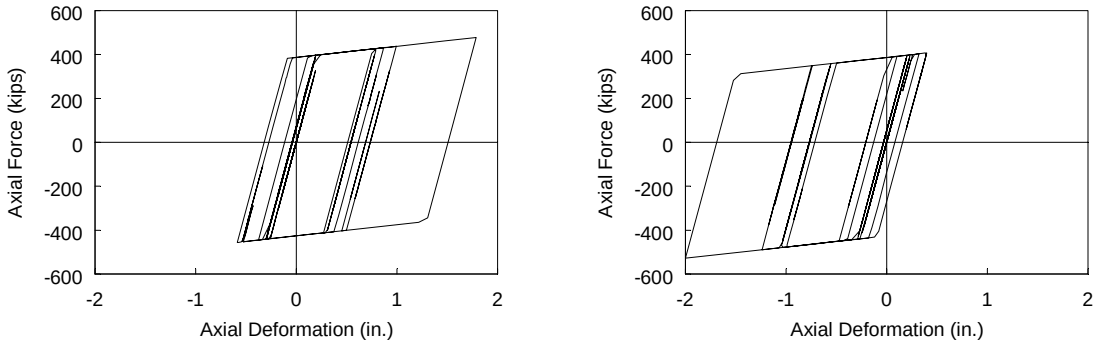

(e) Third Story

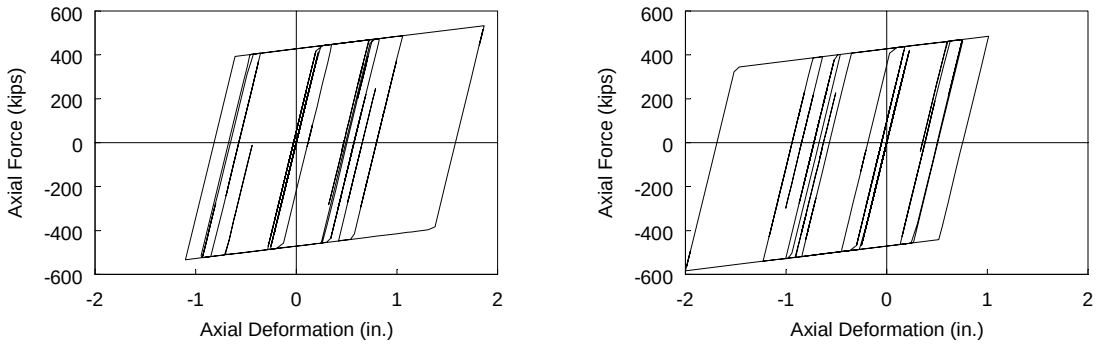

(f) Second Story

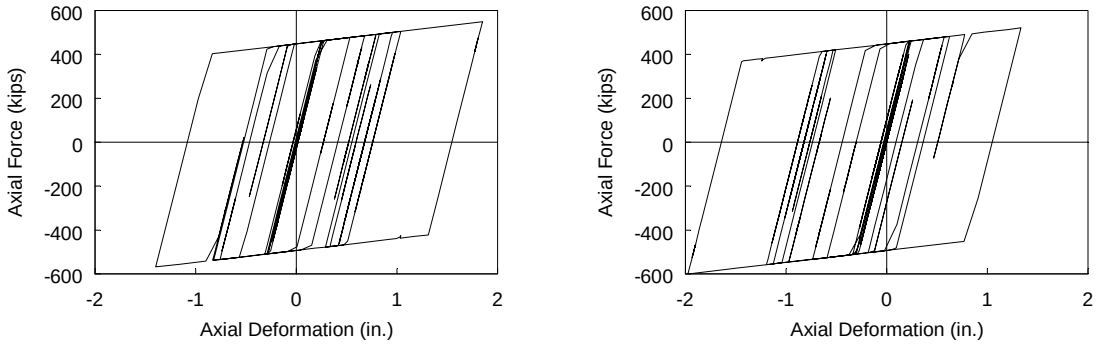

(g) First Story

7-Story BRBF: Brace Axial Load versus Axial Deformation Relationship for Record P19 (cont.)

APPENDIX B: Strain Gage Data

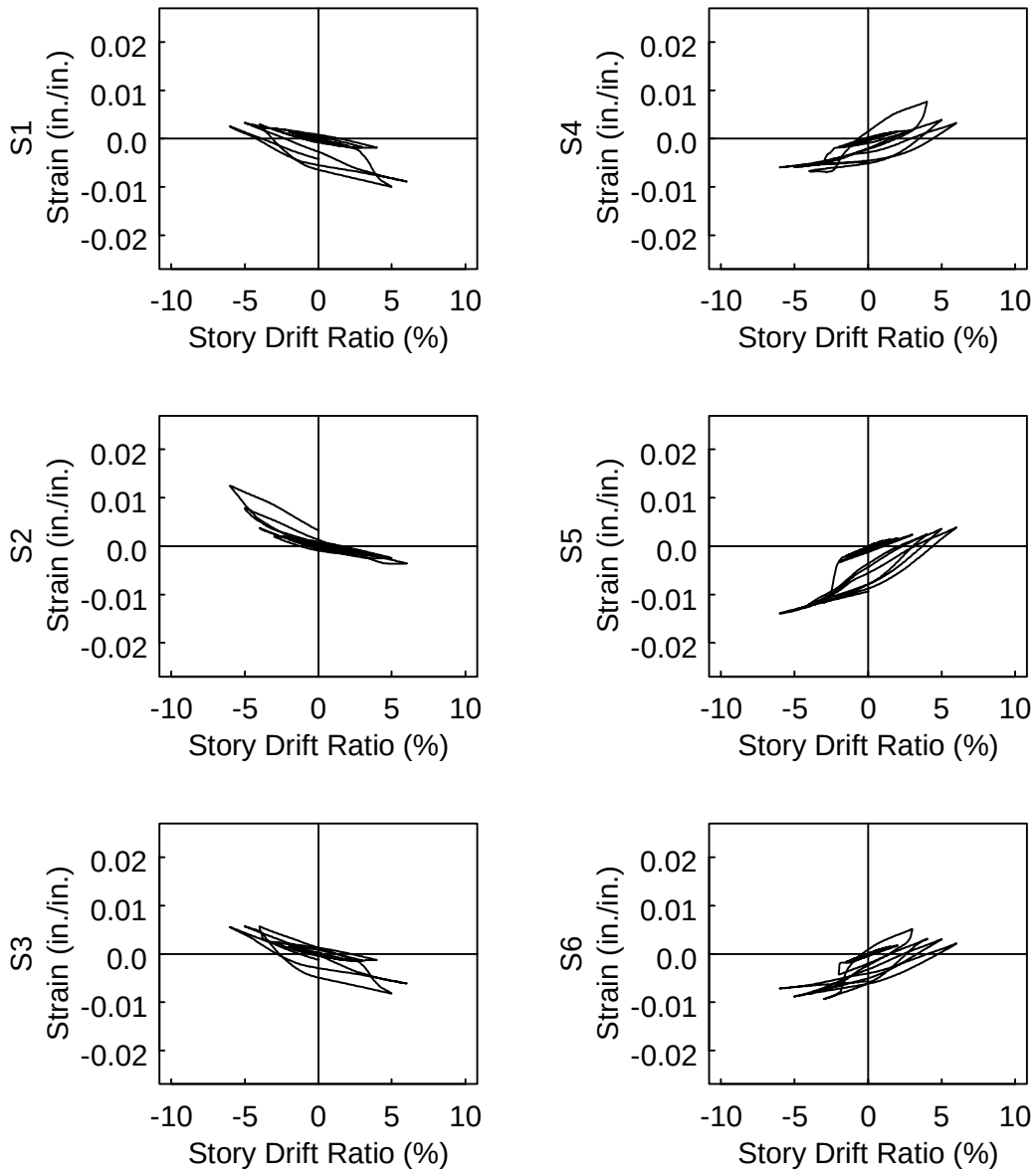

Specimen W14×132-35: Strain Gages S1 to S6

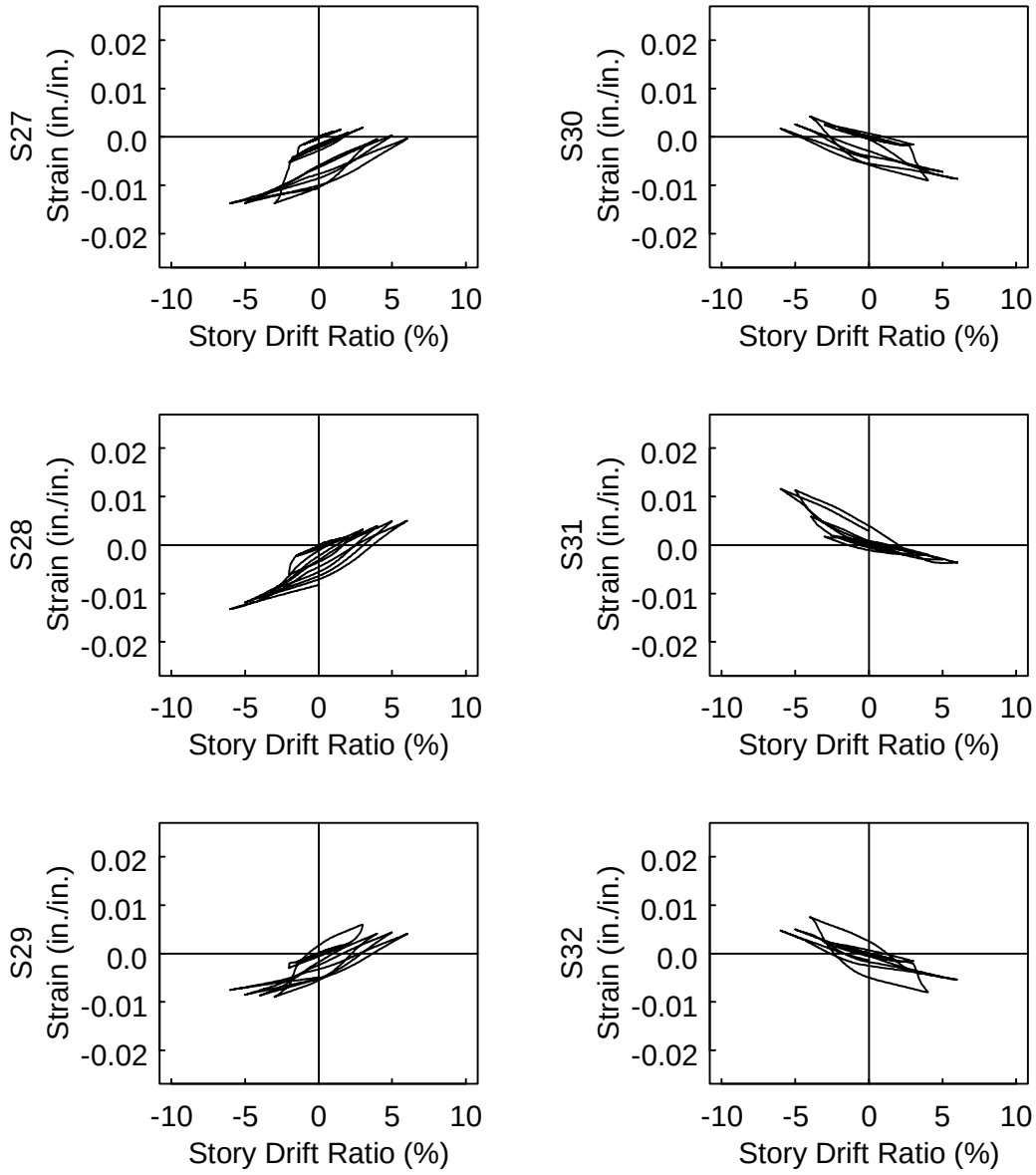

Specimen W14×132-35: Strain Gages S27 to S32

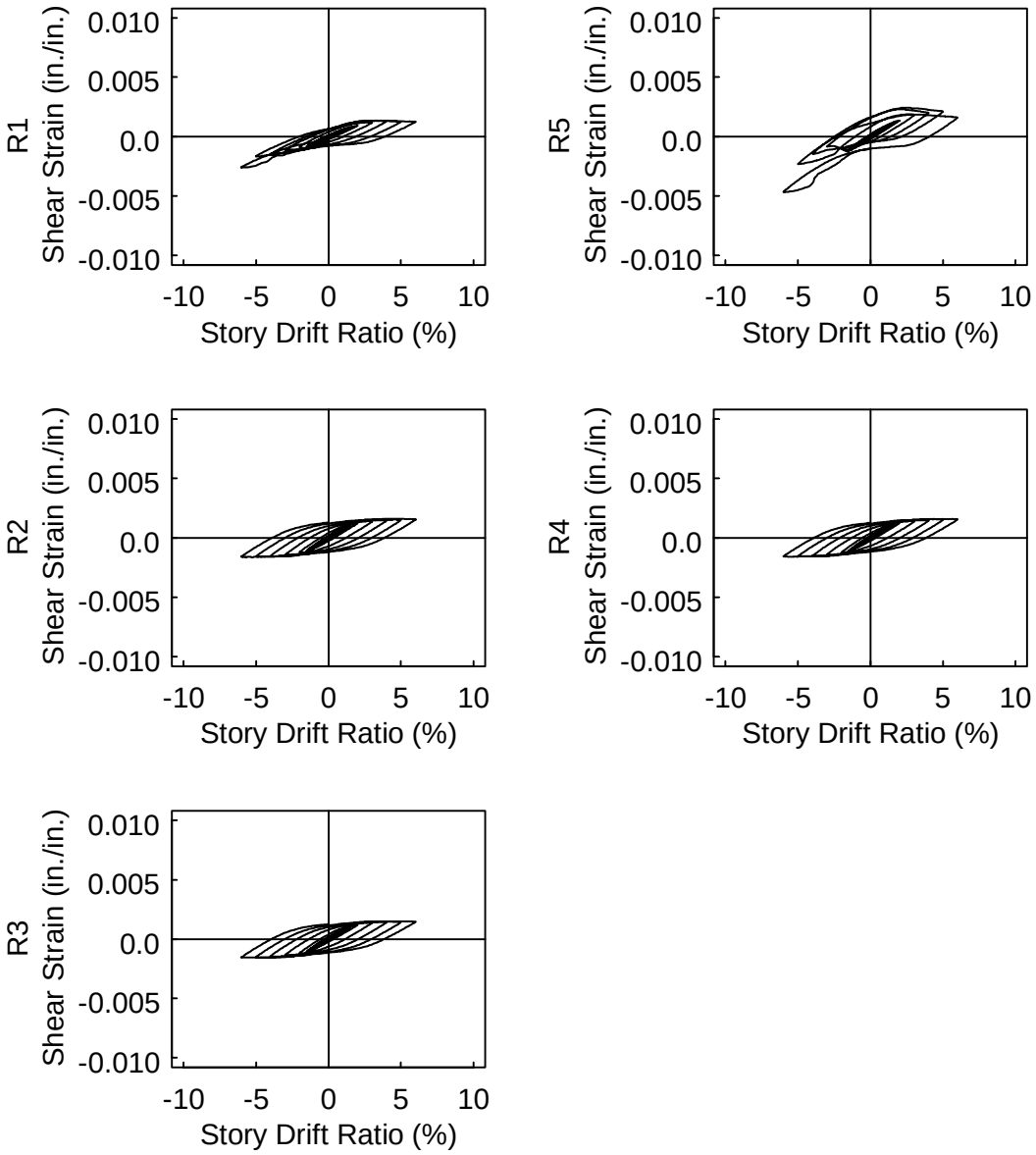

Specimen W14×132-35: Strain Rosettes R1 to R5

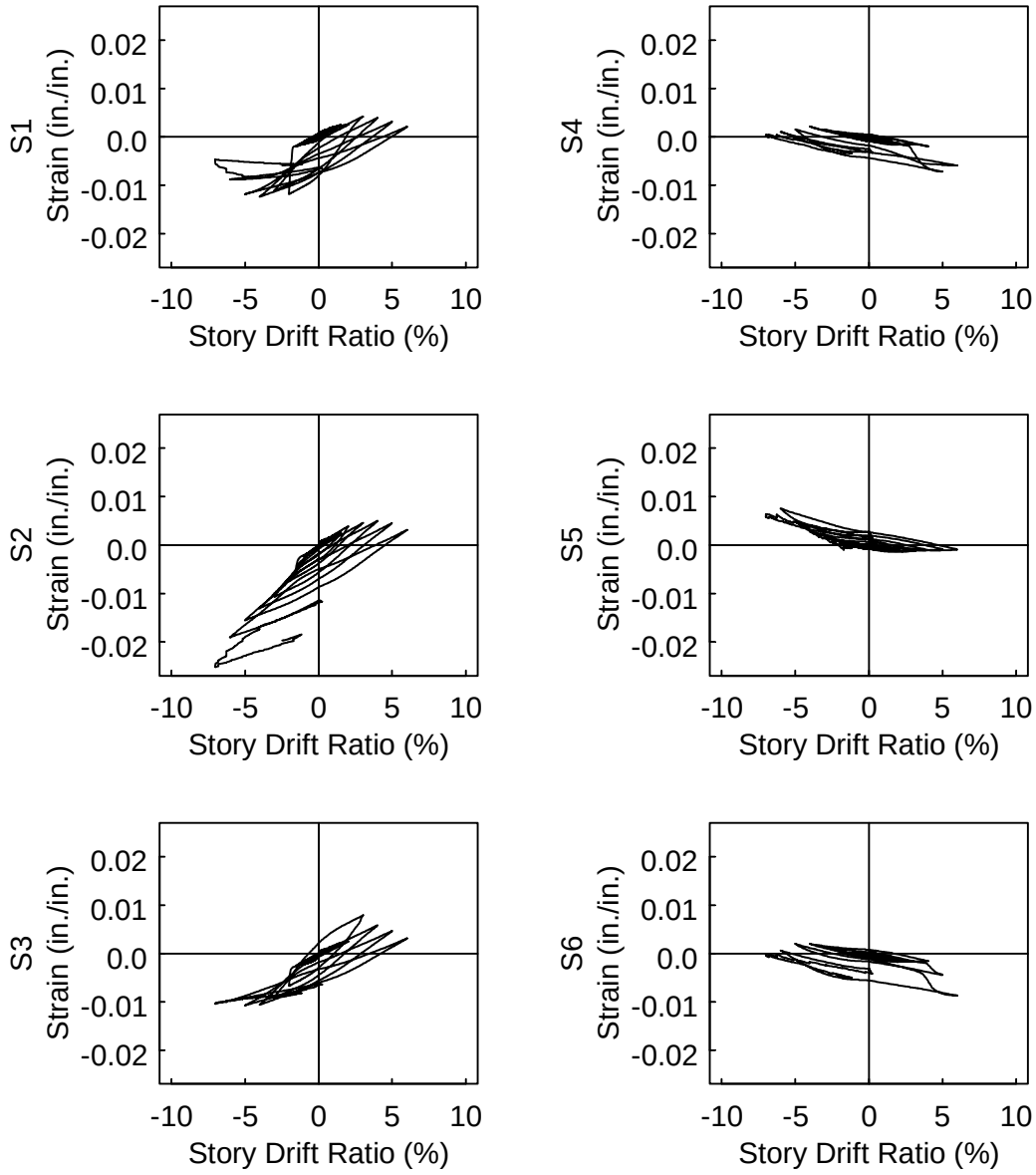

Specimen W14×132-55: Strain Gages S1 to S6

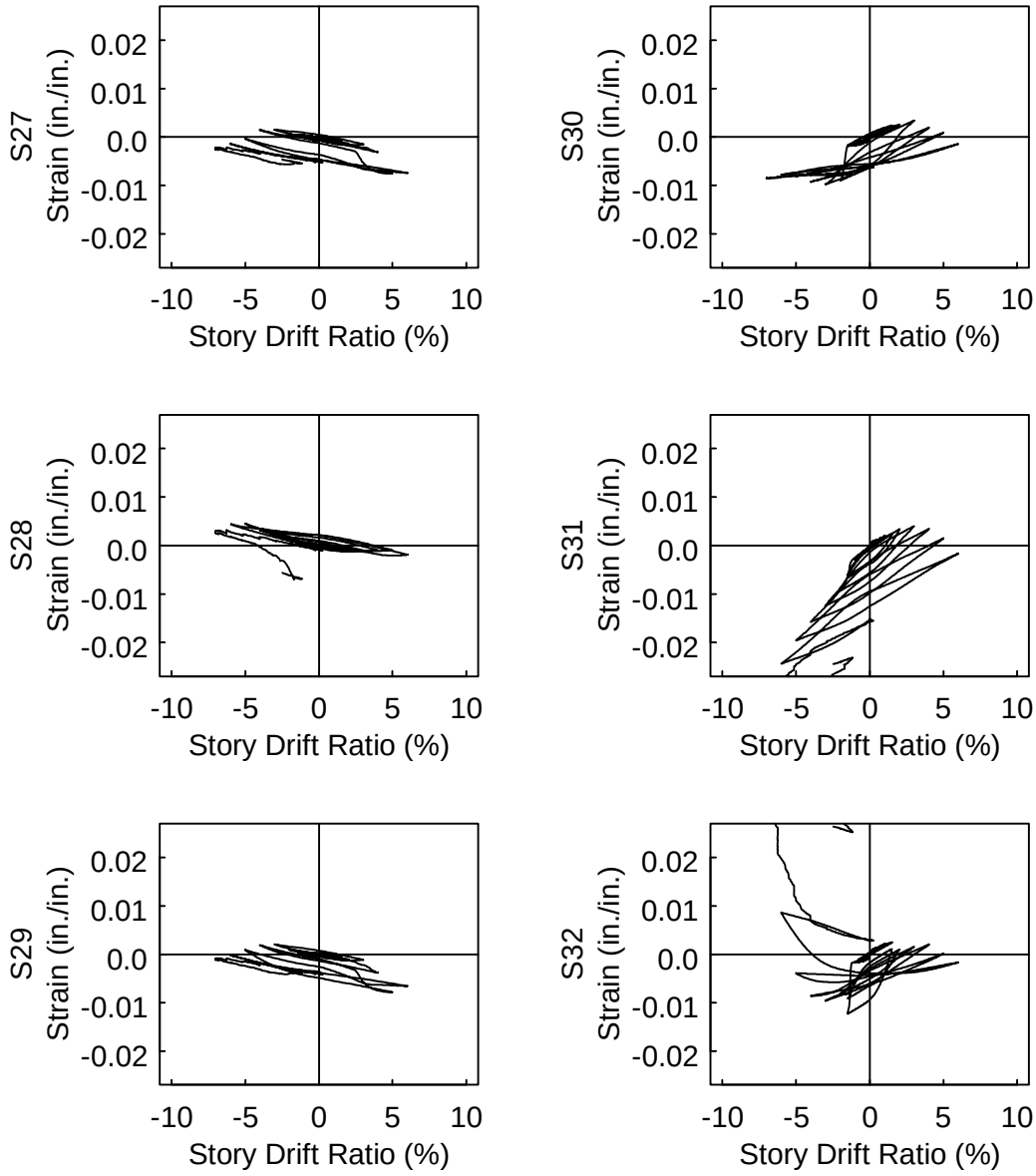

Specimen W14×132-55: Strain Gages S27 to S32

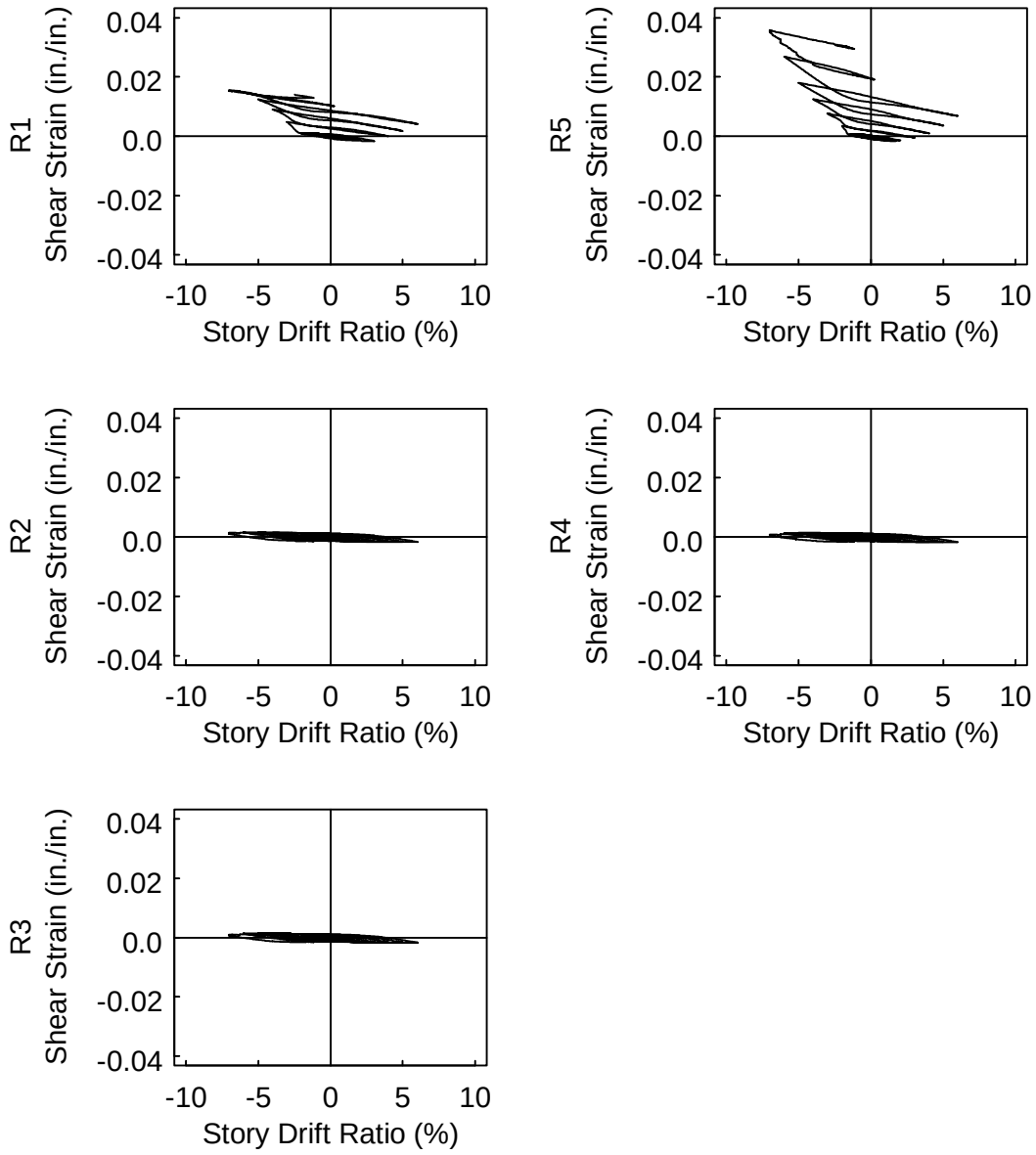

Specimen W14×132-55: Strain Rosettes R1 to R5

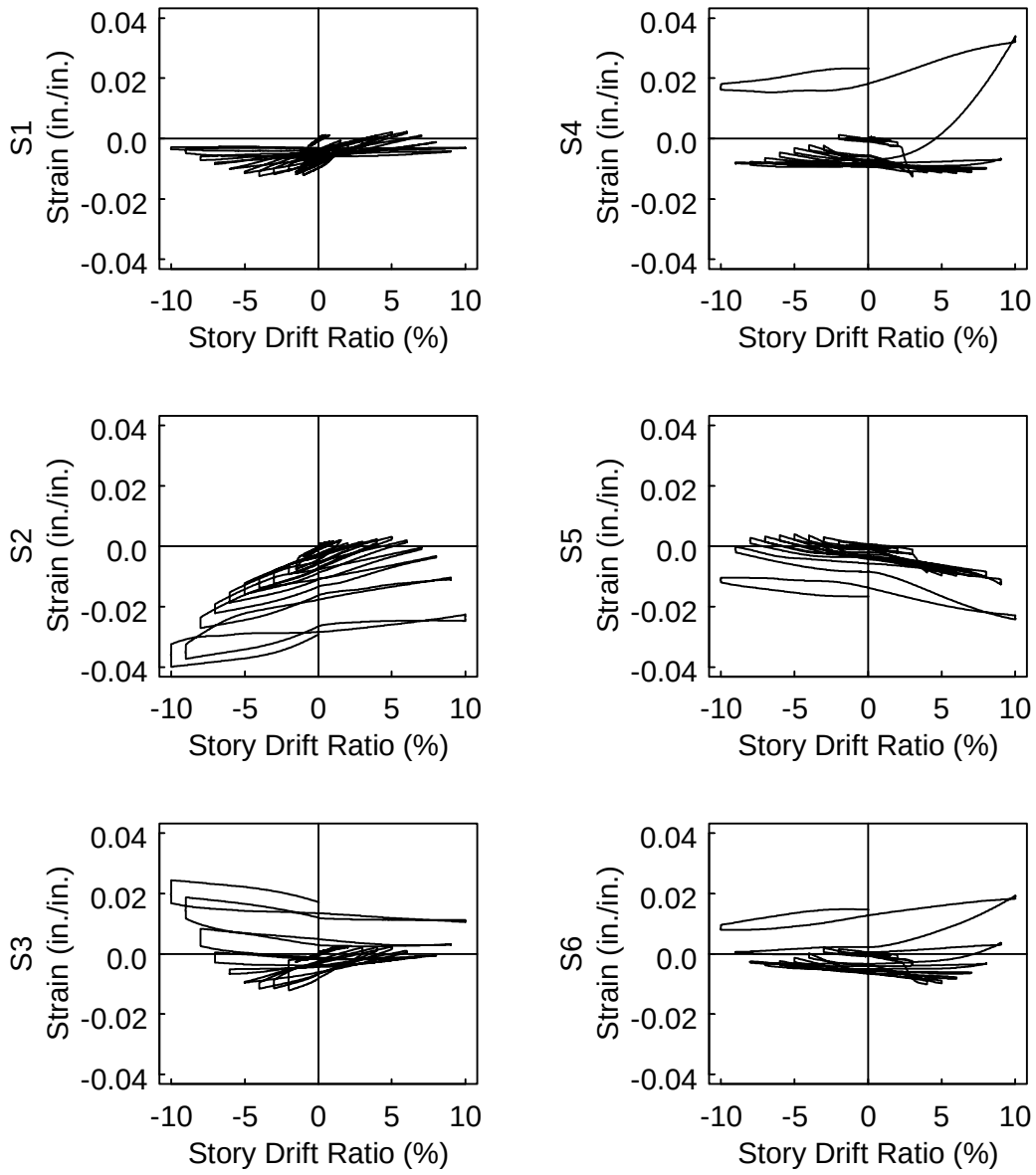

Specimen W14×132-75: Strain Gages S1 to S6

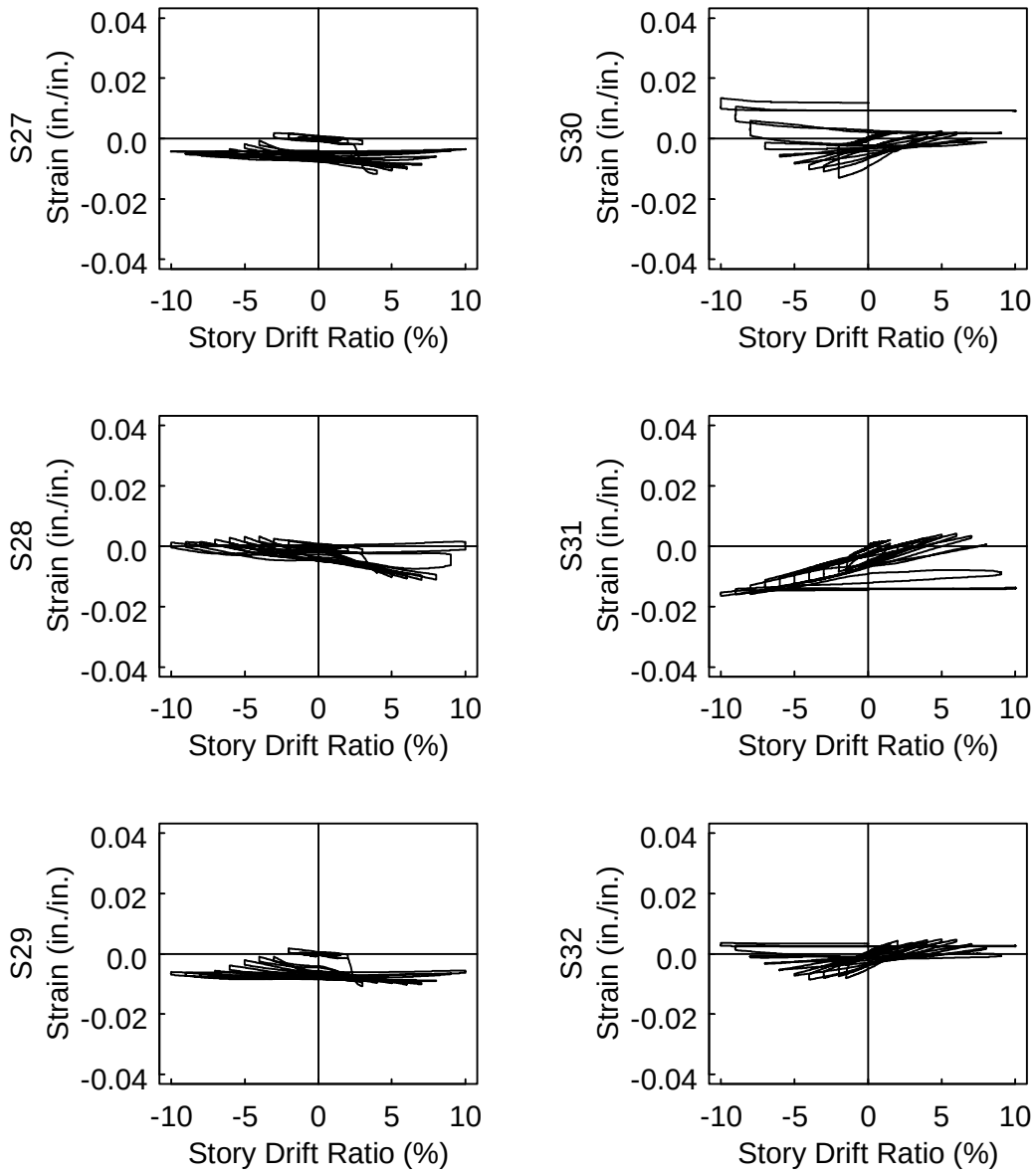

Specimen W14×132-75: Strain Gages S27 to S32

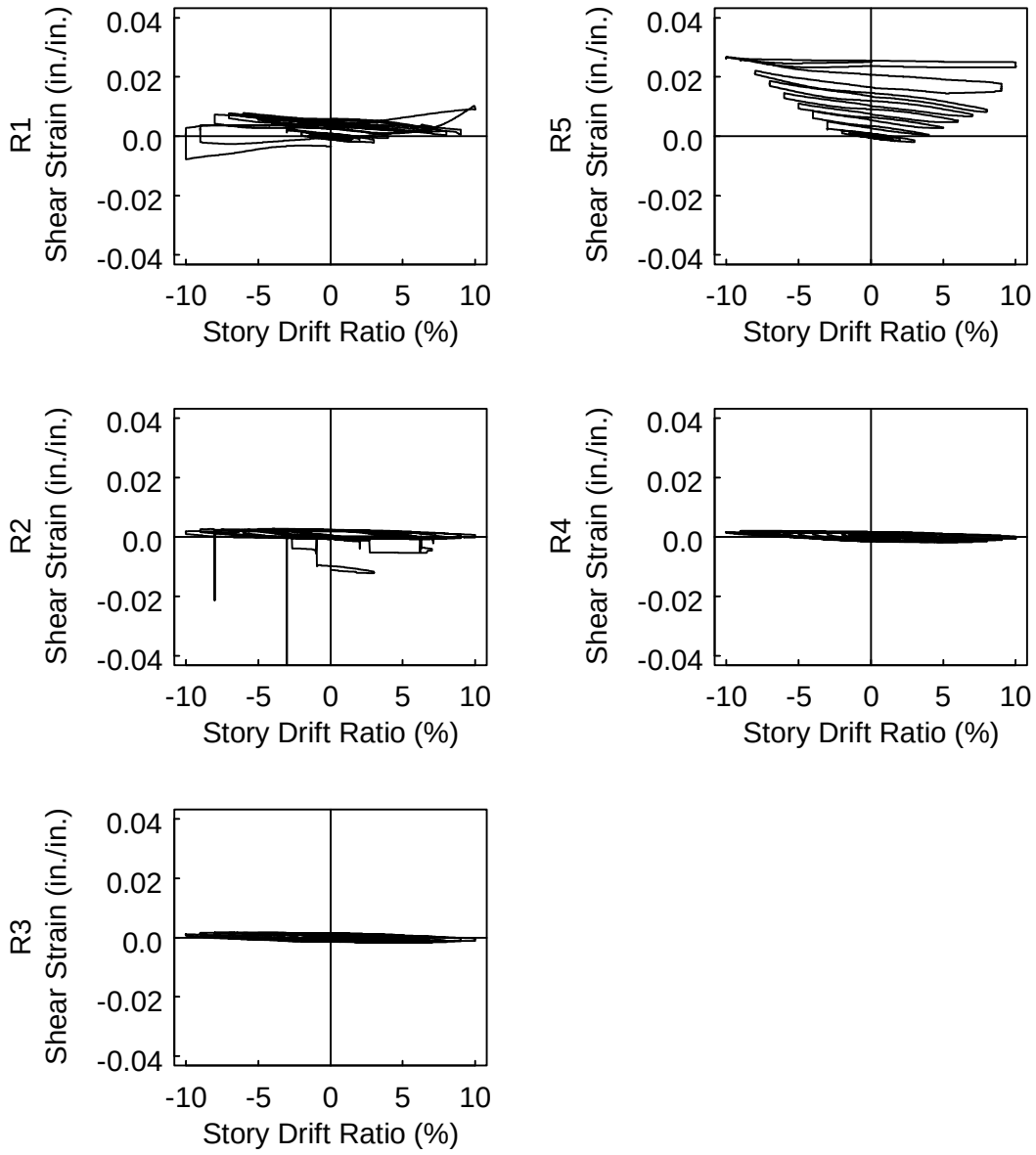

Specimen W14×132-75: Strain Rosettes R1 to R5

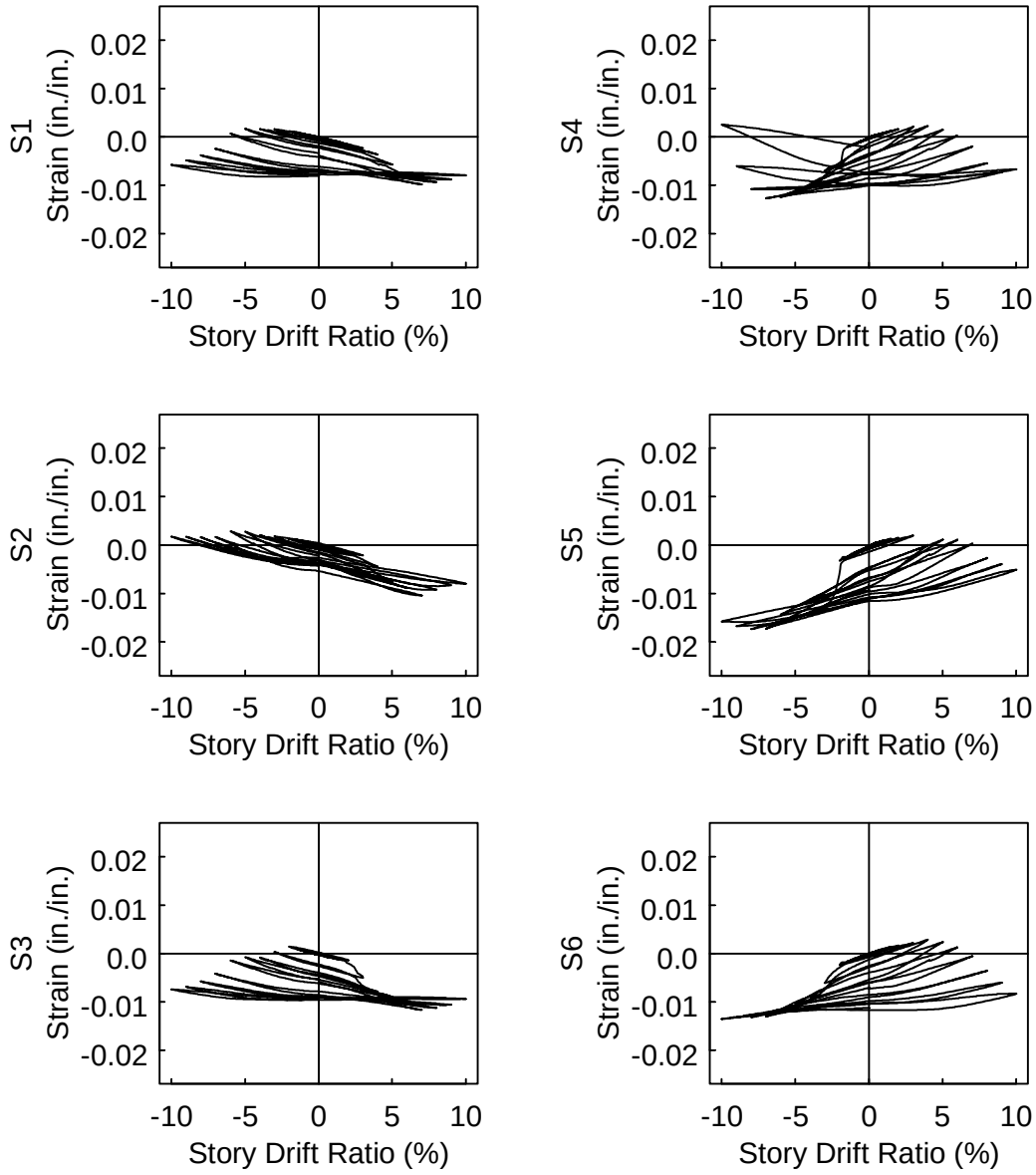

Specimen W14×176-35: Strain Gages S1 to S6

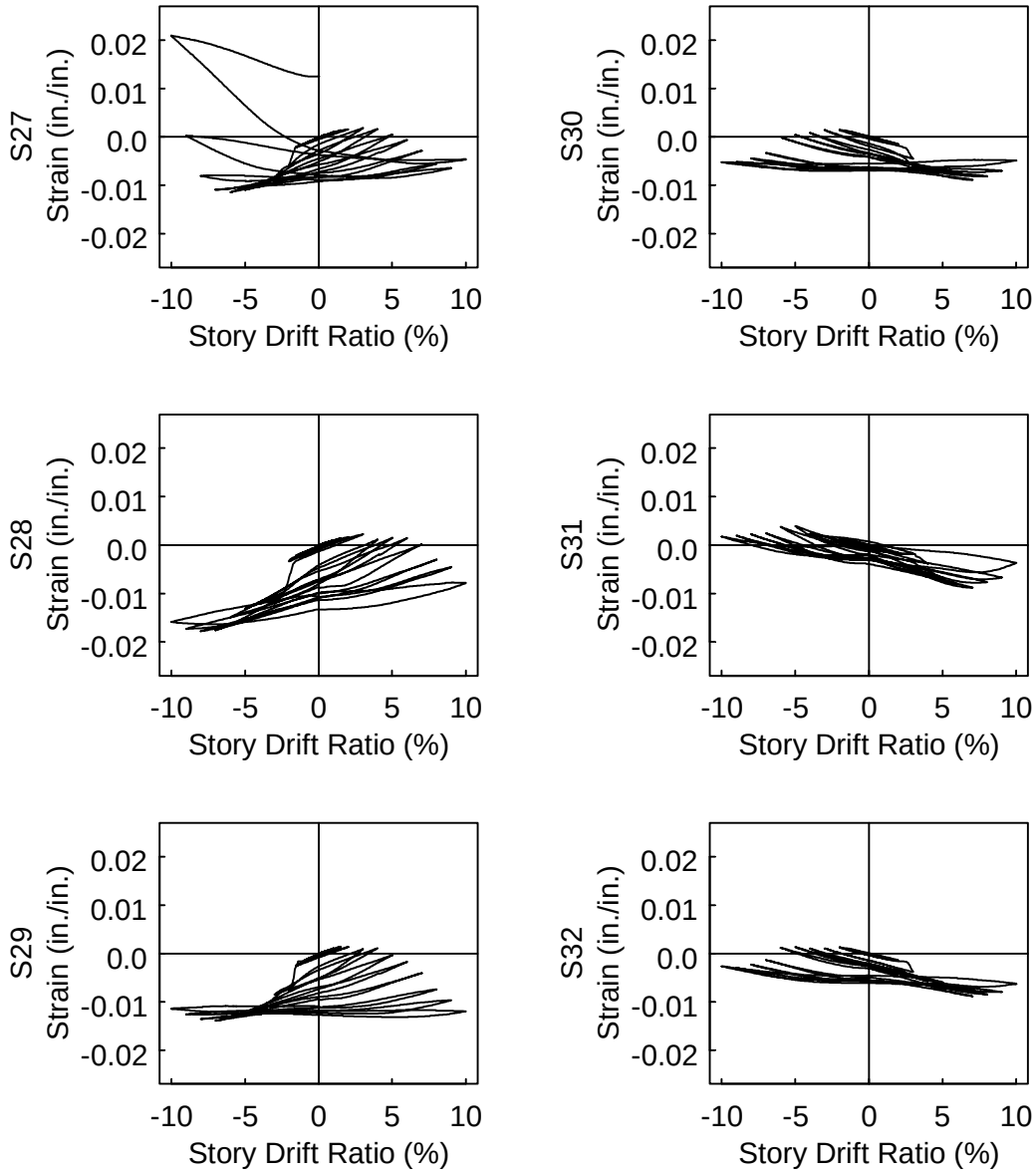

Specimen W14×176-35: Strain Gages S27 to S32

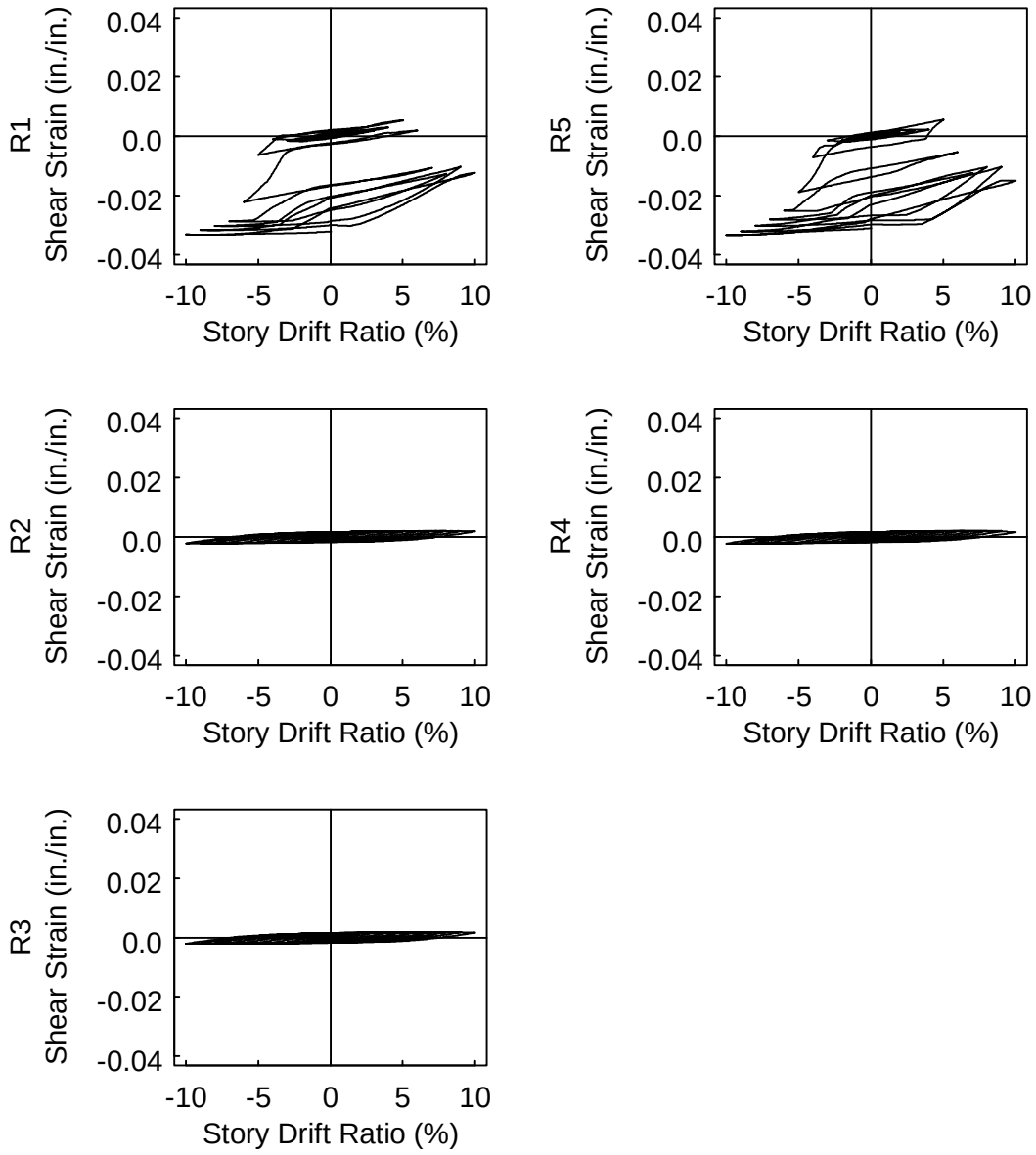

Specimen W14×176-35: Strain Rosettes R1 to R5

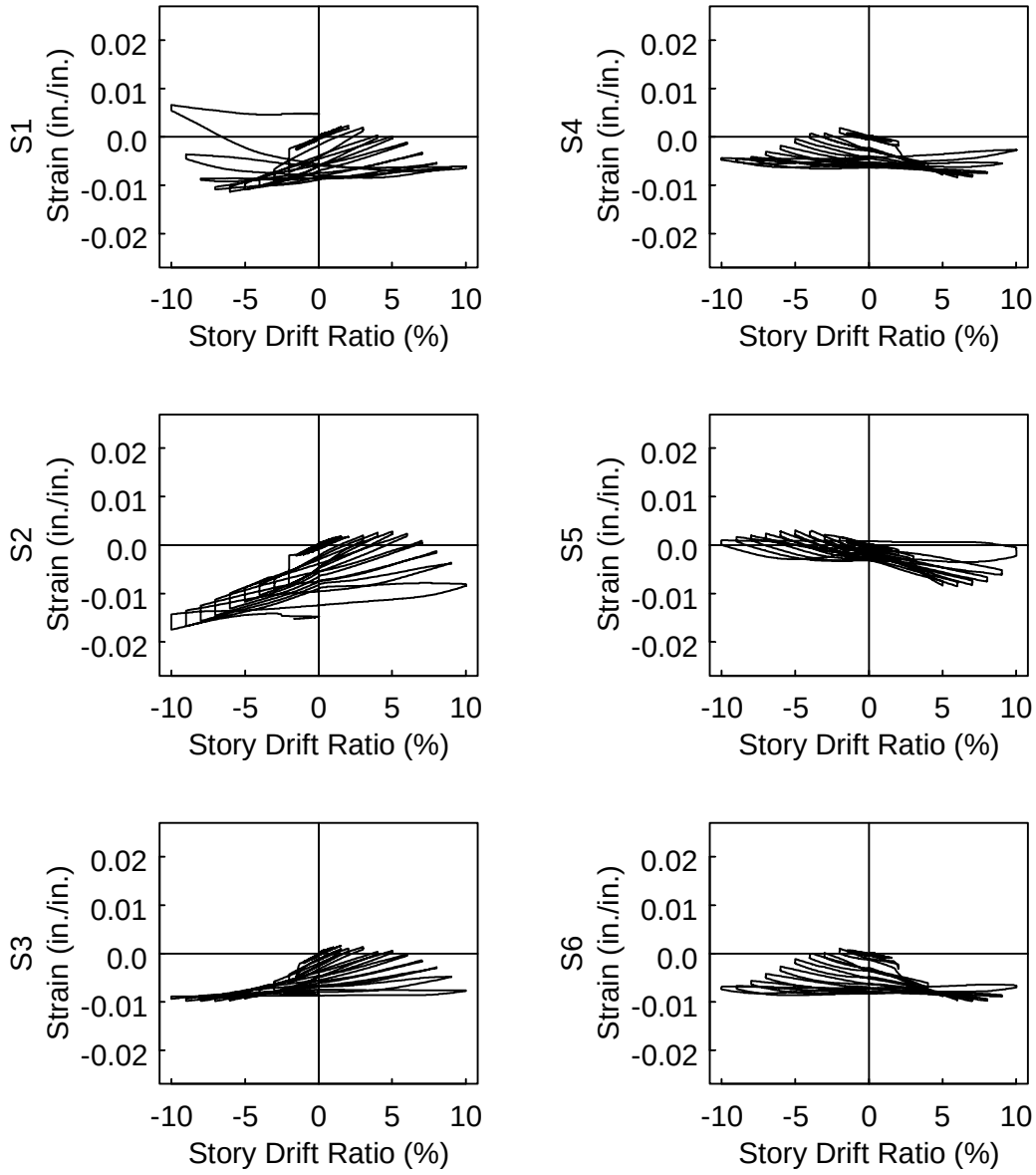

Specimen W14×176-55: Strain Gages S1 to S6

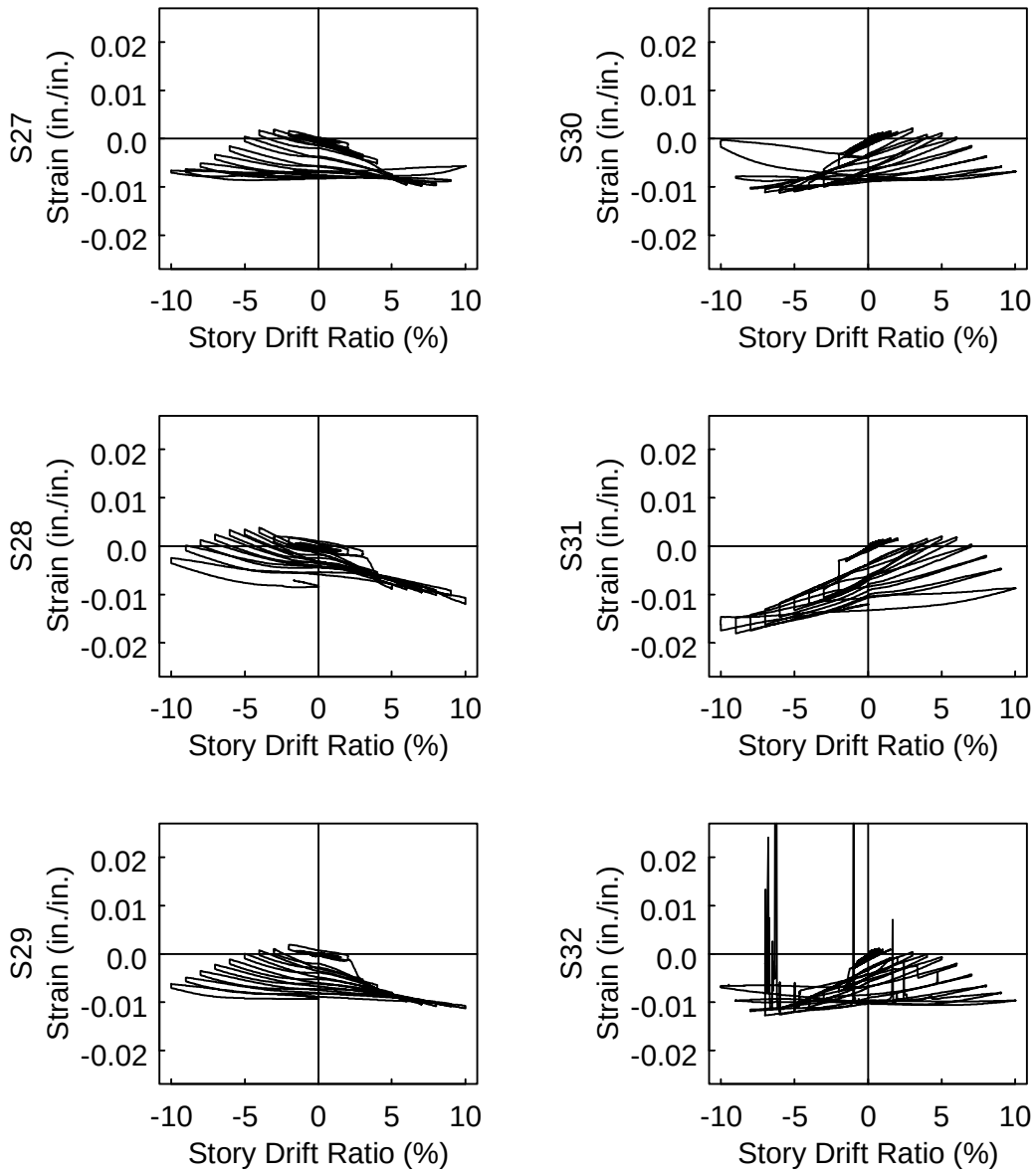

Specimen W14×176-55: Strain Gages S27 to S32

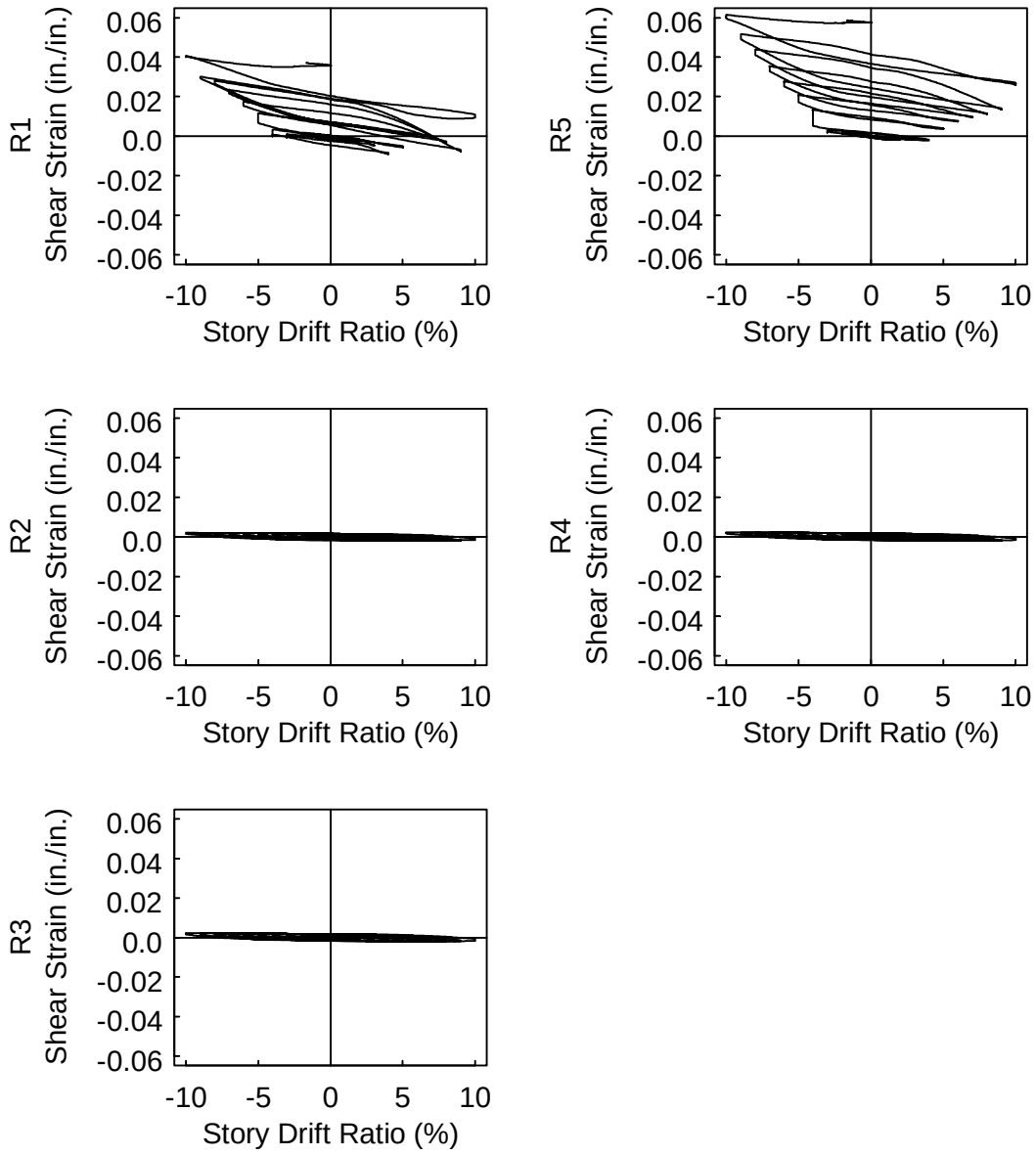

Specimen W14×176-55: Strain Rosettes R1 to R5

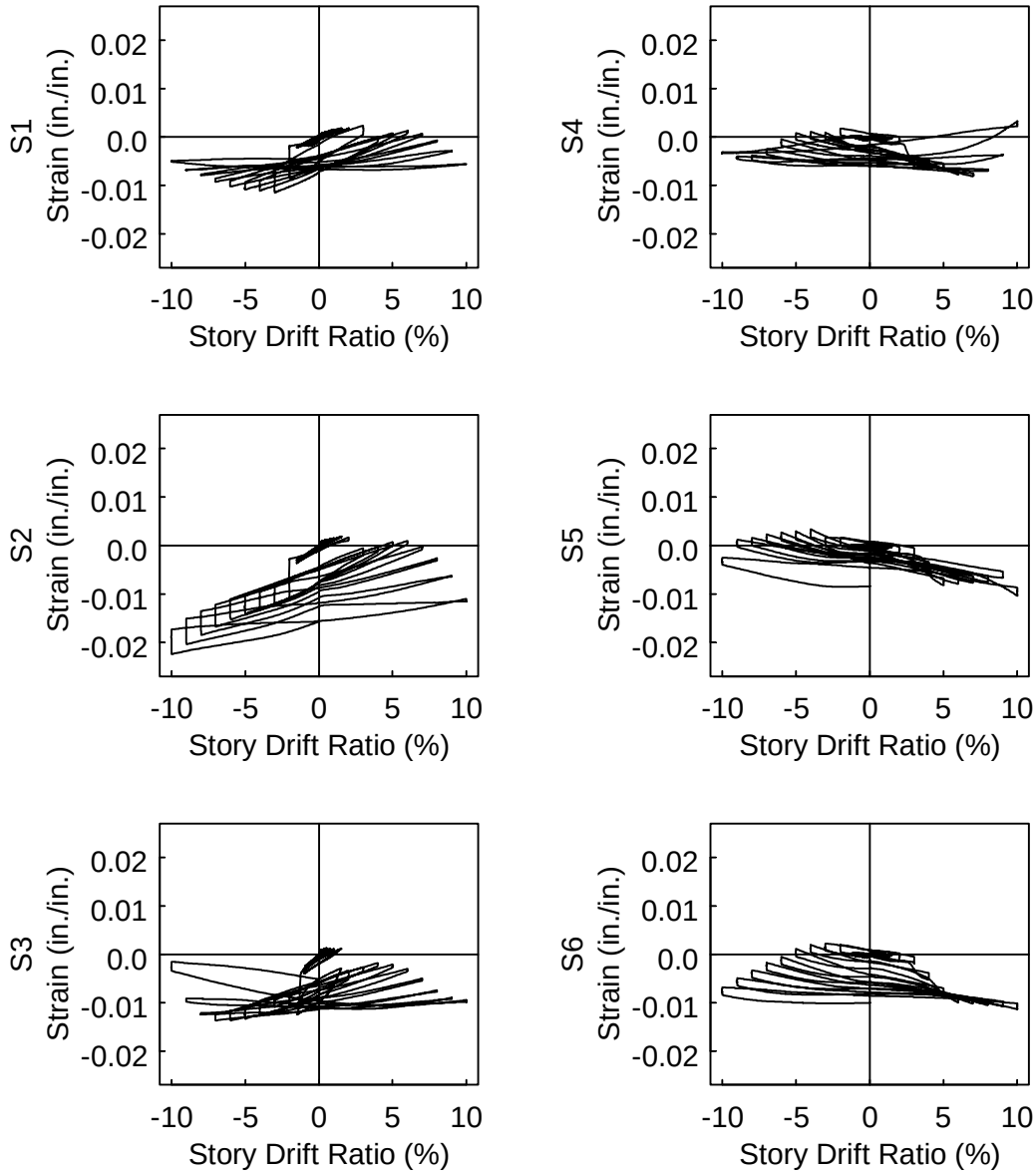

Specimen W14×176-75: Strain Gages S1 to S6

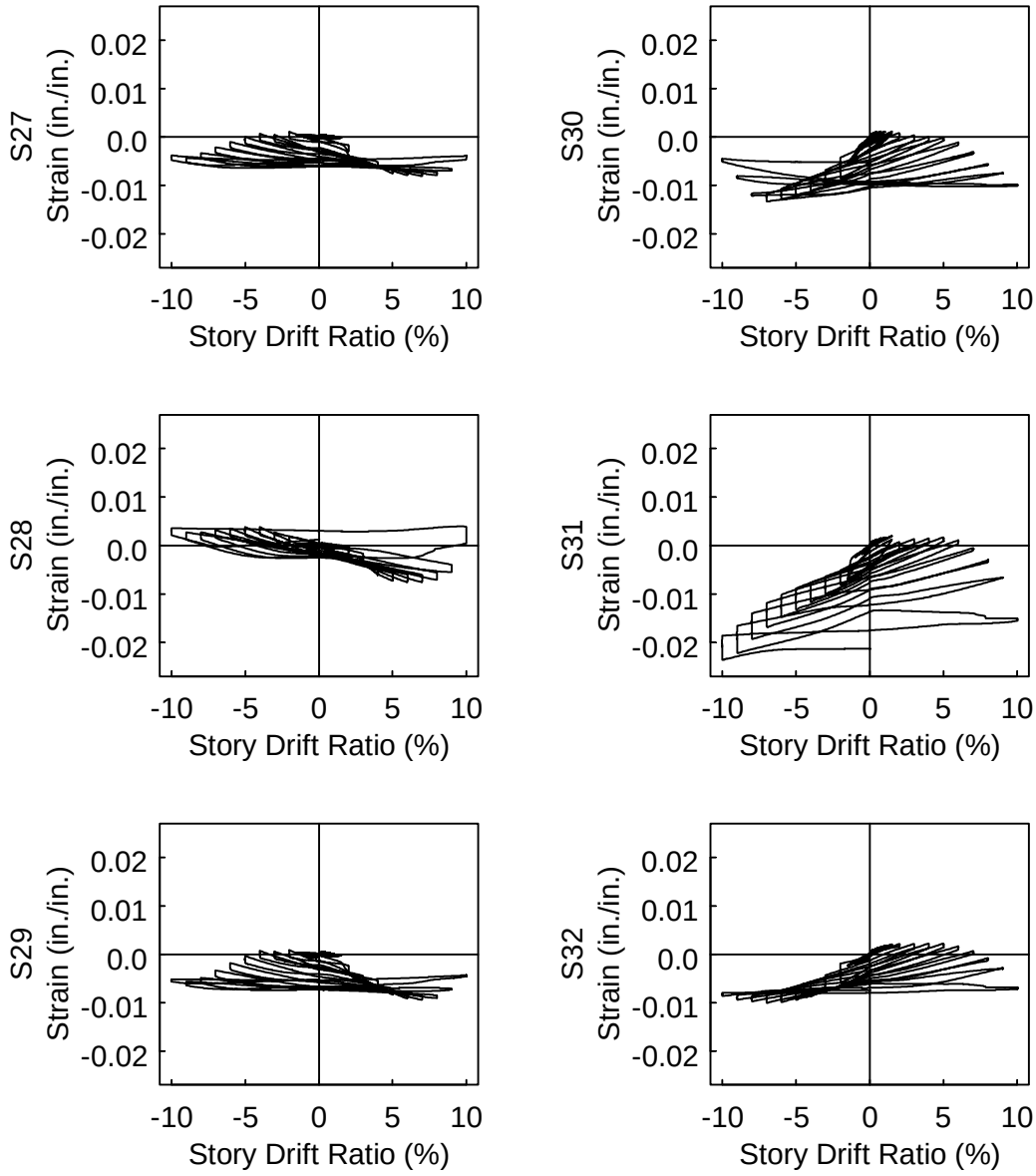

Specimen W14×176-75: Strain Gages S27 to S32

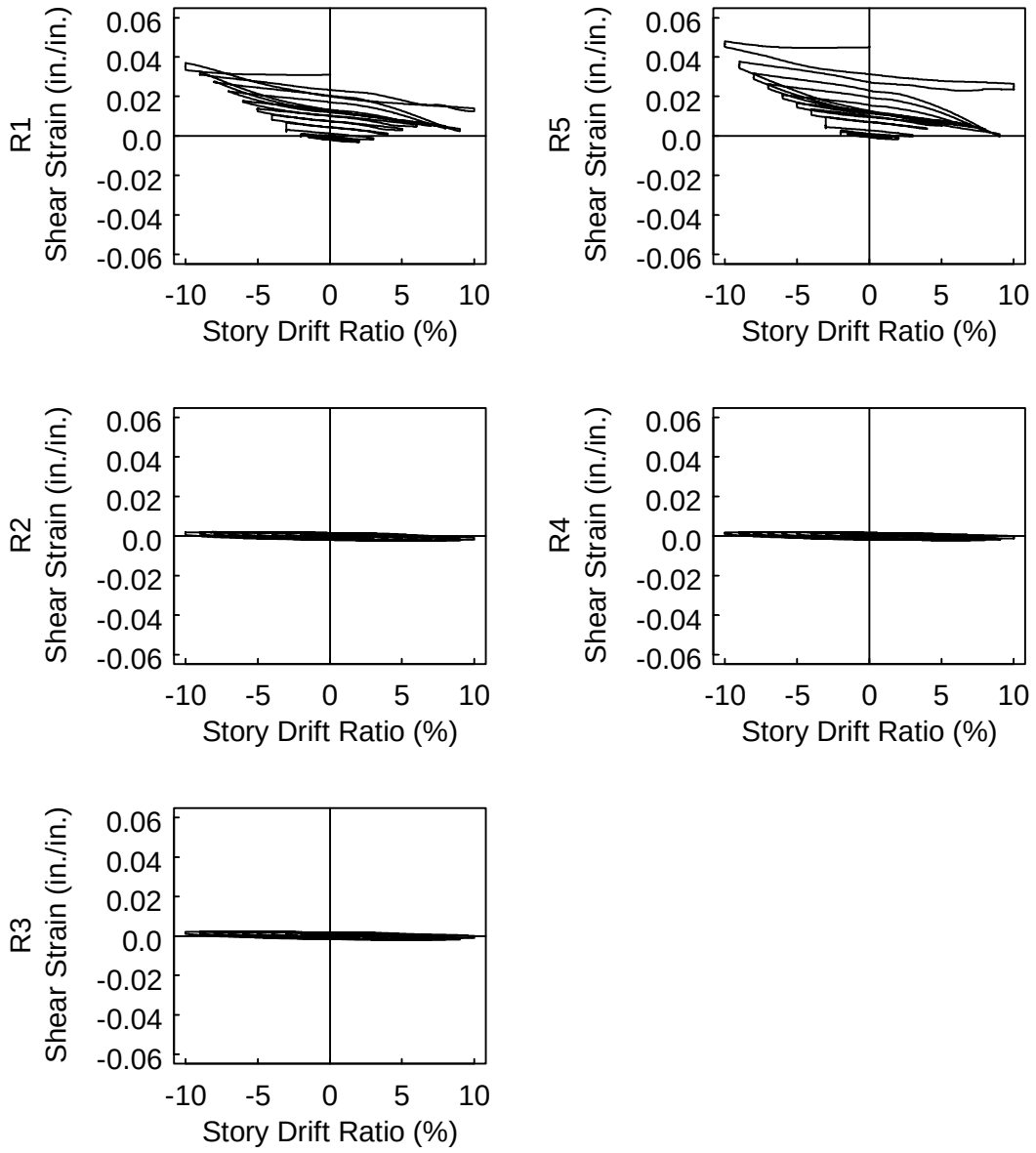

Specimen W14×176-75: Strain Rosettes R1 to R5

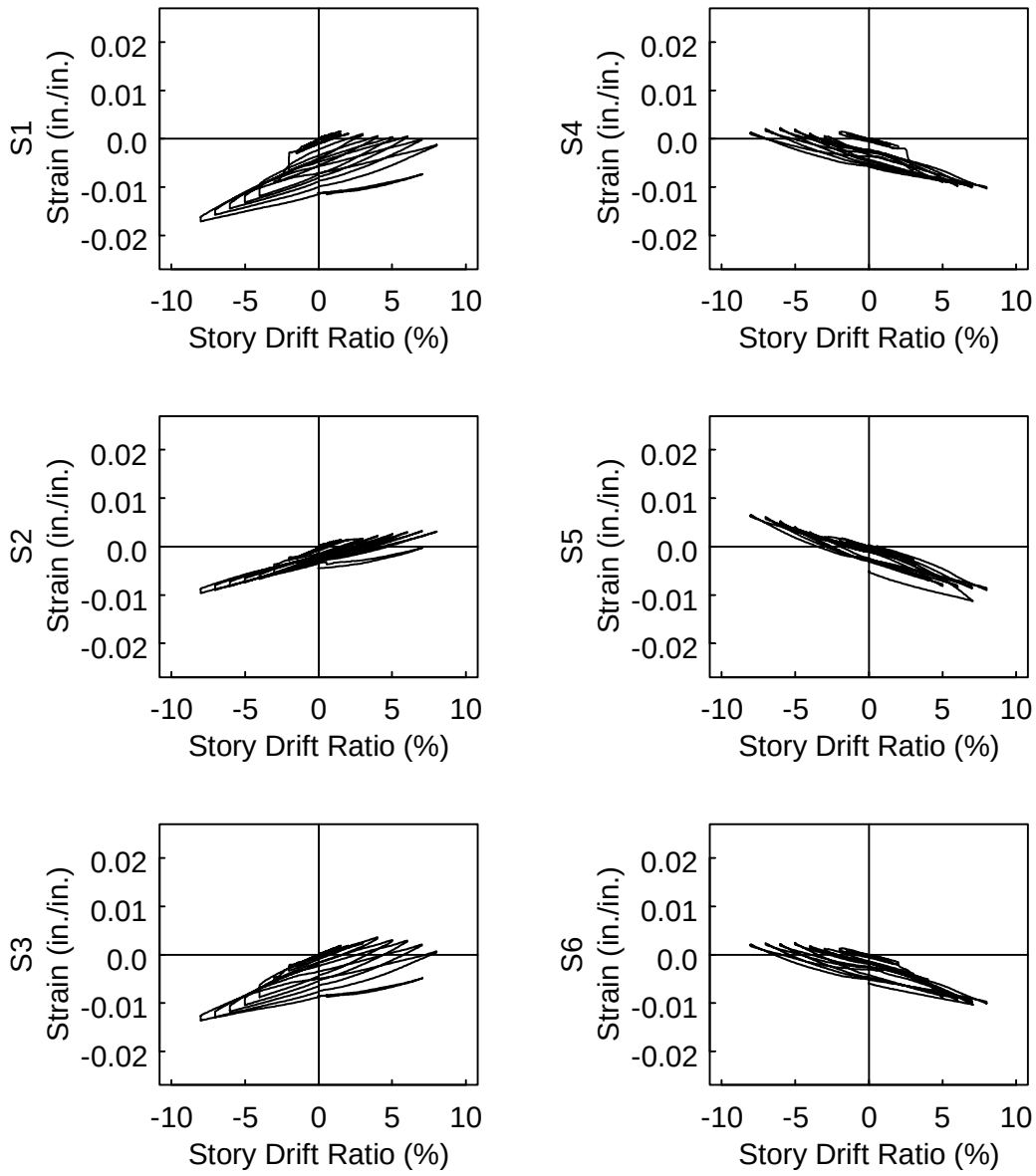

Specimen W14×233-35: Strain Gages S1 to S6

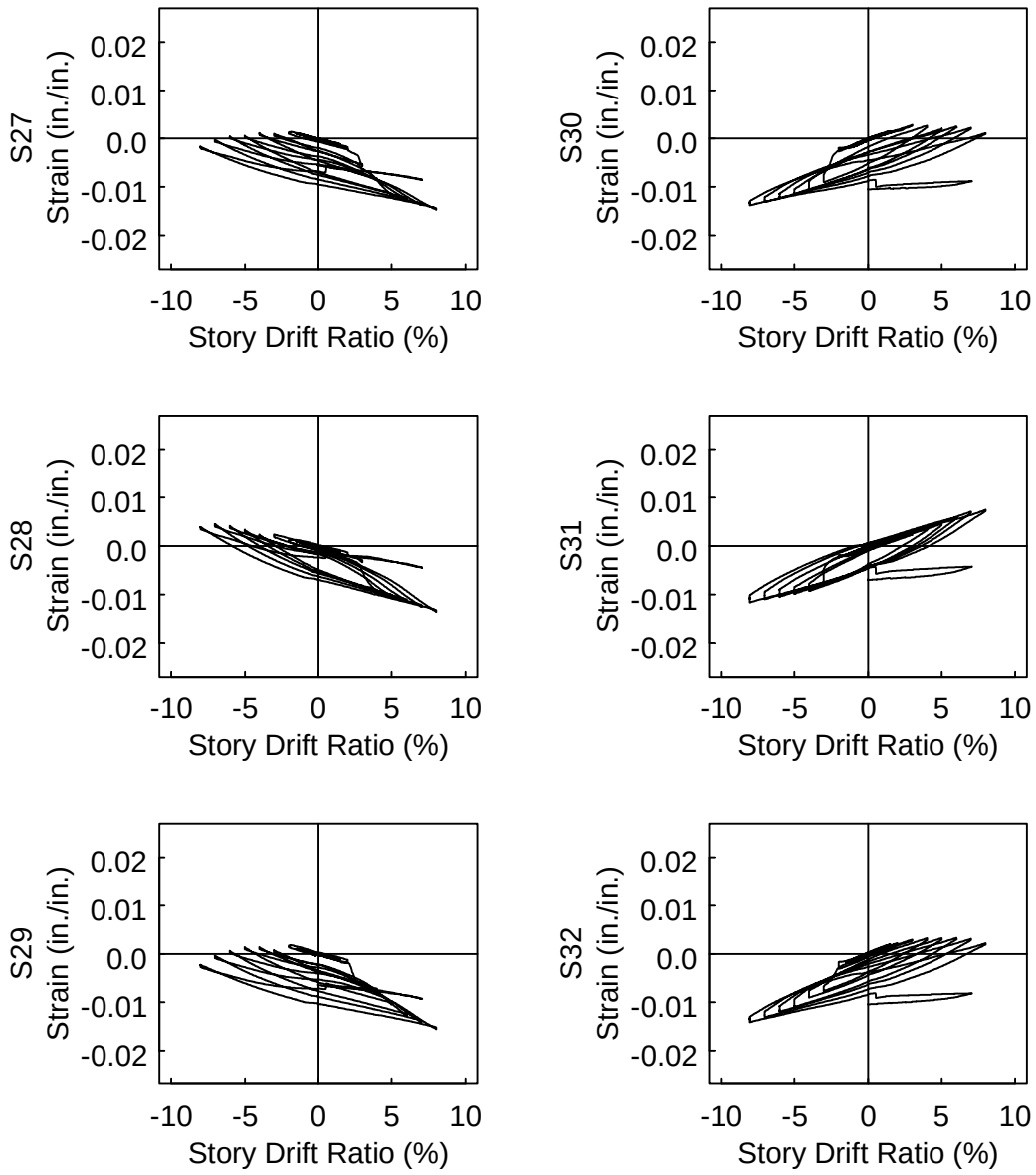

Specimen W14×233-35: Strain Gages S27 to S32

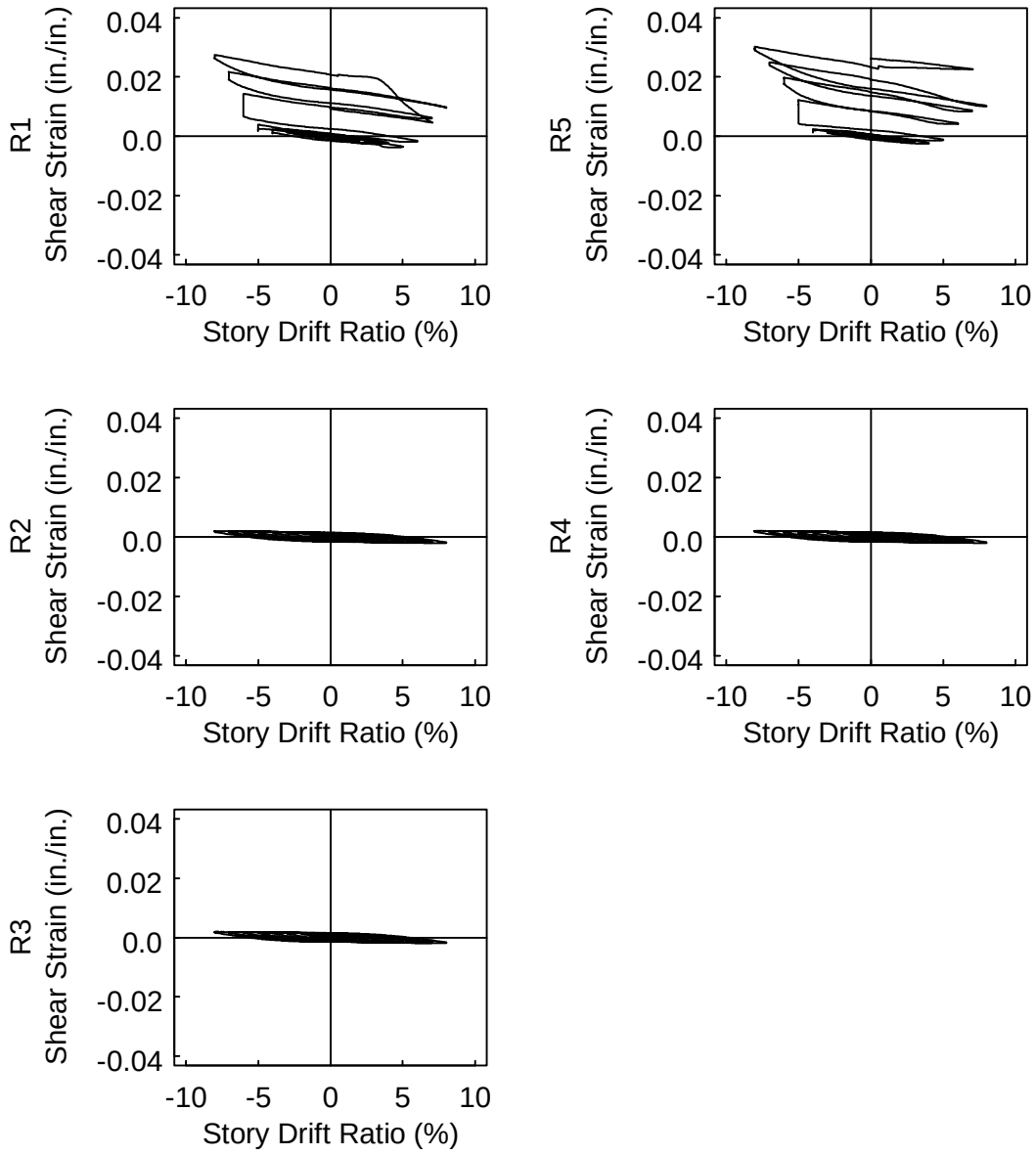

Specimen W14×233-35: Strain Rosettes R1 to R5

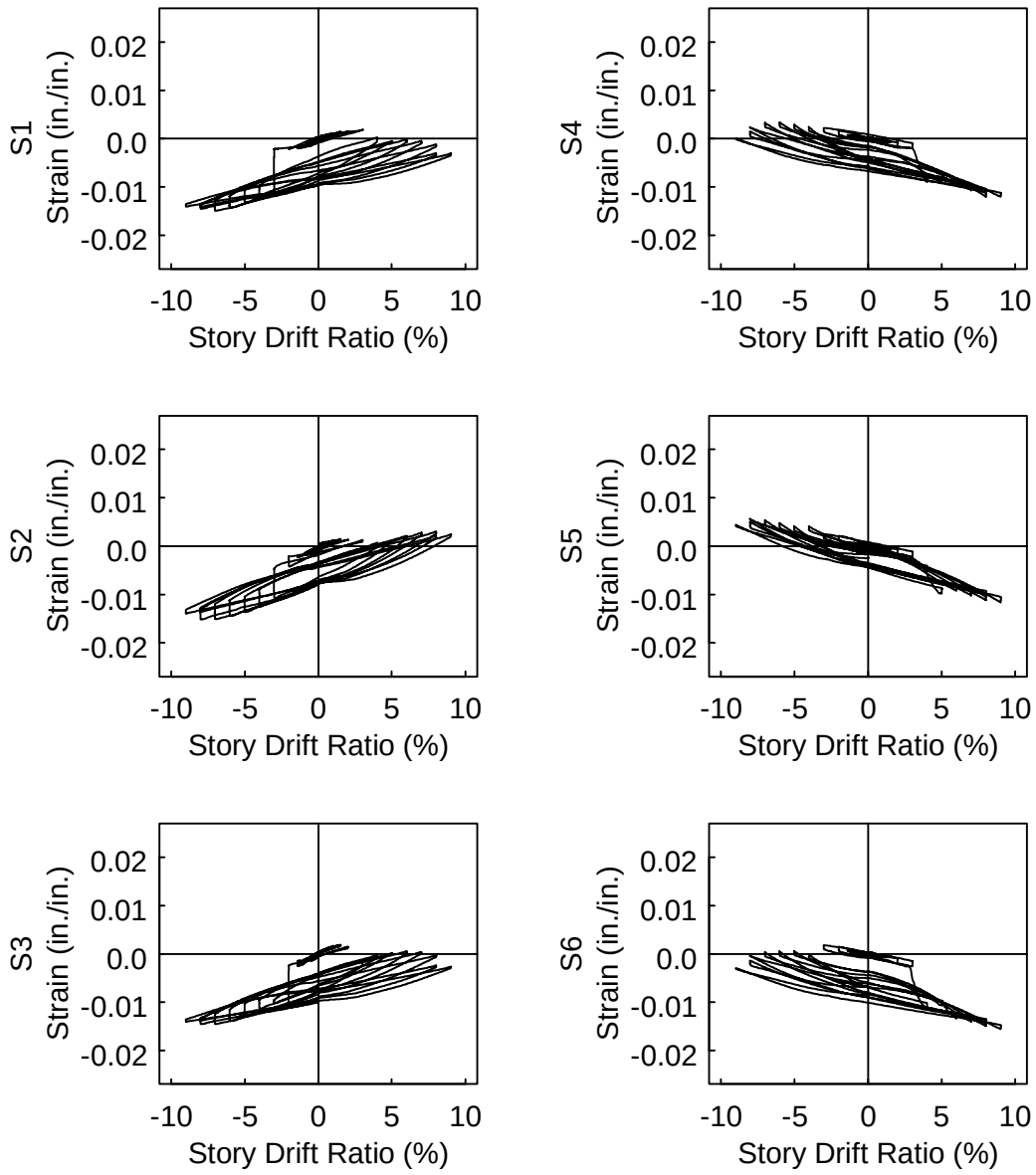

Specimen W14×233-55: Strain Gages S1 to S6

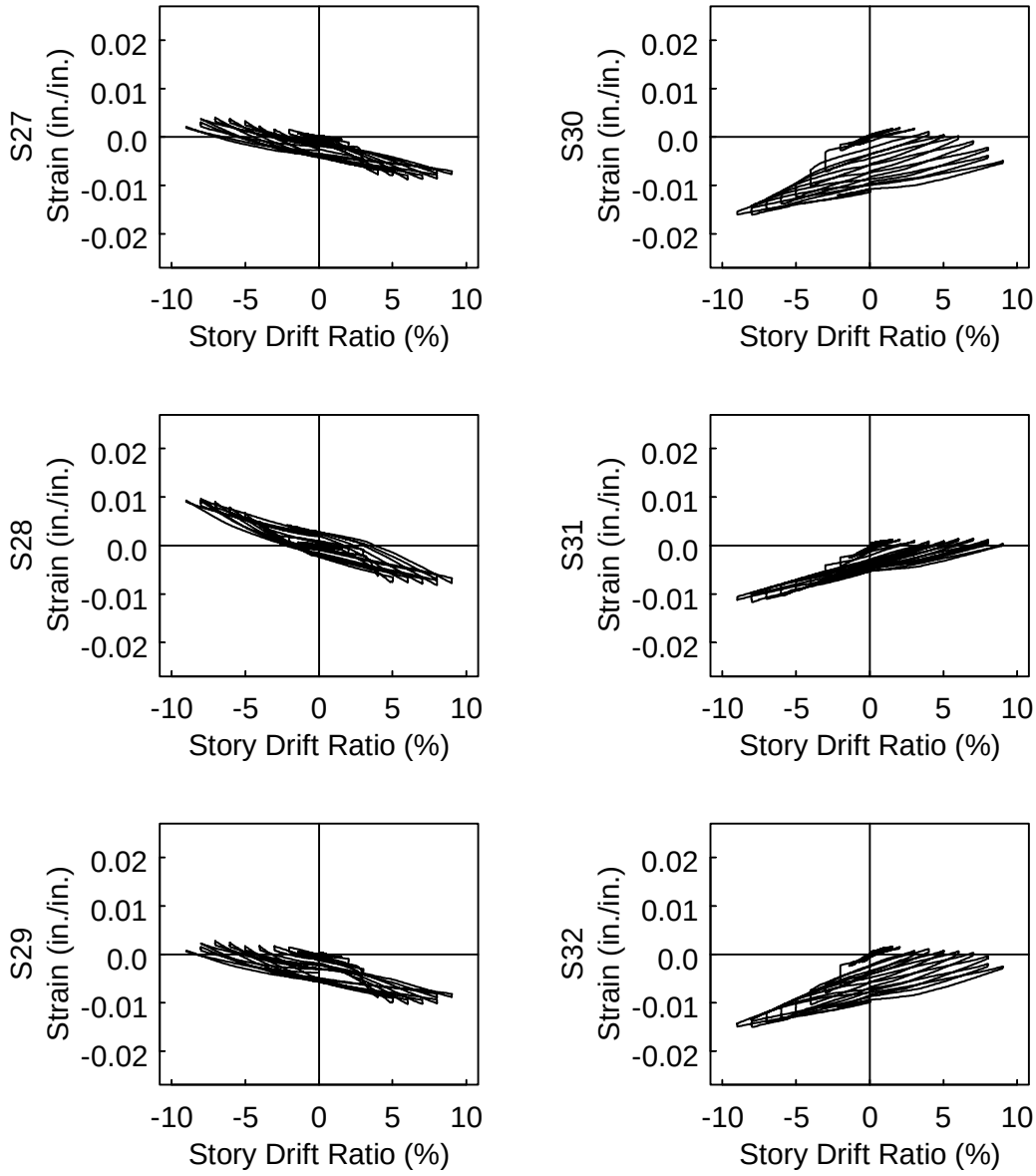

Specimen W14×233-55: Strain Gages S27 to S32

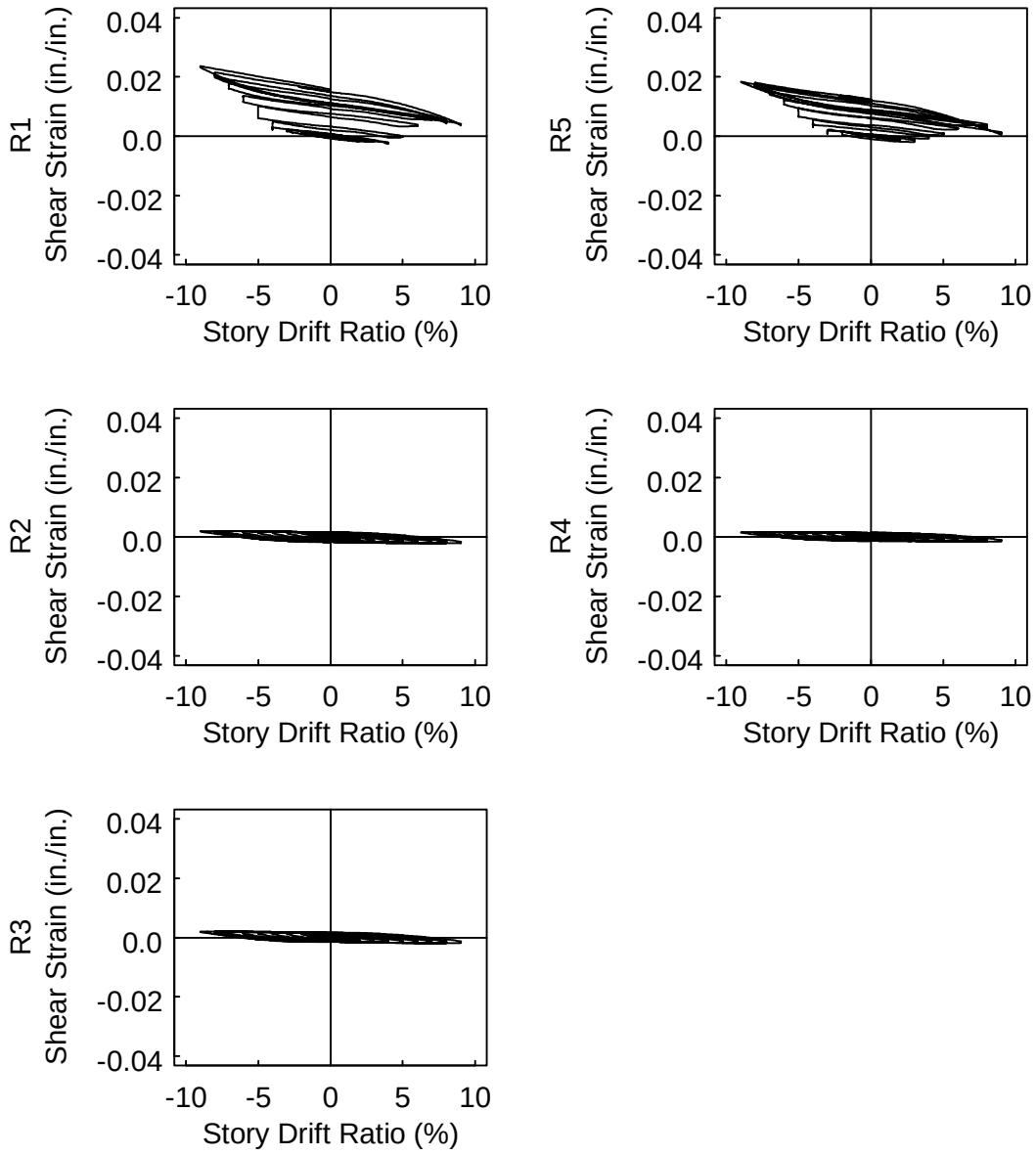

Specimen W14×233-55: Strain Rosettes R1 to R5

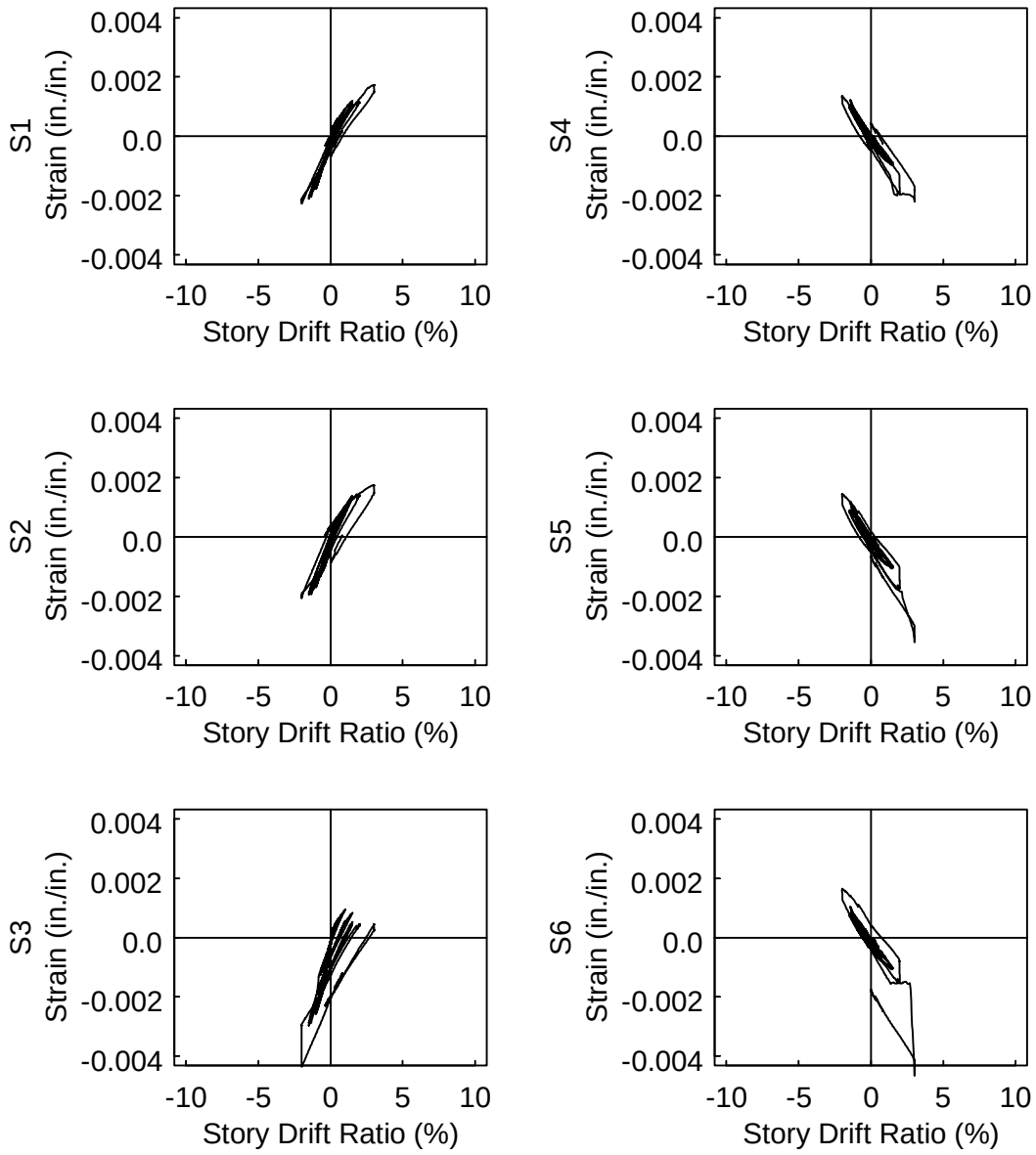

Specimen W14×370-35: Strain Gages S1 to S6

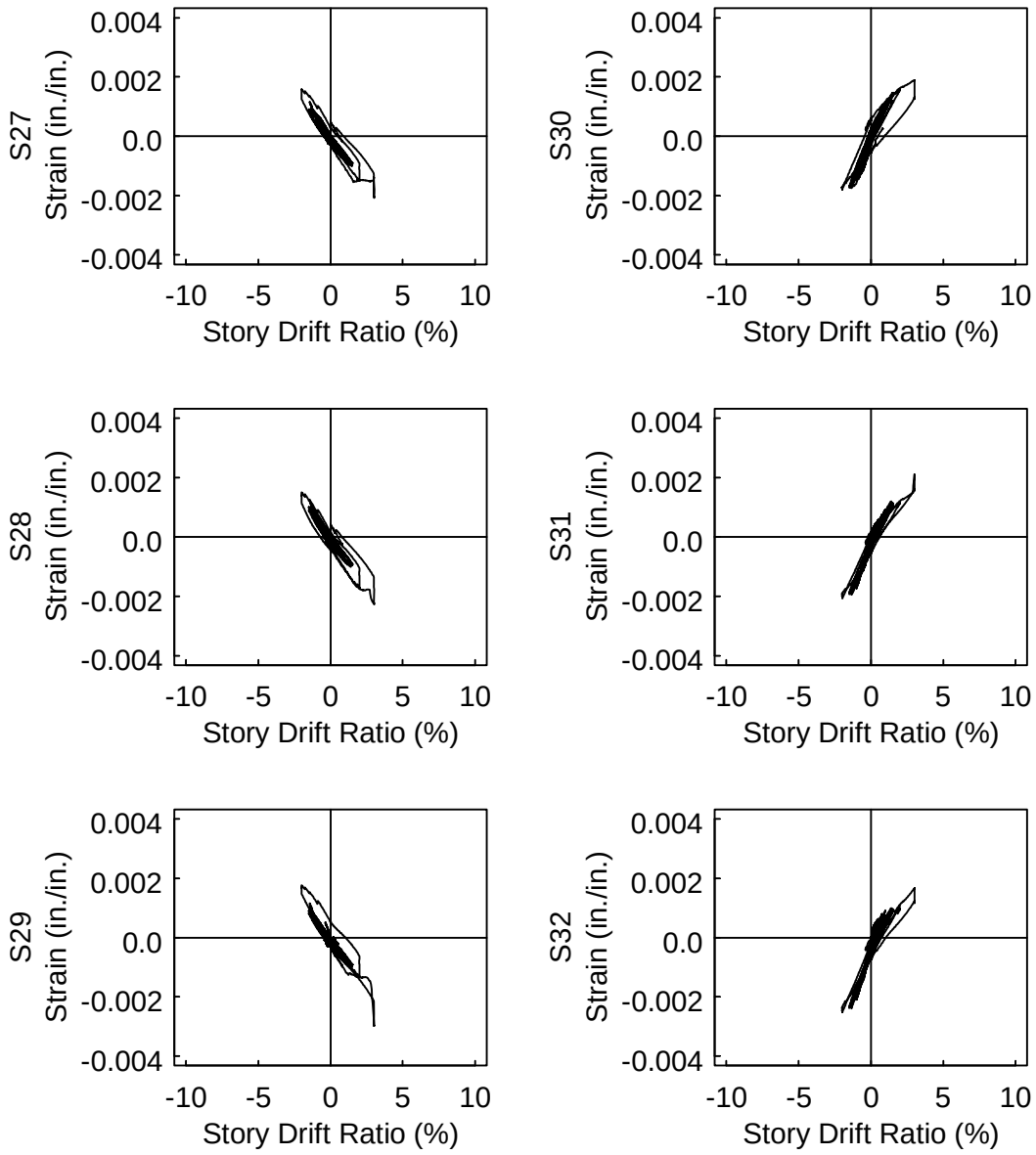

Specimen W14×370-35: Strain Gages S27 to S32

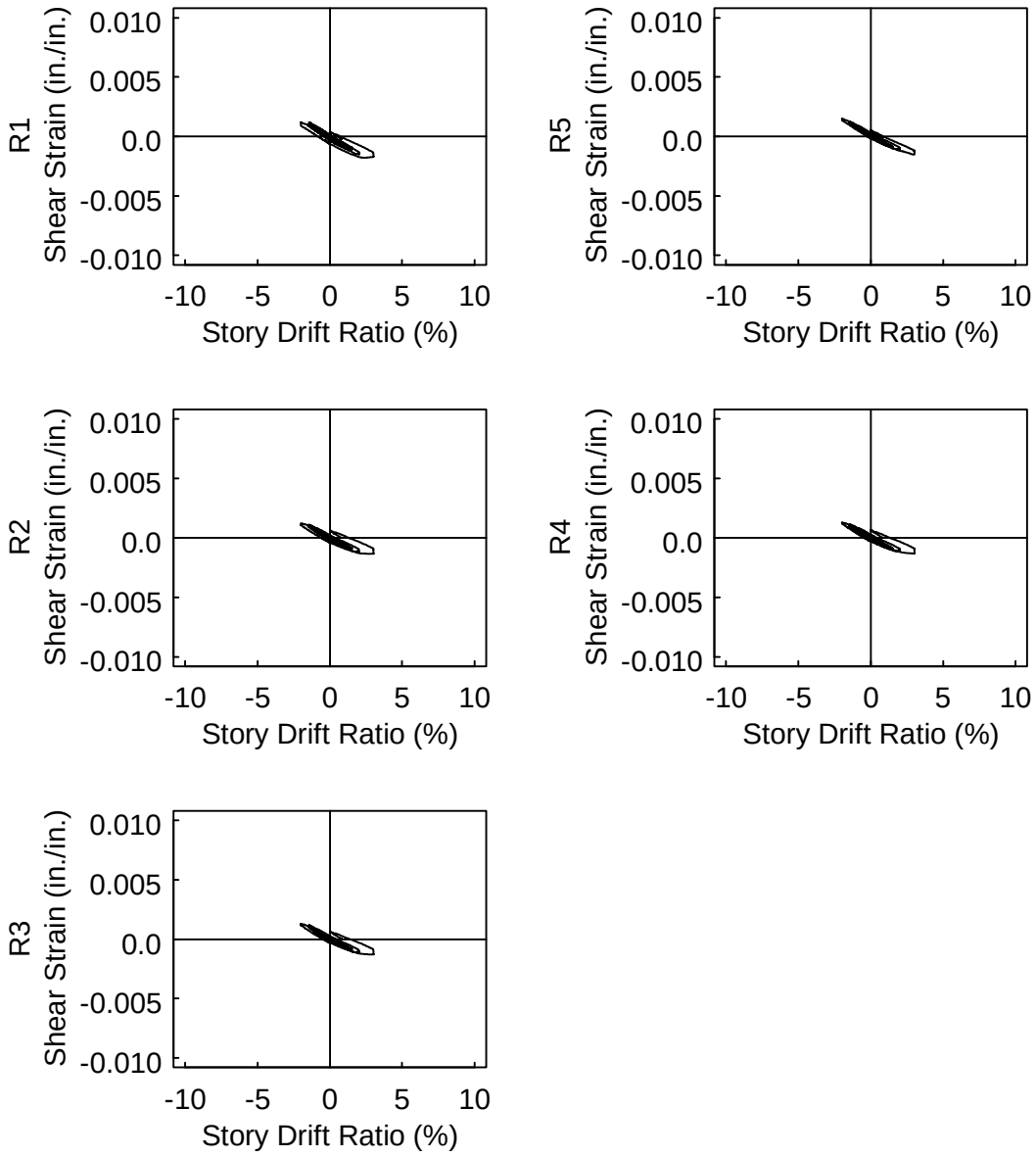

Specimen W14×370-35: Strain Rosettes R1 to R5